POLITECNICO
MILANO 1863

SCUOLA DI INGEGNERIA INDUSTRIALE
E DELL'INFORMAZIONE

Spin dynamics, orbital excitations and charge order in infinite-layer copper and nickel oxides

PhD in
Physics

Author: **Leonardo Martinelli**

Student ID: 947683
Advisor: Prof. Giacomo C. GHIRINGHELLI
PhD cycle: XXXV

to my parents,
to Charlotte

"The consciousness of AC encompassed
all of what had been a Universe,
and brooded over what was now Chaos.
Step by step, it must be done.
And AC said, *Let there be light.*

And there was light–"

Isaac Asimov, *The Last Question*

Abstract

This doctoral thesis is devoted to the investigation of the peculiar properties displayed by infinite-layer cuprates and nickelates, which I carried out during my Ph.D. activity in the group of Prof. G. Ghiringhelli at Politecnico di Milano (Italy). In the last two decades, the group has achieved fundamental results in the field of condensed matter physics, and in particular in the field of strongly-correlated materials. This scientific exploration progressed in parallel with the technical development of Resonant Inelastic X-ray Scattering (RIXS).

Infinite-layer materials are related to the famous class of high-temperature superconducting cuprates. Despite several years of intensive research, many aspects of physics of cuprates still remain unexplained. In particular, a microscopic description of the pairing interaction is still lacking. Although it is known that magnetic fluctuations play a key role, no model can yet give a first-principles description of it. At the same time, the phenomenology outside the superconducting phase is little understood as well, and is possibly the manifestation of a super-entangled state of matter.
The fundamental reason behind this poor understanding is the complexity of the main building block of cuprates: the two-dimensional CuO_2 planes, arranged as a square-lattice of spin-$1/2$ sites. This complexity arises, in essence, from three factors. First, the exceptionally strong correlation between electrons. Secondly, by the reduced dimensionality, which enhances the effect of quantum fluctuations. Third, by the large long-range superexchange couplings which arise from a strong covalency of the planes.

We contribute to the topic by studying infinite-layer cuprates, where the peculiar crystal structure pushes the oxygen-mediate superexchange to the extreme. First, we present a detailed investigation of the magnetic excitations in the infinite-layer cuprate $CaCuO_2$. Using RIXS at the Copper L_3-edge, we provide evidence of an anomaly in the magnetic spectrum close to the antinodal point $(1/2, 0)$ in reciprocal space. We investigate its nature through an innovative combination of measurements, including ultra-high-resolution, polarimetric and detuning RIXS measurements. Referring to

recent theoretical work, our results provide strong evidence in favour of the fractionalization of magnons into spinon pairs. We correlate this behaviour with the exceptionally strong ring-exchange, whose value is enhanced by the large covalency of the system.

The orbital spectrum of infinite-layer cuprates shows fascinating physics as well. In correlated materials, *dd* excitations usually behave as localized, atomic-like transitions. The only exceptions are a handful of one-dimensional cuprate chains, where the full fractionalization of the electrons determines a quasi-particle behaviour of the orbital excitations: *orbitons*. Using RIXS at the Copper L_3 edge on $CaCuO_2$ and Nd_2CuO_4, we report for the first time the presence of mobile orbitons in a *two*-dimensional $3d$ material. Moreover, we show that our experimental observations are incompatible with the current Kugel-Khomskii (KK) model of orbitons in correlated materials. Using an Emery charge-transfer model, we construct an extension of the KK model, introducing a next-nearest neighbours orbiton super-exchange. We show that this model nicely reproduces our experimental findings, and can naturally explain the different behaviour shown by cuprates with and without the apical oxygens. The reason can be traced back, once again, to a prominent role of the oxygen bands, which enhance longer-range exchange interactions.

The second part of this thesis is dedicated to the family of infinite-layer nickelate superconductors, which were first synthetized in 2019. These materials are structurally identical to infinite-layer cuprates: they are composed by a stack of two-dimensional NiO_2 planes, arranged in a square-lattice and with monovalent Ni^{1+} in a $3d^9$ state. Due to their recent discovery, still much is unknown about this class of compounds.
First, we thoroughly investigate the electronic structure of Nickelates using XAS and RIXS at the Ni L_3 and O K edges. In agreement with other recent works, we show that the charge-transfer energy is bigger then in cuprates, and that three-dimensional Nd $5d$ bands are active at the Fermi level. Consequently, we argue that nickelates present a mixed Mott-Hubbard – Charge-transfer character. Additionally, we analyze the different phenomenology displayed by samples with and without an epitaxial $SrTiO_3$ (STO) capping layer. In the former, we report the second independent observation of dispersing magnons, and the first polarimetric measurements revealing unambiguously their magnetic nature. We show that the characteristic energy of magnetic fluctuations softens with doping, in stark contrast to cuprates. Thanks to preliminary calculations, we also correlated this behaviour with the reduced t/U value in the single-band Hubbard picture. In capping-free samples, we discover a much stronger hybridization with 3D Nd bands, which further reduces the electronic anisotropy. We find that this increased three-dimensionality is accompanied by the formation of a charge-ordered

phase.

Overall, our results highlight the importance of two crucial properties in determining the physics of cuprates and nickelates: the strong hybridization between the transition-metal and oxygen bands, and the degree of two-dimensional character.

Contents

List of Figures

List of Tables

Introduction

The main focus of this doctoral thesis is the investigation of the peculiar properties displayed by infinite-layer cuprates and nickelates.

High-critical temperature Copper oxides are one of the most fascinating (and studied) classes of unconventional superconductors. Part of their importance is due to their exceptionally large transition temperatures, which can exceed 130 K at ambient pressure and are still unbeaten. At the same time, their fundamental physics is incredibly complex. After 30 years from their discovery, a microscopic model describing their pairing interaction is still missing. Even their groundstate properties are, to a large extent, still unexplained: their doping-temperature phase diagram is, for example, dominated by numerous competing phases with different broken symmetries. Many of their properties are believed to be manifestation of a very deep entanglement between electrons, which has been dubbed *quantum supreme matter*.
Infinite-layer cuprates are characterized by a peculiar crystal structure. They share the same CuO_2 two-dimensional planes, but the Copper sites are not coordinated with ouf-of-plane Oxygen atoms (the so-called apicals). This has strong impact on their electronic structure. In particular, the charge transfer energy, which quantifies the energy distance between Copper and Oxygen bands, is reduced with respect to other cuprates. Consequently, the longer-range Cu-Cu hopping amplitudes are strongly enhanced. This, as we will explain in the next chapter, has profound implications on the magnetic physics. The spin-$1/2$, antiferromagnetic square-lattice is indeed a very complex system: its pure quantum mechanical nature makes it unstable towards strong next-nearest neighbours and multi-spin interactions. The strong (virtual) mobility of holes also affects the orbital excitations: since they behave similarly to a pseudospin in strongly-correlated systems, this comes with little surprise.

Infinite-layer nickelates share the same structure of their cuprate analogues: two-dimensional planes of NiO_2, arranged in a square-lattice and with monovalent Ni^{1+} in a $3d^9$ state. They have been synthetized very recently, and have generated excitement in the phyiscs community after the discovery of

unconventional superconductivity. Nevertheless, the properties they display are quantitatively different from copper oxides: as an example, the critical temperature is smaller by a factor ten. Correlating these discrepancies to the microscopic parameters might shed light on the mechanisms that lead to the very high superconducting critical temperatures in copper oxides.

The topics described above linked by two fundamental common threads, apart from the obvious one related to their identical crystal structures. The first is the importance of oxygen bands in the description of their properties. Inside the framework of the Hubbard model, the charge-transfer splitting determines the energy of the intermediate states during the virtual hopping of the holes. This has deep consequences on their electronic, magnetic, and orbital structure: as an example, the oxygen bands host the Zhang-Rice singlets in doped cuprates, which are fundamental ingredient for high-temperature superconductivity. Cuprates and nickelates have radically different charge-transfer energies: this is, in essence, the reason behind their radically phenomenology that we will present in the next chapters.
The second common thread is the role of dimensionality. Infinite-layer cuprates, despite a three-dimensional structure, display very two-dimensional electronic physics. It is this "effective" low dimensionality which then determines many of their astonishing properties. On the other hand, some very recent measurements suggest that nickelates have instead a more three-dimensional character.

Interwoven with the study of these materials is an exploration of the capabilities of RIXS. The technique has witnessed fundamental advancements in the last fifteen years, with a constant improvements in energy resolution and the construction of new beamlines in many synchrotrons around the world. In the last two years, the beamline ID32 at the European Synchrotron Radiation Facility (ESRF) has resumed user operation after an important upgrade. The replacement and the new polishing of some optical elements has greatly improved its performance in terms of energy resolution. At the same time, it is now possible to fully exploit the potential of the soft x-ray polarimeter, and to acquire polarimetric RIXS measurements with unprecedented quality. All of these achievements have been fundamental to obtain the results described in this Thesis.

In Chapter 1 we will present a brief introduction of the materials investigated in this thesis: high-T_c superconducting copper oxides. Since this thesis mostly deals with the fundamental magnetic and orbital properties of these materials, we will start with a general discussion on the main building block of cuprates: the two-dimensional, spin-$1/2$, square-lattice CuO_2 planes. We will first present an overview of the experimental phenomenology. Then, we will review the Hubbard model, to which we will often refer in the rest of the thesis. In order to adequately illustrate the complexity of cuprates,

we will also describe their full phase-diagram as a function of doping and temperature.

Chapter 2 and 3 are dedicated to the description of RIXS. We will first introduce the technique on general grounds, outlining the physical mechanism behind the RIXS process. Then, we will derive a formula for the RIXS cross section, the so-called Kramers-Heisenberg equation. This will allow us to state all the conservation laws associated to the RIXS process. We will finally list the set of excitations which can be probed by RIXS, focusing on lattice, magnetic and orbital excitations.
Then, in Chapter 3 we will describe how RIXS is realized experimentally. We will, in particular, focus on the ID32 beamline of the ESRF and the ERIXS spectrometer, which have been used for most of the measurements described in this thesis. We will outline its optical setup, describing some relevant figures on flux, accessible energies, and resolving power. We will also describe the soft x-ray polarimeter installed on the spectrometer, designed by our group at PoliMi and still unique in the world. Finally, we will critically assess the current technical limitations of RIXS, and propose ways to improve its performance in the future.

The next three chapters are the central one of this Thesis, and reports our main results. Chapter 4 presents an investigation of the magnetic excitations in the infinite-layer cuprate $CaCuO_2$. The out-of-plane structure of this compound strongly enhances the multi-spin and longer-range magnetic interactions, which are stronger than in any other known material. Using an innovative combination of measurements including ultra-high-resolution, polarimetric and detuning RIXS measurements, we explore anomalies in the proximity of the antinodal point.

Chapter 5 deals again with cuprates without apical oxygens, but focuses on the orbital excitations. In correlated materials, *dd* excitations usually behave as localized, atomic-like transitions. In one-dimension, however, the reduced dimensionality and the strong exchange integrals cause the appearance of *orbitons*, i.e. collective orbital excitations. Since infinite-layer cuprates have stronger exchange couplings than other 2D materials, we could expect some peculiarity in their orbital spectrum. Using RIXS at the Copper L_3 edge on $CaCuO_2$ and Nd_2CuO_4, we search for possible mobile orbital excitations.

Chapter 6 is dedicated to the investigation of the newly discovered class of superconducting infinite-layer nickelates. It is organized in three different sections. The first one concerns the study of the electronic structure of Nickelates using XAS and RIXS at the Ni L_3 and O K edges. The other two sections are dedicated to the investigation of the low-energy physics in capping-free and STO-capped nickelates. In the former, we discover the presence of a charge-ordered phase with peculiar characteristics. In the

latter, we report the second independent observation of dispersing magnetic excitations, and the first polarimetric measurements.

Finally, Chapter 7 deals with a different but complementary subject: the investigation of electron-phonon coupling (EPC) in two families of superconducting cuprates, $Nd_{1+x}Ba_{2-x}Cu_3O_{6+\delta}$ (NBCO) and $Bi_2Sr_2CaCu_2O_{8+\delta}$ (Bi2212). The role of phonons in HTS is still debated: while EPC alone cannot be the core of the pairing interaction, it has been proposed that a synergy between magnetic fluctuations and phonons might greatly enhance the critical temperature. This proposal is also motivated by recent ARPES work, which reveals a correlation between the strength of the electron-phonon interaction and the magnitude of the superconducting gap. Using RIXS at the O K-edge, we explore the momentum and doping dependence of the EPC.

Chapter 1

High-critical temperature superconducting cuprates

In this first Chapter, we introduce the fascinating class of High-critical Temperature Superconducting (HTS) copper oxides, which will be the main subject of this Thesis. As will be explained in the following, the driving force beneath the peculiar properties of these materials is the correlation between electrons. In Sec. 1.2 we will review some general properties of strongly-correlated materials. We will then describe the general properties of undoped HTS cuprates. Sec. 1.3 outlines their typical crystal structures, as well as their main electronic, magnetic and orbital properties. In Sec. 1.4, we will move to the incredibly complex physics displayed by doped cuprates. We will give a brief description of their temperature-doping phase diagram, and of their most important phases: pseudogap, strange metal, and superconducting phase. We will then focus in more detail on the fate of magnetic excitations upon doping, and on the charge-order phase.

Contents

1.1. High-temperature superconductivity

Superconductivity is undoubtedly one of the most fascinating properties of materials. It is one of the few examples of an evident, macroscopic manifestation of a purely quantum mechanical state.

The first known superconductor is lead, whose properties were discovered by Kamerlingh Onnes in 1911. After that, many more materials were discovered to superconduct at low temperatures. In the '50, Bardeen, Cooper and Schrieffer were also able to provide a successful microscopic description of the phenomenon, the so-called BCS theory. However, the measured critical temperatures were always below 30 K, making their technological employment rather challenging.

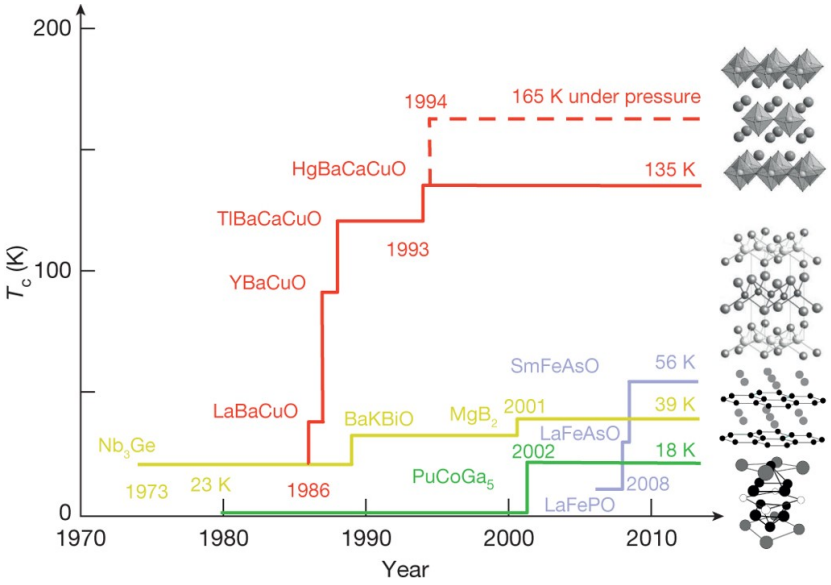

Figure 1.1: Critical superconducting temperatures for different classes of materials, plotted versus their year of discovery. On the right, their representative crystal structure is sketched.

In 1986, J. G. Bednorz and K. A. Mueller discovered that $La_{2-x}Ba_xCuO_4$, a ceramic copper oxide, could reach superconducting critical temperatures far above the predictions of BCS theory [1]. This marked the beginning of the research on High-Temperature Superconducting (HTS) cuprates. Thanks to the work of many more research groups, the first cuprates with critical temperature above the boiling point of N_2 (77 K) were soon synthetized. A summary of the critical temperatures for different superconducting systems is reported in Fig. 1.1. Since liquid nitrogen is much cheaper and easier to produce than liquid Helium, this discovery attracted a lot of attention in view of possible technological applications. Even though other classes of unconventional superconductors have been discovered (e.g. iron pnictides),

copper oxides still hold the record for the highest T_c at ambient pressure (138 K in $Hg_{0.2}Tl_{0.8}Ca_2Ba_2Cu_3O_{8+x}$ [2]).

The research activity on cuprates in the last 30 years has been enormous. The scientific case is so important that it even drove significant development in several experimental techniques, like ARPES and RIXS. Despite all these efforts, a microscopic explanation of superconductivity and other exotic properties of these materials is still lacking. In the next sections, we will briefly review their phenomenology, and list the remaining open questions.

1.2. Correlated electron systems

The properties of many solid materials can be understood in terms of single-particle approaches. These theories are based on the assumption that each electron "moves" independently, inside a periodic field due to the nuclei and the *average* Coulomb potential of the other electrons.
This approximation though fails in those materials where the interaction between the electrons is strong. Such systems are defined as *correlated*, because the motion of an electron is influenced by the all other ones. $3d$ transition metal oxides are probably the most famous example of correlated systems. The relatively localized nature of the $3d$ orbitals indeed translates into a very strong Coulomb repulsion between the electrons occupying them.

Since the number of electrons is huge, the problem of correlated systems is often computationally and analytically intractable. One needs, therefore, to resort to approximated models in order to simplify the treatment.
One of the simplest ones, though incredibly successful, is the Hubbard model. In its basic form, it just assumes two terms in the Hamiltonian. Electrons can *hop* on neighbouring sites with amplitude t (which can be extended to second, third,... nearest neighbours) like in a tight-binding model. However, whenever they occupy the same lattice site, they repel with energy U.

1.2.1. Zaanen - Sawatzky - Allen scheme

The most basic feature of correlated materials is the appearance of an energy gap in the band structure, which is not present in single-particle theories. In $3d$ materials with d^n electrons per site, conduction is given by charge fluctuations of the type $d_i^n d_j^n \rightarrow d_i^{n-1} d_j^{n+1}$. In the Mott-Hubbard scenario, this fluctuations cost an energy $U = E(d_i^{n-1} d_j^{n+1}) - E(d_i^n d_j^n)$, as can be demonstrated with a simple combinatorial count. Phenomenologically, it is like the partially filled $3d$ band gets split into two subbands separated by an energy U: the Lower and Upper Hubbard Band (LHB and UHB). The gap U has to be compared to the typical width $w \sim 8t$ of the $3d$ band. If $U > w$, i.e. the change in kinetic energy is smaller than the Coulomb repulsion, the system

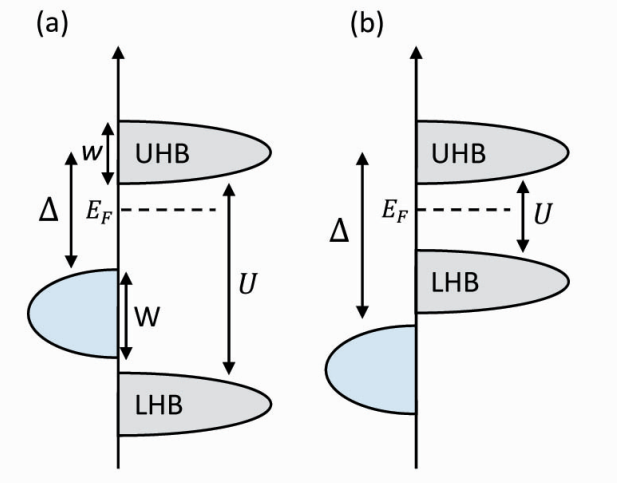

Figure 1.2: Electronic structure of correlated insulators. Ligand band is depicted in light blue, $3d$ bands in light gray. (a): Charge-Transfer insulator, $\Delta < U$ and $\Delta > (W + w)/2$. (b) Mott-Hubbard insulator: $U < \Delta$, and $U > w$.

will become an insulator.

A real description of oxides must, however, take into account the oxygen (or in general ligand) bands. They allow processes of the type $d_i^n \rightarrow d_i^{n+1}\underline{L}$, which create a hole in the ligand band. The corresponding energy is called the *charge-transfer energy* $\Delta = E(d_i^{n+1}\underline{L}) - E(d_i^n)$ [3, 4]. The width W of the ligand will in general be different from that of the $3d$ Hubbard bands.

Zaanen Sawatzky and Allen developed a classification scheme, which is able to predict whether a system is a metal or a insulator, and the character of the valence band. The crucial factors are the widths of the p and d bands (W and w, respectively), Δ and U. Whenever $\Delta, U << w, W$, the system is insulating, and the are two possibilities, sketched in Fig. 1.2. If $\Delta < U$, the ligand bands lie closer to the Fermi level than the LHB, so that the valence band has mostly p-character. In this case, the gap of the material is proportional to Δ, and the material is called a charge-transfer insulator. If $U < \Delta$, the valence band has mostly d-character, and the energy gap in the system is basically proportional to U. In this case, the material is called a Mott-Hubbard insulator.

1.3. Physics of undoped cuprates

1.3.1. Crystal structure

The HTS cuprate materials display a wide range of different crystals structures: three examples are reported in panels (a)-(c) of Fig. 1.3. They are, in essence, layered perovskites with very complicated unit cells that can host

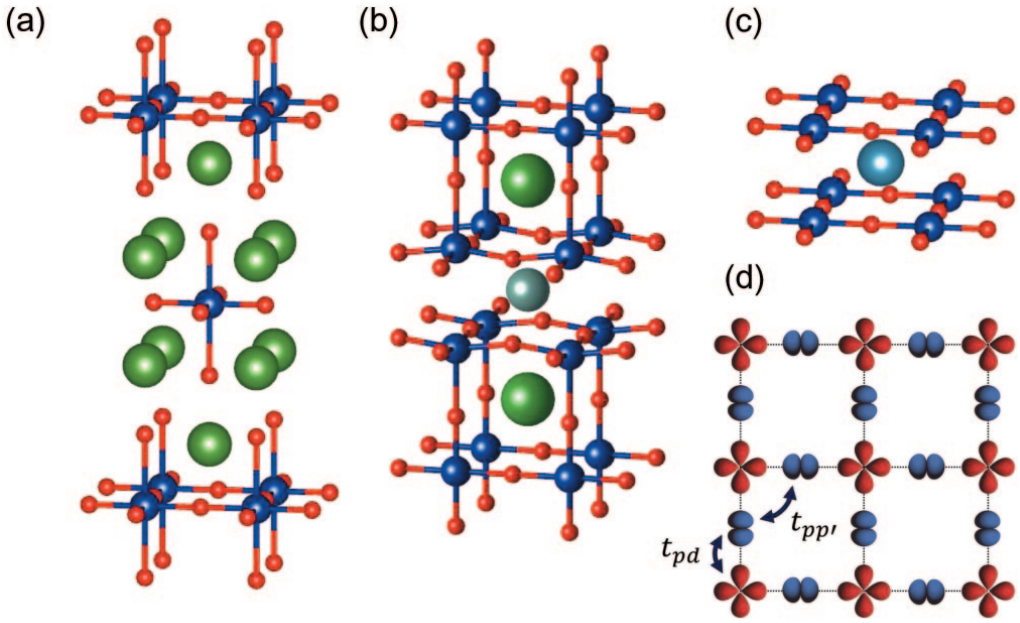

Figure 1.3: Crystal structures of HTS copper oxides. (a): single-layer La_2CuO_4. (b): bi-layer $YBa_2Cu_3O_7$. (c) infinite-layer $CaCuO_2$. (d): Sketch of the CuO_2 planes. Also reported are the two fundamental hoppings t_{pd}, from Cu $d_{x^2-y^2}$ to in-plane O $p_{x,y}$ ones, and $t_{pp'}$, which links two perpendicular oxygen p-orbitals.

several atomic species. However, the share a fundamental building block with a quite simple structure: two-dimensional CuO_2 planes, whose sketch is reported in panel (d) of Fig. 1.3. Each Copper atom is arranged in a square lattice and is coordinated with four oxygen atoms, forming a so-called *plaquette*. The typical in-plane Cu-O distance is $1.92-1.96$ Å, so that the two-dimensional unit cell is of the order of $3.84-3.92$ Å. There is an additional ingredient which is common to most cuprates. In general, the copper atoms might be coordinated with additional oxygen atoms placed along the direction perpendicular to the planes. These are usually called *apical oxygens*. In general, the copper atoms might be coordinate with two, one, or even no apical oxygens: the corresponding environments are depicted in Fig. 1.3 and in Fig. 1.4. Two apicals create CuO_6 octahedra, one gives rise to CuO_5 pyramids, and the structure without them is called *infinite-layer*. The number of apical oxygens has a strong impact on the physics of the materials, as will be discussed in the next sections and in the rest of this thesis.

Outside the copper-oxygen planes, the structures of cuprates differ substantially. In general, the planes are separated by a number of layers called *charge reservoirs*, which contain oxygen and other electronically inert atoms

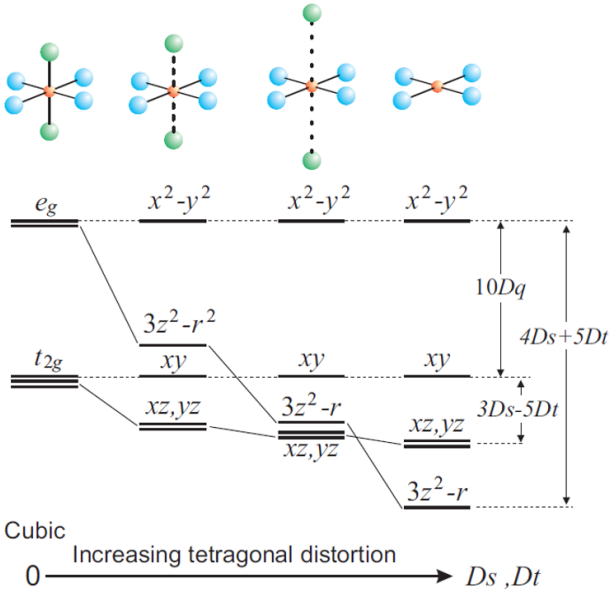

Figure 1.4: Correlation between crystal field energies and local Cu environment in undoped cuprates. The x^2–y^2-z^2 splitting increases when apical oxygens are moved further away from the CuO_2. Readpated from [6].

as rare-earths. As will be explained later, many of the fascinating properties arise when additional holes are introduced in the CuO_2 planes. This doping is commonly obtained by changing the stoichiometry of these reservoir layers, either adding oxygen atoms (like in $YBa_2Cu_3O_{6+\delta}$) and $Bi_2Sr_2CaCu_2O_{8+\delta}$), or with rare-earth substitution (like in $La_{2-x}Sr_xCuO_4$). Part of the introduced charge is then transferred to the planes.

1.3.2. Electronic, orbital and magnetic properties of undoped cuprates

Copper atoms inside the CuO_2 planes are doubly oxidized in all HTS cuprates, with a corresponding $3d^9$ configuration. Therefore, there is a single hole per site. Since there is an odd number of carriers per site, a single-particle picture would predict a metallic behaviour. However, the $3d$ orbitals are quite localized, so that the Coulomb repulsion between them is very strong. Typical values are close to 10 eV [5]. As explained in the previous section, this correlation opens a gap in the electronic structure: charge fluctuations are suppressed and undoped cuprates are insulators. Consequently, the hole is strongly localized on the Copper site.

The d levels are split by the tetragonal/orthorombic crystal field. The symmetry of the groundstate has been determined with several techniques, including soft x-ray absorption spectroscopy (XAS) and resonant inelastic x-ray scattering (RIXS). Like in other $3d$ oxides, the crystal field splits the d

manifold into e_g and t_{2g} states, with the e_g orbitals having higher energy (in electron language) since they point towards the negative ligand ions. They are separated by the so-called $10Dq$ energy, which is of the order of 1.5 eV in the cuprates. However, the different distance between in-plane and apical oxygens gives rise to a substantial tetragonal distortion, parametrized by the Ds and Dt parameters. In particular, the e_g doublet is separated into the x^2-y^2 and z^2 orbitals, with the z^2 having higher energy in hole language. A scheme of the evolution of the d-orbital energies is give in Fig. 1.4. The (x^2-y^2) – z^2 energy splitting increases with the distance of apical oxygens, and is maximum in infinite-layer cuprates where the energy of the z^2 orbital falls below those of t_{2g} states [6]. As will be explained later, this is a crucial parameter, since it is correlated with the superconducting critical temperature [7].

Naturally, the ionic picture is a rough approximation, and the hybridization between the different orbitals cannot be neglected. In particular, the $3d_{x^2-y^2}$ orbitals hybridize with the planar $2p_x$ / $2p_y$ oxygen bands, in the way depicted in panel (d) of Fig. 1.3. In a tight-binding picture, the hopping amplitudes between the σ and π oriented oxygen orbitals are denoted as $t_{pd\sigma}$ and $t_{pd\pi}$, respectively. In cuprates, they are of the order of ~ 1.3 and 0.7 eV, respectively. Inside the ZSA scheme presented in the previous chapter, cuprates are the most famous example of charge-transfer insulators. The energy separation between Cu and oxygen bands is around $2 \div 3$ eV [8–10], much smaller that the splitting between upper and lower Hubbard bands. Moreover, its value is controlled (once again) apical oxygens. In single-layer cuprates, it scales inversely with their distance from the planes [9]. In general, moreover, Δ is lower when the number of apical oxygens is reduced [7, 9]. The charge-transfer energy is therefore particularly small in infinite-layer cuprates, where optical conductivity measurements find a value of ~1.7 eV [11, 12]. The fact that the valence band has mostly p-character has huge consequences on the physics of doped cuprates, as will be explained in the next section.

The magnetic properties of these materials have been studied intensively in the last 20 years, owing to their link to the superconducting properties [8, 13, 14]. Experimentally, it is found that all undoped cuprates are strong antiferromagnets, with Neél temperature even exceeding 300 K [15]. Neutron diffraction has shown that their magnetic structure is consistent with the classical Néel picture of two (ferro)magnetic sublattices with opposite magnetization, reported in Fig. 1.5. The staggered magnetization is reduced by quantum fluctuations (particularly strong in spin-$1/2$ systems) to $\sim 0.55\mu_B$ [16].
The corresponding antiferromagnetic (AF) Brillouin zone is depicted in panel (a) of Fig. 1.5. Its size is half of the real space Brillouin zone, since the AF

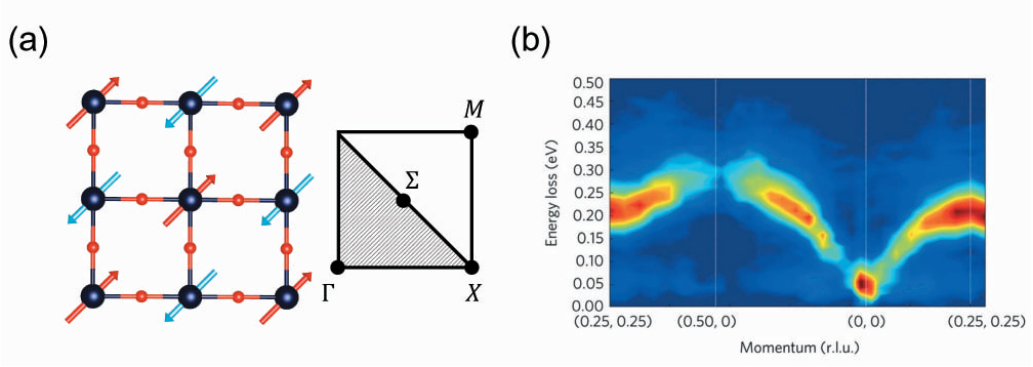

Figure 1.5: (a): antiferromagnetic configuration in undoped cuprates. Also shown in the corresponding Brillouin zone in reciprocal space, with some relevant points highlighted. $\Gamma = (0,0)$, $X = (1/2, 0)$, $\Sigma = (1/4, 0)$, $M = (1/2, 1/2)$. (b): dispersion of magnetic excitations in $YBa_2Cu_3O_{6+x}$ measured by RIXS [23].

order doubles the size of the real-space unit cell. Inelastic Neutron Scattering (first) [17–20] and RIXS (later) [21–24] have revealed the presence of well-defined magnons. Their dispersion is very strong, reaching values of $\sim$300 meV at the AF zone boundary, as it is reported in panel (b) of Fig. 1.5. In undoped materials, the excitations are gapless at the Γ point and at the AF point $M = (1/2, 1/2)$, which hosts a magnetic Bragg peak. Moreover, there is a substantial dispersion along the AF zone boundary, which signals strong longer-range magnetic interactions.

Antiferromagnetism in cuprates arises thanks to the Anderson superexchange interaction [5]. A simple understanding can be grasped in a single-band Hubbard picture. As explained before, charge fluctuations are suppressed by the Hubbard repulsion U. However, the "virtual" hopping of holes is allowed, in the form of a three step process: the hole hops on the neighbouring site, creating a virtual state with high-energy (an effective $\tilde{U}$ related to U and Δ, as explained later), and then hops back at the same site. This process can be understood as a partial "delocalization" of holes, which reduces their kinetic energy. Evidently, such a process can only happen in the spin on neighbouring sites are antiparallel (i.e. antiferromagnetic alignment): in the case of a ferromagnetic alignment, it is forbidden by the Pauli principle since there is only one available state per site. Therefore, the energy of the AF groundstate is lower. More precisely, the process just described has to be intended as a second-order expansion of the Hamiltonian: the localized wavefunction of the hole picks up a non-local contribution, which lowers its kinetic energy. The lowest-order expansion of the Hamiltonian only contains interactions with nearest neighbours $\langle i, j \rangle$ and has the

form

$$\mathcal{H} = J \sum_{\langle i,j \rangle} \mathbf{S}_i \cdot \mathbf{S}_j \tag{1.1}$$

where $J = 4t^2/\tilde{U}$ is the so-called magnetic superexchange, with $t = t_{dd}$ being the effective Cu-Cu hopping amplitude. In two-dimensional cuprates, INS and RIXS find $J \sim 130\,\text{meV}$ [17, 18, 21–24]. In charge-transfer insulators, a more realistic description of the superexchange has to include the oxygen bands, which provide another intermediate state for the superexchange process. In this case, it can be shown that [25]

$$J = \frac{4t_{pd}^4}{\Delta_{\text{CT}}^2}\left(\frac{1}{U_{dd}} + \frac{1}{\Delta_{\text{CT}}}\right) \tag{1.2}$$

where t_{pd}^2/Δ is the effective t_{dd} hopping amplitude. Since in cuprates $\Delta_{\text{CT}} << U_{dd}$, the energy of the intermediate SE process is actually $\sim \Delta_{\text{CT}}$. The characteristic energy of magnetic fluctuations is therefore $\sim t_{dd}^2/\Delta_{\text{CT}}$. Evidently, a higher covalency of the system translates into a larger J [7, 9]. Indeed, cuprates without apical oxygens (including infinite-layers) show the largest energy of magnetic excitations [23].
The nearest-neighbour Heisenberg model is, however, a very rough approximation. The minimal model which gives a reasonable description is a fourth-order expansion of the Hubbard Hamiltonian [17, 23, 26]. Moreover, ARPES measurements clearly show that longer-range hopping integrals t', t'' are definitely not negligible. Introducing them hugely complicates the corresponding magnetic models, because it generates several long-range interactions as well as coupling between more than two spins [26]. Depending on the relative sign and strength of the higher-order magnetic couplings, the system cna host very exotic groundstates and excitations (see e.g. [27]). More on the subject will be presented in Chapter 4.

The large hopping between Cu and O atoms has consequences also for the orbital physics of cuprates. The Hubbard Hamiltonian can be extended to include more than one d orbital, and expanded in powers of t/U as was done to obtain the magnetic Heisenberg Hamiltonian. The result is that the corresponding model for localized electrons has two quantum numbers: the spin $\mathbf{S}$, and the pseudo-spin $\boldsymbol{\tau}$ which quantifies the orbital occupation. With some approximations (hopping only between same orbitals, no Hund's coupling), the spin + orbital Hamiltonian becomes [25, 28]:

$$\mathcal{H} = 2J \sum_{\langle i,j \rangle} \left(\mathbf{S}_i \cdot \mathbf{S}_j\right)\left(\boldsymbol{\tau}_i \cdot \boldsymbol{\tau}_j\right) + E_{\text{CF}} \sum_i T_i^z \tag{1.3}$$

Where the last term is the on-site crystal-field energy. Incidentally, we note that this equation is a rigorous formalization of the Goodenough-Kanamori-

Anderson rules [29]. It is very powerful, since it can account for exotic effects like orbital order. The orbital Hamiltonian has a form virtually identical to that of spins. This suggests that an orbital excitation (i.e. a change of orbital occupation, what is called a *dd* excitation) might "propagate" through the lattice like a spin-wave, what is known as an *orbiton*. A fingerprint of this behaviour would be a **q**-dispersion of the energy of *dd* excitations [28, 30]. The observation of orbitons is, however, rather complicated. First, orbital excitations change the charge distribution around atoms, and therefore strongly couple to phonons [25, 31]. These vibronic effects tend to destroy the quasiparticle behaviour of orbitons [32, 33]. Secondly, in two and three-dimensional materials the motion of orbitons can frustrate the AF background, and they further loose the quasiparticle behaviour [28, 34]. As a result, orbitons have been observed only in a handful of (quasi) one-dimensional cuprate chains [35–37]. A deeper discussion on the subject is provided in Chapter 5.

1.4. Doped cuprates: broken symmetries, strange metal, and superconductivity

The real complexity of cuprates emerges when additional free carriers (holes or electrons) are introduced in the CuO_2 planes. We will focus here on hole-coped compounds, denoting p the number of additional holes per unit cell.

The full phase diagram of cuprates is reported in Fig. 1.6.
Upon doping, long-range AF is rapidly suppressed [8]. Since cuprates are charge-transfer materials, the Fermi level crosses bands with dominant oxygen character upon doping. Actually, it was shown that the most favourable state for doped holes is delocalized over the four p oxygens surrounding the Cu atom, with a spin antiparallel to that of the electron [39]. Such a state is called a *Zhang-Rice singlet*, and has total spin zero: its presence was revealed experimentally by spin-polarized photoemission [40].

The superconducting phase sets in around $p \sim 0.05$, as evident from Fig. 1.6. It is dome-shaped, reaching a maximum T_c at an optimal doping $p \sim 0.16$ and ending around $p \sim 0.26$. Like in convetional superconductors, its onset is accompanied by the emergence of a superconducting (SC) gap Δ. In BCS superconductor the gap is isotropic in reciprocal space [41]. In HTS cuprates, several photoemission studies have demonstrated that the suppression of spectral weight at the Fermi level is anisotropic [42, 43]. In particular, the SC gap has a *d*-wave symmetry: $\Delta = \Delta_0/2(\cos k_x - \cos k_y)$, with the amplitude Δ_0 of the order of 50 meV [10]. The SC state is gapless along the (1,1) direction and maximum along the (1,0) one, and indeed the two directions

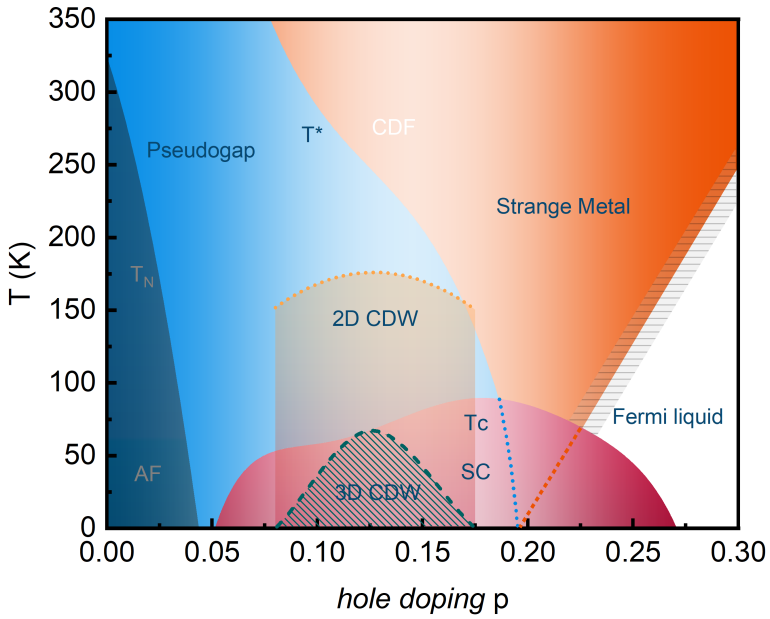

Figure 1.6: Phase diagram of hole-doped cuprates, showing antiferromagnetic, pseudogap, superconducting, and strange metal phases. Also shown are the 2D and 3D CDW domes. Taken from [38].

are dubbed *nodal* and *antinodal*, respectively. Despite the differences with conventional BCS superconductors, a clear Bogoliubov quasiparticle peak can be detected in ARPES experiments [10].
A microscopic theory of superconductivity in cuprates is still missing [8]. There are, however, many hints that magnetic fluctuations are involved. The superconducting transition temperature seems to be positively correlated with the superexchange J [23, 44]. Moreover, a spin-resonance feature appears with the onset of the SC phase (see [14] and references therein). Theoretical works also suggest a similarity between the momentum and frequency dependence of the pairing interactions and of the spin susceptibility [14]. The situation is, however, rather complicated, because long-range interactions cannot be neglected and seem to affect superconductivity as well [9, 45]. Additionally, there is still a debate about the role of phonons. While electron-phonon coupling (EPC) alone cannot account for the very high critical temperatures, a synergistic combination of spin and phonons might enhance T_c [46]. Some recent ARPES measurements also show an intriguing correlation between the EPC of bond-buckling phonon branches and the superconducting gap [47].

The electronic structure is even more interesting outside of the SC dome. High-resolution ARPES measurements have shown that the the depletion of

spectral weight at the antinodal point persists above the SC critical temperature. This *pseudogap* is only concentrated in proximity of the $(1/2, 0)$ point [48], so that the Fermi surface is composed by arcs (see e.g. [10, 48–50]). This depletion of states persists to a temperature T^*, which increases when doping is reduced towards the AF phase [51]. At present, it is not known whether T^* marks a real phase transition or is instead a "crossover" temperature. The pseudogap phase is also accompanied by a great number of broken symmetries. In particular, several form of charge- and spin-orders, and of nematicity (i.e. breaking of the C_4 symmetry at $\mathbf{q} = 0$) have been detected with several techniques (see e.g. [52]). A more detailed description of charge order is given in Sec. 1.4.1.
All these measurements show that T^* drops to zero somewhere close to $p \sim 0.19$. This region of the phase diagram is currently the one that attracts more attention. Some transport and recent RIXS measurements [53, 54] suggest that the pseudogap ends with a Quantum Critical Point (i.e. a phase transition at zero temperature driven by quantum fluctuations). However, recent ARPES measurements suggest instead that the vertical $p = 0.19$ line in the $T-p$ phase diagram marks a temperature-independent boundary [50]. Other magneto-transport measurements question instead the very presence of a sharp phase transition at at this doping [55].

The region of the phase diagram above T^* is called the *strange-metal* phase. ARPES and transport measurements show that no Landau quasiparticle are present, and the electronic properties are dominated by incoherent states [10, 55]. The most famous fingerprint of this phase is a linear-in-T resistivity (see e.g. [56]), accompanied by other anomalous magneto-transport properties [57]. This linear behaviour has been interpreted as a signature of a "planckian" dissipation: the scattering rate τ is proportional to T, and it has the smallest value allowed by quantum mechanics [58]. Interestingly, planckian dissipation is also found in many other materials with strong electron correlations [57]. It was suggested that this phase corresponds to a new state of matter with maximally entangled electrons, named *quantum supreme matter* [59].

1.4.1. Charge and spin order

The pseudgap phase is accompanied by a number of phases with broken translational or rotational symmetries. The most important one is charge-order (or charge-density waves, CDW), a periodic modulation of the valence charge incommensurate to the lattice. Such modulations have been detected through STM [60] and neutron diffraction [61] at first, but mostly with Resonant (Inelastic) X-ray Scattering [40, 62, 63]. The modulation manifests as a weak diffraction peak along the antinodal direction, in a broad range of momenta $\sim (0.15, 0) - (0.35, 0)$ which depends on doping and material.

Resonant scattering experiments have demonstrated that the modulation is one-dimensional in nature. Interestingly their strength is always maximum at a doping $p = 1/8$ in all cuprates. The doping dependence of their wavevector Q_{CDW}, as well as its characteristic value, exhibit important differences between cuprate families. In La-based cuprates, Q_{CDW} increases with doping, while it decreases in ReBCO, Bi2201 and Bi2212 families (cf. [63] and references therein). Additionally, charge order in La-based cuprates is accompanied by a corresponding modulation of spin, with a period that is two times that of the charge. This complex phase is usually referred to as stripe order [61].
CDW emerge below a temperature $T_{\mathrm{CDW}} \sim 150\,\mathrm{K}$, which peaks at the characteristic doping $p = 1/8$, but whose value changes between cuprate families. More importantly, they clearly compete with superconductivity. Their strength either remains constant or drops as T is lowered below the critical temperature [40, 62], while it keeps growing if superconductivity is suppressed by magnetic fields [63]. Moreover, the SC dome has a depression around $p = 1/8$ where CDW are strongest [8].

The exact origin of CDW is still debated. Several experiments have highlighted a coupling between CDW and phonons [64, 65], but a scenario in which CDW arise from nesting of the Fermi surface has also been proposed [66].
Computational studies of the Hubbard model have so far been unable to provide a comprehensive description of the experimental results. On one hand, the presence of a modulation in the charge is a common result in the solution of the single-band Hubbard model [45, 67]. On the other, at present no calculation is able to reproduce the entirety of the experimental observations, incuding the discrepancies among different materials.

1.4.2. Paramagnons

As explained in the previous section, long-range AF order is suppressed at low doping values in hole-doped cuprates. Nevertheless, short-range AF correlations survive until very high doping values. RIXS measurements at the Cu L_3 edge have discovered that magnetic excitations survive in the form of *paramagnons*, i.e. damped magnons [24, 64].
The propagation frequency ω_p of the magnons is, in general, reduced by its undamped value ω_0 by the damping γ, caused by the destruction of the AF order. The damping γ of course increases with doping, but in an anisotropic fashion [24]: it is stronger along the nodal direction, and weaker along the antinodal one. Interestingly, though, the undamped frequency in cuprates *increases* with doping as well [24]. As a result, the propagation frequency of the magnetic excitations remains roughly constant at the $(1/2, 0)$ point, while the excitations get quickly overdamped along the nodal direction. Moreover,

paramagnons retain their "bound" nature even in doped systems, and do not evolve in Stoner excitations [22].
This strange behaviour can be explained by the presence next-nearest neighbour interactions in the $t-J$, and in particular of the three-site term [68, 69].

Chapter 2

Resonant Inelastic X-ray Scattering

In this chapter, Resonant Inelastic X-ray Scattering (RIXS) is introduced on a theoretical ground. First, the RIXS process is described in general terms, and some of the main characteristics of the technique are outlined. Then, starting from the light-matter interaction Hamiltonian we will derive the Kramers-Heisenberg equation, which describes the RIXS cross section. We will discuss its most important implications, explaining how some of the characteristics of the RIXS technique can be inferred from the form of the equation. We will also compare RIXS to other scattering techniques, illustrating the advantages brought by the resonant character, as well as its limitations. We will then outline the set of excitations accessible with RIXS, also referring to the flourishing literature. In particular, we will describe how RIXS can give access phonon, magnetic and orbital excitations in strongly correlated systems, which are the main topic of the present thesis.

Contents

2.1. Introduction

Resonant Inelastic X-ray Scattering is a *photon-in-photon-out*, synchrotron based, spectroscopic technique. A high-brilliant, monochromatic and polarized beam of photons is shined onto a sample. After a (rather complex)

interaction with the system, light is scattered in arbitrary direction, which possibly changes its momentum, energy and polarization state. By measuring the intensity, energy (and polarization) of photons scattered in a certain solid angle, it is possible to track the excitations left in the system as a result of the interaction with x-rays. RIXS shares many common traits to other well-known inelastic scattering techniques as Inelastic X-ray (IXS) or Neutron (INS) scattering, and even with Electron Energy Loss Spectroscopy (EELS). The characteristic which makes RIXS unique is its *Resonant* character. The energy of the incident beam is tuned to match a specific core resonance of the material, which may lie in the soft, tender or hard x-rays regime.

2.2. The RIXS process

In virtue of its resonant character, RIXS is based on a two-step process. The photons, having momentum $\mathbf{k}_i$, energy $\hbar\omega_i$ and polarization $\boldsymbol{\varepsilon}_i$, promote a core electron to an unoccupied state above the Fermi level. The choice of the absorption edge is critical, because it determines, among other technicalities, the range (and the strength) of accessible excitations, as well as the overall intensity of the RIXS signal. Fig. 2.1 shows a sketch of the RIXS process. Incident x-rays have an energy tuned to match a core absorption resonance of the material, so that a core electron is promoted above the Fermi level and leaves a very energetic core-hole behind. Common absorption edges in the soft x-ray regime include the L edge of $3d$ transition metals, K edge of light elements and $M4,5$ edge of lanthanides. The intermediate state, having a core hole, is highly unstable and rapidly ($< 1fs$) decays. While the vast majority of relaxing transitions is made through Auger processes, a fraction of the excited atoms decays by emitting another x-ray photon. This will, in general, have a different $\mathbf{k}_o$, $\hbar\omega_o$ and $\boldsymbol{\varepsilon}_o$ than the incident one. The case in which $\hbar\omega_i = \hbar\omega_o$ is a form of elastic scattering, i.e. of diffraction: indeed, RIXS can be indeed used to detect Bragg peaks. In general, however, photons will lose energy in the scattering process ($\hbar\omega_o < \hbar\omega_i$), and the system will be left in an excited state. In particular, the excitation (or the ensemble of excitations) left in the system will have an energy and momentum given by:

$$E^{exc} = \hbar\omega_i - \hbar\omega_o$$
$$\mathbf{q}^{exc} = \mathbf{k}_i - \mathbf{k}_o$$

plus an angular momentum which can be supplied by the incident photon spin. The range of excitations accessible through RIXS is incredibly large, and will be discussed later.

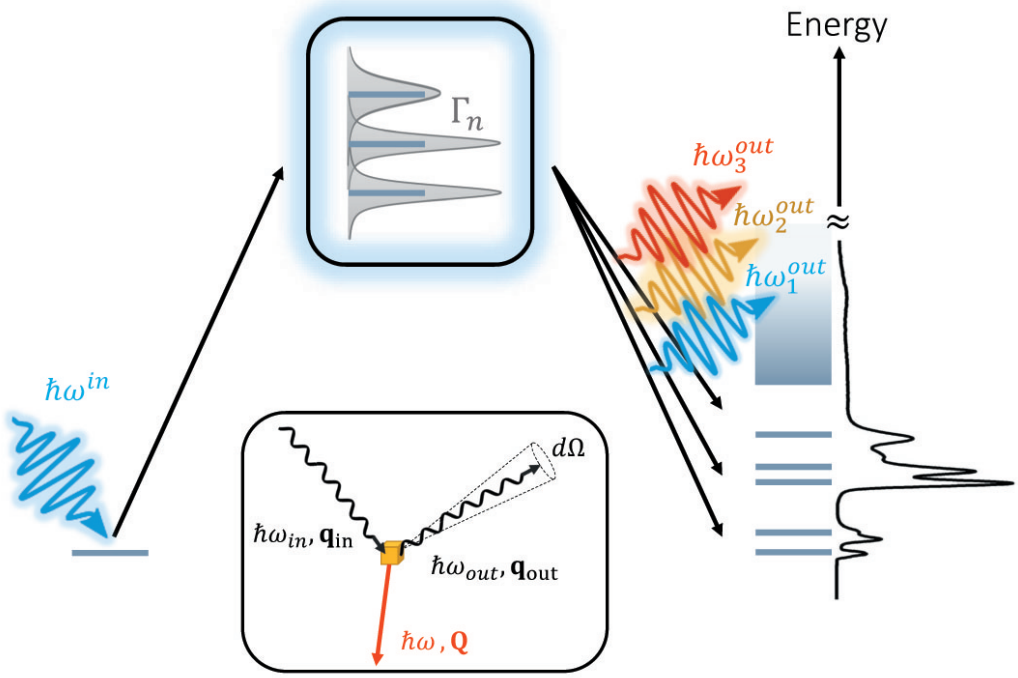

Figure 2.1: Scheme of the RIXS process. Incident x-rays are tuned to a specific absorption edge of the material. They excite a core electron above the Fermi level, create an excited state with a core-hole. After a time $\tau_n = \hbar/\Gamma_n$, the intermediate state relaxes: The core hole is filled and and another x-ray photon is emitted. The energy of the photons depends on the excitations left in the system: in the figure $\hbar\omega_3 < \hbar\omega_2 < \hbar\omega_1$. The sketch in the bottom inset highlights the conservation of momentum during the RIXS process.

Due to its characteristics, RIXS can be understood as the intersection between more standard inelastic scattering techniques, as inelastic neutron scattering (INS) or Electron energy-loss spectroscopy (EELS), and x-ray absorption spectroscopy (XAS). The resonant character indeed gives RIXS *element* and *chemical* sensitivity. The ensemble of excitations visible with RIXS is that characteristic of the specific element corresponding to the absorption edge selected. Moreover, since the oxidation state and the chemical environment also strongly determines the XAS profile, RIXS can distinguish between atoms of the same element sitting on different sites in the unit cell (i.e. it has *site* sensitivity). An example of this is shown in Fig. 2.2, which shows XAS and RIXS spectra measured at Oxygen K-edge in $YBa_2Cu_3O_7$. The material's unit cell hosts two inequivalent oxygen atoms in the two-dimensional CuO_2 planes and in the one-dimensional CuO_3 chains, clearly distinguishable in the XAS. The RIXS spectra collected at the two different edges are shown in panel (a). Evidently, the energy and intensity of the visible excitations (phonons, in this case) are different, because they pertain

to different sites of the unit cell.

The use of x-rays also brings two major advantages. The first one is charge *neutrality*: no electrons are added or removed from the sample in the RIXS process. This means that no charging problems are present when measuring insulating samples, like for example happens in photoemission. The second one is (tunable) bulk sensitivity. The penetration depth of x-rays ranges between 100 nm and 10 µm for the soft and hard x-rays regimes, respectively. This means that no special treatments to clean samples' surfaces are needed. However, this does not prevent to use RIXS for the study of surface states or multilayers. By playing with the experimental geometry (e.g. by decreasing the incident angle of x-rays), the effective penetration depth can be decreased down to a few nanometers, especially in the soft x-ray regime. Another advantage brought by the resonant character is a much higher cross-section relatively to INS. Indeed, while macroscopic sample with ~mm size are needed for neutron studies (an old joke tells that samples must be the size of your *thumb*), RIXS can be used on thin films and even monolayers [70].

However, nothing comes for free. There are two major disadvantages of RIXS with respect to other inelastic scattering techniques. The first one is purely technical: RIXS requires the use of a *core* absorption edge that has to be tuned to the specific material. This means that the incident energy will lie in the $10^2 - 10^4$ eV range. Many of the interesting excitations in solids and liquids, however, lie well below 1 eV, and one needs correspondingly good energy resolution to access them. Practically, this means very high resolving power ($> 10'000$). Neutrons, instead, use much smaller incident energies, so that the requirements in terms of resolving power are less stringent. In principle, energy resolution below 1 meV can be achieved in IXS using sophisticated monochromators. This setups require, however, fixed incident energies, and are therefore incompatible with the tunable incident energy required by RIXS. Additionally, matters are further complicated in the soft x-ray regime: at these energies crystal monochromators are not available and gratings must be used, which are generally difficult to fabricate and have lower performances.

The second disadvantage of the RIXS technique is the complexity of the Kramers-Haisenberg equation. The resonant character greatly complicates the calculation of the RIXS cross section. On the other hand, the response of INS or IXS is usually straight-forward to compute, so that the interpretation of experimental results is much simpler.

2.3. RIXS cross-section

In this section, we derive and comment the the expression for the RIXS cross-section. The first step is, of course, to write the right Hamiltonian that describes the light-matter interaction. In principle, one should start from the full Dirac equation. However, relativistic corrections can be safely ignored provided that the electromagnetic energy is smaller than twice the mass of the electron.

The non-relativistic Hamiltonian is then:

$$\begin{aligned}\mathcal{H} = &\sum_j^N \frac{(\mathbf{p}_j + e\mathbf{A}(\mathbf{r}_j))^2}{2m} + V_{ee} - \sum_j^N e\phi(\mathbf{r}_j) + \sum_j^N \frac{e\hbar}{2m}\boldsymbol{\sigma}_j \cdot \mathbf{B}(\mathbf{r}_j) + \\ &+ \sum_j^N \frac{e\hbar}{2(2mc)^2}\boldsymbol{\sigma}_j \cdot \{\mathbf{E}(\mathbf{r}_j) \times \Big[\mathbf{p}_j + e\mathbf{A}(\mathbf{r}_j)\Big] - \\ &\qquad\qquad \Big[\mathbf{p}_j + e\mathbf{A}(\mathbf{r}_j)\Big] \times \mathbf{E}(\mathbf{r}_j)\} + \\ &+ H_{Darwin} + \int d\mathbf{k} \sum_{\mathbf{k},\varepsilon} \hbar\omega_{\mathbf{k}} \Big(c^\dagger_{\mathbf{k},\varepsilon} c_{\mathbf{k},\varepsilon} + \frac{1}{2}\Big)\end{aligned} \tag{2.1}$$

where $\mathbf{A}$ and ϕ are vector and scalar electromagnetic potentials, respectively, and $\mathbf{E} = -\nabla\phi - \partial_t\mathbf{A}$ and $\mathbf{B} = \nabla\times\mathbf{A}$ are the electric and magnetic fields. H_{Darwin} is the Darwin term, which affects the energy of the s-orbitals. The first three terms represent the kinetic energy, the electron-electron interaction and the electron-crystal interaction of the sample. The fourth term is the interaction between spins and the magnetic field, while the fifth one can be understood as the relativistic spin-orbit coupling. Finally, the last term is the energy of the electromagnetic field.

All in all, after expanding the terms containing $\mathbf{p}$ and $\mathbf{A}$, the Hamiltonian can be written as $\mathcal{H} = H_0 + H'$, where H_0 only contains terms describing the system and the electromagnetic fields, and H' is the interaction Hamiltonian:

$$\mathcal{H}' = \sum_{j=1}^N \left[\frac{e}{m}\mathbf{p}_j \cdot \mathbf{A}(\mathbf{r}_j) + \frac{e^2}{2m}\mathbf{A}^2(\mathbf{r}_j) + \frac{e\hbar}{2m}\boldsymbol{\sigma}_j \cdot \nabla \times \mathbf{A}(\mathbf{r}_j)\right] \tag{2.2}$$

We have neglected all the terms coming from the sixth term in equation 2.1, which are proportional to $\boldsymbol{\sigma}_j \cdot \mathbf{E} \times \mathbf{p}_j$ and $\boldsymbol{\sigma}_j \cdot \mathbf{E} \times \mathbf{A}$. Without entering into the details (which can be found in e.g. [71]), this approximation is justified whenever $\hbar\omega_{\mathbf{k}} \ll mc^2 \sim 511$ keV, which is certainly true for every imaginable absorption edge (even at the Uranium K-edge, ~150 keV). Furthermore, we will also neglect the magnetic term in equation (2.2). This is appropriate whenever the absorption edge selected is electric-dipole allowed [71] (e.g. K

edge of ligand atoms, $L_{2,3}$ of transition metals, $M_{4,5}$ of rare-earths), as will always be in this thesis work.

In order to calculate the cross-section for RIXS, the standard approach is of course to use time-dependent perturbation theory, which expands the matrix elements in powers of $\mathcal{H}'$. In order to carry out the calculation, we assume an incident photon described by momentum $\mathbf{k}_i$, energy $\hbar\omega_i$ and polarization $\boldsymbol{\varepsilon}_i$. The total groundstate of the system before the interaction is therefore $|G\rangle = |g; \mathbf{k}_i, \boldsymbol{\varepsilon}_i\rangle$. We assume that after the interaction, the photon is scattered to ($\mathbf{k}_o$, $\hbar\omega_o$, $\boldsymbol{\varepsilon}_o$) so that the final state of the system is $|F\rangle = |f; \mathbf{k}_o, \boldsymbol{\varepsilon}_o\rangle$.
The transition probability $w_{g\to f}$ between the initial and final quantum states can be elegantly calculated up to second order using Fermi's golden rule [41, 63]:

$$w_{g\to f} = 2\pi \left| \langle F| \mathcal{H}' + \mathcal{H}' \frac{1}{E_i - \mathcal{H}_0 + i\eta} \mathcal{H}' |G\rangle \right|^2 \delta(E_F - E_G) \tag{2.3}$$

where E_g is the energy of $|G\rangle$. After some manipulations, the transition rate can be expressed as:

$$w_{g\to f} = 2\pi \left| \langle F|\mathcal{H}'|G\rangle + \sum_n \frac{\langle F|\mathcal{H}'|n\rangle \langle n|\mathcal{H}'|G\rangle}{E_g + \hbar\omega_{\mathbf{k}_i} - E_n + i\eta} \right|^2 \delta(E_g + \hbar\omega_{\mathbf{k}_i} - E_n) \tag{2.4}$$

where the states $|n\rangle$ are usually called *intermediate* states of the resonant process. While the first-order term (which corresponds to XAS and non-resonant IXS) usually dominates, the second-order term becomes large whenever the incoming x-rays are in resonance with a core-level transition of the material ($E_n = E_g + \hbar\omega_{\mathbf{k}_i}$). To carry out the calculation of the matrix elements, it comes in handy to employ the second-quantization form of the vector potential:

$$\mathbf{A}(\mathbf{r}) = \sum_{\mathbf{k},\varepsilon} \sqrt{\frac{\hbar}{2V\epsilon_0\omega_{\mathbf{k}}}} \left(\boldsymbol{\varepsilon}\, a_{\mathbf{k},\varepsilon} e^{i\mathbf{k}\cdot\mathbf{r}} + \boldsymbol{\varepsilon}^*\, a^\dagger_{\mathbf{k},\varepsilon} e^{i\mathbf{k}\cdot\mathbf{r}} \right) \tag{2.5}$$

where the operator $a_{\mathbf{k},\varepsilon}$ ($a^\dagger_{\mathbf{k},\varepsilon}$) annihilates (creates) a photon with wavevector $\mathbf{k}$ and polarization $\boldsymbol{\varepsilon}$. This notation allows one to express all the different of $\mathcal{H}'$ in terms of the total number of photons created or annihilated. In particular, we see from (2.2) that the relevant terms of the interaction are either linear or quadratic in $\mathbf{A}$: when calculating the first- and second-order transition rate, they will produce a bunch of terms containing different combinations of $a_{\mathbf{k}}$ and $a^\dagger_{\mathbf{k}}$. Since we are interested in a scattering event, i.e. one photon in the initial state and one in the final state, the only terms that are relevant in the matrix elements are those proportional to $a^\dagger_{\mathbf{k}_o} a_{\mathbf{k}_i}$.

To first-order in the transition rate, they can only arise thanks to the $\mathbf{A}$ term of the interaction Hamiltonian. A simple calculation gives

$$w_{g\to f} = \frac{\hbar e^2}{2m\mathcal{V}\epsilon_0}\frac{\boldsymbol{\varepsilon}_i^*\boldsymbol{\varepsilon}_o}{\sqrt{\omega_{\mathbf{k}_i}\omega_{\mathbf{k}_o}}}\langle f|\sum_i e^{i\mathbf{q}\cdot\mathbf{r}}|g\rangle \tag{2.6}$$

where $\mathbf{q} = \mathbf{k}_i - \mathbf{k}_o$ is the momentum transferred to the sample. Evidently, this is a non-resonant process and is usually called Thompson scattering: it is responsible for diffraction (when $\omega_i = \omega_o$, Compton scattering and non-resonant IXS. Whenever the energy of the incident photons is far from every core resonance of the material, it is the one that dominates.

The RIXS scattering channel has to come from the $w^{(2)}_{g\to f}$ term of the interaction, and the leading contribution in this case is given by the $\mathbf{A}\cdot\mathbf{p}$ term. Neglecting the others, the RIXS transition rate can be shown to be:

$$\frac{\hbar e^2}{2m^2\mathcal{V}\epsilon_0}\frac{\boldsymbol{\varepsilon}_i^*\boldsymbol{\varepsilon}_o}{\sqrt{\omega_{\mathbf{k}_i}\omega_{\mathbf{k}_o}}}\sum_n\sum_{j,j'}\frac{\left\langle f\middle|e^{-i\mathbf{k}_o\cdot\mathbf{r}_{j'}}\boldsymbol{\varepsilon}_o^*\cdot\mathbf{p}_{j'}\middle|n\right\rangle\langle n|e^{i\mathbf{k}_i\cdot\mathbf{r}_j}\boldsymbol{\varepsilon}_o^*\cdot\mathbf{p}_{j'}|g\rangle}{E_g+\hbar\omega_{\mathbf{k}_i}-E_n+i\Gamma_n} \tag{2.7}$$

where we have introduced the intrinsic broadening Γ_n of the intermediate state, which is inversely proportional to the intermediate state's lifetime $\tau_n = \hbar/\Gamma_n$. This is determined by radiative (fluorescent), Auger and Coster-Kronig processes, and is usually similar for all intermediate states at a certain edge, $\Gamma_n \sim \Gamma$. Its value is an atomic property and therefore only marginally dependent on the chemical environment, but it strongly increases with atomic number. Some characteristic values are $\Gamma_n \sim 0.15$ eV for K-shells of light atoms, $\Gamma_n \sim 0.28$ eV ($\tau \sim 10$ fs) for the L_3 edge of $3d$ transition metals, and $\Gamma > 1$ eV ($\tau < 1$) fs for the L_3-edge of $5d$ transition metal [72]. We note, incidentally, that including the magnetic term of (2.2) would produce another term in the matrix elements, equal to $\frac{i\hbar}{2}\boldsymbol{\sigma}\cdot\mathbf{k}\times\boldsymbol{\varepsilon}$. It is now easy to show why this term can be neglected when working with an absorption edge which is allowed by electric-dipole. This latter term gives rise to a matrix element of order $|\mathbf{p}| \sim \hbar/\langle r\rangle \sim Z\hbar/a_0 \sim 6\cdot10^{-23}$ kg m/s, while the magnetic one can only induce transitions of order $(\mathbf{k}\cdot\mathbf{r})|\mathbf{k} \sim 10^{-25}$ kg m/s (obtained expanding the exponential factor to order one).

We can now find an expression for the double-differential RIXS cross section. To do so, we just have to multiply (2.7) by the density of photon states in the solid angle $d\Omega = \mathcal{V}\mathbf{k}_o^2 d|\mathbf{k}_o|d\Omega/(2\pi)^3$, and divide by the incident flux $c/\mathcal{V}$. We also sum over f, the final states corresponding to the same energy transfer,

to obtain:

$$\frac{\partial^2\sigma}{\partial(\hbar\omega)\partial\Omega} = r_e^2 m^2 \omega_{\mathbf{k}_o}^3 \omega_{\mathbf{k}_i} \sum_f \left| \sum_n \frac{\langle f|\mathcal{D}|n\rangle \langle n|\mathcal{D}|g\rangle}{E_g + \hbar\omega_{\mathbf{k}_i} - E_n + i\Gamma} \right|^2 \delta(E_g - E_f + \hbar\omega)$$
$$\mathcal{D} = \frac{1}{im\omega_{\mathbf{k}_i}} \sum_j e^{i\mathbf{k}\cdot\mathbf{r}_j} \boldsymbol{\varepsilon} \cdot \mathbf{p}_j \tag{2.8}$$

where $r_e = \frac{1}{4\pi\epsilon_0^2}\frac{e^2}{mc^2}$ is the classical electron radius. The quantity inside the square modulus is obtain called $\mathcal{F}_{fg}$, the *scattering amplitude*. In most cases, one can also use the so-called *dipole* approximation: $e^{i\mathbf{k}\cdot\mathbf{r}_j} \sim e^{i\mathbf{k}\cdot\mathbf{R}_j}$, where $\mathbf{R}_j$ is the position of atom j inside the crystal. Physically, this means that one can neglect variations in the phase of the incident x-rays over the typical size of an atomic orbital: $2\pi\langle r\rangle/\lambda \ll 1$. This holds, for example, for K-edges of light elements ($E < 500$ eV), $L_{2,3}$ edges of $3d$-transition metals ($E \sim 500 \wedge 1000$ eV) and $M_{4,5}$-edges of lanthanides ($E \sim 1000$ eV). With this simplification, and applying a couple of basic quantum-mechanical relations [71]:

$$\frac{\partial^2\sigma}{\partial(\hbar\omega)\partial\Omega} = r_e^2 m^2 \omega_{\mathbf{k}_o}^3 \omega_{\mathbf{k}_i} \sum_f \left| \sum_n \sum_{j,j'} \frac{\langle f|\boldsymbol{\varepsilon}_o^* \cdot \mathbf{r}_{j'}|n\rangle \langle n|\boldsymbol{\varepsilon}_i \cdot \mathbf{r}_j|g\rangle}{E_g + \hbar\omega_{\mathbf{k}_i} - E_n + i\Gamma} \right|^2 \delta(...) \tag{2.9}$$

We also note that two quantum mechanical effects are present in the RIXS cross-section. The first is represented by the summation of *amplitudes* over the intermediate n states: the lifetime of the intermediate state is so short that one cannot know which "path" the RIXS process has passed through, like in Young's experiment. At the same time, scattering amplitudes are also summed over the crystal sites j, j', because one does not know which electron (site) has been excited during the RIXS process. Therefore, while the single absorption and emission processes are surely localized on a certain atom (and this is a consequence of the $\langle f|...|n\rangle \cdot \langle n|...|g\rangle$ factor which is extremely small whenever the excited state lies on a different atom), the excitation left in the system can effectively be "delocalized". This is crucial, for example, to understand why RIXS is able to probe collective excitations like magnons, despite exciting atomic core transitions [73].

Since it will be useful for the next paragraphs, we also state here how the scattering amplitude can be expressed when final states of the RIXS process are atomic-like orbitals. Expressing the dipole operator in second-

quantization formalism [71], we get:

$$\mathcal{F}_{fg} = \sum_{\mu',\nu',\nu,\mu} T_{\mu',\nu',\nu,\mu}(\boldsymbol{\epsilon}_o, \boldsymbol{\epsilon}_i) \sum_i e^{i\mathbf{q}\cdot\mathbf{R}_i} \sum_n \frac{\langle f|c^\dagger_{i\mu'}c_{i,\nu}|n\rangle \ \langle n|c^\dagger_{i\nu}c_{i,\mu}|g\rangle}{E_g + \hbar\omega_{\mathbf{k}_i} - E_n + i\Gamma} \tag{2.10}$$

$$T_{\mu',\nu',\nu,\mu}(\boldsymbol{\epsilon}_o, \boldsymbol{\epsilon}_i) = \langle\phi_{\mu'}|\boldsymbol{\epsilon}_o|\phi_{\nu'}\rangle \ \langle\phi_\nu|\boldsymbol{\epsilon}_i|\phi_\mu\rangle \tag{2.11}$$

where ϕ_μ is the wavefunction of the core hole, and ϕ_ν and $\phi_{\nu'}$ are wavefunctions of the outer-shell orbital. Whenever no inter-atomic interactions are present, T completely determines the amplitude of the scattering process, and is called *atomic scattering factor*.

There are two main types of RIXS processes. Without invoking any complex formalism (which requires the use of Green's functions [71]), we will try to describe them in a phenomenological way. Whenever a core electron is excited above the Fermi level, the resulting state is not an eigenstate of the Hamiltonian. It can, in general, evolve under the perturbation Hamiltonian H_C which contains the interactions between the photoexcited exciton and the rest of the material. It may happen that H_C causes no effect during the intermediate state: the core-hole simply gets filled by another electron in the system. In this case one speaks about a *direct* RIXS process. The cross section is simply determined by the absorption and emission matrix elements. Some examples (as will be explained later) are single magnons, and *dd* excitations. However, it is possible that the final states critically depends on the interaction of the core-hole + photoexcited electron. In this case, the RIXS process is called *indirect*. Examples include phonons and bimagnons in spin-$^1/_2$ systems.

Before moving to describe how RIXS is performed experimentally, we will describe which excitations are accessible to this technique. We will concentrate in particular on phonons, magnetic and orbital excitations, although other types of excitations have been observed with RIXS (e.g. plasmons [74]).

2.4. Excitations accessible through RIXS

2.4.1. Phonons

During the intermediate state of the RIXS process, the charge cloud around the excited atom is perturbed, having an excited photoelectron above the Fermi level and a core-hole. Since the effective potential of the nuclei depends on the electronic configuration, it is not surprising that phonons can be excited through by RIXS. In particular, phonons are excited through an *indirect* RIXS process.

More specifically, the fact that phonons are excited through their interaction with the valence electron (or, better, with the electron-core exciton), makes the RIXS technique rather special. This interaction is exactly what is known as *electron-phonon coupling* (EPC). Its meaning can be explained quite easily: if we consider the total Coulomb energy caused by the ionic potential V_{ion}, $V_{el-ion} = -\int -e\rho_{el}(\mathbf{r}) \sum_j V_{ion}(\mathbf{r}-\mathbf{R}_j)$, and we expand it to second order in the small ion displacements $\mathbf{u}_j = \mathbf{R}_j - \mathbf{R}_j^{eq}$, we get (after lengthy second-quantization calculations described e.g. in [41]):

$$V_{el-ph} = \sum_{\mathbf{k},\sigma} \sum_{\mathbf{q},\lambda} M_{\mathbf{q},\lambda}\, c^{\dagger}_{\mathbf{k}+\mathbf{q},\sigma} c_{\mathbf{k},\sigma} (b_{\mathbf{q},\lambda} + b^{\dagger}_{-\mathbf{q},\lambda}) \tag{2.12}$$

where $\mathbf{k}, \mathbf{q}$ are the electron and phonon momentum, respectively, λ is the phonon polarization and σ is the electron spin. Its interpretation is quite simple: the interaction with the ions scatters the electron from momentum $\mathbf{k}$ to $\mathbf{k}+\mathbf{q}$, by either creating a phonon with momentum $-\mathbf{q}$ or absorbing one with momentum $\mathbf{q}$. Such a process has an amplitude given my $M_{\mathbf{q},\lambda}$, which is precisely the EPC.

This quantity is crucial to explain some complex phenomena in solid-state physics. For example, it changes the electron self-energy close to the Fermi level of electron (the famous "kinks" measured in photoemission). More interestingly, electron-phonon interactions are involved in the formation of polarons, with $SrTiO_3$ being the most fascinating example [75]. However, the most striking consequence of electron-phonon coupling is the fact that it can mediate an attractive interaction between electrons themselves, which is the basis of "conventional", BCS superconductivity [41].

The direct correlation between EPC and phonon intensity in RIXS can actually be expressed rigorously. An exact formula can be obtained by assuming an oversimplified model with a single Holstein phonon (i.e. a "local" phonon, which could describe vibrations in a molecular crystal), with frequency ω_0 and a coupling M to a single $3d$-hole:

$$\mathcal{H} = \sum_i \omega_0 b_i^{\dagger} b_i + M d_i^{\dagger} d_i (b_i^{\dagger} + b_i) \tag{2.13}$$

by performing a so-called canonical transformation, it can be shown that the scattering amplitude between the groundstate $|g\rangle$ and a final state with n' phonons is

$$\mathcal{F}_{fg} = T_{el}(\boldsymbol{\varepsilon}', \boldsymbol{\varepsilon}) \left(\sum_{n=0}^{n=n'} \frac{B_{n',n}(g) B_{n,0}(g)}{\Omega + i\Gamma + (g-n)\omega_0} + \sum_{n=n'+1}^{n=\infty} \frac{B_{n,n'}(g) B_{n,0}(g)}{\Omega + i\Gamma + (g-n)\omega_0} \right) \delta(\omega - n'\omega_0) \tag{2.14}$$

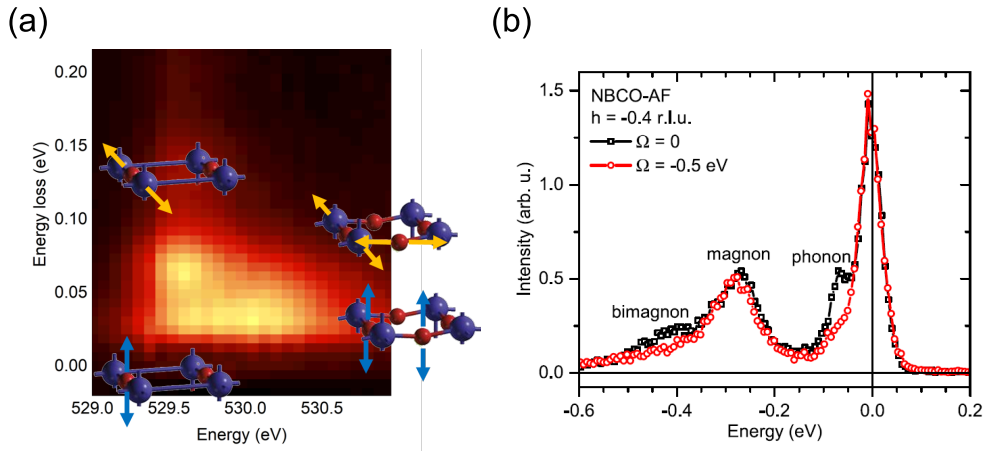

Figure 2.2: Some example of phonons measured using RIXS. (a): RIXS spectra as a function of energy measured in $Nd_{1+x}Ba_{1-x}CuO_{6+\delta}$. Two resonances can be detected at 529.6 eV and 530.1 eV, corresponding to oxygen atoms in the Cu-O chains and Cu-O planes [77]. At each resonance, two phonon modes can be observed: one at 30 meV and one at 60 meV, corresponding to Cu-O buckling and Cu-O stretching modes. This nicely shows RIXS site sensitivity. The small sketches show the direction of the real-space oscillations associated to the modes. (b): behaviour of phonons upon detuning (adapted from [78]).

where Ω is the difference between the incident energy and the main absorption edge (the so-called "detuning" energy), $g = M^2/\omega_0^2$ is an adimensional quantity related to the EPC, and the n is the number of phonons excited in the intermediate state. The $B_{m,n}$ are Franck-Condon factors with a complicated expression [71]. $T_{el}(\boldsymbol{\varepsilon}', \boldsymbol{\varepsilon})$ is the atomic scattering factor for elastic scattering (i.e. without orbital transitions).

Much like in molecules, the absorption of the incident photon brings the system into an excited state with a certain number of phonons n; the backwards transition then leaves n' of them in the final state. Obviously, n' can be higher than one: RIXS can also probe (quite easily, as shown later) phonon overtones (see e.g [76]).

Eq. (2.14) also gives some important insights into the physical mechanism generating phonons. The intensity is inversely proportional to $\Omega + i\Gamma = E_i - E_{\text{res}} + i\Gamma$. It can be shown that this quantity is directly proportional to the effective lifetime of the RIXS intermediate state [79]: the (quite intuitive) meaning is that the phonon intensity is inversely proportional to the lifetime of the intermediate state, when the charge perturbation takes place. This also explains why phonons are not seen at the L_3 edge of $4d$ and $5d$ elements [80, 81], where Γ is much bigger and τ much shorter than at the $3d$ edges. In the limit of small M/Γ, it can be shown that the intensity of single-phonon

excitation reduces to $I^{(1)} \propto |T_{\text{el}}|^2 M^2/|z|^4$, so that $I^{(1)} \propto g$ and the intensity is proportional to the square of the EPC. An example of the behaviour of phonon branches upon detuning is given in panel (b) of Fig. 2.2.

This model can be easily extended to the case in which more phonon modes can be excited coherently during the RIXS process [75]. The first effect is an interdependence between the intensity of a single phonon and the EPC of the other ones. More importantly, this model predicts the appearance of mixed overtones, i.e. peaks in the RIXS spectra corresponding to the simoulatnous excitation of different modes. This is particularly relevant, evidently, when the system has two or more branches with a strong EPC. This is the case of e.g. SrTiO3, which has two high-energy longitudinal optical phonons with comparable EPC. Recent RIXS measurements have indeed found a broad distribution of overtones, which have successfully been interpreted in terms of mixed overtones [82].

Therefore, the EPC of one (or more) phonon branch can be (more or less) directly extracted from RIXS measurements, and this makes the technique rather unique. In particular, two approaches have been used so far to retrieve the EPC. If the phonon overtones have appreciable intensities, Eq. (2.14) can be directly fitted to the spectra to extract g, mostly relying on the ratio between the different overtones. Whenever the ratio M/Γ is instead not enough to measure appreciable overtones, one has to resort to the so-called *detuning* method, which has been described and experimentally applied in [78]. The trick here is to measure RIXS spectra upon detuning the incident energy away from the main resonance: the intensity of the first overtone can then be used to extract g using Eq (2.14).

Despite the strong approximations upon which it is built, this model (developed mostly by L. Ament, K. Gilmore and A. Geondzhian) has given remarkably good results in interpreting RIXS measurements performed at transition metal $3d$-edges. More generally, the model has proven to be adequate whenever the electron and the phonon cloud remain *localized* on the excited site. This is usually the case for $3d$ edges, thanks to the strong Hubbard on-site repulsion. On the contrary, recent experiments performed at the Oxygen edge clearly deviated from the behaviour expected from the model. Since the electrons are clearly delocalized in the $2p$ bands, the assumptions of the model are violated, and the model is not adequate anymore. As an example, the intensity of the phonon branches as a function of incident energy cannot be reproduced by any reasonable EPC, and therefore the detuning method cannot be applied. A deeper discussion on the topic is given in Chapter 7, which focuses on phonon RIXS at the O K-edge in cuprates superconductors.

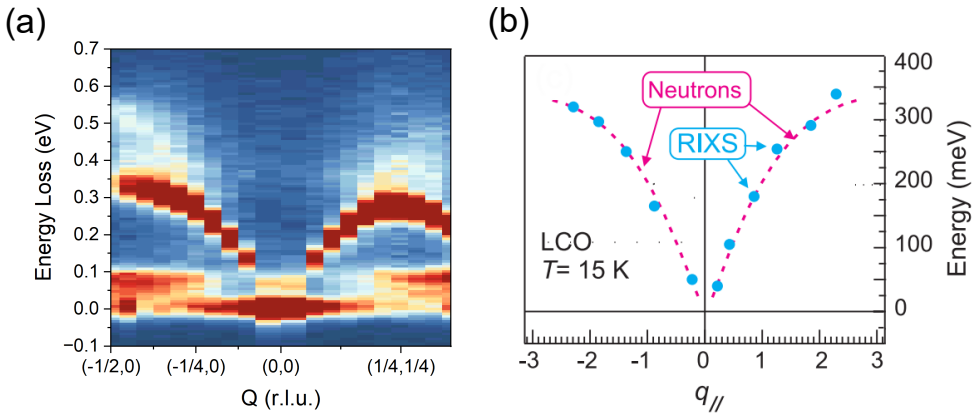

Figure 2.3: Magnetic excitations in cuprates seen with RIXS at the Cu L_3 edge. (a) typical RIXS spectra on undoped cuprates as a function of momentum along the (1,0) and (1,1) directions. Spectra have been measured on a La_2CuO_4 film using σ polarization. The single-magnon is the very intense red peak in the figure. Also evident is the bimagnon excitation above it (the white continuum in the figure). (b) comparison between the dispersion of single-magnon in La_2CuO_4 measured with RIXS (blue dots) and by neutrons (purple line). Taken from [21].

2.4.2. Magnetic excitations

For many years, Inelastic Neutron Scattering (INS) has been the only technique capable to measure the full momentum dependence of magnetic excitations in solid materials. This is because (non-resonant) Inelastic Neutron Scattering (IXS) couple with single-spin flip magnetic excitations only through the magnetic dipole operator, which is very weak.

The resonant character of RIXS should, instead, give the technique sensitivity to magnetic excitations, much like in x-ray magnetic diffraction. This, coupled to the sizeable momentum transfer, should in principle make RIXS an alternative to INS. However, the energy resolution of old spectrometers was by far not enough to resolve magnetic excitation, which lie below 300 meV. With the advent of high-resolution spectrometers AXES and SAXES [83], it was finally demonstrated that RIXS can indeed probe the transverse magnetic fluctuations [21] (see Fig. 2.3(b)).

The physical reason for which RIXS can probe transverse magnetic fluctuations is the spin-orbit coupling of the photoexcited hole. If the spin of the core, photoexcited hole is not definite (i.e. is not a good quantum number), then in certain conditions the dipole matrix elements in Eq. (2.9) can be non-zero even if $|f\rangle$ and $|g\rangle$ have different spin. More elegantly, the spin-orbit interaction allows orbital and spin-orbital angular momentum to be exchanged.

To be more precise, we can focus on RIXS at $L_2, 3$ edge of $3d$ transition metals, which is the main topic of this thesis and corresponds to $2p \rightarrow 3d$ transitions. To simplify matters even further we assume a $3d^9$ configuration with an empty $x^2 - y^2$orbital, like in the case of Cu^{2+} or Ni^{1+} in tetragonal symmetry. This allows us to express the cross section for magnetic excitations in a rather simple way, using some approximations. The $2p$ levels are very localized, we can assume only on-site transition ($j = j'$). Moreover, the spin-orbit splitting is large (several eV), so that we can restrict to the L_3 subset. Additionally, there is only empty sate in the $3d$ orbitals, so that all the reachable intermediate states have the same energy E_n. In this case, the scattering amplitude $\mathcal{F}_{fg}$ for a single-site, spin flip transition simplifies to [71]:

$$\mathcal{F}_{fg} = T_{L_3}(\epsilon', \epsilon)\frac{1}{i\Gamma}\sum_i e^{i\mathbf{q}\cdot\mathbf{R}_i}\langle f|c^\dagger_{i,\downarrow}c_{i,\uparrow}|g\rangle \tag{2.15}$$

$$T_{L_3} = \sum_{j=1}^{4}\left\langle 2p_j\middle|\boldsymbol{\epsilon}_0^*\cdot\mathbf{r}\middle|3d_{x^2-y^2,\downarrow}\right\rangle\left\langle 3d_{x^2-y^2,\uparrow}\middle|\boldsymbol{\epsilon}_i\cdot\mathbf{r}\middle|2p_j\right\rangle \tag{2.16}$$

RIXS is therefore able to probe single spin-flip excitation provided that T_{L_3} is not zero. It can be shown that, in $3d^9$ systems with a $x^2 - y^2$ groundstate, this is possible whenever the spin is not aligned in the z-direction [71, 84, 85]. Luckily, in cuprates and nickelates the spin is always aligned in the xy plane [86–88], and single-flip excitations are visible. While the matrix element in Eq. (2.15) is clearly related to a single-site transition, the summation of amplitudes over the lattice sites $\sum_i \exp(i\mathbf{q}\cdot\mathbf{R})$ effectively "delocalizes" it. Indeed, a standard bosonization technique shows that RIXS effectively measure the single-magnon dispersion [71].

There is also a more elegant way to express the RIXS cross section for magnetic excitations in terms of spectral functions, which helps to clarify the grounding physical mehcanism. It can be shown that, for a $S = 1/2$ system, the differential cross section $\partial\sigma/\partial\Omega$ is proportional to $|\langle f|\sigma^{(0)} + \sigma^{(1)}/s\cdot\boldsymbol{\epsilon}_0^*\times\boldsymbol{\epsilon}_i\cdot\mathbf{S}_j|g\rangle|^2$ [85]. This equation highlights that a spin-flip process flips the polarization of the incoming light: the cross-product $\boldsymbol{\epsilon}_0^*\times\boldsymbol{\epsilon}_i$ must be different from zero. The physical meaning is a transfer from angular momentum from the photon to the system.
An example of typical RIXS spectra as a function of momentum are shown in panel (a) of Fig. 2.3.

Single spin-flip excitations are not, however, the only type of magnetic excitations visible in RIXS spectra. In general, since RIXS is a photon-in-photon-out technique, it can excite $\Delta S = 0, 1, 2$ transitions [85] (actually, in systems with more than one hole, the interaction between orbital angular momentum and spin makes other multi-magnon processes visible [89]).

In the case of $S = 1/2$ systems, like 2D cuprates, the cross section of $\Delta S = 2$

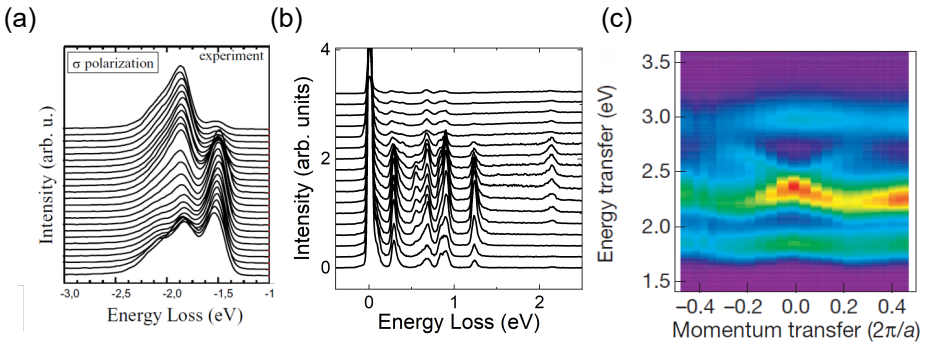

Figure 2.4: Example of orbital excitations measured using RIXS. (a) *dd* excitations in $LaCuO_4$ as a function of momentum [6]. (b) Multiplet of *ff* excitations measured in $PrBa_2Cu_3O_{6+\delta}$. (c): Collective orbital excitations (orbitons) measured in Sr_2CuO_3 (adapted from [35]).

excitations is zero, but $\Delta S = 0$ (non-spin-flip) are instead accessible. In particular, there is another excitation which is visible in the RIXS spectra of cuprates, as can be seen in Fig. 2.3(a). It follows a similar dispersion as the magnon, and has an energy about 50% higher. Moreover, its intenisty clearly grows at high-momentum transfer close to the AF magnetic zone boundary. Interestingly, it also shows a peculiar energy dependence, decreasing faster upon detuning than the the magnon and the *dd* excitations [78]. Such a behaviour, reminiscent of what happens with phonon excitations, suggests an indirect RIXS process. This feature has been successfully interpreted in terms of a bimagnon excitation, i.e. the creation of two magnons with no total change in spin ($\Delta S = 0$). The origin of this excitation is in the suppression of the superexchange interaction during the intermediate state of the RIXS process. Indeed, the non-magnetic, metastable $3d^{10}$ blocks all magnetic couplings. This interaction can be written in the form $\sum_{i,j} -J_{i,j} p_i^\dagger p_i \mathbf{S}_i \cdot \mathbf{S}_j$, where $p^\dagger$ (p) creates (annihilates) a core-hole. Since this does not commute with the Hamiltonian, excitations are created in the intermediate state. With a bit of math [71], it can be shown that the corresponding scattering operator that enters in the cross-section must leave S_z unchanged. Therefore, only an even number of magnons can be created. Evidently, this is an indirect RIXS process. Bimagnons, similarly to phonons, exhibit a faster decay in intensity upon detuning [78].

2.4.3. Orbital excitations

The electronic configuration of the atomic orbital can be split into multiplets by Hund's rules and/or the crystal field. During the first stage of the RIXS process, a core electron is promoted into one of the empty states. After the second transition, the system might be left in one of the higher-energy multiplet (provided that the orbital was not empty in the groundstate, like

in Ti^{4+} or Ce^{4+}). In a one-electron picture, this happens whenever another electron fills the core hole. Such final states are usually named orbital (or multiplet) excitations.

In the case of $3d^9$ systems, the situation is particularly easy. Since there is a single hole, the d orbitals are just split by the crystal field of the system which is of the order of 1–3 eV. Conversely, spin-orbit interaction of the $3d$ states is quite small (a few meV) and is usually neglected. The RIXS cross section can be computed using Eq. (2.10) considering $\mu = 2p_{J,m_J}$ (one of the six $2p$ states), $\nu = 3d_g$ (empty d orbital in the groundstate), and $\nu' = 3d_f$ (empty d orbital in the final state). In general, the initial and final hole can also have opposite spin. The atomic scattering factor T can be calculated in a simple one-electron picture, by expanding the wavefunctions and the dipole operator in terms of spherical harmonics.

It should be noted that the scattering amplitude still contains a sum over the lattice sites, modulated by $e^{i\mathbf{q}\cdot\mathbf{R}_i}$. In the simplest case, orbital excitations behave as purely atomic transitions: their energy is independent from the transferred momentum $\mathbf{q}$. This is what happens, for example, in the majority of high-T_c cuprates [6], where the intensity of the excitation agrees very nicely with the single-ion calculations. In fact, most of correlated materials exhibit atomic-like dd excitations.

In general, however, orbital excitations might also exhibit a collective nature. In a single-particle picture, the crystal-field-split levels forms bands, whose energy depends on momentum $\mathbf{q}$. Therefore, in this case it is quite natural to expect a dispersion of the dd excitations, which simply reflects the energy difference between the bands. However, in correlated systems, the strong Coulomb repulsion suppresses charge correlations and bands are no longer observable [10]. One would, therefore, expect a purely atomic behaviour of dd excitations. It turns out, instead, that other mechanisms might give rise to a collective nature of orbital excitations and a corresponding dispersion in reciprocal space. One of them is the fractionalization of the charge, spin and orbital degrees of freedom in one-dimensional systems. An example of collective orbital excitations measured in one-dimensional Sr_2CuO_3 is given in panel (c) of Fig. 2.4. We will discuss this topic in much more detail in Chapter 5.

Chapter 3

RIXS experimental set-up

The RIXS technique has been known for more than 30 years, as a kind of resonant x-ray emission. However, it only become extremely popular in the last 15 years: this is mainly because of two reasons.
The first one is the appearance of third-generation synchrotron facilities, which greatly outperformed the previous ones in terms of photon flux, stability, and brilliance. The second, and probably most important one, is the great advance in the design of dedicated RIXS spectrometers. In particular, the driving force behind the rebirth of RIXS has been the extreme increase in the energy resolution (and therefore of resolving power), which gave access to excitations lying in the 10^1-10^2 meV regime.

In this chapter, we will describe how RIXS is performed at synchrotron facilities. As an example, we will review the setup of the ERIXS spectrometer installed at the ID32 beamline at the ESRF. The spectrometer was designed jointly by the ESRF and our group at PoliMi, and started operation in 2016. First, we will outline the optical setup of the beamline, explaining the purpose of the different elements. We will then describe the sample stage and the ERIXS spectrometer, also mentioning the multilayer mirror used for polarization analysis. We will end the chapter by giving relevant figures on flux and energy resolution, for different beamline configurations.

Contents

3.1. ID32 beamline

The ID32 beamline is installed at the European Synchrotron Radiation Facility (ESRF), in Grenoble. The synchrotron underwent the *Extremely Brilliant Source* upgrade in 2018-2020, which made it the first fourth generation light source in the world. The ring has a circumference of 844 m, and runs with an electron energy of 6 GeV.
The ID32 beamline is the only soft x-ray beamline at the ESRF. It is dedicated to the study of the electronic and magnetic properties of quantum materials, and hosts two endstations: an XMCD and a RIXS branch. Since this thesis does not include XMCD studies, we will just focus on the RIXS branch. The beamline provides x-ray in the $400 \div 1600$ eV range, which covers the K-edges of light elements, the $L_{2,3}$ range of $3d$ transition metals and the $M_{4,5}$ edge of lanthanides.
The source of the beamline is a pair of helical APPLE-II undulators, 1.6 m long and equipped with NdFeB magnets with a period of 88 mm (and a minimum gap of 16 mm). The two can produce x-rays with either linear horizontal (i.e. in the plane of the ring), linear vertical or circular polarised light. The degree of light polarization is close to 100% at all photon energies. Recently, a phasing unit was installed between the undulators: this is just a one-period undulator, which is able to phase the electron beam passing through the second undulator. There are two advantages of this: first, it increases the photon flux of about 30% at low photon energies (~ 500 eV); secondly, it produces a single point source, as if there was a single undulator. Each of the undulators can produce beams with a brilliance of $4.5 \cdot 10^{14}$ ph/s/0.1%BW/200 mA at an energy of 900 eV [90].

3.1.1. Beamline optics

In order to understand the beamline design, it is useful to state which are the goals of a beamline dedicated to RIXS.

- Focus the x-ray beam on the sample down to the smallest vertical size (the horizontal size can remain a bit larger, due to reasons that will be explained later). Typical values lie usually in the ~ μm range for the vertical dimension, and about 10 times larger in the horizontal direction.
- Narrow down its energy bandwidth to make it as monochromatic as possible. Since the total (combined) resolution ΔE_{COMB} of the instrument is usually $\sqrt{2}\Delta E_{BL}$, state-of-the-art RIXS beamlines usually reach 20 meV bandwidth at the Cu L_3 edge (930 eV).
- Keep the beamline transmission as high as possible, by minimizing the number of optical elements and working in grazing incidence geometry.

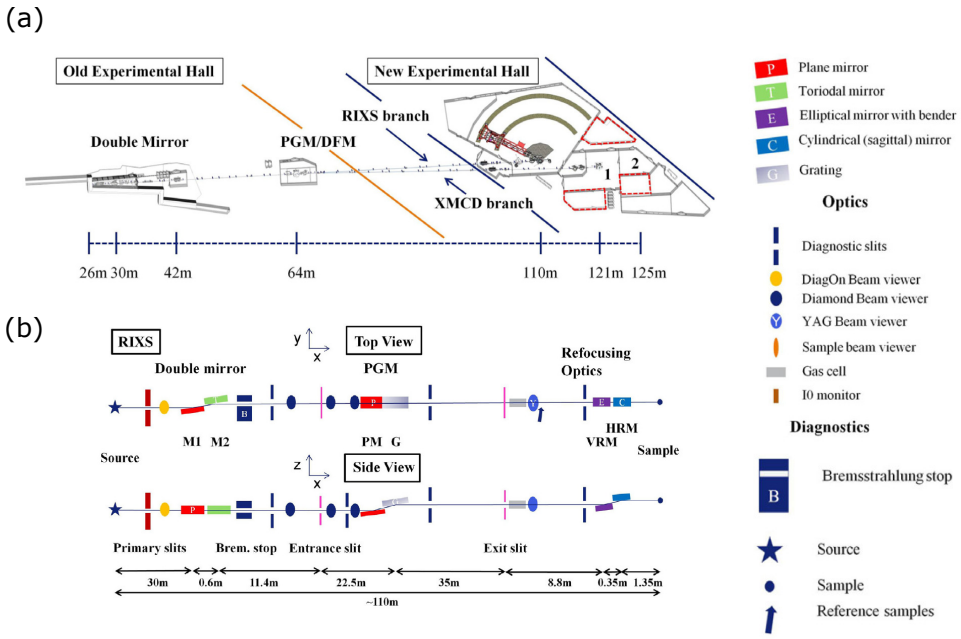

Figure 3.1: Scheme of the ID32 beamline. (a): sizes of the ID32 beamline and the RIXS experimental hall. (b) Scheme of the top and side view of the ID32 beamline. The legend for the symbols used is provided on the right. Both panels adapted from [90].

A scheme of the beamline optics is presented in Fig. 3.1.

Since the beamline uses soft x-rays, all chambers containing the optical elements are kept in Ultra-High Vacuum (UHV), 10^{-9} mbar. First, a set of two deflecting mirrors is used to displace the beam of 16 mm while keeping it parallel, so that a tungsten Bremmstrahlung stop can be inserted. The first mirror is flat, while the second one is a toroidal mirror that focuses the beam vertically and collimates it in the horizontal direction. At the vertical focus of M_2, an entrance slit is place to define the source point of the monochromator. The slit is usually set to 30 μm in order to transmit most of the intensity.

PGM

The second part of the beamline is a Plane-Grating Monochromator (PGM), that is used to produce a highly monochromatic beam. It is based on the SX700 design and consists of four optical elements:

- an entrance slit, which defines the source of the PGM;
- An upward-facing plane mirror with gold coating. The mirror is liquid-nitrogen cooled to 123 K, where the expansion coefficient of silicon is close to zero, to mitigate distortions caused by x-ray heating;

- a set of four downward-facing Variable Line Spacing (VLS) gratings, with mean line density equal to 300 and 900 lines (for the XMCD branch) and 800 and 1600 lines/mm (for RIXS);
- an exit slit, which is used to select the desired bandwidth and beam size on the sample.

This design is a direct evolution of the Dragon monochromator [91], which was used in older beamlines. The core of the setup if the plane-VLS grating, which disperses the different energies in the vertical direction. The density of the grooves along the beam direction is made as a polynomial law: $n(x) = a_0 + a_1 x + a_2 x^2$. By choosing appropriate values for a_1 and a_2, one can zero the defocus and comma over a large energy range $400 \div 1600$ eV without changing r_1 and r_2. The exit slit at the end of the PGM is used to filter the desired energies: its size, which can be adjusted with a $\sim \mu$m precision, is used to determine the energy resolution (as well as the beam size on the sample, as explained later), but strongly affects the photon flux which scales almost linearly with it. Usually, a 15 μm value is a good compromise between energy and transmitted intensity. The choice of the grating (800 lines/mm vs. 1600 lines/mm) is of crucial importance in a RIXS experiment: the 1600 grating provides a better resolution, but decreases the flux of a factor ~ 4. Consequently, it is seldom used.

Refocussing optics

The last part of the beamline is made of two mirrors which are used to vertically and horizontally focus the beam onto the sample. The new refocussing optics was installed in 2018, during the dark period of the EBS synchrotron upgrade.

The source of the system is the collimated beam selected by the exit slit of the PGM. The first is an elliptical mirror which focuses the beam in the vertical direction, and is followed by a cylindrical mirror which focus the beam in the sagittal plane. Both mirrors have a Pt coating and have a combined reflectivity of $\sim 60\%$. The slope error of the new optical elements is below 100 nrad. The beam size on the sample can be brought down to 1.8 µm in the vertical direction and 4 µm in the horizontal one. As will be explained later, the resolution of the RIXS spectrometer is only affected by the vertical dimension. Therefore, keeping a small size in the horizontal is not necessary. In fact, usually the beam size in the horizontal direction is kept at much larger values, closer to 20 µm, in order to reduce the x-ray flux per unit area on the sample and reduce sample damage. The last mirror is electrically isolated, so that the drain current can be measured to have a reliable estimate of incident photon flux. The total flux impinging on the sample depends on the incident photon energy, as well as on the choice of

the PGM used. In the case of the 800 lines/mm grating, the photon flux at the Cu L_3 energy (930 eV) is around $\sim 2 \cdot 10^{11}$ photons/s, and it goes down to $\sim 6 \cdot 10^{10}$ at the Oxygen K-edge energy (530 eV). When the 1600 lines/mm grating is used, the flux at the two edges decreases almost by a factor four ($\sim 2 \cdot 10^{11}$ and $\sim 6 \cdot 10^{11}$ photons/s, respectively).

3.1.2. Sample chamber and stage

At the end of the beamline, x-rays enter into the sample chamber, which has a diameter of 711 mm and was designed and built by CINEL. The chamber hosts a four-circle diffractometer manufactured by HUBER (panel (a) in Fig. 3.2), equipped with six degrees of freedom. The whole structure can rotate around the vertical axis (angle θ, -20°+185° range), and supports a cradle which can rotate around the χ axis (±45° range). This cradle supports finally the sample stage that can rotate around the ϕ axis (360° range). The sample is usually glued on copper hexagons (usually coated in gold). It can be brought in the centre of rotation by translating it perpendicularly to the sample stage (y-direction, ±6 mm range), and its surface can be moved with respect to the centre of rotation by the x and z translations (±12 mm range). The sample chamber has three silicon diodes on the inner circle, which can rotate on a large angle range. They are usually employed for sample alignment. The main feature of the chamber is the possibility to rotate the port to the ERIXS spectrometer without breaking vacuum.

3.2. ERIXS: a state-of-the-art RIXS spectrometer

We will now describe the design and the performance of the ERIXS spectrometer, installed at beamline ID32. The spectrometer was designed jointly by ESRF and Politecnico di Milano, and commissioned in 2016.

Its design is an improvement of the SAXES spectrometer installed at the ADRESS beamline of the Swiss Light Source. It is also very similar to other ultra-high-resolution spectrometers, as the one installed at the I21 beamline of Diamond Light Source and the hRIXS spectrometer installed at the SCS beamline of the European XFEL. A picture of the instrument is reported in Fig. 3.2(c).

ERIXS has a total length of about 10 m from the sample stage to the detector. It was the first soft x-ray RIXS spectrometer to allow for a continuous rotation of the scattering arm. Thanks to the innovative design of the chamber, the motion can be realized without breaking the UHV inside the sample chamber: in particular, the spectrometer can cover all scattering

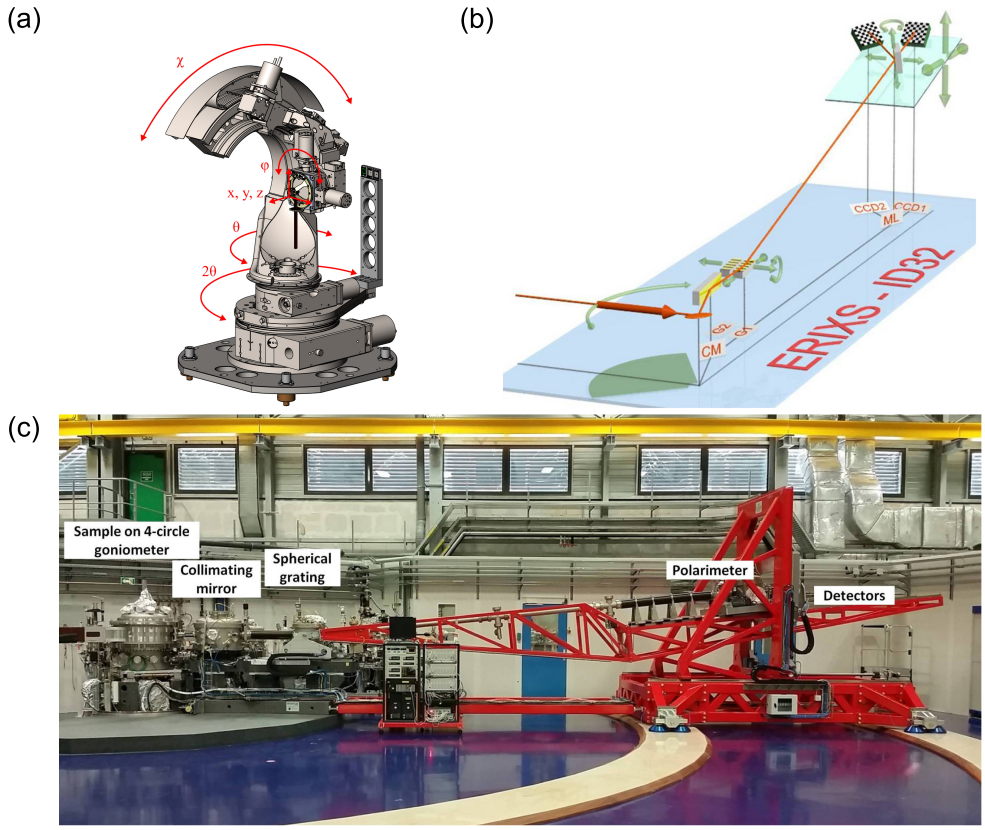

Figure 3.2: (a) Picture of ERIXS. (b) Scheme of the ERIXS spectrometer. The parabolic-cylindrical collimating mirror (CM) collimates the beam in the horizontal directions. Two intercheangeable gratings ($G1$ and $G2$) disperse and focus the energies onto detector CCD_1. Multilayer ML and CCD_2 are used for polarization analysis. All panels adapted from [90].

angles between 50° and 149.5°. It is composed of a steel structure, which is mounted on 8 airpads (IBS D300). By applying a 5 bar air pressure, the entire structure rises of approximately 70 µm and can slide onto two circular marble rails. The floor and marble tiles have a high planarity (less then 400 µm height differences over 10 m). The spectrometer moves with a speed of about 0.2 deg/s, and its position is measured with an encoder.

First, a 600 mm parabolic-cylindrical mirror is placed at ~ 1.1 m from the sample, in a separate chamber. The mirror collects 20 mrad at an incident angle of 2%, and is used to collimate the beam in the horizontal direction. Its purpose is to increase the horizontal acceptance of the spectrometer: since the detector size is ~ 2.5 cm, the acceptance without the mirror would be just 2.5 mrad. Considering a reflectivity of the mirror equal to 0.6, the mirror increases the acceptance of a factor 7. The horizontal collimation is also necessary for the soft x-ray polarimeter, as will be described later.

The second (and last) optical element of ERIXS is a spherical-VLS grating,

which is located at a distance of $r_1 = 2.5 \pm 0.4$ m from the sample. The grating disperses the scattered energies and focuses them onto a two-dimensional CCD detector, placed at a distance r_2. The total length of the spectrometer $r_1 + r_2$ is close to 12 m, constrained by the dimension of the experimental hall. The variable line density is again exploited, as in the beamline PGM, to zero the defocus term and the comma aberration. However, the fact that the grating is spherically bent gives a nice additional property: it allows one to increase the angle between r_2 and the focal plane (and therefore of the scattered beam on the detector) up to 25°, which is needed to guarantee a good operation of the CCD detector. Moreover, magnification is close to 1, so that the source is imaged on the detector. The only drawback of this single-optical-element design is that, in order to zero the defocus and comma over the entire range, one has to change r_1, r_2 and α. Therefore, the entire chamber of the gratings can be slided along the beam direction by ±0.4 m, and the gratings are mounted on a high-precision goniometer which allows a pitch rotation (±5°) and a vertical translation. The chamber hosts two different gratings, having an average line density equal 1400 and 2500 lines/mm, respectively. The two gratings were polished during the 2018 ESRF dark period, and a new slope error <100 nrad was obtained. Since the slope error is, at present, the main limitation to the energy resolution of the spectrometer, the new polishing allowed to substantially increase the resolving power. As for the beamline PGM, a higher line density increases the resolving power but also decreases the throughput. All the specifications about energy resolution and flux are given in the next Section.

At the end of the spectrometer, a final chamber hosts a Andor Ikon direct-illuminated soft x-ray CCD detector. Even if the scattered x-rays are dispersed only along the vertical direction, the beam is not focused in the horizontal direction and the detector is two-dimensional, with a total of 2048×2048 pixels, 13.5 µm in size. The detector is not vertical, but forms an angle of 20° with respect to the incident x-ray beam. This allows to: i) decrease the effective pixel size, and therefore the contribution of the CCD spatial resolution to the total resolving power, and ii) to place the CCD along the focal plane of the grating, at least at the Cu L_3-edge energy. Thanks to single-photon detection and centroiding algorithms (described in Sec. 3.2.3) , the effective resolution is around 7 µm. In order to reduce the dark current, the detector is cooled with a Peltier cell down to −90 °C. Thanks to single-photon counting and low temperature, the spectra are indeed background-free, as explained in Sec. 3.2.3.

3.2.1. ID32 + ERIXS performance

The beamline upgrade which began in 2018 and ended in 2020 allowed to increase the combined resolving power of 25% over the entire energy range

(400 – 1600 eV) without a reduction in the through-put. Depending on the choice of the PGM and the spectrometer gratings, the beamline can work with three setups: low-, medium-, and high-resolution. Table 3.1 reports the energy resolution, resolving power and relative flux of the three configurations before and after the upgrade. The resolution was determined as the width of a pure elastic peak, measured in a non-resonant way on a piece of carbon tape. The low-resolution setup uses the 800 lines/mm grating of the

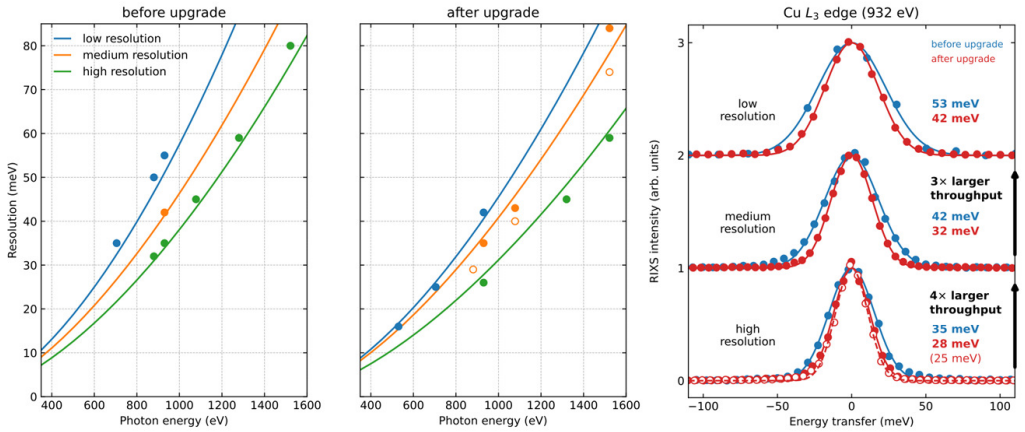

Setup	PGM grating	ERIXS grating	ΔE(930) eV	ΔE/E	Rel. Flux
Low-res.	800 lines/mm	1400 lines/mm	42 meV	22′000	12
Med-res.	800 lines/mm	2500 lines/mm	32 meV	30′000	4
High-res.	1600 lines/mm	2500 lines/mm	26 meV	40′000	1

Table 3.1: Beamline and spectrometer performance. (a): Resolving power before the 2019 upgrade. (b): resolving power after the upgrade. (c) experimental resolution measured from the width of a pure elastic peak for low-, medium-, and high-resolution setups. The table summarizes some relevent specifications of the different configurations. All values refer to 15 µm exit slit. Figures were adapted from the beamline poster at the ESRF.

PGM and the 1400 lines/mm of the spectrometer. The combined resolution at the Cu L_3 edge is close to ~ 40 meV, with a corresponding resolving power of 22′000. The distance in energy between two adjacent experimental points is (at 930 eV and with the normal parameters used for data extraction, see Sec. 3.2.3) ~9 meV. The medium resolution setup is realized with the 800 lines/mm PGM grating and the 2500 lines/mm spectrometer grating. The combined resolution at the Cu L_3 edge is 32 meV, so that the resolving power is 39′000. The energy separation between adjacent points is now smaller by a factor 2500/1400 ~ 1.8, and equal to ~5.5 meV. However, the corresponding photon flux is smaller by a factor three with respect to the

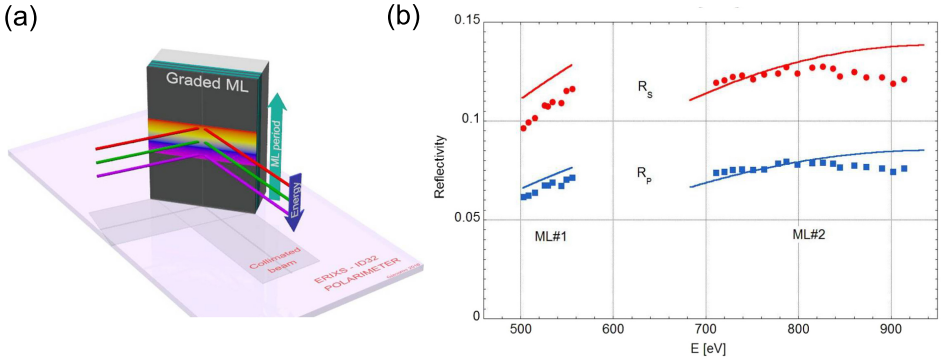

Figure 3.3: (a) Scheme of the multilayer used for polaraztion analysis. Arrows indicate the gradient of the multilayer period and of the energy of the impinging beam. (b) Energy ranges and reflectivity of the two multilayer mirrors installed in the chamber. Red (blue) dots are experimental values for σ (π) polarization. Solid lines are calculated values. Both panels adapted from [90].

low-resolution setup. The high-resolution setup uses the 1600 lines/mm and 2500 lines/mm gratings, respectively. The energy resolution at the Cu L_3 edge is 26 meV, with an astonishing resolving power of 36′000. The energy step is determined by the spectrometer grating and is therefore the same as in the medium-resolution setup. However, the photon flux is reduced by a factor 12 with respect to the low-resolution setup, so that this configuration is seldom used.

As can be evinced from panel (c) of Fig. 3.1, the energy resolution of the beamline in the low-resolution setup now matches what could be achieved previously in the medium-resolution configuration. This allowed to perform experiments with the same resolution but with a flux increased of a factor 3.

3.2.2. Polarimeter

The ERIXS spectrometer is the only one in the world equipped with a soft x-ray polarimeter, which allows to disentangle the scattered beam into its vertically- and horizontally-polarized components. The optical scheme of the polarimeter is depicted in Fig. 3.3. The core of the polarimeter is a multilayer mirror, which is inserted in the optical path right before the CCD detector and reflects the beam onto a second CCD detector, identical do first one. The principle of the setup is the different reflectivity R of the horizontal (also denoted π) and vertical (σ) components of the beam. The two components are then retrieved, after a little algebra, by measuring a RIXS spectrum

with and without the reflection on the multilayer. The chamber hosts two mirrors, which are designed to cover the 670-960 eV and the 500-560 eV energy ranges. Each of them is a superlattice of W/B_4C, obtained by coating flat Si substrates. The incidence angle on the multilayer with respect to the surface is close to the Bragg condition $\sin\theta = n \cdot hc/(2d \cdot E)$, but not exactly equal. It is indeed chosen to maximize the following figure of merit:

$$M = S_{\text{eff}} R_{\text{avg}} = \left(\frac{R_\sigma - R_\pi}{R_\sigma + R_\pi} \right)^2 \cdot \sqrt{R_\sigma R_\pi} \tag{3.1}$$

where R_{avg} is the average reflectivity of the multilayer and S_{eff} is the square of the so-called Sherman parameter, which quantifies the normalized difference in the reflectivities. At the Copper L_3 edge ($\sim$ 930 eV), the optimum angle is $\theta = 20°$, which gives $R_\sigma \sim 0.14$ and $R_\pi \sim 0.085$, so that $R_{\text{avg}} \sim 0.112$ and the Sherman is ~ 0.25. It must be noted, however, that since the multilayer works in the Bragg condition, the reflectivity strongly depends on the incident energy. Even in the relatively small energy range of a RIXS spectrum, variations in the reflectivity cannot be neglected. Therefore, the multilayer is *graded*: the superlattice period changes with the vertical coordinate, so that the Bragg condition is satisfied in an acceptable energy range ($\sim$ 20 eV) for a fixed θ. The grading also allows to cover different edges using the same incidence angle. In particular, the period gradient matches the dispersion of the G_1 grating (1400 lines/mm) of the spectrometer, and goes from 2.77 nm to 1.91 nm over a total height of 120 mm.

We also stress that thanks to the parabolic mirror, the beam is collimated and θ is the same along the horizontal profile of the beam, so that the grating has to be graded only along the vertical direction. The horizontal size of the multilayer is 80 mm, enough to accept the 22 mm wide beam at the working $\theta \sim 20°$.

3.2.3. RIXS data extraction

At the end of the spectrometers, the scattered x-rays are collected using a two-dimensional CCD detector. Each absorbed photon produces an electron cloud inside each pixel, which is then amplified and collected by the acquisition chain, producing two-dimensional images. An example of an image collected by the detector is shown in Fig. 3.4. The energy of the photons is encoded in the vertical position on the detector. Since the beam is horizontally collimated, photons with the same energy are spread over (almost) horizontal iso-energetic lines easily visible in Fig. 3.4. A RIXS spectrum is then built by integrating all the photons along these lines to obtain *energy loss - intensity* curves. The iso-energetic lines are actually slightly tilted,

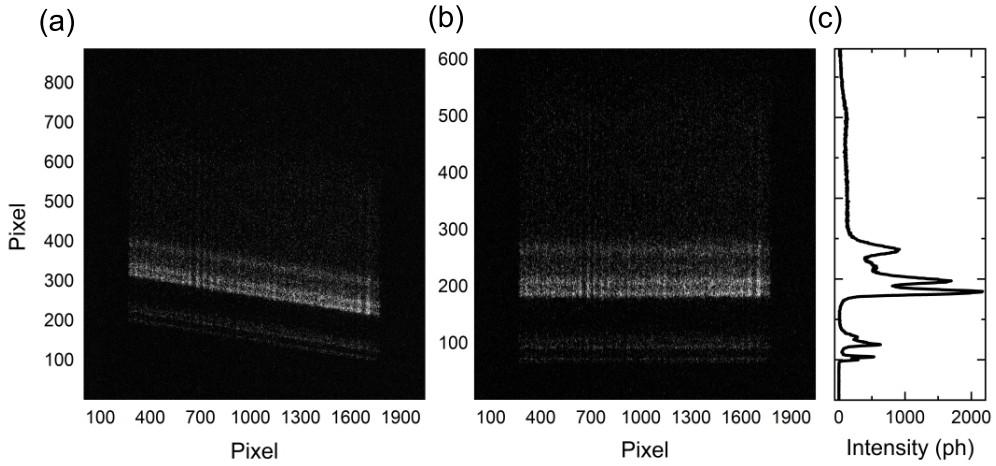

Figure 3.4: (a): example of a RIXS image acquired by the CCD detector (actually, a sum of 15 equivalent images). (b) same image in (a) after slope correction. (c) RIXS spectrum obtained by integrating image (b) along the isoenergetic lines.

due to a small offset in the roll-angle of the grating, so that a correction is needed (usually called curvature-correction).

The total intensity on the detector is usually quite low. Its precise value depends on the absorption the characteristics of the sample and the absorption edge, but usually, even when using the low-resolution setup, is of the order of 10^{-4} photon/pixel/s (although of course not equally distributed on the detector). Therefore, during a reasonable acquisition time of ~ 1 minute, a single pixel receives much less than a photon. Moreover, the electron cloud generated by a photon ($\sim E\,[\text{eV}]/3.6$ electrons) diffuses over a length of 25 µm, so that it spreads on several pixels. These two properties can be used to employ single-photon detection algorithms to enhance the spatial resolution of the detector (and therefore the energy resolution of the spectrometer). The exact procedures are described in [92], but the main idea is to use the number of electrons on the pixels adjacent to the one which has absorbed a photon to reconstruct its position with sub-pixel resolution. In particular, the electrons on the adjacent pixel are used to calculate a "centre of mass" of the photon position. The SPC algorithm allows to decrease the spatial resolution of the CCD from 25 µm to 7 µm. usually, ones bins the spectra using 2.7 points per original pixel.
While the resolution of the detector is just one of the many factors that determine the total energy resolution of the spectrometer, such an improvement allows to gain $\sim 5 \div 10$ meV.

Chapter 4

Fractional spin excitations in infinite-layer $CaCuO_2$

The results presented in this Chapter have been published as *"Fractional Spin Excitations in the Infinite-Layer Cuprate $CaCuO_2$"* by L. Martinelli, D. Betto, K. Kummer, R. Arpaia, L. Braicovich, D. Di Castro, N. B. Brookes, M. Moretti Sala, and G. Ghiringhelli, Physical Review X 12, (2022).

The magnetic spectrum of cuprates has been studied intensively in the last years, because of its connection to superconductivity. In essence, the problem translates to the physics of the spin-½ square-lattice antiferromagnet.

Most of the dynamics is relatively-well comprehended. For low values of the next-nearest neighbour couplings, the groundstate is close to the classical Neél state with two magnetic sublattice, and the fundamental excitations are $\Delta S = 1$ magnons. However, anomalies have been detected in the magnetic response close to the $(1/2, 0)$ point in reciprocal space, where discrepancies are observed with respect to the predictions of Linear Spin Wave Theory (LWST). Interestingly, they are shared between very different materials, hinting at a fundamental property of the spin spin-½ square-lattice which is not yet understood. Experiments also suggest that the magnitude of such deviations from the LSWT scenario is correlated with the strength of longer-range couplings.

What happens when the magnitude of longer-range and multi-spin couplings are comparable to the nearest-neighbour exchange? State-of-the-art calculations suggest that the system might become close to phase transitions towards different kinds of Resonating Valence Bonds States. Moreover, the usual bosonic spin-waves can fractionalize into pairs of $\Delta S = 1/2$ excitations: two-dimensional spinons. In this chapter, we report RIXS measurements on the magnetic dynamics of the infinite-layer cuprate $CaCuO_2$. In this compound, the absence of the apical oxygens strongly enhances the value of the long-range magnetic interactions. Correspondingly, the anomaly at the

antinodal point X is extremely evident and shows large quantitative differences with respect to the other compounds. To reveal its nature, we exploit the unique capabilities of the ID32 beamline and the ERIXS spectrometer. With an innovative combination of direct, polarimetric and detuning RIXS spectra, we provide evidence for the partial fractionalization of magnons into two-dimensional spinons.

Contents

4.1. Introduction: magnetism of the spin-1/2 square lattice

The antiferromagnetic (AF) spin ½ square lattice is one of the fundamental systems in modern consensed mattery physics. Partly, this is because of its implication in the longstanding problem of high temperature superconductivity in two-dimensional cuprates [8]. However, the interest in it also stems from its purely quantum mechanical nature. Despite the expected instability in two-dimensions, the magnetic ground state is usually of Néel–type: two magnetic sublattices with opposite magnetization, kept stable thanks to Dzyaloshinskii-Moriya interactions weak inter-layer coupling [86, 93, 94]. Surprisingly, the linear spin-wave theory (LSWT), which describes the magnetic excitations as spin-1 bosonic quasiparticles and is basically the first order of a $1/S$ expansion, provides a good description of the magnetic spectrum in most of the 2D Brillouin zone [17, 23, 93, 95], and of static thermodynamic properties [96, 97]. However, the antinodal region close to the magnetic zone boundary, which is related to short-wavelength physics, exhibits large deviations from this simple framework [18, 93, 98, 99]. In particular, in the vicinity of the $(½, 0)$ point, experiments reveal a loss

of magnon spectral weight and the simultaneous emergence of a continuum at higher energies. These observations are not captured by LSWT, not even when it is extended to higher orders of the $1/s$ expansion [100]. One proposed interpretations is in terms of multi-magnon processes, i.e., excitations that involve a number of magnons greater than one [101–103].

The multi-magnon picture has indeed been used to (partially) reproduce the experimental results in compounds where the nearest-neighbour interaction is by far the dominant one. Example include the organic cuprate copper deuteroformate tetradeurate (CFTD), or even $Sr_2CuO_2Cl_2$ [104].
However, recent theoretical work has suggested that the peculiarities at the magnetic zone boundary might arise from the proximity to exotic magnetic phases without long-range antiferromagnetism. Some examples include the resonating valence bond (RVB) [13, 98], the AF* [105], and the valence bond solid (VBS) [106–108] states. The basic feature of these purely quantum mechanical ground states are pairs of $1/2$-spins arranged into local singlets [13]. Their most fascinating property is the fractionalization of bosonic magnons into unbound (or almost-unbound) magnetic excitations carrying spin $1/2$, usually referred to as spinons. Phenomenologically, one can imagine the existence of a spinon band, which is gapped in the Néel ground state. This band has a dispersion minimum at $(1/2, 0)$, where the magnon energy is instead maximum [98, 105, 108, 109]. The corresponding mixing of the two bands in the proximity of this point could then transfer spectral weight from the magnon to the higher-energy spinon and give rise to the continuum measured around $(1/2, 0)$ [108]. At short wavelengths, deconfined spinon pairs become more similar to magnons and the two types of spin-1 excitations mix, in a similar fashion as in the exciton-polariton picture [108]. While in one-dimension the separation (deconfinement) of two spinons is complete, as has been observed in the case of spin-$1/2$ chains and ladders, in two-dimensions the deconfinement would be only partial [108], unless the system is a pure spin liquid [107]. It has also been put forward that the aforementioned fractionalization can be present even in the pure Heisenberg-AF copper deuteroformate tetradeurate, which still hosts the magnetic anomaly [98, 108]. However, the experimental results were later interpreted also with a LSWT scenario in the presence of a strong magnon-magnon interaction [103], casting doubts on the actual observation of spin fractionalization in that case. Cuprates are candidates for the discovery of fractional magnetic excitations. The RVB ground state, originally proposed by Anderson [13] in the context of high-T_c superconductivity, is challenged (in undoped compounds) by the evidence of Néel AF order coming from experiments. Nevertheless, the $(1/2, 0)$ anomaly is a common feature. The low-energy magnetic physics of cuprates emerges from fundamental Hubbard-Emery Hamiltonian [10, 39, 110, 111]. The minimal model which describes it involves interactions (sketched in Fig. 4.1) among first (J_1), second (J_2) and third (J_3)

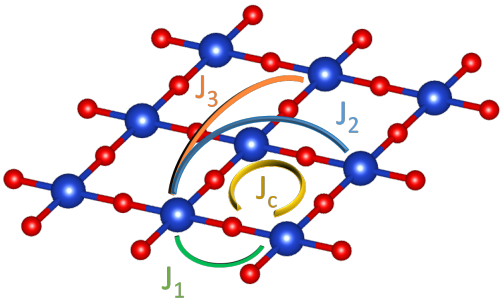

Figure 4.1: Scheme of CuO_2 planes. Oxygen atoms are depicted in red, Copper atoms in deep blue. Coloured solid lines show the spin interactions emerging from a Hubbard-like Hamiltonian as explained in the text.

nearest neighbours, plus another multi-spin interaction that couples four spins in a Cu_4O_8 plaquette, usually called ring exchange [17, 23, 112]. Modern Quantum Monte Carlo calculations have suggested that the partial deconfinement of spinons might be enhanced by the presence of frustrating next-nearest neighbor [113–116] or multi-spin couplings [106–108, 117]. In particular, many studies have demonstrated that ring-exchange J_c is by far the most important term [17, 23, 102] among the longer-range interactions.

Therefore, cuprates with very strong multi-spin interactions are of interest in this context. Experimentally, the value of these interactions is strongly correlated with the presence of the so-called apical oxygens. They are placed along the out-of-plane direction, and are directly coordinated with the in-plane Cu atoms like explained in Sec. 1.3. In particular, a larger distance between apicals and CuO_2 (and therefore a smaller coordination), or even their absence, reduces the energy separation between Cu and Oxygen bands (the so-called charge transfer energy Δ). This separation determines the total energy of the virtual states in the Cu-Cu hopping process. Therefore, a smaller charge-transfer energy strongly enhances all the Cu-Cu hopping terms [9, 118]. This, in turn, increase the strength of the magnetic interactions [23].

$CaCuO_2$ (CCO) belongs to the class of infinite-layer cuprates, which have no apical oxygens. It has by far the strongest long-range magnetic interactions among cuprates, with a particularly large ring exchange J_c [21, 23]. Therefore, it is the ideal candidate in the quest for magnon fractionalization. Previous studies of CCO had already shown the presence of the anomaly at the X point, and had brought a rough estimate of the J-values. However, the actual nature of the anomalous spin spectrum was never determined. In this work, we study $CaCuO_2$ by resonant inelastic x-ray scattering (RIXS) at the Cu L_3 edge. We exploit several innovative techniques to unravel the magnetic spectrum close to the $(1/2, 0)$ point, and provide evidence that this anoma-

lous dynamics is more consistent with a continuum of spinon pairs than with a multi-magnon scenario. In Sec. 4.2 we report including information about samples growth and describe the technical details of the experimental measurements. In Sec. 4.3 and in the related subsections we then present the results of our measurements. In particular, in Sec. 4.3.1 we present the momentum dependence of the energy and intensity of the magnetic excitations, where a clear anomaly close to $(1/2, 0)$ point is evident. In Sec. 4.3.2 we present polarimetric RIXS measurements with unprecedented quality and resolution, which points towards an interpretation of the anomaly in terms of fractionalization instead of multiple magnons. Finally, in Sec. 4.3.3 we report an incident-energy dependence of the magnetic spectrum, which further supports our interpretation. Section 4.4 presents a discussion of the experimental results, where we also provide a more precise estimate of the longer-range magnetic interactions.

4.2. Experimental Details

4.2.1. Samples

The crystal structure of $CaCuO_2$ displayed in panel (a) of Fig. 4.2, is that of infinite-layer cuprates. It is a stack of CuO_2 planes separated by electronically inert Ca^{2+} ions. Cu^{2+} is in a $3d^9$ configuration, with a single hole in the $3d$ shell and a corresponding spin $1/2$. Infinite-layer cuprates cannot be doped by standard means: doping with oxygen intercalation leads to a complex unit cell [119]. Superconductivity was, however, obtained in heterostructures [120] and superlattices [121, 122] by doping through the interface (for example with $SrTiO_3$).

The CCO films were prepared by the group of Prof. Daniele Di Castro, at Università di Roma Tor Vergata. The films were grown with pulsed-laser deposition (KrF laser, $\lambda = 248$ nm) at a temperature of 600 °C and with an oxygen pressure of 0.1 mbar, on a $NdGaO_3$ (NGO) (1 1 0) substrate. The substrate holder and CCO target (prepared by a standard solid-state reaction [120, 121]) were kept at a distance of 2.5 cm. To verify the quality of the samples and determine the lattice parameters, we have performed laboratory x-ray diffraction. Symmetric Reciprocal Space Maps (RSM) around the 002 reflection of CCO allowed to determine the out-of-plane lattice constant $c = 3.184$ Å, as well as the film thicknes $t = 31 \pm 1$ nm. Asymmetric RSM around the 103 reflection were used to determined the in-plane lattice constants $a = b = 3.862 \pm 0.004$ Å.

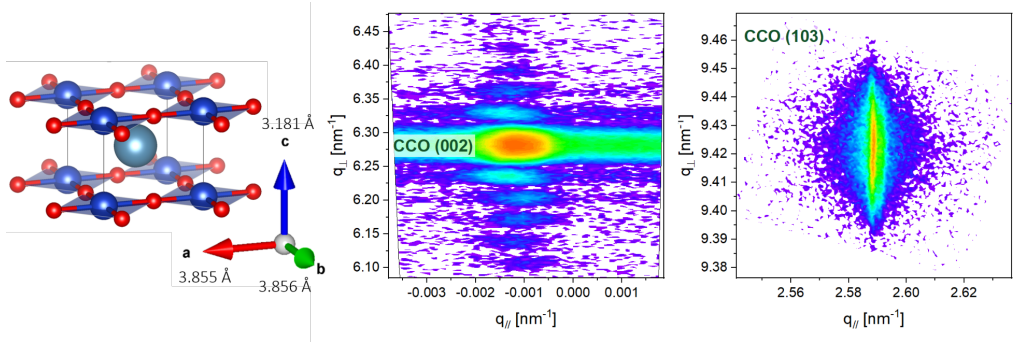

Figure 4.2: $CaCuO_2$ (CCO) sample characterization. (a): crystal structure of CCO. The lattice constants determined by diffraction are reported close to the corresponding axes. (b): symmetric Reciprocal Space Map (RSM), showing the 002 reflection of the CCO film. The Kiessig fringes, due to the finite thickness of the sample, are clearly visible. (c): asymmetric RSM of the 103 peak, which allows to determine the in-plane lattice constants.

4.2.2. RIXS measurements

RIXS was performed at the ID32 beamline of the European Synchrotron Radiation Facility (ESRF) in Grenoble (France), using the ERIXS spectrometer [90, 123]. A sketch of the experimental geometry adopted during the measurements is given in Fig 4.3(d). The CuO_2 planes were perpendicular to the scattering plane. We name σ (π) the polarization state perpendicular (lying into) the scattering plane, and we add a prime symbol (σ', π') for the polarization states of scattered x-ray photons. To reveal the nature of the magnetic anomaly at the antinodal point we employed all the degrees of freedom of the RIXS technique: momentum transfer, (linear) polarization of incident-photon and scattered-photon [123], and incident photon energy close to the absorption resonances. The results of the measurements are reported in sections 4.3.1 (momentum dependence), 4.3.2 (polarimetric RIXS) and 4.3.3 (energy dependence), respectively.

The transferred momentum was changed rotating the angle θ, while the scattering angle (2θ) was kept fixed at 149.5° for most of the measurements. We indicate the transferred momentum $\mathbf{q}_\parallel$ with the set of coordinates (H, K, L) in reciprocal lattice units (r.l.u.), i.e., using the set of the reciprocal lattice vectors $a' = 2\pi/a$, $b' = 2\pi/b$ and $c' = 2\pi/c$ as a basis. By convention, we assign negative (positive) values of H and K to grazing-in (grazing-out) geometries, as portraied in the inset of Fig. 4.3(d). We label the high-symmetry in-plane points $(0, 0)$, $(1/4, 1/4)$ and $(1/2, 0)$ as Γ, Σ and X, respectively. Te drawback of keeping the scattering angle fixed is that L is constantly changing whenever we change H (i.e. we rotate θ). Therefore, we also performed some scans with fixed L by rotating the ERIXS spectrometer, exploiting the continuous rotation of the scattering arm 2θ [90]. The resolution was deter-

mined by measuring the width of a non-resonant elastic peak on silver paint. Its value was ~ 48 meV for the standard RIXS measurements (momentum incident-energy dependence). To precisely determine the lineshape of the magnetic spectrum, we also acquired a ultra-high-resolution RIXS spectrum at $(-0.43, 0)$, suing a grazing-in configuration with σ incident polarization (for reason that will be clarified later). The measured resolution is an unprecedented value of ~ 26 meV, made possible by the recent upgrade of the beamline described in Chapter 3. Unless specified, the incident energy of the x-rays was fixed at the Cu-L_3 resonance (~ 931 eV). The counting time was 30 min for the momentum and incident-energy dependence, and 5 h for the ultra-high-resolution spectrum.

RIXS spectra with polarization sensitivity, presented in Sec. 4.3.2, were measured at $(+1/2, 0)$ using both π and σ incident polarization states. The measured resolution was 45 meV, much better than in any of the previously published measurements [37, 74, 124]. . The soft x-ray polarimeter allowed us to disentangle the parallel the crossed $(\pi\sigma', \sigma\pi')$ and parallel $(\pi\pi', \sigma\sigma')$ components of the RIXS spectra, which correspond to spin-flip ($\Delta S = 1$) and spin-conserving ($\Delta S = 0$) final states respectively. The former can be assigned to he magnon and related fractional continuum, and to odd number of multi-magnons the latter to two-magnon excitations. The acquisition time of polarimetric RIXS spectra was 6 h to compensate for the very low efficiency of the soft x-ray polarization analyzer (~ 10%). The experimental error-bars have been estimated using the expressions reported in Ref. [124]. In particular, they are about three times stronger than in direct (i.e. without polarization analysis) RIXS measurements

Detuning RIXS spectra, presented in Sec. 4.3.3 were acquired at four different incident photon energies, at and below the Cu L_3 absorption edge ($\Delta E_{\text{in}} = 0, -0.150, -0.450, -0.675$ eV). The momentum transfer was kept fixed at $(-0.43, 0)$ i.e., in a grazing-in geometry, and we used σ incident polarization. With this setup we could achieve comparable cross sections for the $\Delta S = 0$ and $\Delta S = 1$ scattering channels, and thus unravel the nature of the different spectral features. The spectral weight of magnons scales with the XAS absorption profile, while it falls more rapidly for the latter. This behaviour is due to the fact that the bimagnon intensity depends on the effective lifetime of the intermediate state, which is lower when the incident energy is detuned from the absorption edge. This has been verified in Refs. [125] and [78]. Spectra at increasing distance from the Cu L_3 resonance have been acquired for longer times to counterbalance the decrease in the signal. In particular, the spectrum at resonance was counted for 30 min, the one at lowest incident energy for 2 h. The temperature was kept at 20 K for all the measurements to reduce radiation damage and minimize the intensity of anti-Stokes features close to the elastic line.

4.3. Experimental Results

4.3.1. Momentum dependence

Experimental spectra acquired at different $\mathbf{q}_\parallel$ are reported in Fig. 4.3(a). The use of π polarization and grazing-out geometry enhances the intensity of spin-flip excitations [6, 71]. In the following, we will often make the approximation that the RIXS intensity in this geometry is purely related to spin-flip events. This holds because the charge excitations are not in this energy range in undoped cuprates, and the small $\pi\pi'$ spectral contribution can be neglected. Furthermore, we will take it to be proportional to the dynamical spin susceptibility measured by inelastic neutron scattering: a discussion on the validity of this approximation is given in Sec. 4.4.
Away from the $(1/2, 0)$ point, spectra are dominated by a sharp magnon quasiparticle peak, and show a very weak continuum. The energy width of the magnon, which is related to its lifetime, is comparable to the experimental resolution close to the $(1/4, 1/4)$ and $(0, 0)$ points, and is in general very small in most of the Brillouin zone. This can be ascribed to the absence of doping (also testified by the absence of a particle-hole continuum) and to the very high quality of the sample evident from diffraction measurements. The spectral weight of the magnon weight clearly decreases towards the X point. Simultaneously, another feature present between the magnon energy and ~ 800 meV evidently increases in intensity. While this phenomenology had already been already observed in cuprates [17, 23, 100], we note that in the other materials the single magnon remains the dominant excitation in the spectrum (see e.g. [104]). On the contrary, in $CaCuO_2$, the single magnon peak is dwarfed by a broad and asymmetric continuum, and is nearly undetectable. Panels 4.3(b,c) highlight that this anomaly is confined to a region of radius ~ 0.1 r.l.u. around the antinodal point.

As mentioned in the previous Section, changing $\mathbf{q}_\parallel$ with fixed scattering arm 2θ means that the out-of-plane component $\mathbf{q}_\perp$ will change too, so that the L value is not the same at the different (H, K) points. In particular, L goes from ~ 0.46 to ~ 0.22 when moving along the antinodal direction $((0, 0) \rightarrow (0.5, 0))$. However, the magnetic structure of CCO is known to be more three-dimensional than that of other cuprates. This is testified, for example, by the non-zero energy of the magnon at $(0, 0, L)$ with non-integer value of L [23, 126]. To verify that the anomaly at the X point is not due to the 3D structure of CCO, we also measured RIXS spectra along a limited range of the same path in the 2D Brillouin zone, but at constant $L = 0.3$. While the magnon energy is evidently different in the two datasets at the Γ point, the difference decreases at larger H values and basically vanishes for momenta above $H > 1/8$, as reported in Fig. 4.3(d). This suggests that the anomaly at the $(1/2, 0)$ point is negligibly affected by the value of L.

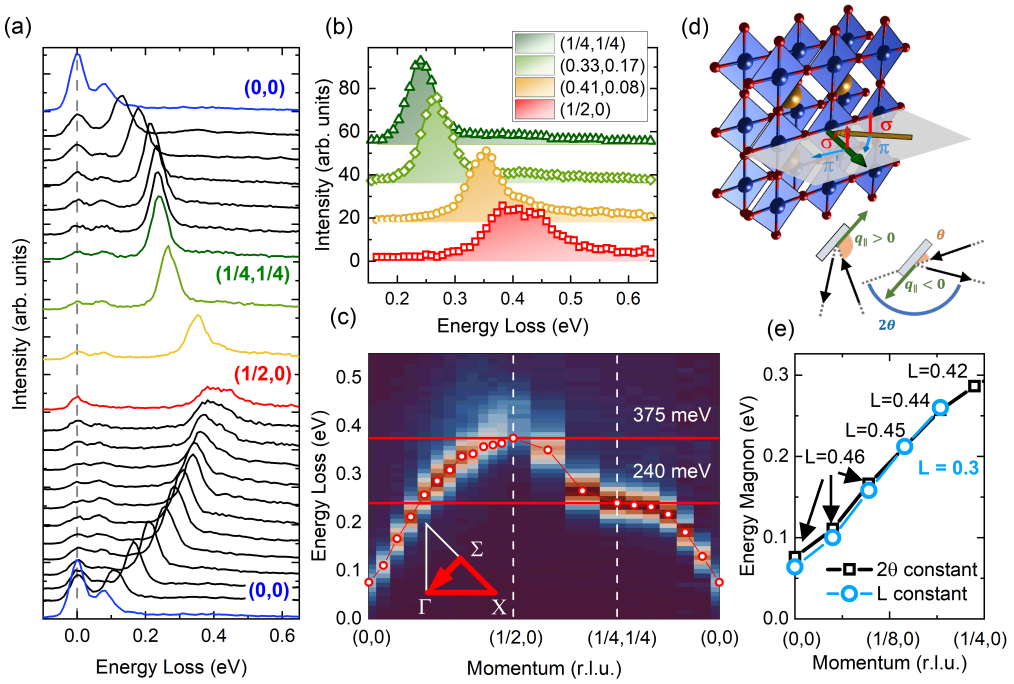

Figure 4.3: (a): RIXS scans as a function of momentum, measured with incident π polarization and in grazing-out geometry. (b): Evolution of RIXS spectra along the AF zone boundary. Scans have been divided by the spin-flip cross section. (c): Dispersion of the single-magnon along the path depicted in the inset. The red circles correspond to the energies extracted by fitting the data (error bars are of the size of the dots). The two red, horizontal solid lines highlight the magnon energy at the X and Σ points. (d) Sketch of $CaCuO_2$ structure and scattering geometry used for RIXS experiments. Cu atoms are depicted in blue, oxygen atoms in red and Ca cations in gold. Also shown are the polarization states of incident and scattered light. Polarization lying in the (perpendicular to) the scattering plane is named π (σ). The small inset explains the convention on grazing-in and grazing-out geometries. The shaded orange area is the incident angle θ, the scattering angle 2θ is drawn in blue, and the light-green arrows are the in-plane components of the transferred momentum. (e) Dispersion of magnetic excitations along the antinodal line measured with constant scattering angle (black squares, variable L) and constant L (light blue circles, changing the scattering angle). L values are reported for each point for the black curve. Scans were measured with incident π polarization and grazing-out geometry.

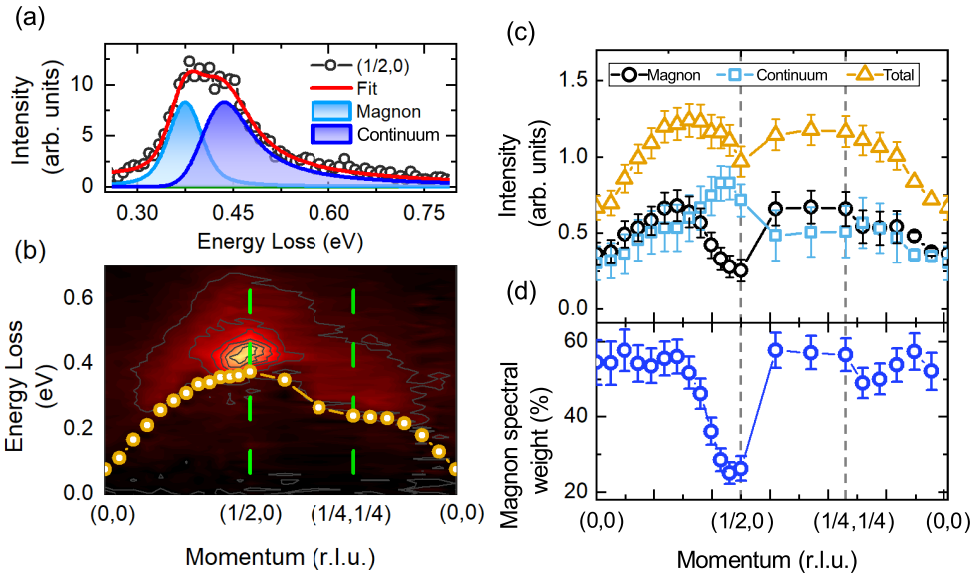

Figure 4.4: (a) Fitting routine of the RIXS spectrum at $(1/2, 0)$ measured with π polarization. The single-magnon peak and the higher-energy continuum are shown in light and deep blue, respectively. The total fitting curve is in red, no shading. (b) Momentum dependence of high-energy continuum. Elastic, phonon and magnon peaks have been subtracted. The energy of the magnon extracted from the fitting is reported in gold circles. The scans have been divided by the spin-flip cross-section, which only depends on experimental geometry [6]. (c) Spectral weight (determined as the area below the curves) of the single-magnon, of the high-energy continuum and of the total magnetic spectrum as a function of momentum. (d) Ratio between the intensity of the single-magnon peak and of the total magnetic excitations.

The false-color map shown in panel (c) of Fig. 4.3 reports the RIXS intensity along the reciprocal-space path shown in the inset. The energy of the single magnon, obtained by a fitting procedure described later, is highlighted by the red dots. The large energy ($E_X \approx 375$ meV) at the antinodal point and the strong dispersion along the antiferromagnetic zone zone boundary ($\Delta E_{\mathrm{MZB}} = E_X - E_\Sigma \approx 135\,\mathrm{meV}$) signal large values of J_1 and J_c, which are probably the largest among all known materials [23, 127].

We concentrate our analysis on the behaviour of the single-magnon and the continuum in the proximity of the X point. In order to extract momentum dependence of their spectral weight, we have performed a fitting of the spectra in the $[0, 0.8]$ eV energy range as depicted in panel (a) of Fig. 4.4. We used a Gaussian profile for the elastic and phonon peaks (which were assumed to be resolution limited), a Voigt lineshape for the single magnon (whose intrinsic lorentzian linewidth can be not negligible), and an asymmetric Lorentzian profile (similar to what was used in [24]) for the high-energy

continuum above it. Spectral weights were taken as the areas below the fitted curves. In panel (b) of Fig. 4.4 we plot the intensity map along the Γ–X–Σ – Γ path (the same used in panel (b) of Fig. 4.3) after removing the other featues (elastic, phonon and single magnon). The energy of the single magnon peak extracted form the fitting is reported in yellow circles.

The fitting procedure allows us to to determine how the intensities of single magnon and continuum change as a function of momentum. The outcome of the analysis is shown in panel (c) of Fig. 4.4. All the intensities have been divided by the RIXS spin-flip cross section, which only depends on the experimental geometry. This is justified since the spectral weight predominantly belongs to the $\Delta S = 1$ scattering channel in this geometry, as explained before. Evidently, the total weight of magnetic excitations decreases when approaching the antinodal point. However, the intensity of the single-magnon drops much more sharply, and is for a good part transferred to the higher-energy continuum. Incidentally, we note that the spectral weight is small but not zero at the Γ point, due to the three-dimensional character of the magnetic structure of the material [23]. However, this has basically no effect on the short-wavelength physics, as we will thoroughly demonstrate in the next sections. The transfer of spectral weight is better highlighted by the ratio between the intensities of the magnon and of the higher-energy continuum, which is reported in panel (d) of Fig. 4.4. This quantity is also useful because it is independent of any normalization of the RIXS spectra (e.g. cross-section and self-absorption corrections). Far from the X point, the single magnon contribution contributes to ~60% of the total magnetic intensity; this value drops by a factor of 3 to ~20% at the X point. This deviation is confined within 0.1 r.l.u. around X.

In the past, the asymmetric shape of the magnetic spectrum around the X point was interpreted as a damped magnon [22, 24, 128], possibly combined with bimagnon excitations of similar intensity [21, 71]. To check how much does the bi-magnon contribute to the spectra, we performed measurements with incident σ-polarized light and grazing-incidence geometry (negative H). In this configuration the calculated single ion cross section predicts comparable intensity for both $\sigma\sigma'$ and $\sigma\pi'$ channels [6], i.e., the $\Delta S = 0$ (even order multiple magnon) and $\Delta S = 1$ (single magnon) contributions, respectively. We tried to define as precisely as possible the shape of the magnetic spectrum close to X (at $(-0.45, 0)$, precisely), where the three magnetic features are well visible (magnon peak, continuum and bimagnon). To do so, we used the high-resolution setup of the Id32 beamline (described in Chapter 3) to achieve the best available energy resolution (26 meV at the Cu L_3 edge) . The spectrum reported in panel (a) of Fig. 4.5 demonstrates that the high energy continuum cannot be interpreted just as a tail of a broadened magnon peak, but rather as an independent spectral feature.

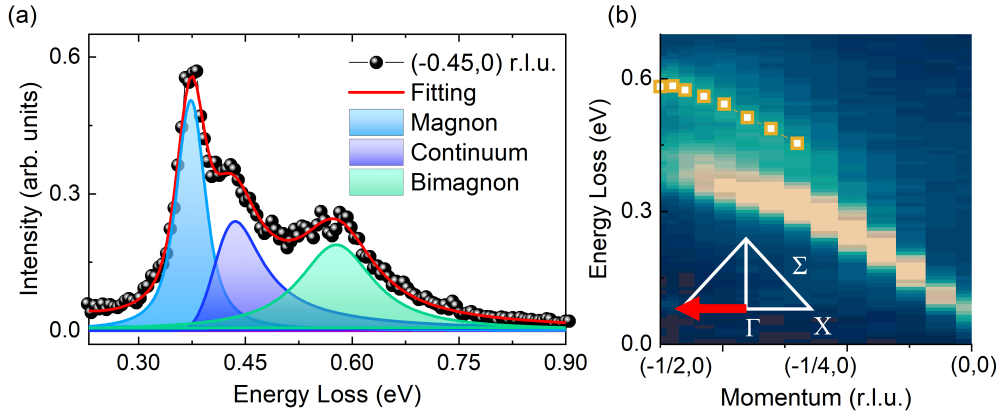

Figure 4.5: (a): Ultra-high-resolution (≈ 26.3 meV) RIXS spectra measured at $(-0.45, 0)$ with σ incident polarization. (b): False-color RIXS map along the $\Gamma \to X$ line, measured with σ incident polarization and in a grazing-in geometry. The energy of the bi-magnon extracted with through a fitting procedure is reported in yellow squares.

Fitting the spectrum we obtain a sharp quasiparticle peak of the magnon at 340 meV and a satellite feature at 440 meV with a width of 33 ± 5 meV. The use of incident σ polarization also allows us, through a comparison with the spectra shown in Fig. 4.3 [6, 71], to disentangle the contribution of the local bi-magnon, peaked at ~550 meV. Its momentum-dependence along the $\Gamma \to X$ direction, acquired with medium resolution and reported in Fig. 4.5(b), confirms that this feature is more intense at the AF zone boundary. These characteristics are consistent with bi-magnon excitations, which arise from the suppression of superexchange interactions during the $3d^{10}$ RIXS intermediate state (see Chapter 2) [71, 100]. We can therefore exclude that the high-energy continuum at the X point, closer in energy to the magnon peak, is a local bimagnon. This implies that the same is true also in the spectra measured with π polarization at positive in-plane momentum H, since the even multiple-magnon contribution are further minimized in this configuration.

4.3.2. Polarimetric measurements

We have demonstrated that the higher-energy continuum is not due to the relatively-well defined (local) bi-magnon, which arises from the suppression of superexchange during the RIXS intermediate state. However, this does not exclude other types of spin-conserving excitations. Indeed, although significant, the separation of the two channels according to the incident polarization is not always straightforward outside the single-ion model. In fact, it was recently shown in $Sr_2CuO_2Cl_2$ (SCOC) that one has to introduce non-local scattering operators to fully account for the RIXS spectral line-

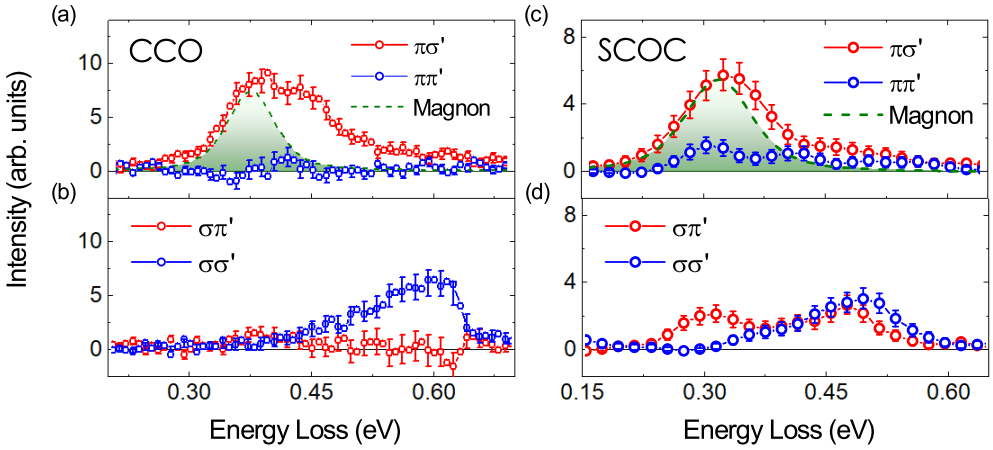

Figure 4.6: RIXS spectra with polarization resolution collected at the X point in CCO [panels (a) and (b)] and in SCOC [(c) and (d)]. In both cases, blue curves denote the parallel (non-spin-flip) channel, the red ones the crossed (spin-flip) channel. Panels (a) and (c) report the spectra with incident π polarization, whereas panels (b) and (d) he spectra measured with incident σ polarization, which maximizes the non-spin-flip scattering channel. Note that the energy resolution of the SCOC data is worse than that of CCO data ($\approx$ 65 meV versus 45 meV) [104], so that the lineshape appears to be broader.

shape [104]. To fully unravel the nature of the anomaly at the X point we performed polarimetric RIXS measurements, i.e. RIXS measurements with sensitivity on the linear polarization of the scattered photon [90, 123, 124]. Determining the σ' and π' polarization components of the scattered X-rays allows us to separate the crossed and parallel channels, which correspond to excitations carrying $\Delta S = 1$ and $\Delta S = 0$.

We present in Fig. 4.6 the set of polarimetric RIXS spectra acquired at the X point in CCO and SCOC. In both samples, the incident-π spectra present a stronger crossed channel contribution (red symbols). However, whereas the parallel (blue dots) contribution is still sizeable in SCOC, it is undetectable at all energies in CCO. The high-energy continuum visible in CCO clearly belongs to the crossed $\Delta S = 1$ channel. On the other hand, when σ polarization is used the predominant channel is of parallel character (blue) in CCO but present a mixed character in SCOC. These measurements also confirm that the local bimagnon contribution is indeed a relatively well-defined peak around $\sim$ 540 meV (which corresponds to $\approx 3J$), as we had guessed from the ultra-high-resolution spectra. Interestingly, in CCO we observe no signature of the complicated multi-magnon features emerging in SCOC [104].

4.3.3. Detuning dependence of magnetic features

One of the advantages of the RIXS technique is that the resonant character provides an additional degree of freedom in the measurements. The behaviour of an excitation upon detuning the incident energy can provide significant information regarding the nature of an excitation [78].

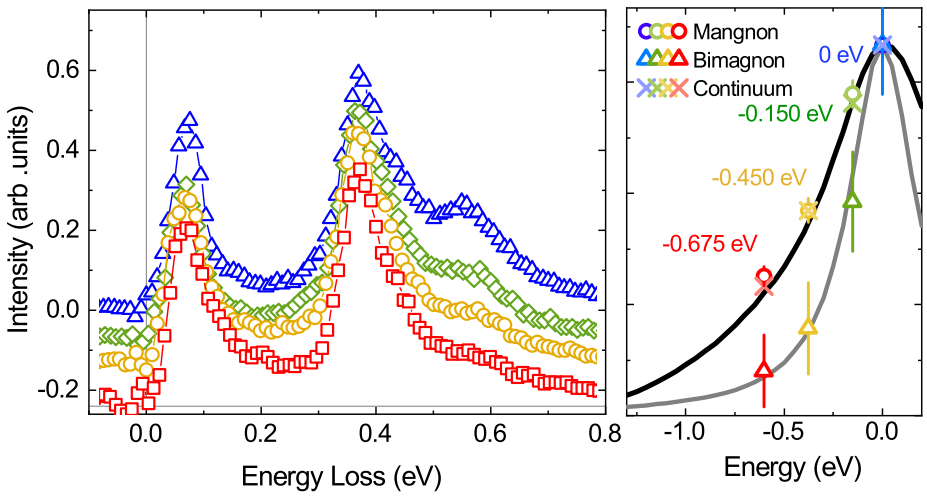

Figure 4.7: Left panel: RIXS spectra measured at several incident energies. The elastic peak has been removed for clarity. The spectra were acquired at $(-0.43, 0)$ using σ incident polarization. The scans in the figure have been normalized to the value of the XAS profile at the corresponding incident energy. The right panel reports the XAS spectrum (solid black line), and the intensities of the single-magnon peak (circles), of the higher-energy continuum (crosses) and of the bi-magnon (triangles). The gray solid line is a guide to the eye. All the measured intensities have been normalized to their resonance value, and are plotted against the value of the incident energy relative to the XAS resonance. The experimental errors on the intensity of the continuum and the single-magnon are smaller than the size the symbols.

Therefore, we have measured the magnetic RIXS spectrum at a few incident energies below the main Cu L_3 resonance, plotted in Fig. 4.7. The sharp peak at ~80 meV corresponds to the Cu-O bond-stretching phonon mode [126], which is also visible in the scans of Fig. 4.3, but is more evident here thanks to the favourable scattering geometry. Performing the same fitting procedure described in Sec. 4.3 we extract the incident-energy dependence of the magnon, the bi-magnon and the continuum excitations. Comparing them to the XAS profile (see inset) it is evident that the $\Delta S = 1$ continuum above 400 meV share the same energy dependence of the single magnon and of the absorption spectrum. The bi-magnon intensity, on the other hand,

decreases faster upon detuning, as previously observed [78, 125, 129]. Incidentally, we also note that the phonon mode also shows a starker intensity decrease. This is a further evidence that the continuum is excited via the same direct-RIXS process as the single magnon. Its intensity is not affected by the lifetime of the RIXS intermediate state, as opposed to the bi-magnon.

4.4. Discussion

Our measurements unequivocally reveal that the high-energy continuum visible in the RIXS spectra in the proximity of the X point has pure $\Delta S = 1$ character. Moreover, it is generated by the same direct RIXS process as the single-magnon. Thus, this high energy continuum is compatible with a decay of magnons into spinon pairs [98, 106, 108, 116]. Factional excitations in the spin-1/2 AF square lattices arise in several Heisenberg-like models [98, 105, 106, 108, 113–115, 117]. At the same time, spinon pairs were invoked before to explain the anomalous high-energy magnetic dynamics in cuprates [18] and pseudospin-1/2 iridates [99]. Nevertheless, no clear experimental evidence of their existence in two-dimension was ever reported. It is important to highlight that the emergence of spinon pairs at the AF zone boundary is not in contradiction with the presence of Néel AF order in this system. In fact, accordin to recent QMC calculations, a broad, gapped spinon band above the magnon energy is present when the Néel phase is close to some exotic magnetic phase without long-range order. Its dispersion has a maximum at the Σ point $(1/4, 1/4)$ and a minimum at X $(1/2, 0)$, where the magnons reach their maximum energy. This results into a mixing of the two excitations in the proximity of this wavevector, made possible by the (quasi-)degeneracy in energy and by the common $\Delta S = 1$ nature [130]). It is important tounderline that two-spinon excitations in 1D spin systems have been observed with RIXS in the last years [35, 37]. In interpreting the data, we have supposed that the RIXS spectral function of the spin-flip channel (in which we are mainly interested) is, in spin-1/2 cuprates, basically proportional to the dynamical structure factor measured in inelastic neutron scattering. This correspondence is indeed rather well-established, having received in the last years sound experimental confirmation [35, 37, 104, 128, 131] and theoretical foundation [85, 132, 133].

The X-point magnetic anomaly is clearly stronger in CCO than in other cuprates. To understand why this happens, we have extracted the magnetic constants of the underlying Heisenberg model. We consider the usual Hamiltonian, which basically comes from a fourth order expansion of the one-band

Hubbard model [17, 26, 112, 134]. With the definitions given in Fig. 4.1(a):

$$\begin{aligned} H = J_1 \sum_{ii'} \mathbf{S}_i \cdot \mathbf{S}_{i'} + J_2 \sum_{ii''} \mathbf{S}_i \cdot \mathbf{S}_{i''} + J_3 \sum_{ii'''} \mathbf{S}_i \cdot \mathbf{S}_{i'''} \\ + J_c \sum_{\langle ijkl \rangle} (\mathbf{S}_i \cdot \mathbf{S}_j)(\mathbf{S}_k \cdot \mathbf{S}_l) + (\mathbf{S}_i \cdot \mathbf{S}_l)(\mathbf{S}_k \cdot \mathbf{S}_j) \\ - (\mathbf{S}_i \cdot \mathbf{S}_k)(\mathbf{S}_j \cdot \mathbf{S}_l) \end{aligned} \tag{4.1}$$

This model is extremely complex to solve, and so far only attempts on small cluster have been made [135]. However, a grasp on the couplings at play can be obtained with a standard linear spin-wave approach to lowest order (large spoin S). While our data clearly reveal a failure of this approximation close to the X point, this procedure is possibly correct for the rest of the dispersion in the Brillouin zone, and is still useful to make a comparison with other cuprates [17, 23, 26, 127]. In this framework, there is a simple analytical expression that relates the magnon energy at the X and Σ and the values of J_1, J_c [17, 26]:

$$\frac{J_1}{J_c} = \frac{3}{10} \frac{1 + \Delta E_{\mathrm{MZB}}/E_{\mathrm{X}}}{\Delta E_{\mathrm{MZB}}/E_{\mathrm{X}}} \tag{4.2}$$

Using the values extracted from Fig. 4.3(c), eq. (4.2) yields $J_c \approx J_1$.

A better estimate can be obtained by directly fitting the measured dispersion within a linear spin-wave calculation. In particular, we have used the Matlab-based software spinW [136]. The direction of the magnetic moments of Cu atoms has been set along the [110] direction like for the other cuprates [26, 93, 98]. The factor Z_c, which quantifies the renormalization of energies due to quantum fluctuations, has been kept fixed to 1.18, again following the literature [17, 18, 93, 98]. In principle, however, there is (to our knowledge) no formal proof that this should hold with such high values of higher-order magnetic couplings. This is surely a topic for further investigation. The result of the fitting is displayed in Fig. 4.8(a). It yields $J = 172 \pm 7$ meV, $J_c = 167 \pm 20$ meV and $J_\perp = 7 \pm 3$ meV. These values are a bit different from the ones found in [23]: this is mainly due to a better estimate of the single-magnon energy close to $(1/2, 0)$, due to the improved energy resolution (~ 42 meV in our work, 60 meV in Ref. [23]). The value of $J_c/J \approx 0.97$ obtained from this global fitting procedure is in very good agreement with the one calculated with eq. 4.2. The value of $J_\perp$, which quantifies the inter-layer interaction, is also consistent to what has been found by inelastic neutron scattering measurements in the bi-layer cuprate $YBa_2Cu_3O_{6+x}$ [61, 137]. This similarity should be expected, since the distance between the two CuO_2 layers in the YBCO unit cell is the same as in CCO. The only differences is that no 3D order is found in YBCO, since the CuO_2 bilayers are too far apart from each other. This value results in $J_1/J_\perp \approx 25$.

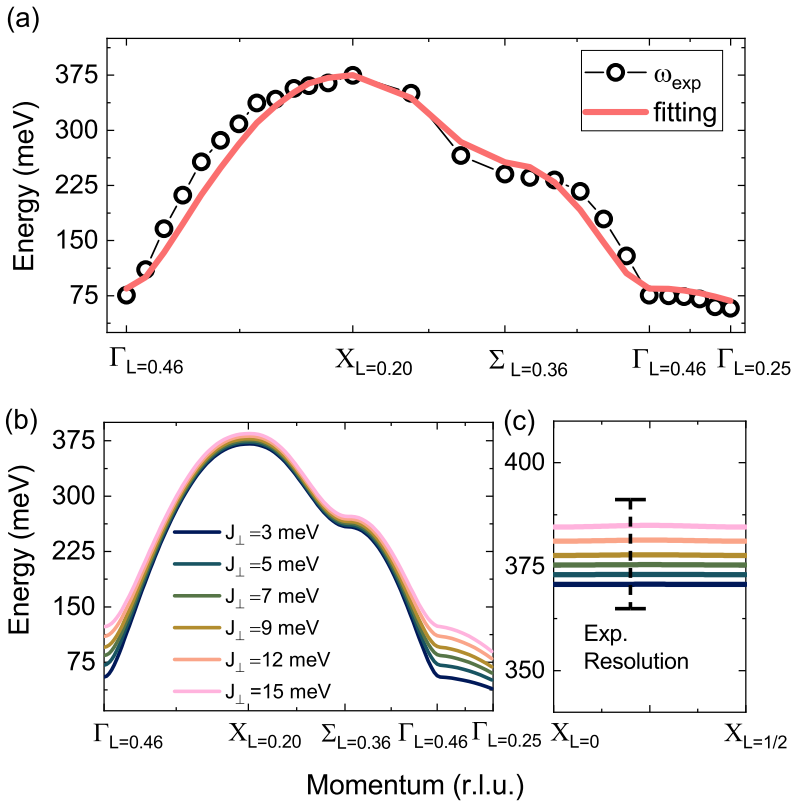

Figure 4.8: Summary of fittings and calculations performed with the spinW software. (a): LSWT fitting of the measured single-magnon dispersion. The 2D (H, K) coordinates of the momenta are labelled with their greek letter as explained in Sec. 4.2. The subscripts report the L values. The reciprocal-space path between $\Gamma_{L=0.46}, X_{L=0.20}, \Sigma_{L=0.36}, \Gamma_{L=0.46}$ are circle arcs in the $H-L$ plane. The last segment is a straight line. (b): simulated dispersion along the same path for several $J_\perp$ values. (c): Calculated L-dependence at the 2D $(1/2, 0)$ point for the same $J_\perp$ values of panel (b). Black dotted line represent our highest experimental resolution (26 meV).

We have performed further simulations to verify that, in a LWST framework, the zone-boundary physics of the magnetic excitations is effectively two-dimensional. First, we have calculated the change in magnon dispersion as a function of $J_\perp$, which was varied in a reasonable range ($3-15$ meV). The result is shown in Fig. 4.8(b). The only discernible effects of $J_\perp$ are observed very close to the Γ point. On the other hand, close to the zone boundary, the differences in the curves fall well below our best experimental resolution (26 meV). Additionally, the energy of the single magnon close to the X point is not affected by changes in L. This is evident from panel (c), which reports the single-magnon energy along the $(1/2, 0, 0) \rightarrow (1/2, 0, 1/2)$ line. The dispersion of all the curves is lower than 1 meV (not even visible

in the figure). This further demonstrates that the inter-layer coupling has a negligible effect on the physics in the proximity of the X point.

Going back to the ring exchange, the extracted value of J_c/J_1 is the largest among copper oxides. In La_2CuO_4 the J_c/J value is ~ 0.29, in $Sr_2CuO_2Cl_2$ ~ 0.42 [104, 127], in single-layer $Bi_2Sr_2CuO_6$ ~ 0.62 [23] and in the $RBa_2Cu_3O_6$ it is close to ~ 0.7.
Therefore, it is natural to correlate the emergence of the high-energy continuum, which we interpret as composed of fractionalized magnetic excitations, to the amazingly strong ring-exchange J_c. The emergence of spinons in the spectrum of the spin-1/2 square-lattice in the presence of strong multi-spin couplings (as the ring-exchange J_c) was suggested some years ago and is now well established in modern calculations [106–108, 117]. Interestingly, a recent ED study [135] performed on the same Hubbard Hamiltonian we used has shown that, at $J_c/J \approx 1$ the excitation spectrum at $(1/2, 0)$ breaks into a continuum of states very close in energy. This is very similar to what has been calculated for Neél-VBS and Neél-RVB transitions [106, 113–116].

4.5. Conclusions

We have used RIXS to perform a deep investigation of the magnetic spectrum in the infinite-layer cuprate $CaCuO_2$. We have analysed its dependence on momentum, incident and scattered polarization, and incident x-ray energy. The momentum dependence reveals a high-energy continuum in the region close to the X point, which clearly cannot be reconciled with the picture of a broadened single-magnon. The dependence on incident polarization rules out thy hypothesis that this continuum is due to local bi-magnons. Instead, its interpretation in terms of a spinon-pairs continuum is strongly supported by: i) the polarimetric analysis, which highlights its purely spin-flip nature and ii) by the detuning analysis, which demonstrates that it arises from a direct RIXS process like the single-magnon. Basically all square-lattice AF materials show a deviation from a LWST picture. It was even observed in systems (like organic cuprates) where the nearest-neighbour coupling is by far the dominant interaction [93]. However, in CCO the effect is greatly enhanced even with respect to other high-temperature superconducting cuprates. We also observe a simultaneus suppression of the even multi-magnon excitations. An estimate of the longer-range spin interactions suggests that the root of these phenomenology lies in the exceptionally large value of the ring-exchange term J_c. This strong value is caused by the absence of apical oxygens, which lowers the charge-transfer energy and enhances the Cu-Cu hopping amplitude [7, 9, 23]. It would be interesting to perform the same investigation on undoped Nd_2CuO_4. This material is not an infinite-layer, but still lacks "direct" apical oxygens [88], and should

therefore show a large J_c/J similarly to CCO.

In conclusion, we provide in this Chapter strong experimental evidence in favour of the presence of fractional spin excitations in a layered cuprate. Spinon pairs are a well known feature in one-dimensional magnetic systems, but different theoretical approaches predicted that they arise also in two-dimensional AF square-lattices [105–108, 116]. However, their observation in layered cuprates was never conclusive so far [18]. Our results might, in principle, support the assignment of the high-energy continuum in the proximity of the $(1/2, 0)$ point to fractional spin excitations also in other cuprates. More generally, we demonstrate that the short-wavelength physics of spin excitations is strongly affected by multi-spin interactions, as was suggested by several models [101, 107, 135].

Chapter 5

Orbital excitation in infinite-layer cuprates

This chapter deals with the analysis of orbital excitations in infinite-layer cuprates. In particular, we report the first unambiguous observation of a collective nature of *dd* excitations in a two-dimensional $3d$ material, i.e. an *orbiton*. Using RIXS at the Cu L_3 edge, we show that in the infinite-layer cuprates $CaCuO_2$ and Nd_2CuO_4 the xy disperses with a bandwidth of ~50 meV, while no dispersion is measured in other cuprates. We show that a Kugel-Khomskii model with negative *next*-nearest neighbour orbiton exchanges is able to quantitatively describe the experimentally observed behaviour. We trace the origin of such negative exchanges back to the strong covalency and the large oxygen-hopping integrals caused by the absence of apical oxygens.

Contents

5.1. Introduction: orbitons in one- and two-dimensional correlated materials

There are two main ingredients that characterize strongly-correlated materials: the presence of a strong, localizing repulsion between the electrons of the d-metal cations, and large hopping amplitudes mediated by the ligand anions (such as Oxygen or Fluorine), which instead would tend to delocalize the carriers over the lattice sites [25]. These opposite tendencies determine the appearance of several orders and broken symmetries, leading to a corresponding number of collective excitations [138–140]. Similarly to electronic charge [141, 142] and spin [17, 64, 143], also the d-orbital degree of freedom can display collective nature, especially in the so-called Kugel-Khomskii systems [144, 145].

The essential physics of orbital order and excitations can be captured assuming an extended version of the Hubbard model, with hopping integrals between all the different orbitals, plus the on-site energies caused by the crystal field. The Hamiltonian for such a model is described in Sec. 2.4.3. Assuming that $t_i/U \ll 1$, which is certainly the case for cuprates, the Hamiltonian can be reduced to something similar to a Heisenberg model. In particular, it can be shown that the vector $\boldsymbol{\tau}_i$, describing the occupation numbers of the different orbitals at site i, behaves similarly to a spin [144]. Such models are usually referred to as Kugel-Khomskii (KK) models [25, 31].

Since there is a finite hopping amplitude also for the excited orbitals, and since the Hamiltonian is very similar to the usual Heisenberg interaction, we can naively expect to observe a collective nature of the orbital excitations. In particular, we can expect that the energy of a dd excitation will depend on its momentum $\mathbf{q}$, i.e. we expect to see a dispersion of the energy.

Such phenomenology has been indeed found in one-dimensional cuprates such as Sr_2CuO_3 and Ca_2CuO_3, which consist of weakly-interacting CuO chains. In particular, the dispersion of the $x^2-y^2 \to xy$ and $x^2-y^2 \to xz/yz$ excitations is immediately visible in RIXS spectra, as shown for Sr_2CuO_3 in Fig. 5.1. It has a characteristic lens-like dispersion, with a maximum at the Γ point and a π-period in reciprocal space. This shape is reminiscent of the holon dispersion in the t-J model. This is not a coincidence: it can be shown that an orbital excitation in a AFM lattice behaves much like a hole [28], moving with with amplitude $t \sim J/2$. There is also a very intuitive explanation of why the orbital excitations can propagate coherently through the lattice. After the excitation, the orbiton hops to the neighbouring site, exciting a spinon (i.e. a magnetic domain wall). Subsequently, the orbiton can propagate without paying additional energy. The situation is not significantly altered when one takes on-site Hund's coupling into account (J_H)

[146], since its effect scales with $J_H/U \sim 0.1$.

However, the observation of orbitons is far from being easy, even in one-dimensional compounds. One of the reason is that the orbital excitation tend to couple strongly to phonons. Whenever a *dd*-excitation is created, the symmetry of the charge cloud at a certain lattice site is perturbed. In general, we can expect that this perturbation will excited one or more phonon branches whenever the electron-phonon coupling with the photoexcited electron is not zero [71]. Such *dressing* of the orbital excitations will then strongly reduce the bandwidth of the orbiton dispersion [32].

In two and three dimensions, the situation is even worse. Orbitons have been unambiguously identified only in $5d$-compounds such as iridates [80, 81]. However, since in this materials the groundstate is strongly split by spin-orbit, they cannot be really thought of as a pure orbital excitations. However, while the physics is different, the resulting Hamiltonian has the same form as for the $3d$ cuprates. The calculated and measured dispersion has the same shape than in the 1D cuprates, with a maximum at the Γ point.
In $3d$ transition metal oxides, where orbital and spin remain good quantum numbers, no definitive observation of orbiton has been achieved. In materials characterized by alternating-orbital order (and ferromagnetic alignment), such as manganites [147, 148] and titanates [149], no clear signature of dispersing orbitons was found, contrary to theoretical predictions [30].
In compounds exhibiting ferro-orbital order, like the high-temperature superconducting cuprates, no traces of orbitons has likewise been found [6]. The main reason is that, in two dimensions, the mechanism which allows the orbiton to hop coherently through the lattice is hindered by the so-called *magnetic string effect* [34]. This will be explained in detail in the next sections.

In this Chapter we present a systematic RIXS study of the orbital excitations in cuprates with (La_2CuO_4) and without apical oxygens ($CaCuO_2$ and Nd_2CuO_4). The measurements on Nd_2CuO_4 have been performed in collaboration with Prof. Riccardo Comin and Dr. Jonathan Pelliciari. In La_2CuO_4, the *dd* excitation behave as localized atomic transitions. Instead, in $CaCuO_2$ (CCO) and Nd_2CuO_4 (NCO) we measure a sizeable dispersion of the t_{2g} excitations (xy and xz/yz). More importantly, the shape of the dispersion is at odds with the one expected from a simple KK model with nearest-neighbour orbiton coupling. In section 5.2, we describe in detail the experimental methods and present the RIXS result. Next, in Section 5.3, we discuss these results and introduce a new KK model which is able to give a quantitative description of the measured behaviour. Finally, we outline the implications of our results for the physics of cuprates and strongly-correlated systems in general.

5.2. Experimental methods

5.2.1. Samples

We have investigated three different two-dimensional cuprates. La_2CuO_4 (LCO) was taken as a representiative for cuprates with apical oxygens. The LCO film was grown by pulsed laser deposition (KrF excimer laser, $\lambda = 248$ nm) on $LaSrAlO_4$ (001) (LSAO) substrate. The substrate holder was at a distance of 2.5 cm from the LCO target, which was prepared by standard solid-state reaction method. Before the growth, the substrate was pre-annealed in situ at 700 °C under 1 mbar oxygen for 10 min. During the growth, the substrate temperature was around 700 °C and the oxygen pressure around 0.8 mbar. After the growth, to obtain a more insulating LCO, the film was post-annealed in vacuum at 200 °C for 30 minutes [150]. Lattice constants of LCO are $a = b = 3.77$ Å and $c = 13.1$ Å.
Films of CCO with a thickness of 30 nm were grown by pulsed laser deposition (KrF excimer laser with $\lambda = 248$ nm) on $NdGaO_3$ (NGO) (1 1 0) substrate, at $T \sim 600$ °C and in a 0.1 mbar oxygen pressure. The substrate holder was kept at a distance of 2.5 cm from the CCO target, which was in turn prepared with a standard solid-state reaction [120, 121].

5.2.2. RIXS measurements

The RIXS experiments on LCO and CCO samples were carried out at beamline ID32 of the ESRF, while samples of NCO were measured at I21 beamline of Diamond Light Source, UK [151]. NCO measurements were performed in collaboration with the group of Prof. Riccardo Comin of MIT. The scattering angle θ_{sc} was kept fixed at 149.5° (154°) for CCO and LCO (NCO), and the momentum scans along the $\Gamma \rightarrow X$ and $\Gamma \rightarrow \Sigma$ directions were acquired by rotating the incident angle θ, while the azimuthal angle ϕ was used to select the (1,0) and (1,1) directions. Polarized RIXS spectra were collected using the soft X-ray polarimeter installed on the ID32 beamline [90] at two selected points: (1/2,0) and (~ 0.1,0). The energy was kept fixed at the Cu L_3 resonance (~ 931 eV). We employed both incident linear-vertical (σ) and linear-horizontal (π) polarizations. Total resolution was estimated to be ~ 43 meV both for normal and polarimetric scans. The temperature was kept at 20 K to minimize sample damage. All of the spectra have been corrected for self-absorption effect as described in [124].
For CCO and LCO, self-absorption correction was taking the finite thickness of the sample into consideration.

5.3. Results and discussion

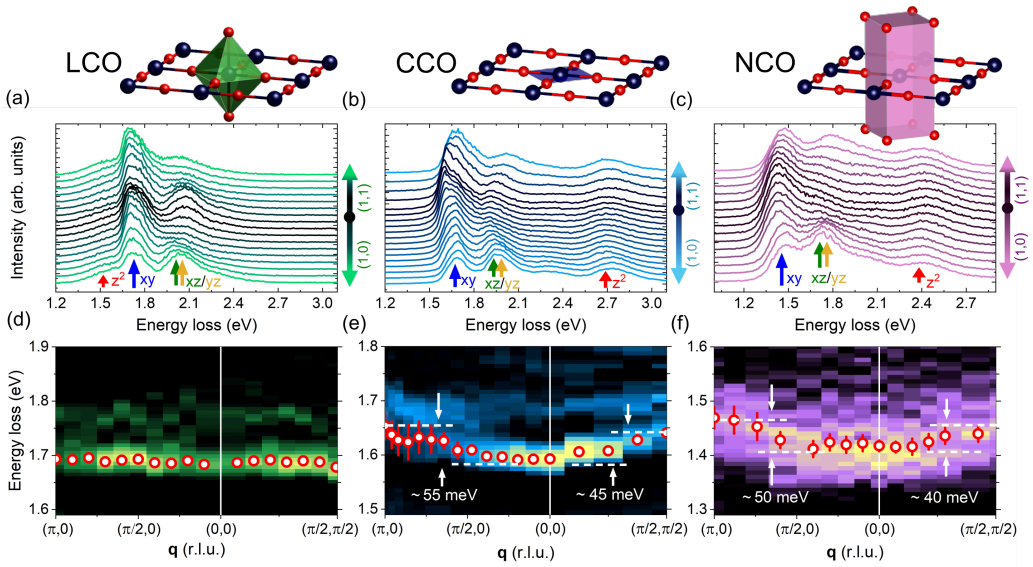

Figure 5.1: Overview of Cu L_3 RIXS spectra, acquired with σ incident polarization, for LCO, CCO and NCO. Panels (a)-(c): under the respective schemes of the Cu coordination, we show stacks of RIXS spectra as a function of the transferred momentum $\mathbf{q}$ along the $(1,0)$ and $(1,1)$ directions. The labels report the symmetry of the *dd* excitations as determined from previous measurements [6]. (g)-(i): map of the (inverted) second derivative of the scans of panels (d)-(f), zoomed on the energy range of the xy excitation. Red dots highlight the position of local maxima, corresponding to the position of peaks in the original RIXS spectra. Note that the energy scale is the same in the three panels but centered at different absolute energies.

5.3.1. Experimental results

We now report the experimental results on the three samples, leaving the discussion for the next section. Panels (a)-(c) of Fig. 5.1 present the momentum dependence of the orbital excitations in LCO (left), CCO (centre) and NCO (right) along the high-symmetry directions $(1,0)$ and $(1,1)$, measured with σ incident polarization. The spectra are composed by three main peaks, which correspond to the transitions between the x^2-y^2 groundstate and the other d orbitals split by the tetragonal crystal field [6]; the symmetry of the final state is reported by the labels below the curves. The different order of the excitations can be ascribed to the different degree of tetragonal distortion between LCO and the infinite layer compounds [6].

The x^2-y^2 ground state is separated by ~ 1.5 eV from the second lowest-energy (in hole-language) orbital, so all three compounds are characterized by a stiff ferro-orbital order and we can rule out possible quantum fluctuations between nearly-degenerate ground states. In turn, the virtual hopping of the single hole in the x^2-y^2 empty state gives rise to strong AF interac-

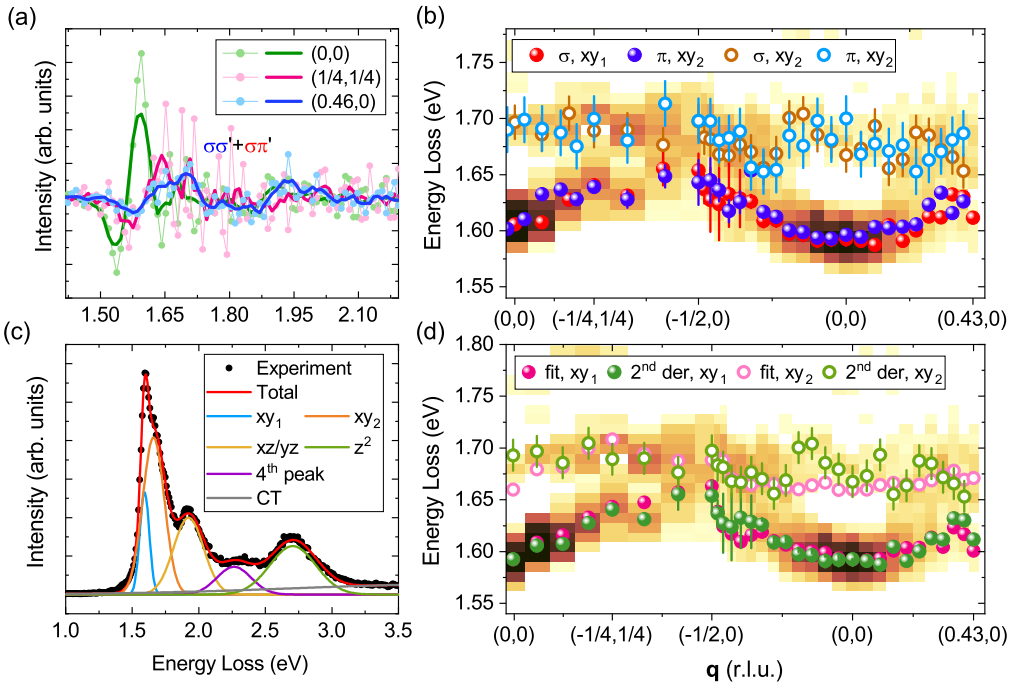

Figure 5.2: Different procedures and datasets used to obtain reliable estimates of the dispersion. All figures refer to CCO. (a): Example of the extracted (inverted) second derivative of RIXS spectra in Γ and X. (b) Map of the dispersion of the xy excitation on an extended path. Blue (red) dots are the maxima in the second derivative extracted from scans measured with π (σ) incident polarization. The path in reciprocal space followed with the two polarizations is reported in the inset. (c) Example of fitting procedure. The different peaks used are reported labelled in the legend. CT stands for 'charge-transfer'. (d): energy of the xy excitation extracted from maxima in the inverted second derivative and fitting procedure.

tions between neighbouring sites (in agreement with Goodenough-Kanamori rules), and indeed all samples show dispersing magnetic excitations at energies < 0.5 eV (not shown in Fig. 5.1, see the previous chapter). The momentum dependence of the intensity is mostly due to the RIXS matrix elements, which depend on photon polarization and experimental geometry [6]. Moreover, the peaks are generally sharper in the CCO and LCO samples due to higher sample quality. As evident from panels (a)-(c) of Fig. 5.1 the energy of the peaks in LCO is constant with **q**, while the energy of the xy and xz/yx excitations shows an appreciable dispersion for CCO and NCO. In order to obtain a quantitative estimation, we have proceeded in two ways. First, we have extracted the (inverted) second derivative of the RIXS spectra, shown in panel (d)-(f) of Fig. 5.1. An example of some second derivatives extracted at the Γ and X points is shown in Fig. 5.2. The dispersion was then extracted as follows: we selected the first relative

maximum of the curves 8smoothe dover 5 points), and then calculated a centre of mass with the adjacent 2 points to cope with the noise of the scans. To further verify the presence of a sizeable dispersion we have repeated the procedure on spectra extracted with σ and π incident polarization, and with grazing-in and grazing-out geometry. As shown in panel (b) Fig. 5.2, there is a very good agreement between the two sets of data. Secondly, we have estimated the dispersion by a direct fitting of the experimental data. The peaks corresponding to the *dd* excitations have been modelled with Gaussian lineshapes. The fact that there is basically no evidence of a Lorentzian lineshape is interesting, because it suggests that the width of the peaks is not due to the finite lifetime of the excitations. An example of the fitting procedure is reported in panel (c) of Fig. 5.2. As evident from panel (d) in the same figure, the two approaches (second derivative vs. fitting) yield comparable results. Close to the X point, where the determination is less accurate, we take the energy separation between two adjacent points as a measure of the errorbars. In LCO, the xy excitation shows no dispersion within the experimental error, while for CCO it exhibits a dispersion of 60 ± 15 meV and 50 ± 5 meV along the (1,0) and (1,1) directions, respectively. The energy has a maximum at $(\pi, 0)$ and $(\frac{\pi}{2}, \frac{\pi}{2})$ and minimum at the Γ point (0,0). A similar, though smaller, dispersion is observed for NCO (50 ± 20 meV and 40 ± 10 meV respectively). A closer inspection of the xy excitations reveals that there is satellite peak about 50 meV above the main edge. Such a small energy separation suggests that one of the two also involves a spin-flip event. Careful analysis reveals that the higher-energy peak has a basically a flat dispersion (see panel (b) of Fig. 5.2).

The xz/yz excitation also displays a clear dispersion in CCO and NCO, especially strong along the (1,1) as evident from panel 5.1(b). Additionally, there is another striking difference between LCO and the cuprates without apical oxygens, namely the presence of an additional broad feature between the main xz/yz and z^2 peaks. In principle, the presence of four crystal field excitations with different energies would be compatible with a lattice symmetry lower than tetragonal (e.g. orthorombic). This is what happens, for example, in one-dimensional cuprates [35–37]. However, diffraction measurements on CCO clearly show that the system is tetragonal so that the xz and yz orbitals have the same energy. An hint on its origin can be grasped by analyzing the momentum dependence of the different features. This is reported, for scans collected with σ incident polarization, in Fig. 5.3. The solid lines are results of single-ion atomic calculations [6], simply rescaled by a global amplitude factor. Experimentally measured values are reported with symbols, and have been extracted by fitting the spectra as described before. Overall, the qualitative agreement is very good. The measured intensity of the xy excitation is smaller than the predicted one, but this might be due to the asymmetric lineshape of the peaks, which is not captured in

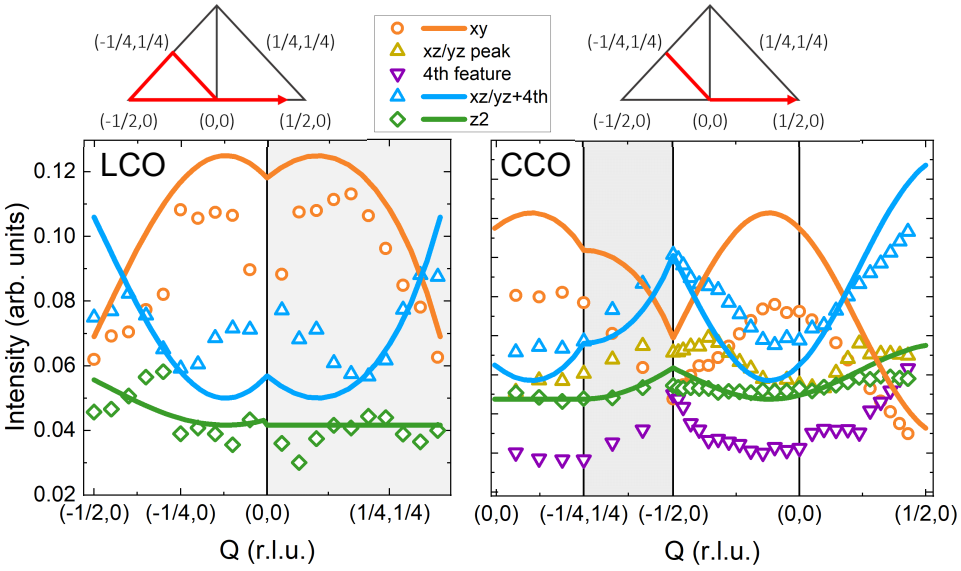

Figure 5.3: Intensity of *dd* excitations intensity as a function of momentum. Symbols are values extracted from fitting the spectra as described before. Solid lines are the result of single-ion calculations [6]. left panels refer to LCO, right panel to CCO. Top insets report the reciprocal space path followed. Note that the global scale of the intensity is different in the two cases and should not be compared.

our fitting procedure and could lead to a wrong assignment of the spectral weight. The discrepancies might also be due to the absence of spin-orbit coupling in the single-ion calculations. Evidently, the xz/yz excitation intensity only agrees with calculations when the intensity of the peak and the broad continuum are added together.

5.3.2. Discussion

The dependence on the wave-vector of the *dd* excitation energy, never reported so far for layered cuprates, can be interpreted as the dispersion of orbitons in the Kugel-Khomskii model, properly adapted for the 2D AFM square lattice. The idea is that the orbital excitation can move among copper sites via an orbital superexchange (SE) process. Although in cuprates the 'bare' electronic hopping is blocked due to the strong on-site Coulomb repulsion U, a perturbative, three-step SE hopping is allowed [25]. The simplest choice would be to consider couplings between the nearest neighbours (NN), as sketched in panel (a) of Fig. 5.4. For instance, for an xy excitation at a given site, the xy hole can move to a NN site through a hopping integral t_b; the NN site becomes thus occupied by two holes with different symmetry (x^2-y^2 and xy) and antiparallel spins, which costs an energy $U-2J_H$ [152]; finally the x^2-y^2 hole can move by hopping t_a to the the original site,

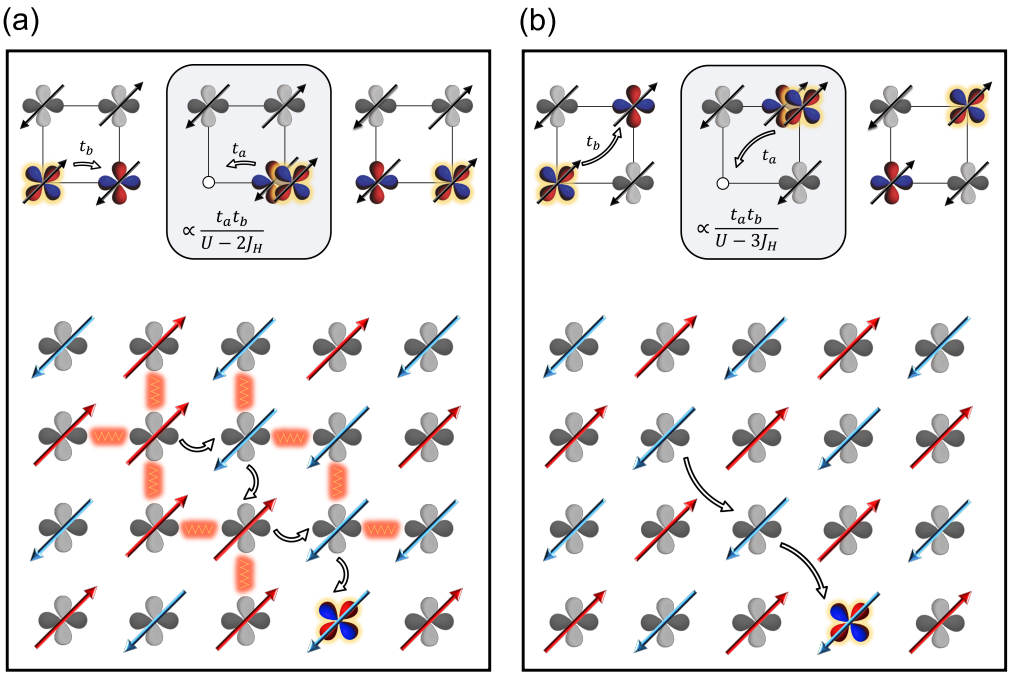

Figure 5.4: Schematic representation of orbiton motion. Panel (a): hopping to NN site. Panel (b): hopping to NNN site. In both panels, the top scheme shows the three steps of orbiton hopping. Bottom panels, instead, show the result of subsequent hopping events. Glowing orange lines connect misaligned spins. Note that we are ignoring the processes (due to J_{H}) that flip the spin of the excited state.

resulting in the SE parameter $J^{\mathrm{orb}}_{\mathrm{NNN}} \propto t_a t_b/(U - 2J_H)$.

However, this type of hopping is killed by the so-called *magnetic string effect* [34, 81]. An intuitive explanation is outlined in the bottom scheme of panel (a) in Fig. 5.4. If we ignore J_{H}, the spin of the excited orbital is conserved through the hopping process [28, 146]. Since the lattice has AF order, successive hoppings leave a string of misaligned spins and are therefore energetically unfavourable. This mechanism, which is obviously absent in one-dimensional systems, tends to localize the orbiton and strongly reduce the bandwidth of the dispersion [34, 36]. We remark that this behaviour is essentially analogous to the motion of a holon (i.e. the charge part of a hole) in a AFM lattice [153], described in a $t - J$ model. A more detailed calculation shows that a small quasi-particle dispersion survives thanks to the presence of antiferromagnetic quantum fluctuations, which "heal" the defects left by the motion of the orbiton [34]. However, with parameters realistic for 2D cuprates the bandwidth W turn out to be extremely small, of the order of $\sim 0.1J \sim 10$ meV. More importantly, as in the case of the spin-polaron [153] the quasi-particle dispersion has a *minimum* at the $(\pi/2, \pi/2)$, which is a robust feature of the $t - J$ model.

This is at odds with the experimental results. First, the measure dispersion has a bandwidth of order $\sim J/2$. Secondly, we find a *maximum* at the Σ point and a minimum at Γ. Interestingly, the measured shape is more consistent with the expected dispersion of an *orbital wave*, i.e. a free orbiton that propagates with no coupling to the magnetic AF background [28]. The mapping to the $t-J$ model shows, however, that orbitons are strongly coupled to spins. Therefore, the question is: is it possible to obtain a free orbiton dispersion in two dimensions?

The answer is yes. A hint on the solution comes from the observed difference between CCO, NCO and LCO. It is well known that the absence of apical oxygens decreases the charge-transfer energy Δ, and increases longer-range superexchange interactions [9]. The trick is, therefore, to realize that the coupling between orbitons and magnetic excitations is a consequence of considering orbital SE processes between *nearest neighbours*, which have anti-parallel spin configuration. Instead, SE processes between *next*-nearest neighbours (NNN) couple Cu atoms within the same AF sublattice, with the same orientation of the spins. An example of orbiton motion on a NNN site is sketched in panel (b) of Fig. 5.4. In this case, as evident from the bottom scheme in panel (b), the motion of the orbiton does not create any magnetic defects. This also holds in the case of spin-orbital excitations, in which the spin of the excited orbital is flipped in the RIXS process (not shown in the figure).

The inclusion of NNN orbiton hopping seems therefore reasonable, but comes at a price. First of all, a physical mechanism capable of generating a sizeable hopping term must be provided. Secondly, in order to get an upward dispersion at the Γ the orbiton SE coupling $J_{\rm NNN}$ must turn out negative. Indeed, it can be shown that the dispersion relation induced by NNN processes has the form:

$$\varepsilon_{\mathbf{q}} = 2J^{\rm orb}_{\rm NNN}\,\cos\left(2\pi q_x\right)\cos\left(2\pi q_y\right) \tag{5.1}$$

which has precisely the measured shape provided that $J^{\rm orb}_{\rm NNN} < 0$.

In order to solve both issues and calculate the NNN SE coupling, we have used single-cell perturbation theory including explicitly the oxygen atoms. In particular, we have considered a Cu_4O_8 plaquette as shown in Fig. 5.5. The relevant parameters of the model are: (i) the on-site Hubbard repulsion U on Cu atoms and the charge-transfer energy Δ; (ii) the crystal-field energy of the xy orbital ε_{xy}; (iii) the crystal field splitting between the oxygen σ and π bonding orbitals $\varepsilon_{\pi\sigma} < 0$; (iv) the Hund's exchange $J_{\rm H}$ between holes in the same shell; (v) the Cu-O hopping integral $t_{pd\sigma}$ ($t_{pd\pi}$) with σ (π) oxygen orbitals. Finally, we introduce two essential ingredients: (vi) the O–O hopping t_{pp} between nearest-neighbour oxygens, which happens through the Copper $4s$ orbitals; (vii) a certain degree of covalency, i.e. a mixing between the x^2–y^2

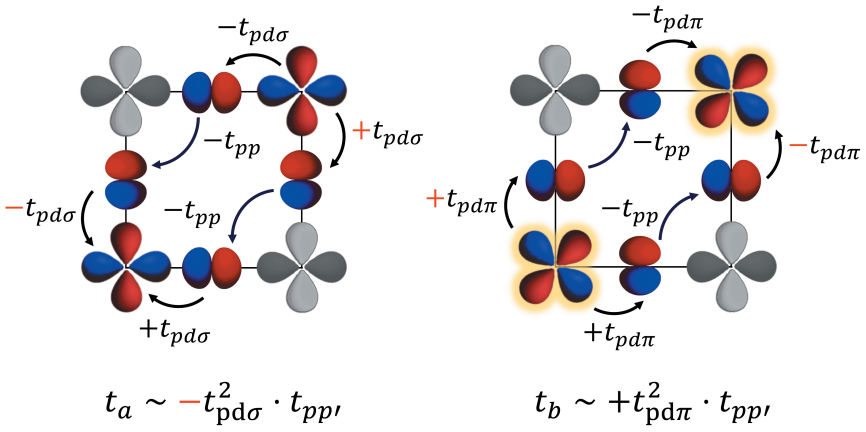

Figure 5.5: Sketch of the effective hopping between NNN x^2-y^2 orbitals (t_a, left panel) and xy orbitals (t_b, right panel). The 'Slater-Koster' hopping terms [155] between oxygen and copper orbitals ($t_{pd\sigma}$, $t_{pd\pi}$ and t_{pp}) are defined in the usual way, cf. [152, 154]. In both cases, the two different paths across the plaquette interfere constructively. However, the number of negative signs (highlighted in red) is different in the two cases, so that $t_a t_b < 0$.

and xy orbitals and the bonding/anti-bonding oxygen states. In particular, it turns out that the x^2-y^2 (xy) orbital can only hybridize with the oxygen anti-bonding σ orbital $|A\sigma\rangle$ (bonding π, $|B\pi\rangle$) [154]. The one-particle states are then $|\phi_-\rangle = \cos\psi\ |x^2-y^2\rangle + \sin\psi\ |A\sigma\rangle$ and $|\xi_-\rangle = \cos\psi\ |xy\rangle + \sin\psi\ |B\pi\rangle$, with the angle ψ quantifying the covalency and depending on t_{pd}, t_{pp} and Δ (see Appendix A).

Some of the interesting results of this model can be understood even without entering in the full details of the calculations. The NNN orbiton hopping t_{NNN} is the results of a three-step process. We consider the xy for simplicity (right panel of Fig. 5.5). It turns out that this orbital can only hybridize with the oxygen bonding π orbitals [154], so the signs of the oxygen wavefunctions are taken accordingly. First, the xy hole hops to a neighbouring π-oxygen site (e.g. the one right above), with an amplitude $\propto t_{pd\pi}$. Secondly, it hops "around the corner" to another oxygen atom with an amplitude $-t_{pp}$: the minus sign comes from the signs of the wavefunctions of the two oxygens. Finally, it hops to the top-right Cu atom, again with an amplitude $\propto -t_{pd\pi}$. The two processes involving different oxygen paths interfere constructively. Overall, the total amplitude for the NNN hopping is $t_b \propto t^2_{pd\pi}\, t_{pp}$. In the case of the x^2–y^2 orbital, the process is similar, with an important difference: the orbital can only hybridize with the oxygen anti-bonding σ orbitals [154]. This changes the signs and amplitudes) of the pd hoppings: as can be seen from the left panel of Fig. 5.5, the result is that the overall hopping amplitude becomes $t_a \propto -t^2_{pd\sigma}\, t_{pp}$. Therefore the net SE orbiton process, being

	$t_{pd\sigma}$	$t_{pd\pi}$	$t_{pp'}$	Δ	$\varepsilon_{\pi\sigma}$	ε_{xy}	U	J_H	$\boldsymbol{J}_{\mathrm{NNN}}$
CCO	1.3	0.65	0.65	1.6	−1.6	1.0	8.0	1.0	−14
LCO	1.3	0.65	0.65	2.5	−2.5	1.0	8.0	1.0	−5

Table 5.1: Parameters of the charge transfer model used here (all in eV with the exception of J_{NNN}, which is in meV). See text for more details. First row refers to CCO, second one to LCO.

proportional to the product $t_a t_b$, picks up a negative sign. The simple picture presented here is actually a simplification. More realistically, one should first build the oxygen bonding and antibonding orbitals, and then the full one-particle states by mixing the Copper and Oxygen wavefunctions. The hopping "around the corner" is just the result of the delocalization of the electron on the four oxygen orbitals of the plaquette. Therefore, the NNN orbiton SE J_{NNN} can be just calculated with second-order perturbation theory, much like the coupling between NN. A more rigorous explanation of the model is provided in Appendix A. The orbital SE therefore becomes:

$$J_{\mathrm{NNN}} = -\frac{16\nu(\sqrt{2})^2 t_{pp'}^2 \sin^2\psi \sin^2\phi}{\cos^2\psi \cos^2\phi \,(U - 3J_H)} \tag{5.2}$$

Evidently, it critically depends on t_{pp} and Δ, which enters the equation through the covalency ψ (see the Appendix for full details).

It has to be checked whether a reasonable set of parameters is able to produce a sizeable J_{NNN}. U can be taken as 8 eV, which is a typical value for cuprates [7, 9]. $\Delta \sim 1.7 \div 1.8$ eV can be estimated for CCO from optical absorption [11, 12], and calculated Crystal field parameters do not depend on covalency or interactions and can be reliably estimated from DFT calculations. For CCO From Ref. [156] we can set $\varepsilon_{xy} \sim 1$ eV and $\varepsilon_{\sigma\pi} \sim 1.6$ eV. Hund's coupling is usually of the order of $0.8 \div 1$ eV in cuprates, see e.g. [37]. The hopping parameters are more difficult to gauge. $t_{pd\sigma,\pi}$ should depend mostly on the in-plane lattice constant, which is roughly the same for all cuprates. We can therefore estimate $t_{pd\sigma} \sim 1.3$ eV and $t_{pd\pi} \sim 0.7$ eV from calculations [156, 157] and XPS of one-dimensional cuprates [158]. Finally, t_{pp} can be estimated from fitting to ARPES data to be of the order $0.7 \div 1$ eV [7, 9]. In tabl 5.1 we present a set of parameters which gives $J_{\mathrm{NNN}} \sim -0.014$ meV, in agreement with the value extracted from the experimental data. Of course, there are many different combinations of the aforementioned parameters that can give rise to the expected J_{NNN}. Panel (a) of Fig. 5.6 shows the comparison between the experimentally measured dispersion (black dots) and the calculated one using our SE model with NNN exchange. Evidently, the model agrees remarkably well with the experiment.

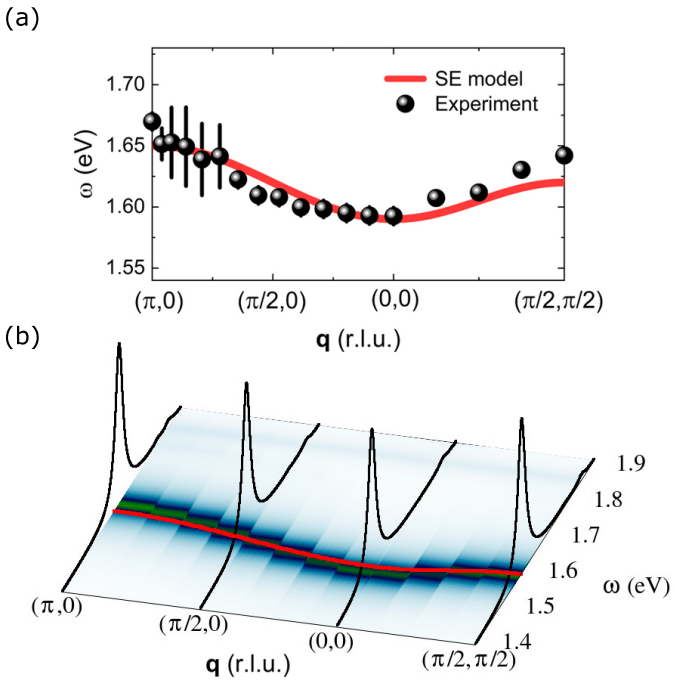

Figure 5.6: Dispersion relation ε_k for the (xy) orbiton in CCO: (a) obtained from the RIXS experiment (points) and the SE model (red line), (b) obtained from the numerical exact diagonalization (ED) of the multi-orbital Hubbard model on 4×4 (green color) and the SE model (red line). The line spectrum of the xy orbiton spectral function is also shown. See text for further details.

In order to further check the validity of our model, we have compared it with a numerical study of the multi-orbital Hubbard model. In particular, we have used Lanczos' Exact Diagonalization (ED) procedure on a 4x4 cluster considering the generic Hamiltonian:

$$
\begin{aligned}
H_{\rm tot} &= H_{\rm kin} + H_{\rm CF} + H_{\rm int}, \quad \text{with} \\
H_{\rm kin} &= t_{{\rm NN},A} \sum_{\langle i,j\rangle,\sigma} c^\dagger_{i,\sigma,A} c_{j,\sigma,A} + t_{{\rm NN},B} \sum_{\langle i,j\rangle,\sigma} c^\dagger_{i,\sigma,B} c_{j,\sigma,B} + \\
&\quad + t_a \sum_{\langle\langle i,j\rangle\rangle,\sigma} c^\dagger_{i,\sigma,A} c_{j,\sigma,A} + t_b \sum_{\langle\langle i,j\rangle\rangle,\sigma} c^\dagger_{i,\sigma,B} c_{j,\sigma,B} \\
H_{\rm CF} &= \Delta_b \sum_{i,\sigma} n_{i,\sigma,B} = \Delta_b \sum_{i,\sigma} c^\dagger_{i,\sigma,B} c_{i,\sigma,B} \\
H_{\rm int} &= U \sum_{i,\alpha=A,B} n_{i\alpha\uparrow} n_{i\alpha\downarrow} + \frac{U'}{2} \sum_{i,\sigma} \sum_{\alpha\neq\beta} n_{i\alpha\sigma} n_{i\beta\bar{\sigma}} + \frac{1}{2}(U' - J_H) \sum_{i,\sigma} \sum_{\alpha\neq\beta} n_{i\alpha\sigma} n_{i\beta\sigma} \\
&\quad - J_H \sum_{i,\alpha\neq\beta} (c^\dagger_{i\alpha\uparrow} c_{i\alpha\downarrow} c^\dagger_{i,\beta\downarrow} c_{i\beta\uparrow}) + J_H \sum_{i,\alpha\neq\beta} (c^\dagger_{i\alpha\uparrow} c^\dagger_{i\alpha\downarrow} c_{i\beta\downarrow} c_{i\beta\uparrow})
\end{aligned}
$$

which contains kinetic, crystal field, and interaction terms. ED is useful because it automatically contains all possible superexchange processes, in-

cluding the magnon-orbiton vertex neglected in the orbital-wave picture described above. The calculated spectra are shown in panel (b) of Fig. 5.6. Evidently, the agreement between experiment, SE model and ED calculations is very good. Moreover, the ED spectra are still dominated by a strong quasi-particle peak, with a very weak incoherent continuum. The fact that the magnon-orbiton interaction does not lead to the destruction of the quasi-particle peak is surprising, and it is due to the dominant NNN coupling.

The last important thing to be checked is whether our model is able to explain why no dispersion of orbitons is seen in LCO (and in all the other cuprates with apical oxygens). Many of the parameters ($t_{pd}, U, J_{\mathrm{H}}, \varepsilon_{xy}$) are basically the same for all cuprates and cannot account for the differences in the two classes of materials: the only two which show appreciable variation with the number of apical oxygens are Δ and t_{pp} [9]. In particular, Δ is larger when one or two apical oxygens are present: for example, $\Delta \sim 1.8$ eV for CCO (no apicals), $\Delta \sim 2.1$ eV for $YBa_2Cu_3O_6$ and $\Delta \sim 2.5$ eV for LCO. The physical explanation is quite simple. The negatively-charged apical oxygens make it more costly to place an electron on Cu site, increasing the value of $\varepsilon_d - \varepsilon_p$. Moreover, part of the Cu hole will be on the apical p_z orbital, reducing the in-plane oxygen content (and therefore ψ will decrease). At the same time, can expect t_{pp} to decrease with the number of apical oxygens as well. Indeed, t_{pp} depends on how easy an electron can be transferred between adjacent in-plane oxygens across the $4s$ orbital of Cu [7]. Therefore, it depends on the charge-transfer energy ε_{s-p}, which increases as well if apicals are present. Using $\Delta = 2.5$ eV and $t_{pp} = 0.5$ eV, we get $J_{\mathrm{NNN}} = -0.003$ eV, which would yield an orbiton bandwidth of 10 meV, definitely too small to be measured.

In conclusion, we have for the first time reported the presence of orbitons, i.e. of collective dd excitations, in a two-dimensional $3d$ material. We have shown that the measure dispersion cannot be in any way reproduced with a KK model with nearest-neighbour interactions. Instead, we have successfully interpreted the observed behaviour in terms of orbital super-exchange processes mostly due to next-nearest neighbour interactions. Since these interactions couple Cu atoms on the same magnetic sublattice, no dramatic interaction with magnons is expected, and therefore they should give rise to a free-orbiton dispersion (i.e. an orbital wave). Single-cell perturbation theory shows that such NNN interactions are possible provided that the system has high covalency (i.e. large Cu-O mixing induced by low charge-transfer energy Δ) and sizeable oxygen-oxygen hopping t_{pp}.
The observation of a sizable dispersion of orbital excitations in cuprates only in special cases holds a twofold importance. Firstly, it is, for the first time, unequivocally shown that pure dd excitations can have a collective nature besides the 1D systems. Secondly, the amplitude of the dispersion is related

to NNN hopping parameters, at least in the AFM lattice case. Moreover, the dispersion might be potentially larger for ferromagnetic order. We note that longer-range hopping is at the origin of the peculiar properties of spin-excitations of CCO, with spinon-like behavior emerging close to $(\pi, 0)$, again in analogy to 1D spin systems [159]. Finally, the role of oxygens in explaining the physics is not solely quantitative. A canonical Hubbard-like description would not yield a negative sign of the orbital superexchange J_{NNN}: one has to go 'back' to the charge transfer (Emery) model to retrieve the correct sign. This not only underline the fundamental role played by oxygens in the determining the physics of cuprates, but also proves the importance of the different orbital phases.

Chapter 6

Charge and spin excitations in Infinite-layer Nickelates

Part of the results presented in this Chapter have been published as *"Charge and Spin Order Dichotomy in $NdNiO_2$ Driven by the Capping Layer"* by G. Krieger, L. Martinelli, S. Zeng, L. E. Chow, K. Kummer, R. Arpaia, M. Moretti Sala, N. B. Brookes, A. Ariando, N. Viart, M. Salluzzo, G. Ghiringhelli, and D. Preziosi, Physical Review Letters 129, (2022), which I co-first authored.

Four years ago, the group lead by Professor Harold Y. Hwang at Stanford University discovered superconductivity in monovalent Nickel films of the form $ReNiO_2$, where Re is a rare-earth atom [160]. The main properties of these films is that their electronic structure mimics the one of cuprates. They are composed by stacks of two-dimensional NiO_2 (separated by Re^{3+} cations), coordinated in a square-lattice fashion, and Ni^{1+} is in a $3d^9$ state. Evidently, these compounds are (or, at least, should) be very similar to the infinite-layer cuprate $CaCuO_2$. This discovery, which is surely one of the major breakthrough of the last decade, generated a surge in related research. The structural, electronic and magnetic properties have since then been studied intensively with several techniques. Indeed, despite being fascinating by themselves, they offer the unique opportunity to investigate how superconductivity is affected by a set of parameters radically different than the one usually explored with cuprates.

In this chapter, we report XAS and RIXS measurements performed on different types of Nickelates films. First, we investigate the difference in the physics of the material induced by the presence of a thin STO capping layer, which seems to have a large effect in determining its properties. First, we give an overview of the electronic structure in both type of samples, by means of XAS and RIXS at the Ni L_3 and Oxygen K edge. Then, we concentrate on the low-energy physics of both samples, which shows very surprising dif-

ferences. In the capping-free ones, we find a phase with broken translation symmetry, which rapidly decreases with doping but shows no appreciable temperature dependence. In the capped films we report the second independent observation of dispersing magnetic excitations. We study in detail the magnetic dynamics as a function of doping, also by means of polarization-resolved RIXS at the Ni L3 edge.

Contents

6.1. Introduction

Unconventional superconductivity in cuprates is still one of the most fascinating problems in physics. It is essentially the result of a precise set of ingredients: a $3d^9$ metal cation, having spin $1/2$, arranged in a two-dimensional square-lattice of the form MO_2, with a x^2-y^2 orbital groundstate. Over the years, there have been many attempts to replicate the structure of cuprates with other materials. Iridates, such as Sr_2IrO_4, allowed to investigate how superconductivity is affected by a large spin-orbiton coupling. More recently, it was proposed that AgF_2 could display physics very similar to cuprates [161, 162].

Another, intuitively more simple route is to replace Cu^{2+} with Ni^{1+}. Indeed, it was long ago predicted that nickelate-based heterostructures, such as $LaNiO_3/LaAlO_3$ superlattices [163, 164], could display high-temperature

superconductivity. This proposal stimulated an important experimental activity aimed at stabilizing a Ni-3d^9 configuration with reduced dimensionality. A partial splitting of the Ni-e_g states was obtained through strain in $LaNiO_3$ thin films [165] and in $LaTiO_3/LaNiO_3/LaAlO_3$ heterostructures [166–168], but no superconductivity was found. In 2019, superconductivity was eventually discovered by the group of Prof. Harold Hwang below 15 K in $Nd_{0.8}Sr_{0.2}NiO_2$ thin films deposited on the (001) surface of $SrTiO_3$ (STO) [160]. The main step to achieve this result was an oxygen de-intercalation of the perovskite $Nd_{1-x}Sr_xNiO_3$, via a solid-state chemical reaction denoted as *topotactic reduction*. This films of $Nd_{1-x}Sr_xNiO_3$ are place in seals vacuum envelopes with CaH_2 powder, and heated up to ~300 °C. The hydrogen present in the powder extracts oxygen atoms, leading to an infinite-layer structure with Ni-3$d^{(9-x)}$ ions in a square planar lattice, equivalent to that of cuprates. Soon after it was realized that superconductivity could also be obtained using other rare earths, like La or Pr [169].

Soon after this discovery, the properties of this new family of nickelates were intensively investigated using x-ray absorption spectroscopy (XAS), resonant inelastic x-ray scattering (RIXS), and electron-energy loss spectroscopy [170] [170–172], as well as with calculations. Immediately, some important differences with cuprates were found. First, these experiments showed that the energy gap between O-2p and Ni-3d bands is higher in the nickelate infinite-layer films ($\sim 4 \div 5$ eV) than in layered cuprates ($\sim 2 \div 3$ eV) [173]. At present, the most accepted interpretation is that nickelates belong to the mixed Mott-Hubbard Charge-Transfer region of the Zaanen–Sawatzky–Allen classification scheme [174–177]. This implies that the injection of holes leads towards a (partial) Ni-3d^8 electronic configuration. This is at odds with cuprates, classified as charge-transfer insulators, where doped holes mostly reside on the oxygen sites, forming the so called Zhang-Rice singlets Cu-3$d^9\underline{L}$ [178, 179]. Secondly, in infinite-layer nickelates there is a sizable contribution of the rare-earth-5d bands at the Fermi level. This leads to an hybridization between Nd-5d and Ni-3d states [170, 173], whereas in cuprates the interlayer cations do not contribute to the low-energy electronic states. Moreover, this coupling leads to a sizeable *self-doping* in the undoped compound, which exhibit a bad-metal behaviour. According to calculation, a band with dominant 5d character crosses the Fermi level at the Γ point, creating an electron pocket in the two-dimensional Brillouin zone [170, 180].

Besides these differences, the analogy with cuprates is still strong. Recently, it was even strengthened by the observation of magnons in $NdNiO_2$ [181]. In particular, a dispersion very similar to the one in cuprates was found, although with a smaller bandwidth. Interestingly, underdamped magnetic excitations were found so far only in nickelates that had been capped with epitaxial STO before the topotactic reduction, while the capping is not nec-

essary to obtain superconductivity [182].

Another important feature characteristic of all cuprates is the charge density instability of hole-doped CuO_2 planes [118, 183, 184]. It emerges in the fashion of charge density waves (CDW) in a certain region of the temperature-doping (T–p) phase diagram [56, 185–187], and of charge density fluctuations (CDF) over a much more extended range of T and p values [188–190]. On the contrary, in infinite-layer nickelate thin films the charge density waves and fluctuations have been more elusive. At the time in which the measurements presented here were taken, no evidence of CDW or CDF had been found in nickelates.

6.2. Experimental Methods

6.2.1. Samples

This chapter deals with the investigation of thin films of infinite-layer $NdNiO_2$. The samples we used in our investigation were grown by the group of Dr. Daniele Preziosi, at the University of Strasbourg. Since their synthesis is new and still not well-established, we report a summary of the growth procedure, structural and transport properties. More details can be found in the supplemental material of [191] and in [192].

$NdNiO_2$ films have been obtained thanks to topotactic reduction of the thin films (10 nm) of the perovskite phase $NdNiO_3$, grown on STO. Doping was achieved thanks to substitution of (nominally) Nd^{3+} with Sr^{2+} in the perovskite phase to obtain $Nd_{1-x}Sr_xNiO_2$. We have explored doping corresponding to $x = 0$ (undoped), $x = 0.05$, $x = 0.2$. Samples have been realized in two different ways: with and without an epitaxial layer of STO ($\simeq 1$ nm, 3 unit cells), which was deposited on the perovskite phase. Topotactic reduction was then performed with CaH_2 powder, at temperature of 240 °C for 30 h in the case of capped samples, for 14 h in the case of capping-free ones. The appearance of the infinite-layer phase was verified by means of laboratory x-ray diffraction, shown in panel (a) of Fig. 6.1. In particular, the topotactic reaction shifts the (00l) diffraction peak, corresponding to a change in the c-axis parameter roughly equal to 0.4 Å. The evolution of the c-axis in the infinite-layer phase is depicted in panel (b) in the same Figure: in particular, c-axis goes from c = 0.328 nm for the undoped sample to 0.336 nm for the superconducting one (x = 0.2). It is important to underline that, according to x-ray diffraction, no significant structural differences exist between capping-free and capped samples.

The resistivity curves for capped and capping-free samples are provided in panels (c)-(e) of Fig. 6.1. In NNO 0% and NSNO 5%, it is very evident an

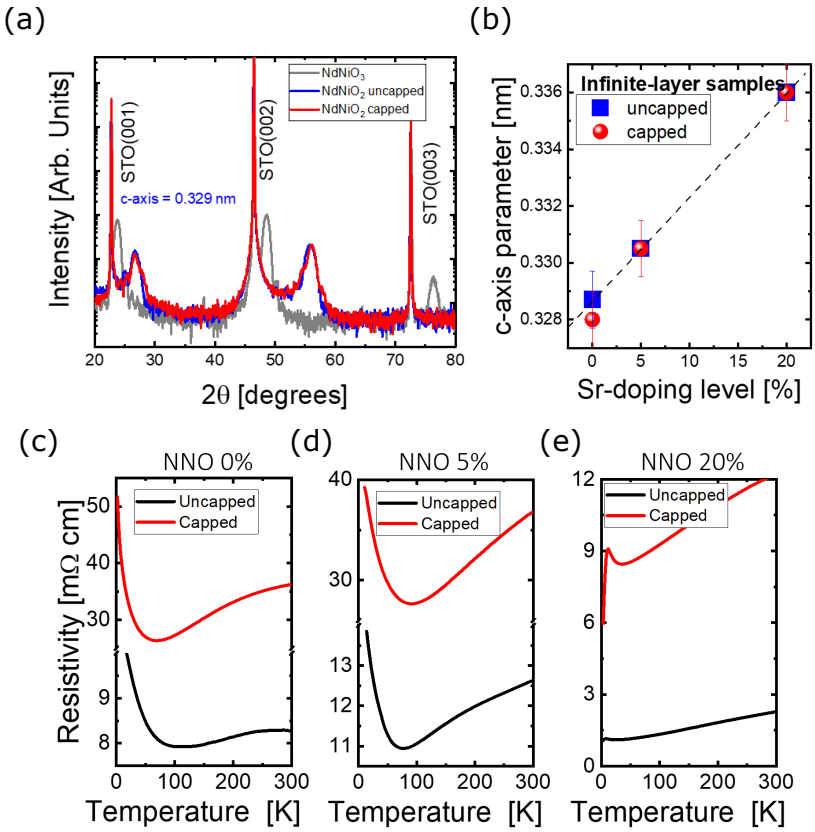

Figure 6.1: Overview of diffraction and resistivity measurements on NSNO films. (a): x-ray diffraction on perovskite $NdNiO_3$, capping-free undoped $NdNiO_2$ (NNO) and STO-capped NNO. (b) c-axis variation with Sr-doping level in capped and capping-free samples. (c)-(e): resistivity as a function of temperature for capping-free and STO-capped films at different doping levels (0%, 5%, 20%).

upturn below 100 K, which sets a logarithmic dependence of the resistivity. This has been observed before, and assigned to the formation of Kondo singlets between Nd-5d conduction electrons and localized Ni $3d_{x^2-y^2}$ spins. At the same time, increasing doping values induce a strange metal behaviour, and the resistivity becomes more linear at high temperatures. In the STO-capped NSNO 20% film, the onset of superconductivity can be detected below 10 K. While the capping-free sample presented in panel (e) is not superconducting, we note that analogous samples prepared by the group of Ariando at the National University of Singapore are instead superconducting [193].

6.2.2. XAS and RIXS measurements

XAS measurements were performed both at the Nickel L_3 edge and at the oxygen K-edge. In particular, XAS at the Ni-edge were performed at the ID32 beamline of the ESRF (France), while XAS at the O-edge were performed at beamline I21 at Diamond Light Source (UK). In both cases, measurements were acquired in Total Electron Yield (TEY) to maximize surface sensitivity. We employed both σ and π incident polarizations in a grazing-incidence geometry ($\theta < 20°$). This allowed us to probe the response of the system to photons with polarization along the NiO_2 planes (when using σ polarization) or mostly perpendicular to them (when using π polrization).

RIXS measurements at the Ni L_3 edge and at the Nd M_4 edge were collected at the ID32 beamline of the ESRF. RIXS at Oxygen K-edge was instead measured at beamline I21 of Diamond Light Source. In both cases, the experimental geometry employed during the experiment is shown in Fig. 6.2. The infinite-layer films were kept perpendicular to the scattering plane, and the scattering angle was fixed at $\theta_{sc} = 150$. In the case of Ni L_3 measurements, the incident angle θ was rotated to change the projection of the transferred momentum $\mathbf{q}$ on the two-dimensional NiO_2 planes. For Oxygen K-edge, θ was kept fixed at very grazing incidence (5°) to maximize the surface sensitivity. This was necessary to limit the amount of signal coming from the $SrTiO_3$ substrate, which also contins Oxygen.

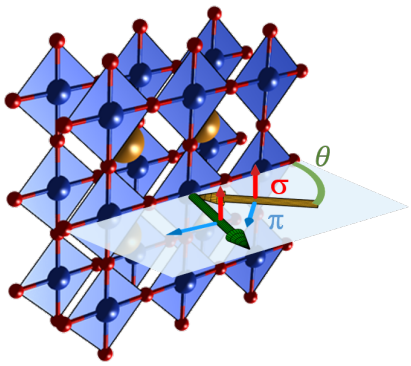

Figure 6.2: Experimental geometry used in RIXS measurements on nickelate films. Ni, Nd and O atoms are drawn as blue, gold and red spheres, respectively. Highlighted are the incident angle θ., as well as the linear polarization states of the incident and scatterd x-ray beams.

The angle φ of the manipulator was used to put either the (1,0) or the (1,1) direction in the scattering plane. For measurements at the Ni L_3 edge, which is sensitive to single spin-flip magnetic excitations [85], we have also employed the soft x-ray polarimeter installed on beamline ID32 [90]. The convention on the labels $\sigma, \pi, \sigma', \pi'$ is also sketched in Fig. 6.2. The spectra presented here have *not* been corrected for self-absorption effects due to the very low thickness of the films (10 nm). In principle, assuming an almost two-dimensional sample, normalization can be performed simply multiplying the measured intensity by $\sin\theta$, which is proportional to the spot area of the x-rays on the sample surface. We only do

this, however, in the specific cases where we assign meaning to the measured intensities. Temperature was, unless specified, kept at 20 K in order to minimize sample damage.

The first part of this chapter deals with the investigation of the electronic structure of $Nd_{1-x}Sr_xNiO_2$ (NSNO) films with and without the STO capping layer. Then, we will study in detail the low-energy physics of the two types of samples.

6.3. Electronic structure of NSNO films

In this section, we report XAS and RIXS results on STO-capped and capping-free NSNO samples. In particular, we will present measurements performed both at the Nickel L_3- and the Oxygen K-edge. We will focus on the high energy part of the RIXS spectra ($E_{\text{loss}} > 0.5\,\text{eV}$), with the aim of obtaining information on the electronic structure of the nickelate films. We will also stress the different phenomenology displayed by films with and without the STO capping layer.

6.3.1. Capped NSNO films

We will start by reviewing and discussing the results on the NSNO films capped with epitaxial STO films, which display physics more similar to the one of cuprates.

First, we have measured XAS spectra of samples as a function of doping and polarization, shown in Fig. 6.3. We also report the XAS profile of NiO, which has been taken as a reference for $3d^8$ systems. The absorption spectrum consists mainly of a single resonance, which can be safely assigned to the Ni^{1+} state. In all the samples investigated, however, the main resonance has a shoulder at higher energies, which evidently grows as a function of doping. By comparison with NiO, we assign this feature to Ni^{2+}. Finally, the inset in Panel (c) shows that both peaks exhibit a sizeable linear dichroism. In particular, putting the incident x-ray polarization perpendicular to the NiO_2 planes reduces the absorption coefficient by a factor ~2. We note, however, that the dichroism is less marked than in the cuprates [77], and this might indicate that the groundstate has a non-zero contribution from d-orbitals with z character (e.g. z^2).

In panel (b) and (c) of the same figure we report RIXS spectra as a function of doping and incident energy. The dd excitation sit, in this material, between 1 eV and 2 eV. A comparison between the undoped NNO sample and a corresponding RIXS spectrum acquired on CCO shows that the orbital excitations are similar in shape: this can be explained with the similar

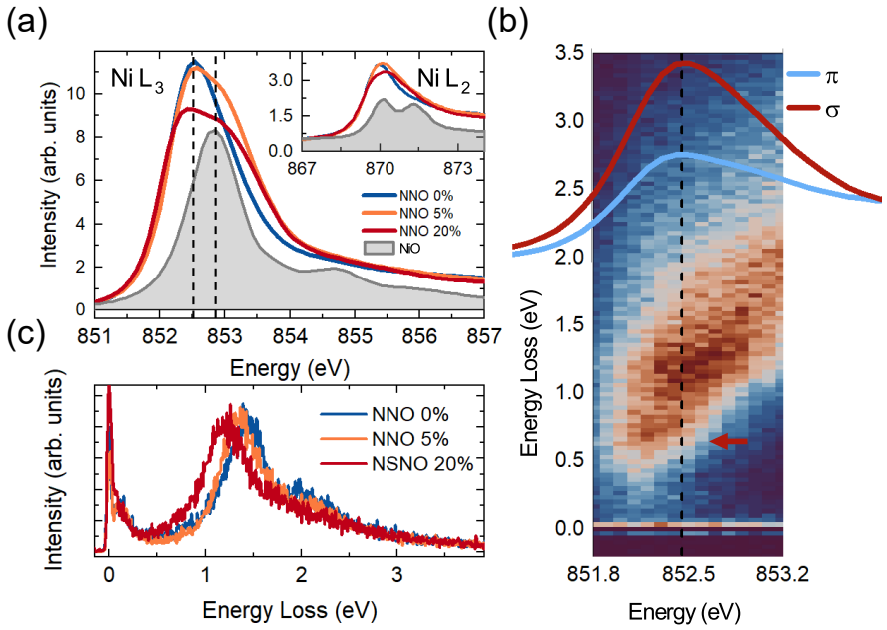

Figure 6.3: Overview of XAS and RIXS spectra on STO-capped NSNO films measured at the Nickel L-edge. (a): XAS spectra of NNO 0%, NSNO 5%, NSNO 20% and NiO, used as a reference for a $3d^8$ system. All spectra have been acquired with σ incident polarization. (b): RIXS spectra of the same three samples, collected at $\mathbf{q} = (0.18, 0)$ on the main resonance energy, with π polarization. (c) RIXS spectra as a function of energy measured on NNO 0%. The arrows highlights the position of the 0.6 eV feature. Also shown are the XAS spectra measured with σ and π incident polarization.

crystal structure of the two types of films. The absolute energies are, however, smaller in nickelates by approximately $\sim 30\%$. Moreover, the energy of the peaks clearly softens upon Sr doping. This is at odds with hole-doped cuprates, where the peaks broaden [124] but their energies remains more or less constant. Panel (c) reports RIXS spectra as a function of incident energy, measured in a grazing-in configuration ($\theta = 10°$), where the incident polarization is mostly perpendicular to the NiO_2. The RIXS spectra also reveal another feature at 0.6 eV, which is completely absent in cuprates, and has been observed before in NSNO films [170]. DFT calculations suggest that it might be linked to a charge-transfer excitation between Ni and Nd bands [170]. Therefore, it can be interpreted to a $3d^8R$ state, where R corresponds to an electron in the rare-earth $5d$ band. This interpretation is strengthened by its polarization dependence, shown in panel (c)-(d) of Fig. 6.4 for capping-free samples. Measuring RIXS spectra in grazing-incidence geometry ($\theta = 10°$) and rotating the polarization $\boldsymbol{\epsilon}$ from π to σ, we can probe the out-of-plane character of the different excitations exploiting the anistropy of the e_g orbitals. Evidently, the $3d^8R$ feature appears stronger with π polarization, i.e. with $\boldsymbol{\epsilon} \perp NiO_2$, indicating a sizeable out-of-plane

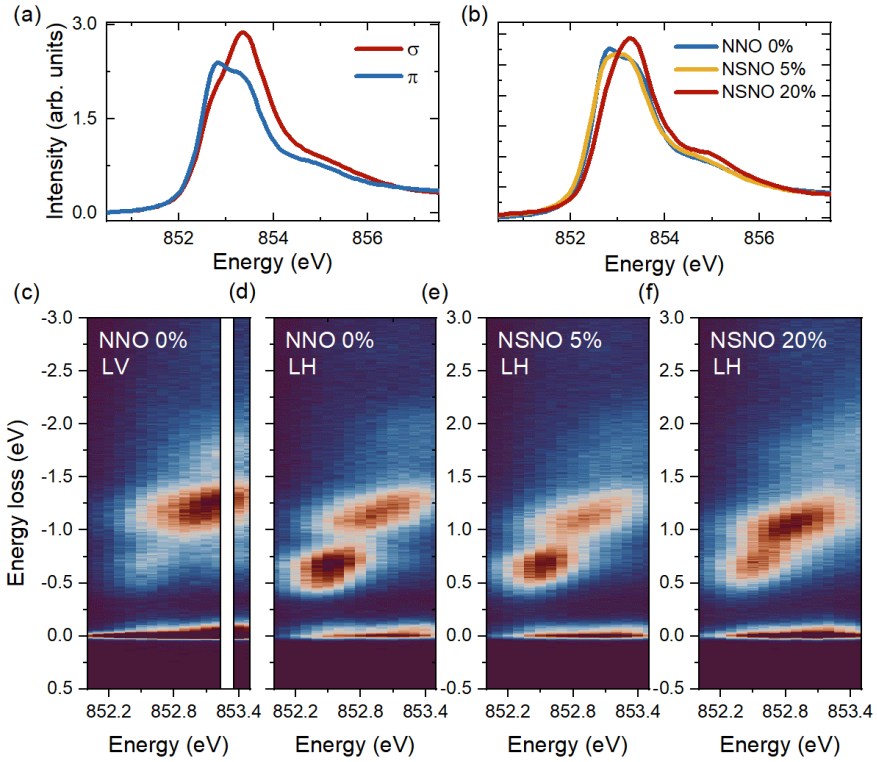

Figure 6.4: Overview of XAS and RIXS measured on capping-free NSNO films. (a): linear dichroism in the XAS, measured at θ = 20° with π and σ polarizations. (b) Doping dependence, measured with π polarization at θ = 20°. (c)-(f): RIXS spectra as a function of energy, collected at θ = 10° and T = 20 K, on undoped NNO (a,b), $Nd_{0.95}Sr_{0.05}NiO_2$ (c), $Nd_{0.80}Sr_{0.20}NiO_2$ (d). Incident polarization is indicated by the labels in the figures.

contribution.

6.3.2. Capping-free NSNO films

We will now describe XAS and RIXS measurements on capping-free NSNO films, highlighting the strong differences with respect to the capped films.

In order to get insights into the electronic structure of capping-free NSNO films, we first measured the linear dichroism by means of XAS at the Ni L_3 edge. We report the results in panel (a) of Fig. 6.4. XAS spectra were acquired at an incident angle of 20° with linear-vertical (σ, parallel to the NiO_2 planes) and linear-horizontal (π, almost perpendicular to them) polarizations. The XAS is clearly composed by two features, one pre-edge at 852.5 eV and another one at 853 eV. By comparison with the capped films and the NiO reference, we can assign the high energy peak to Ni^{2+}; the comparison with capped NSNO films instead suggests that the lower energy

feature is linked to Ni^{1+}. Interestingly, the Ni^{1+} peak shows an opposite linear dichroism than expected for a x^2-y^2 groundstate: it is stronger with $\boldsymbol{\epsilon} \perp NiO_2$ and weaker with $\boldsymbol{\epsilon} \parallel NiO_2$, opposite to cuprates. This behaviour suggests that the z^2 orbital might have a sizeable occupation, indicating a strong hybridization with the out-of-plane Nd atoms. In panel (b) we report the doping dependence of the XAS spectra. The relative magnitude of the Ni^{1+} and Ni^{2+} clearly decreases upon doping.

The differences in the electronic structure clearly echo in the RIXS maps shown in panels (c)-(f) of Fig. 6.4, acquired in grazing-incidence geometry ($\theta = 10°$). The capping-free samples show a very strong $3d^8R$ feature at 0.6 eV, whose peak intensity surpasses that of the dd excitations. Comparison between panels (c)-(d) also shows that this peak depends strongly on the incident polarization. In particular, its intensity is much stronger with incident π polarization, perpendicular to the NiO_2 planes. As opposite to the capped samples, it also shows a marked doping dependence decreasing upon Sr doping. This behaviour can be naturally linked to the reduction of the Ni^{1+} peak intensity in the XAS, which is reported in panel (b).

6.3.3. Oxygen K-edge XAS and RIXS

One of the most fundamental parameters that control the physics of Mott insulators is the charge transfer (CT) energy Δ. Its value is actually very difficult to extract from RIXS spectra collected at the Nickel L_3. XAS and RIXS spectra at Oxygen K-edge are, instead, an obviously better choice. However, experiments are technically very difficult since oxygen is present both in the films and in the substrate ($SrTiO_3$). The penetration depth of $NdNiO_2$ at these energies is of the order of 200 nm [194], which is much bigger than the thickness of the films (10 nm). To cope with this, we have measured the XAS in drain current mode, which is mostly sensitive to the surface of the samples. We have verified that the Total Fluorescence Yield signal is, even at $\theta = 20°$, basically indistinguishable from the one measured on STO. For the same reason we have acquired spectra at very grazing incidence ($\theta = 5°$), to maximize the effective thickness of the NSNO films.

The XAS spectra measured on STO-capped films, capping-free ones, and STO reference are reported in Fig. 6.5. We also report XAS measured on the two cuprates YBCO AF ($p < 0.02$) and YBCO UD ($p = 0.07$) films.

XAS on capped samples show stark differences with respect to cuprates. In the latter, there is a clear pre-edge which can be assigned to hybridization between oxygen bands and the Upper Hubbard Band (UHB) of Copper [77]. The additional pre-edge at even lower energies is instead related to the formation of Zhang-Rice (ZR) singlets, and is a clear indication that doped holes mostly reside on Oxygen atoms. In capped nickelates, instead,

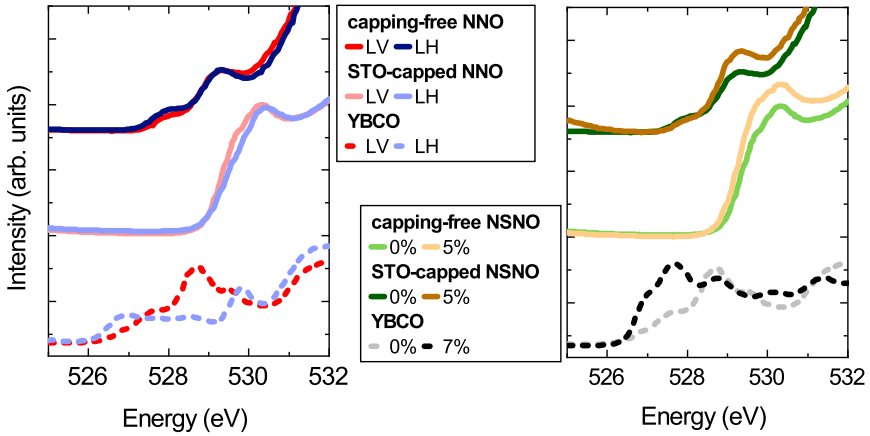

Figure 6.5: Oxygen K-edge XAS on STO-capped, capping-free NSNO and YBCO for comparison. Left panel: linear dichroism. Right panel: doping dependence.

no clear pre-edge can be detected, which suggests a bigger value of the CT energy Δ. No clear doping dependence can be found either, as opposed to the strong doping dependence displayed by the cuprates. In the case of capping-free films, the situation seems again different, with two pre-edge features appearing at 528.2 eV and 529.4 eV. However, while in cuprates the UHB and ZR mostly involve in-plane orbitals and exhibit a strong linear dichroism, no evident dichroism is present in capping-free NSNO films (left panel of Fig. 6.5). This is again consistent with Ni L_3 edge data, which suggest a more three-dimensional character. Additionally, the doping dependence is mild, and only a change in the intensity of the 529.4 eV feature can be detected.

RIXS spectra have been measured at very grazing incidence ($\theta = 5°$) to cope with the low thickness of the films. Nevertheless, the effective penetration depth at this incident angle is larger than 20 nm, two times the thickness of the films. Therefore, RIXS spectra still contain appreciable signal coming from the STO substrate. Fig. 6.6 present an overview of RIXS spectra on capping-free and STO. Panels (a) and (b) show stack of RIXS spectra as a function of energy on capping-free NNO and STO. Evidently, the spectra of the nickelate sample are strongly polluted by STO, dominated by a broad feature above 4 eV. However, a clear signal can be identified at smaller energies, which is clearly due to NNO since the STO RIXS spectra do not contain any features below 4 eV. In order to disentangle the contribution from NSNO films at higher energies, it was necessary to carefully remove the contribution from STO. The spectra can be decomposed as $I_{\mathrm{TOT}} = c_1 \cdot I_{\mathrm{NNO}} + c_2 \cdot I_{\mathrm{STO}}$. It is pretty straightforward to calculate the coefficients c_1, c_2. The signal from NSNO is unaffected by the presence of the STO substrate.

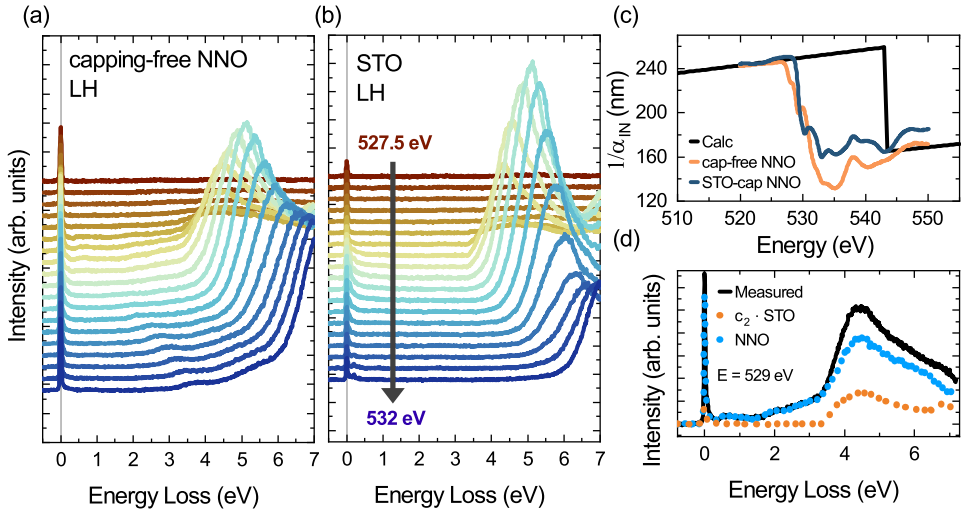

Figure 6.6: Extracting pure NSNO signal from measured spectra. (a): raw RIXS spectra on capping-free NNO 0% film. (b): raw RIXS spectra of STO. (c) Black curve is the calculated attenuation length on $NdNiO_2$ [194]. Orange and blue curves are the reciprocal of measured XAS on capping-free and STO-capped NNO 0%, respectively, scaled by the same amplitude factor.

The signal of STO is, instead, reduced from the one of an exposed STO surface, since the incoming and scattered x-rays have to pass through NNO. We call d the thickness of the NSNO film, and α_{in} (α_{out}) its absorption coefficient at the incident (outgoing) energy ω_{in} (ω_{out}). $\theta = 5°$ is, as always, the incident angle while $\chi = 180° - (\theta_{\text{sc}} - \theta) = 31°$ is the exit angle from the sample surface. The paths of incident and scattered x-rays through NSNO are $d_1 = d/\sin\theta$ and and $d_2 = d/\sin\chi$, respectively. The signal coming from STO is then reduced by $e^{-\alpha_{\text{in}} d_1} \cdot e^{-\alpha_{\text{out}} d_2}$, where the first factor comes from the attenuation of the incident signal when passing through NSNO, and the second one from the attenuation of the outgoing signal scattered from STO. This subtraction procedure requires knowledge of the absolute value of the absorption coefficient. The XAS signal acquired through drain current is, however, just (approximately) proportional to it. To get an estimate of its absolute value we have performed calculations using the Lawrence Berkeley Laboratory simulator [194]. This software is not able to predict the real shape of the absorption profile close to resonances, but is quite accurate in predicting its value before and after absorption edges. Panel (c) in Fig. 6.6 shows a comparison between measured and calculate absorption coefficient α, where the experimental one has been rescaled by a global factor. Evidently, the software reproduces fairly well the change in α before and after the edge.

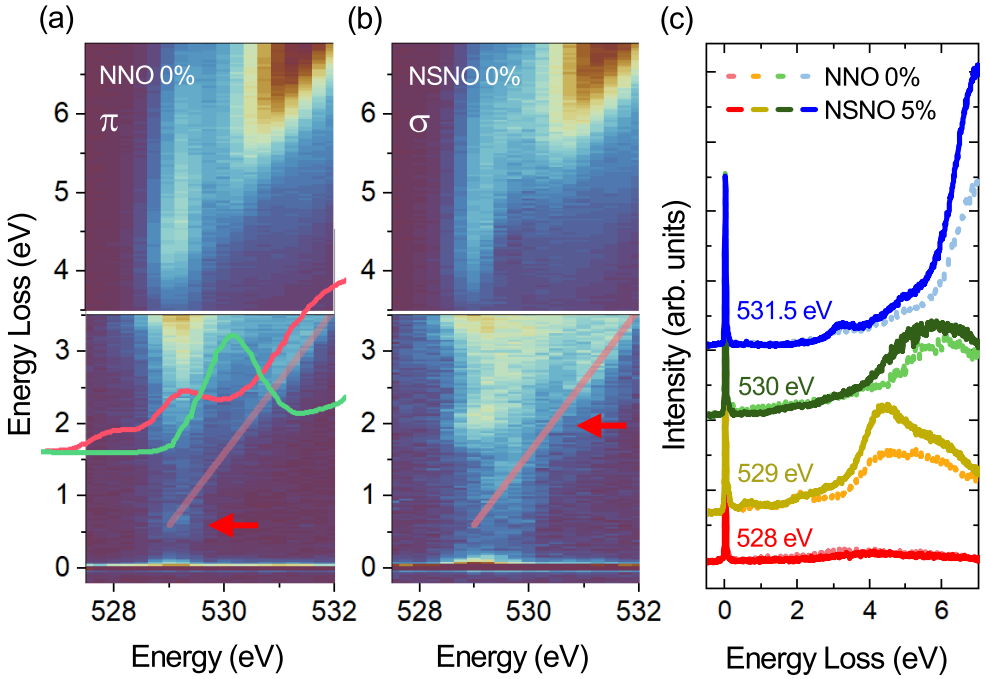

Figure 6.7: RIXS O K spectra on capping-free samples. (a)-(b): spectra on NNO 0% with incident π and σ polarization, respectively. Note that the intensity scale in the top and bottom panel is different for clarity reasons. Panel (a) also report XAS of NNO 0% (red curve) and of STO (green curve). (c) Doping dependence for scans at different energies.

An example of the subtraction procedure is given in Panel (d). Fig. 6.7 present an overview of "pure" NNO spectra, with STO contribution subtracted. We will first describe the results on capping-free samples, for which RIXS energy maps are available. Panel (a) shows a stack of RIXS spectra as a function of incident energy, acquired with π incident polarization, with the STO signal subtracted as described above. Panel (b) displays RIXS on the same sample, but measured with incident σ polarization. Evidently, the main feature is a broad continuum starting above 3.8 eV. Its onset can be considered a good estimate of the order of magnitude of the charge-transfer energy Δ. Moreover, there are additional features below CT peaks. In the spectra acquires with π polarization is very evident the 0.6 eV feature, which is instead less visible in the spectra measured with incident σ. Another feature is present between 1 and 2 eV, mostly evident with σ polarization. This is the energy at which dd excitations are present at Ni L_3 edge, although the lineshape is completely different. Above the pre-peak energy (529 eV), both the $3d^8\underline{R}$ feature and the dd show a fluorescent behaviour (i.e. the energy of scattered x-rays remains constant, and the excitations moves on a straight line in the incident energy-energy loss maps, as highlighted in panels (a) and

(b)). Panel (c) reports the measured doping dependence on NNO 0% and NSNO 5%. Evidently, at the energy of the pre-edge in the XAS spectrum (529 eV), an appreciable doping dependence is measured, with an overall increase in the intensity of the CT continuum above 4 eV.

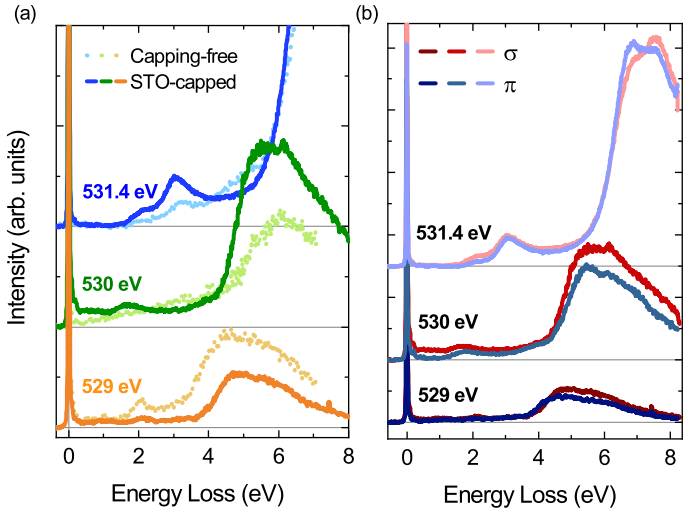

Figure 6.8: Overview of RIXS spectra on STO-capped samples. (a) comparison of STO-capped and capping-free samples at different incident energies. (b): polarization dependence at different incident energies.

Spectra acquired on STO-capped samples are reported in Fig. 6.8. Panel (a) shows the differences between the two types of films at different incident energies. Overall, the spectra look similar, with a few discrepancies. The broad and intense feature associated to CT excitations has an onset at slightly higher energies in the capped samples, around 4 eV. Moreover, the intensity of the spectra is higher in capping-free samples at 529 eV. This is because the onset of XAS is set at higher energies in capped samples, as evident from Fig. 6.5. At the same time, no appreciable polarization dependence is present in the spectra, with the exception of the low-energy region of the RIXS spectrum measured at 530 eV.

6.3.4. Discussion

XAS and RIXS spectra allows us to draw a clear picture of the electronic structure of infinite-layer nickelates. We will first begin with a discussion of the STO-capped films, where the interpretation is easier.

The presence of a sizeable linear dichroism in the XAS at the Ni L-edge is compatible with a strong contribution of in-plane orbitals to the groundstate. Due to the structural similarity to cuprates, it is safe to assume that the Ni^{1+} hole has a dominant x^2-y^2 character, as in the cuprate superconductors. This interpretation is further confirmed by several DFT calculations [156,

180, 195]. There are, however, crucial differences with respect to cuprates. First of all, Oxygen K-edge XAS does not show features below the main edge of the absorption. In particular, the UHB and ZR peaks, evident in cuprates, are absent in nickelates. At the same time, the CT excitation visible in the Oxygen K-edge RIXS spectra have an onset at 4 eV, much bigger than the 2 eV of cuprates. These measurements clearly reveal that the charge-transfer energy Δ is higher in nickelates.

This fact is also confirmed, indirectly, by Ni L_3 XAS and RIXS. First of all, the high-energy shoulder of the Ni L_3 XAS clearly increases with doping, as visible in Fig. 6.3(a). This is at odds with hole-doped cuprates [77], where instead only a mild doping dependence is observed. A simple explanation is that the additional holes doped into the planes have a mostly Ni-character, so that the groundstate changes from (mostly) Ni^{1+} to Ni^{2+}. This interpretation, which was put forwards also by other recent experimental works [171], is also strengthened by the comparison with NiO (again shown in Fig. 6.3(a)), and is a confirmation that oxygen bands lie away from the Fermi level. The doping dependence of the *dd* excitations, which soften upon doping (Fig. 6.3(b)), is also at odds with hole-doped cuprates. It is, instead, more similar to the behaviour displayed by electron-doped cuprates where the *dd* harden upon doping. This experimental fact again reinforces the idea that the doped holes mostly reside on Ni sites in nickelates. This, indeed, would decrease the effective energy separation between the Fermi level in the $x^2 - y^2$ band and the other d-orbitals, so that the absolute energies of the *dd* excitations is reduced.

This interpretation put infinite-layer nickelates closer to the class of Mott-Hubbard insulators in the Zaanen-Sawatzky-Allen scheme [196]. This is a huge difference with respect to cuprates, which instead are perhaps the best example of Charge-Transfer insulators. The magnitude of the charge-transfer energy is a crucial parameter in the cuprates, because it determines, among other, the strength of the superexchange interaction J, and its behaviour upon doping [9, 25, 69]. The bigger value of Δ found in nickelates might explain why the critical temperatures are ten times smaller in infinite-layer nickelates.

Nevertheless, our XAS and RIXS measurements at the Oxygen K-edge reveal, for the first time, that oxygen bands are not completely inactive in the low-energy physics. While no pre-edge is visible in the XAS, a clear doping dependence is observed in the XAS profiles of Fig. 6.5 and the in RIXS spectra of Fig. 6.8. Thus, nickelates probably have a mixed charge-transfer Mott-Hubbard character. We note that very recent measurements on the similar Ruddlesden-Popper compounds also favor this more complex interpretation [177].

Another difference with respect to cuprates is the presence of a particle-hole continuum at intermediate energy losses (0.1 – 0.6 eV) even samples without Sr doping. Its presence implies a non-zero doping even in the nominally undoped compounds. DFT indeed predict that Nd 5*d* bands are active at the Fermi level [74, 180, 195], and give rise to a sizeable *self-doping*. The strong 0.6 eV feature visible in the RIXS maps if Fig. 6.3 is also possibly related to the Ni-Nd hybridization, like was suggested in previous papers [74]. This interpretation is also supported by its polarization dependence: its intensity is indeed much stronger when the incident polarization is perpendicular to NiO_2 planes, which suggests an out-of-plane character. However, our measurements reveal for the first time that this feature is visible both at the Ni L_3 and O K-edge. This clearly indicates that the oxygen bands are not completely inactive in the low-energy physics of nickelates.

Our measurements reveal also puzzling differences in the electronic structures of STO-capped and capping-free samples. The Ni L_3 XAS seems compatible with a mostly Ni^{2+} groundstate, and exhibits very ow doping dependence. At the same time, the Ni^{1+} feature exhibits an opposite linear dichroism. This implies a more out-of-plane character of the Ni groundstate and a greater occupation of the z^2 orbital. Perhaps more surprisingly, the Oxygen K-edge XAS exhibits two pre-peaks at 528.2 eV and 529.4 eV. Furthermore, the intensity of the $3d^8\underline{R}$ is much higher than in the STO-capped samples. It also resonates at the 529.4 eV of the XAS. Overall, these results can be interpreted as a stronger hybridization between Ni-3*d* and Nd-5*d* bands and a higher occupation of the z^2 in the groudstate. The origin of this different phenomenology is not yet established. One of the hypothesis that has been put forward is the presence of intercalated hydrogen, which is present in the CaH_2 powder used for the topotactic reaction. However, one would expect to observe a corresponding high-energy phonon (plus overtones), which should have an energy between 400 and 600 meV. We note that a similar reasoning was recently used to detect oxidised oxygen inside Li-batteries through RIXS [197]. The absence of any evident phonon mode seems to rule out this scenario.

6.4. Magnetic excitations in capped films

In this section, we report measurements of the magnetic excitations in STO-capped NSNO films. We will first give an overview of the experimental results, and then disucss their implication for the physics of superconducting nickelates.

Fig. 6.9 shows the measured momentum dependence of the low-energy region of undoped NNO. Evidently, the spectra are dominating by a dispersing feature in the energy range 0 meV – 200 meV. The shape of the dispersion,

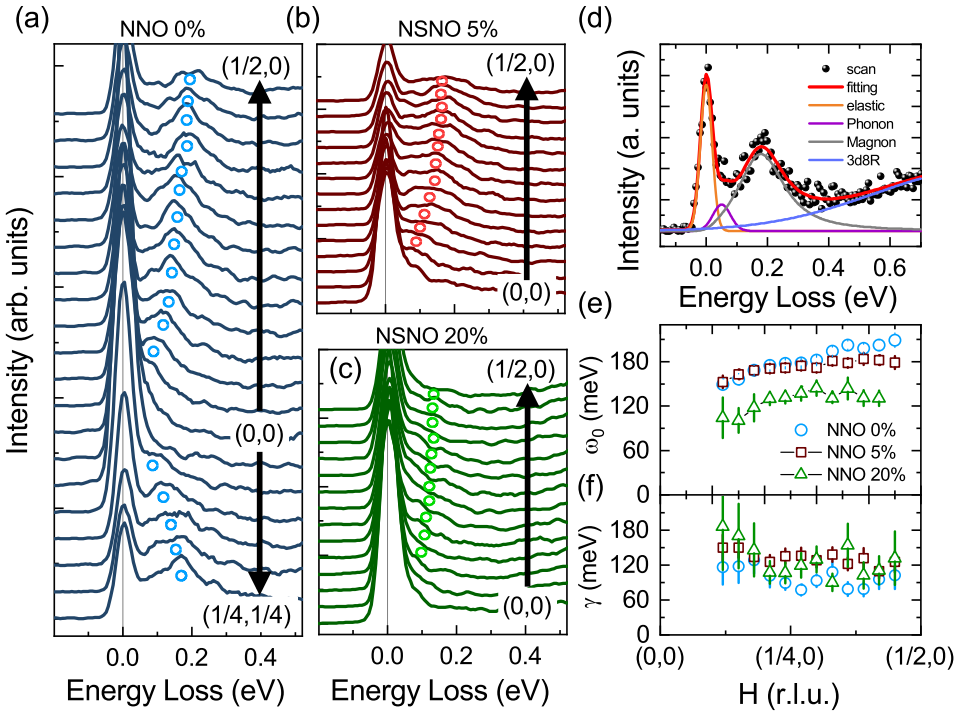

Figure 6.9: Overview of magnetic excitations in capped NSNO films. (a)-(c): Stack of RIXS spectras as a function of momentum in NNO 0% (a), NSNO 5% (b) and NSNO 20% (c). (d): example of fitting procedure. (e): undamped energy ω_0 extracted from fitting. (f) damping γ extracted from fitting.

as well as the energy range, allow us to safely identify this excitation with a magnon. We also remark that ours is the second independent observation of magnons in infinite-layer nickelates, and our results agree well with those published previously [181]. It is well known that in cuprates, the profile of the magnetic susceptibility in doped compounds can be relatively well described in terms of a damped harmonic oscillator [198]. The *propagation* frequency $\omega_p = \sqrt{\omega_0^2 - \gamma^2}$ of the excitation is reduced from the bare *undamped* value ω_0 because of the broadening, quantified by the parameter γ.

To extract these parameters, we have fitted the spectra using Gaussian profiles for the elastic peak and the phonon peak, and a damped harmonic oscillator for the magnon excitation. We have also added a broad gaussian profile to fit the tails of the $3d^8R$ peak. An example of the fitting is provided in panel (d) in Fig 6.9. This allows us to extract ω_0 and the width γ, whose values are reported in panels (e)-(f) Fig. 6.9 . The damping is sizeable despite the nominal absence of Sr dopant in the sample. This is consequence of the self-doping induced by the hybridization between Cu $3d$ and Nd $5d$ bands, although also structural/chemical disorder might also play

a role. Nevertheless, the excitation is underdamped ($\gamma < \omega_0$) in most of the Brillouin zone, so that there is a non-zero propagation frequency. A simple linear spin-wave fitting of the dispersion, performed with the software SpinW, gives an estimate of the superexchange $J \sim 60$ meV and of the next-nearest neighbour exchange $J' \sim -10$ meV. This value is about half of that found in cuprates. Assuming that the Cu – O hopping and the on-Coulomb repulsion U do not change drastically between the two compounds, this reduction is consistent with a higher value of the charge-transfer energy Δ, which controls the strength of the effective Cu – Cu hopping t.

The doping dependence also shows remarkably differences with respect to cuprates. The RIXS spectra along the $(1,0)$ direction show barely any dispersion at all. Fitting the spectra using the damped oscillator model reveals two important facts. First, the excitations are overdamped at all points along the antinodal (1,0) direction. Secondly, the undamped frequency ω_0 of the nickelate films clearly decreases with doping. At the same time, the damping does not evidently increase. Similar results have been found also by the Stanford group of Dr. Wei-Sheng Lee [181], and in subsequent experiments on other nickelate films [199].

Overall, the behaviour of the magnetic excitations upon doping appears to be very different from cuprates. In particular, in cuprates the undamped frequency is rather insensitive to the doping level, and even slightly increase from undoped to over-doped samples. Additionally, the propagation frequency ω_p close to the $(1/2,0)$ point remains rather constant up until $p = 0.21$ [200]. In order to better disentangle the shape of paramagnons, and to highlight the differences with respect to cuprates, we have acquired RIXS spectra with polarization sensitivity. Fig. 6.10 reports the result for nickelates and cuprates. In particular, we have chosen antiferromagnetic $NdBa_2Cu_3O_{6+x}$ (YBCO AF $p \sim 0$) and optimally-doped $NdBa_2Cu_3O_{6+x}$ (YBCO OP, $p = 0.16$) as a representative case for cuprates. In the case of NSNO films, spectra have been acquired at $\mathbf{q} = (0.36, 0)$, where magnon energy is almost maximum and the intensity is still strong. Incident polarization was π, as in Fig. 6.9. In cuprates, we used a similar value $\mathbf{q} = (0.4, 0)$, and again incident π polarization. The experimental noise is higher in cuprate spectra due to a lower acquisition time.

Panels (a)-(d) show that the the (para-)magnon excitation is well visible in NdBCO samples and in undoped NNO, while the shape drastically change in NSNO 20%. The ratio between spin-flip and non-spin-flip is also lower in this compound. Panels (e)-(f) reveal the most striking difference between cuprates and nickelates. In the former, the energy of the maximum of the magnon remains almost constant with doping. In particular, damping γ increases and the peak becomes broader, but the undamped frequency slightly increases as well [200]. The net result is that along the (1,0) direction the

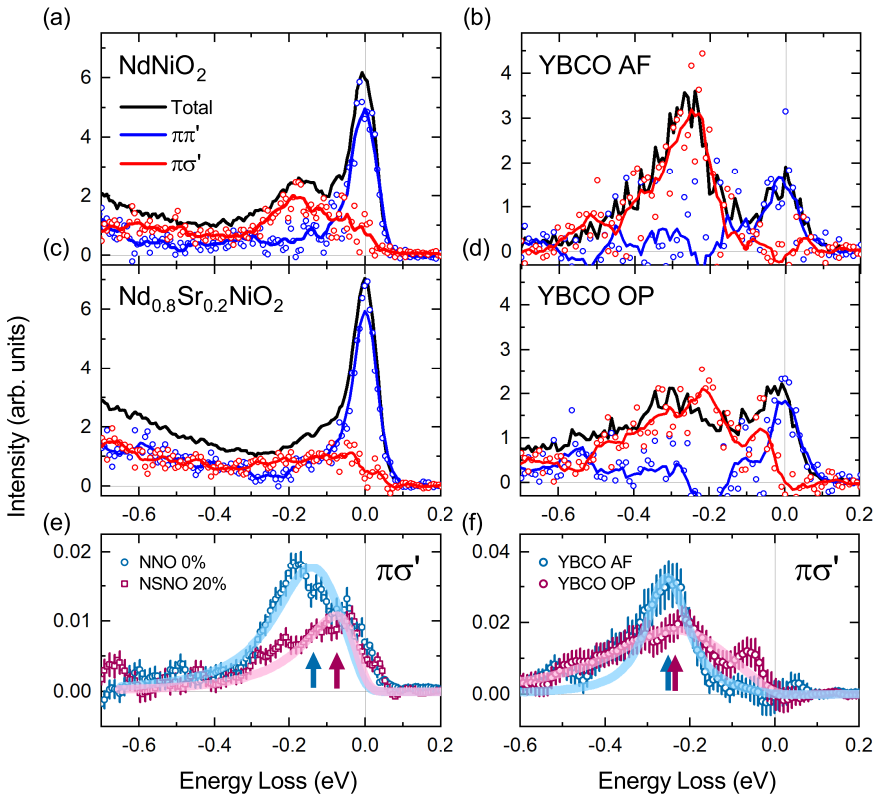

Figure 6.10: Polarimeter measurements on Ni- and Cu-compounds. (a)-(c): Polarimetric RIXS spectra on NNO and NSNO collected at $(0.36, 0)$. Points are raw data, solid lines are curves smoothed over 7 points. (e) Comparison between $\pi\sigma'$ spectra on NNO and NSNO 20%. Points are experimental data smoothed over 7 points. Solid lines are fitting with damped harmonic oscillator lineshapes. Arrows indicate the position of maxima. (b),(d),(f): same as left panels, but for NdBCO AF and NdBCO OP ($p = 0.17$).

propagation frequency ω_p remains constant. This fact is perhaps surprising, since in a doped system the effective number of magnetic neighbouring sites is lower (an effect called spin dilution). However, it has been measured in previous experiments [200] and verified by Quantum Monte Carlo calculations [69]. The reason is the presence, in the low-energy Hamiltonian, of a so-called *three-site* term [68, 69]. This interaction lowers the energy the energy of the AF lattice in the presence of doped holes, but also increases the energy of a single-site spin flip.

An early hypothesis that was put forward to explain the different behaviour of cuprates and nickelates regarded the effective orbital character of the doped holes. While in the cuprates they mostly reside on oxygen bands (forming Zhang-Rice singlets), in nickelates they have mostly Ni-character,

as we demonstrated in the previous section. Therefore, spin dilution was identified as the reason beneath the softening of the single-magnon energy. We note, however, that the *hardening* of the undamped frequency, typical of cuprates, is obtained in a single-band Hubbard model, where no information on the orbital character of the doped holes is retained. Therefore, one should find another explanation.
To this aim we have performed, in collaboration with Dr. Maciej Fidrysiak (University of Krakow), some preliminary calculations using a Variational Wave Function approach with an inverse number of fermionic flavours (VWF + $1/\mathcal{N}_f$) [201]. The advantage of this approach is that we can fit the entire spin-flip RIXS spectrum, which has contributions from paramagnons and particle-hole excitations, with a few parameters: t, t' and U. If we fix t and t' based on DFT calculations, which usually predict accurate values of hopping amplitudes, we can then just use t/U as a parameter. The calculations nicely fit the experimental lineshape both at high and low doping levels. Additionally, the demonstrate that a lower value of t/U in a single-band Hubbard model is enough to explain the softening of magnetic excitation in nickelates.

6.5. Charge-order capping-free NSNO films

The most striking difference between capped and capping-free samples comes however from a comparison between the low-energy region of the RIXS spectra. First, there is no evidence of dispersing magnetic excitations in the range 0 – 200 meV at any of the doping levels investigated. The spectra only display a non-dispersing tail of the elastic peak, which extends until ~ 100 meV.

The most important finding concerns the elastic peak itself. In panel (a) of Fig. 6.11 we report a map of RIXS spectra collected as a function of momentum along the (1,1) and (1,0) directions in the undoped sample (NNO 0%). While no feature are evident in the (1,1) direction, the (1,0) shows a clear peak in the intensity of the elastic at the (quasi) commensurate wavevector $(1/3, 0)$. This is consistent with the presence of a periodic modulation of the charge in the system, i.e. with the presence of *charge-order* (CO) [185]. Integrating the quasi-elastic intensity in the range ±100 meV and plotting it against the momentum along the (1,0) direction, we get the curves plotted in panel (b). The peak is relatively narrow in momentum space, with a full-width-at-half-maximum (FWHM) of ~ 0.06 Å, corresponding to a correlation length in real space of $1/(\pi \cdot \text{FWHM})$ ~ 20.7 Å. Moreover, the feature present a high-resonant behaviour, disappearing when the incident energy is tuned a few hundreds of meV away from the main Ni L_3 resonance. At a first glance, this phenomenology seems similar to the one observed in cuprates, where

a CDW is found at similar wavevectors with a strong resonant character [62, 143, 185].

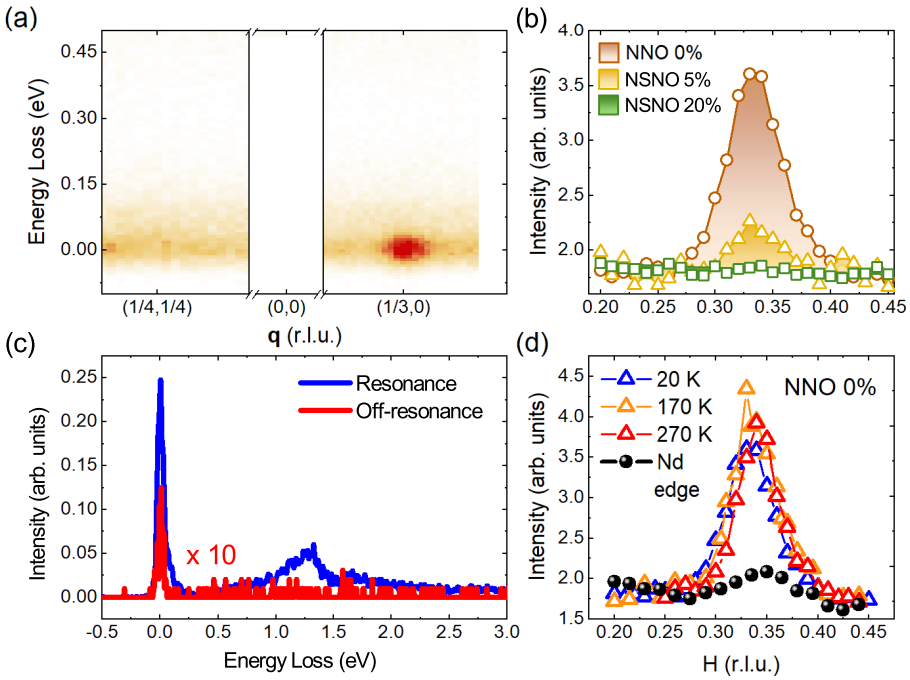

Figure 6.11: Overview of charge order in capping-free nickelates. (a): RIXS spectra as a function of momentum along the (1,1) direction (left part) and (1,0) direction (right part). (b): Doping dependence of the CO peak. Intensity has been calculated as the integral of the RIXS spectra in the quasi-elastic region (±150 meV). Intensities of NSNO 5% and NSNO 20% have been slightly shifted vertically (less than 10%) to match the tails of the NNO sample. (c): RIXS spectra at the wavevector of CO ($\mathbf{q} = (1/3, 0)$), on the Ni L_3 resonance and off-resonance (850 eV). The off-resonance spectrum has been multiplied by a factor 10 for clarity reasons. (d): Temperature dependence of CO peak on NNO 0%. Black dots refer to spectra acquired at the Nd M_5 edge, at $T = 20$ K.

However, some other characteristics are markedly different. The intensity of the modulation shows a clear doping dependence, shown in panel 6.11(b). It is reduced by a factor 3 in the NSNO 5% sample, and disappears completely in the NSNO 20% one. This is at odds with cuprates, where instead the quasi-critical CO peak has maximum strength at doping $p \sim 0.11$, and is absent below $p \sim 0.07$ [62, 185, 188]. Additionally, the observed charge-order does not show any clear temperature dependence in the range 20 K – 270 K, as reported in panel (c). This is again at odds with cuprates, where CO gradually develop below a certain $T_{CO} < 200$ K [62, 143, 185]. Actually, a T-independet CDW has been found in some over-doped cuprates, like in single-layer $(Bi,Pb)_{2.12}Sr_{1.88}CuO_{6+\delta}$ at $p \sim 0.215$. However, CO in overoped

cuprates peaks at low momentum values $\mathbf{q} \sim (0.14, 0)$, very different from the periodicity observed here. Interestingly, CO is a common feature of quasi-2D Nickelates like the trilayer $La_4Ni_3O_8$ and single-layer Ruddlesden-Popper $La_{2-x}Sr_xNiO_4$. These materials do indeed show a stripe-order with a periodicity of 3 unit cell, but the modulation takes place in a direction rotated by 45° with respect to Ni – O bonds [202, 203]. Additionally, we have verified that a peak in the elastic intensity is also visible in RIXS spectra acquired at the Nd M_5 edge (~980 eV). This edge probes the Nd $4f$ states, but it is indirectly sensitive to the $5d$ states.

The striking differences in the physics of capped and capping-free infinite-layer nickelates is puzzling, and requires further studies to be unraveled. However, our result highlight very well-defined correlations between the different features observed. The absence of STO-capping layer (actually, of any capping layer in general) seems to have three effects. First, it reduces the two-dimensional character of the material, as evident from the loss of linear dichroism in the XAS. This might indicate a substantial mixing, in the groundstate, between the x^2-y^2 and the z^2 orbitals. Secondly, it increases the hybridization between Ni-$3d$ and Nd-$5d$ orbitals, as indicated by the substantial increase in the intensity of the (putative) $3d^8R$ feature at 0.6 eV. The fact that this feature is more evident with $\boldsymbol{\varepsilon} \perp NiO_2$ is consistent with the increase in the out-of-plane character of the Ni electronic structure. Moreover, we have verified that CO is clearly seen at the Nd M_5 edge, which indirectly probes the $5d$ states. The link between CO and Ni – Nd hybridization is also reinforced by their doping dependence: both of them are clearly reduced with Sr-doping. Moreover, it destroys the magnon dispersion, leaving a small tail of over-damped magnetic excitations below 120 meV.

6.6. Conclusions and future perspectives

The research on nickelates has just begun, and much has yet to be discovered. The spin physics seems, to some extent, clear. The much higher charge-transfer energy lowers the value of the Cu-Cu hopping amplitude. As a result, the whole scale of magnetic excitations is lower than in cuprates. Our calculations also suggest that the lower t/U ratio can explain the softening of magnetic excitations upon doping. However, it remains to be determined what is the expected consequence of the different spin physics on superconductivity. Can the energy softening along the antinodal direction explain the different transition temperatures?
Do nickelates have a pseudogap phase like the cuprates? Is there any charge order in capped nickelate films?

At the same time, the huge differences in the physics of capped and capping-

free samples is still mysterious. Can the capping layer have an appreciable effect on the entire "bulk" of the films? Is the presence of intercalated hydrogen involved? Why is the presence of the capping layer apparently not precluding the presence of superconductivity, and could this mean that it is only the interface between STO and NSNO that superconducts?

Chapter 7

Electron-phonon coupling in bilayer HTS cuprates

The results presented in this chapter have been published as *"Doping Dependence of the Electron-Phonon Coupling in Two Families of Bilayer Superconducting Cuprates"*, by Y. Peng, L. Martinelli, Q. Li, M. Rossi, M. Mitrano, R. Arpaia, M. M. Sala, Q. Gao, X. Guo, G. M. De Luca, A. Walters, A. Nag, A. Barbour, G. Gu, J. Pelliciari, N. B. Brookes, P. Abbamonte, M. Salluzzo, X. Zhou, and K.-J. Zhou, Physical Review B 105, (2022), and selected as Editor's suggestion.

The electron-phonon coupling (EPC) is the fundamental glue that provides Cooper pairing in conventional superconductors. Instead, its role in the high-T_c superconducting cuprates is still debated. By means of resonant inelastic x-ray scattering at the oxygen K-edge, we conduct a thorough investigation of the EPC in $Nd_{1+x}Ba_2Cu_3O_{7-\delta}$ (NBCO) and $Bi_2Sr_2CaCu_2O_{8+\delta}$ (Bi2212) at different doping levels, from the underoped region ($p = 0.07$) to overdoped one ($p = 0.21$). To analyze the data, we employ a localized Lang-Firsov model that also includes the coherent excitations of several phonon modes. While we show that the effects due to electronic band dispersion are not negligible, we are able to quantify the relative values of EPC matrix elements in the two cuprate families. In NBCO, the careful choice of the excitation energy also allows us to disentangle the phonon modes related to the CuO chains from those related to the two-dimensional CuO_2 planes. We find that, in both families of cuprates, the electron-phonon coupling decreases with doping at large momentum transfer ($\mathbf{q}_\parallel = (0.25, 0)$ r.l.u.), whereas it shows a non-monotonic trend at smaller momenta (e.g. $\mathbf{q}_\parallel = (0.1, 0)$). We attribute this behaviour to the dynamical screening of mobile carriers. Additionally, we find that an enhancement of the phonon intensity close to charge-density-wave excitations, whereas the extracted EPC strength is less sensitive to their presence. In conclusion, we perform a comparative study of two bi-layer cuprate families. We identify general trends in the EPC for the cuprates as a

function of doping, and we also provide an important experimental input to the theories invoking a synergistic role of this interaction in d-wave pairing.

Contents

7.1. Introduction

In conventional superconductors, the pairing interactions critically depends on the electron-phonon coupling, which provide the glue for Cooper pairing [204, 205]. The role of EPC in cuprate high critical temperature superconductors (HTS) is, instead, still intensively debated. On the one hand, different experimental techniques such as angle-resolved photoemission spectroscopy (ARPES) [47, 206–211] and scanning tunneling microscopy (STM) [212–214] have found evidence of an interaction between lattice vibrations and onset of superconductivity. On the other hand, many other experimental observations favor a scenario in which spin fluctuations provide the dominant source of pairing [14, 215, 216]. Indeed, the superconducting order parameter has a $d_{x^2-y^2}$ symmetry [217], and the superconducting phase emerges in proximity to a strong antiferromagnetic one. It is important to underline, however, that this interpretation does not explicitly preclude a possible role of phonons in enhancing electron pairing. For example, it has been shown that a synergy between electron-phonon and electron-electron interactions might lead to an enhancement of the critical temperature T_c in HTSs. Indeed, recent theoretical work has highlighted a strong correlation between T_c and the EPC of the out-of-plane bond-buckling oxygen phonon branches (also referred to as "B_{1g}" modes) [46]. In particular, materials with the highest EPC of B_{1g} phonons also display the highest T_c.

The identification of the dominant source of electron pairing is also complicated by the complex phase diagrams of HTS. The pivotal parameter that determines the nature of the ground state at a given temperature T is the number of holes present in the CuO_2 planes (i.e. the doping p). By changing p the system crosses phases with competing spin-, charge- and possibly pair-density-waves; a pseudogap phase with a peculiar electronic landscape; and, finally, and strange metallic behavior with puzzling and still poorly understood transport and thermodynamic properties [8, 56, 63, 218–221]. In the underdoped region of the phase diagram ($p<0.16$), some of the phonon branches get renormalized by the onset of charge-density-wave (CDW) correlations. This is similar to the behaviour of conventional metals, where the electron-phonon interactions cause the formation of charge-density modulations [222]. Recent IXS and RIXS studies have indeed measured an anomalous softening of the phonon energy, and enhanced EPC in the vicinity of the charge-ordering wavevector [65, 223–226].

At the same time, the electron-phonon interactions is also affected by the onset of the pseudogap phase in the same doping range. In HTS this happens at a temperature T^*, below which a partial gap opens along in the density of states along the antinodal $(1,0)$ direction in reciprocal space [227]. The pseudogap temperature T^* decreases with doping and falls to zero at a critical doping $p_c = 0.19$, where transport measurements report a change of carrier density from p to $1+p$ [53]. Interestingly, a recent ARPES study on the bilayer cuprates $Bi_2Sr_2CaCu_2O_{8+\delta}$ (Bi2212) has revealed a rapid change of the EPC of the bond-buckling B_{1g} phonon branch (~ 38 meV) across the pseudogap phase boundary [47]. To better understand these observations, it is fundamental to investigate how the coupling between electrons and phonons evolves with doping across the entire phase diagram of cuprates, from the low-doping region to the Fermi liquid one ($p > p_c$).

Measuring the full EPC vertex $M(\mathbf{k},\mathbf{q})$ is quite challenging, as it in general depends on both the fermionic ($\mathbf{k}$) and the bosonic ($\mathbf{q}$) momenta. Some techniques, like ARPES, can only probe the $\mathbf{k}$ dependence of the EPC via the self-energy of the electrons, which intrinsically averages over the phonon momentum $\mathbf{q}$. On the other hand, scattering tehcniques (e.g. IXS and INS) probe the dependence of $M(\mathbf{k},\mathbf{q})$ on the bosonic momentum $\mathbf{q}$ through the line width of phonons, averaging over the fermion momentum $\mathbf{k}$. Time-resolved, pump–probe optical spectroscopies can extract the strength of the electron-boson coupling by measuring the relaxation time, but can only access small momentum transfers close to the Γ point [228]. Recently, it was shown that RIXS can be a very effective tool to determine the EPC. In particular, RIXS can access a sizeable region of the Brillouin zone, and has an intrinsic element specificity, thanks to the interaction between the phonons and the photoexcited electrons during the intermediate state [229]. Similarly

to IXS, RIXS probes the momentum transfer $\mathbf{q}$ of the phonon, integrating over the fermionic momenta $\mathbf{k}$ [78, 230]. Theoretical models have shown that, in the case of mobile electrons, the summation over $\mathbf{k}$ can also be modulated electron occupation or by the orbital character [78, 229, 230]. In the limiting case where the electron mobility can be neglected, for example because of a strongly localizing core-hole potential, the EPC can be simply extracted from the intensity of the RIXS spectra. In particular, it can be calculated with two different approaches: from the ratio between the intensity of the fundamental phonon peak and its overtones [76, 229, 231], or by tracking the phonon intensity as the energy of the incident beam is detuned from the resonance [78, 232].

Prior RIXS studies of EPC in the 2D cuprates have focused primarily on the Cu L_3-edge [78, 226, 232]. However, it is well known that in doped cuprates the Fermi level crosses bands with a dominant oxygen $2p_{x,y}$ orbital character [233]. Moreover, it is believed that the modes most relevant to electron pairing are the high-energy optical oxygen branches [46, 209]. Therefore, it is of crucial importance to also investigate the EPC at the O K-edge. At this edge, the RIXS process involves $1s \rightarrow 2p$ transitions. In the intermediate state, the charge perturbation has a dominant $2p$ orbital character (plus a spherically symmetric core hole, on whose influence we will discuss in the next sections). At the same time, RIXS experiments at the O K-edge benefit from a higher energy resolution [90, 151], and longer intrinsic lifetime of the photoexcited hole than at the copper L_3-edge [234]. This last property enhances the phonon intensity, which is positively correlated with the lifetime of the RIXS intermediate state [71, 78].

In this work, we have studied the interaction between $2p$ electrons and the high-energy optical phonon branches in two families of HTS cuprates: bilayer Bi2212 and $Nd_{1+x}Ba_{2-x}Cu_3O_{7-\delta}$ (NBCO), using RIXS at the Oxygen K-edge. We have extracted the EPC using a localized model based on a Lang-Firsov transformation (to which we will refer as a Lang-Firsov model in the following) [235–237] that accounts simultaneously for bond-buckling and bond-stretching branches. Combining the results on the two cuprate families, we discover that EPC strength monotonically decreases with doping at $\mathbf{q}_\parallel = (-0.25, 0)$ r.l.u., whereas the trend becomes non-monotonic at smaller momentum transfer. The observed doping dependence of the EPC is in agreement with the non-uniform screening model discussed in previous theoretical work [46]. Additionally, We have also studied the effect of charge-density waves on EPC. Finally, our measurements we clearly demonstrate that the detuning method for EPC extraction, which has given excellent results at the Cu L_3 edge, is not applicable at the Oxygen K-edge. Our results provide important information on the general trends of EPC in cuprate superconductors, and also highlight important limitations of the current the-

oretical models of phonon RIXS.

7.2. Methods

7.2.1. Sample characterization

In this study, we have employed thin films of $Nd_{0.97}Ba_{2.03}Cu_3O_7$ (NBCO) and single-crystals of $Bi_2Sr_2CaCu_2O_{8+\delta}$ (Bi2212).

The NBCO samples were grown on $SrTiO_3$ and had a thickness of 100 nm, with two different doping levels: a heavily underdoped sample with critical temperature T_c = 38 K (UD38, $p \simeq 0.07$), and an optimally-doped sample with T_c = 92 K (OP92, $p \simeq 0.16$). The growth was realized by the group of Dr. Marco Salluzzo in the laboratories of CNR-Spin. Determined in-plane lattice constants were $a = b = 3.9$ Å, while the out-of-plane lattice parameter was $c = 11.714$ Å in the UD38 sample and $c = 11.74$ Å in the OP one. NBCO samples were prepared in the way described in Refs. 238 and 239. Epitaxial thin films were deposited using high oxygen-pressure diode sputtering on 10×10 mm^2 $SrTiO_3$(100) single crystals. The substrates were previously etched in a BHF solution (pH = 5.5) and annealed at 950°C in 10 Torr of pure oxygen. We performed topography and friction measurements (in contact mode), which show well-ordered TiO_2-terminated surfaces. The typical size of terrace is of the order of 200 nm [239]. Optimally and underdoped NBCO films were deposited using targets of $Nd_{0.97}Ba_{2.03}Cu_3O_7$ and $Nd_{1.2}Ba_{1.8}Cu_3O_7$, respectively. The Nd-excess at the Ba site gives rise to a reduced hole-carrier concentration (and therefore to a corresponding underdoping), but the structural and morphological properties remain similar to those of the optimally-doped films. All films were deposited in an atmosphere made up by 95% of oxygen and 5% of argon, with a total pressure of 1.7 Torr. We used 920°C temperature deposition with a corresponding growth rate of 0.01 nm s^{-1}. The temperature was then lowered to 500°C with the same pressure. Finally, the chamber was filled with 400 Torr of oxygen. The samples were then annealed in this conditions in order to reach full oxygenation. Laboratory x-ray diffraction shows that the rocking curves around the (001) and (005) reflections of all the films have a FWHM of 0.03° and 0.08°, respectively, comparable to the resolution of the diffractometer [238]. This indicates a very small orientation misalignment between individual domains in each sample. The structure remains coherent along the c-axis for the entire thickness of the film, as demonstrated by the clear Pendellösung fringes surrounding the (001) peak, visible also 100 nm thick films. Additional information can be found in Ref. [238–240]. The resistivities of NBCO samples as a function of temperature,are shown in Fig. 7.1(a). The suerconducting transition temperature T_c is very evident in both cases.

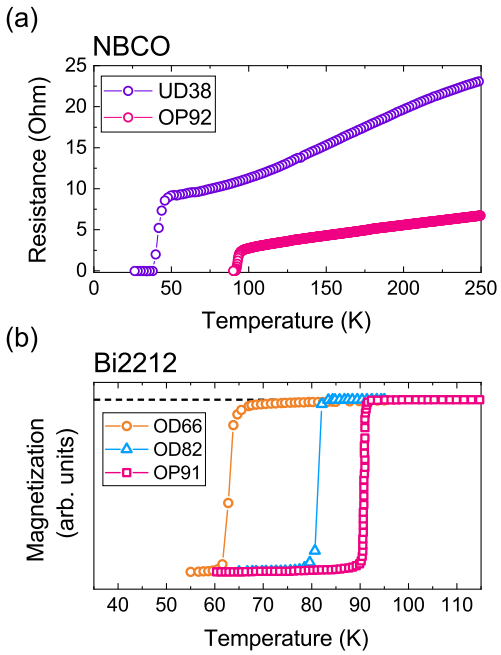

Figure 7.1: (a) Resistance (in Ω) of underdoped (UD) and optimally-doped (OP) NBCO films plotted as a function of temperature. (b) T-dependence of the magnetization for the three Bi2212 single crystals as a function of temperature, acquired in a 1 Oe magnetic field. The horizontal dashed line represents the zero of magnetization.

$Bi_2Sr_2CaCu_2O_{8+\delta}$ (Bi2212) single-crystals were grown by the group of Prof. Yingying Peng at the University of Peking. Optimally-doped samples were grown by the travelling solvent floating zone method [241, 242]. We obtained overdoped samples with $T_c \sim 82$ K (OD82) through annealing in an oxygen atmosphere of 0.2 MPa, at 500°C, for 5 days [243]. The heavy overdoping of sample OD66 ($T_c \sim 66$ K) was obtained through annealing in 12 Mpa of oxygen at 550°C for five days. The lattice parameters are $a = b = 3.8$ Å and $c = 30.89$ Å. The high quality of the samples is testified by the very sharp superconducting transitions, which display a width of 2 K, as reported in in Fig. 7.1(b). We determined the critical temperatures from AC magnetic susceptibility measurements, acquired with a Quantum Design MPMS XL-1 system using a magnetic field of 1 Oe.

7.2.2. RIXS experiments

We have performed RIXS measurements at the O K-edge. RIXS spectra on NBCO samples were measured at the I21 beamline of the Diamond Light Source, UK [244]. The combined energy resolution was determined to be 34 meV by measuring the full width at half maximum (FWHM) of the elastic line, acquired non-resonantly on a carbon tape. We used a fixed temperature

of 20 K to minimize radiation damage.

The RIXS measurements on Bi2212 were performed at the soft x-ray inelastic beamline (SIX) 2-ID of the National Synchrotron Light Source II, at Brookhaven National Laboratory [245]. The combined energy energy resolution was ~ 33 meV, measured in the same way as at Diamond Light Source. All measurements were performed at 35 K to reduce sample damage. All the momentum values reported in the next section are measured in reciprocal lattice units (r.l.u.).

For both types of samples, the RIXS spectra were collected with σ incident polarization (perpendicular to the scattering plane) to enhance the charge signal. The scattering angle was kept fixed at 150°. We employed a grazing-in geometry, which by convention corresponds to negative parallel transferred momentum $\mathbf{q}_\parallel$, as sketched in Fig. 7.2(g).

7.2.3. The Lang-Firsov Localized Models

The first model developed to describe phonon excitation during the RIXS process was the local, single-site model introduced in Ref. [229], which was meant to be applied for measurements at the Cu L_3-edge. The model was derived from the following Hamiltonian:

$$\mathcal{H} = \epsilon_0 n_d + \omega_0 b^\dagger b + M \sum_\sigma n_d (b + b^\dagger), \tag{7.1}$$

where $d_\sigma^\dagger$ and $b^\dagger$ are the creation operators of an electron with spin σ and local phonon mode, respectively, $n_d = \sum_\sigma d_\sigma^\dagger d_\sigma$, and M is the electron-phonon coupling (EPC) constant. This is related to the dimensionless coupling parameter $g = (M/\omega_0)^2$. This local model is based on the very simplifying assumption that both the phonon and the photoexcited electron are *local*, i.e. they cannot travel through the lattice at any stage of the RIXS process. The model was indeed first developed for moleculr crystals, where the phonon modes actually were the normal vibrations of the molecule at each site. In this limit, the RIXS intensity can be computed exactly using a so-called Lang-Firsov transformation, which gives:

$$I(q, \Omega) = \sum_n |A_n(\Delta + \mathrm{i}\Gamma)|^2 \delta(\omega_0 n - \Omega), \tag{7.2}$$

where Δ is the detuning (i.e. the energy difference) of the incident energy from the XAS resonance, Γ is the half-width of the RIXS intermediate state, and

$$A_n(z) = \sum_m \frac{B_{n,m}(g) B_{m,0}(g)}{z - \omega_0 (m - g)} \tag{7.3}$$

with

$$B_{n,m} = (-1)^n \sqrt{e^{-g} n! m!} \sum_{l=0}^{m} \frac{(-g)^l g^{\frac{n-m}{2}}}{(m-l)! l! (n-m+l)!} \tag{7.4}$$

being the Franck-Condon factor ($B_{n,m}$ actually stands for $B_{\max(n,m),\min(n,m)}$).

In Ref. [236] the authors recently generalized this single-site model to the case of multiple phonon branches coupled to the electrons. In this extension, each phonon is allowed to be coherently excited. This is important for the cuprates, where we expect the photoexcited electron to interact with several phonon branches [230]. In the following, we consider the case of two main phonon modes, again described by a local Hamiltonian [236]: the out-of-plane oxygen buckling and the in-plane oxygen stretching modes,

$$\mathcal{H} = \quad \epsilon_0 n_d + \sum_{\lambda=1,2} \left[\omega_\lambda b_\lambda^\dagger b_\lambda + M_\lambda n_d (b_\lambda + b_\lambda^\dagger) \right]. \tag{7.5}$$

We can then compute the RIXS cross section, and obtain

$$I(q,\Omega) = C_{\text{scale}} \sum_{n_1,n_2} |A_{n_1,n_2}(\Delta + \mathrm{i}\Gamma)|^2 \delta\Big(\sum_{\lambda=1,2} n_\lambda \omega_\lambda - \Omega \Big), \tag{7.6}$$

where

$$A_{n_1 n_2} = \sum_{m_1 m_2} \frac{D_{n_1 m_1}^{n_2 m_2}(g_1,g_2) D_{m_1 0}^{m_2 0}(g_1,g_2)}{\Delta + \mathrm{i}\Gamma - \sum_{\lambda=1,2} \omega_\lambda (m_\lambda - g_\lambda)}. \tag{7.7}$$

Where C_{scale} is an overall scale factor for the amplitude, independent of momentum, detuning and common to all the phonon branches, which we use to rescale the intensity to match the experimental curves. The coefficients D in Eq. (7.7) are actually a product of Franck-Condon factors

$$D_{n_1,m_1}^{n_2,m_2}(g_1,g_2) = B_{n_1,m_1}(g_1) B_{n_2,m_2}(g_2), \tag{7.8}$$

where $g_\lambda = (M_\lambda/\omega_\lambda)^2$.

The model's coupling constants M_λ are the quantities that have to be determined from the experiments. The simplest strategy is simply to fit the energy loss dependence of the lattice excitations plus their overtones. Since their relative intensities are insensitive to the absolute scale of intensity, the prefactor C_{scale} will not have any effect on the extracted coupling constants. Nevertheless, including this factor allows us to disentangle any additional modulation in the intensity that are unrelated to the EPC, e.g. from overlapping CDW excitations.

We stress that both models presented here completely neglect the mobility of the electron photoexcited during the RIXS process. Nevertheless, the simple

expressions for the RIXS cross section [Eqs. (7.2) and (7.6)] obtained from these drastic approximations are very useful to fit the experimental data. The parameters that determine the intensity of phonon excitations are: i) the EPC parameter of the different modes g_λ, ii) the inverse of the core-hole lifetime Γ, ii) and the detuning energy Δ. Throughout the chapter, we will treat g_λ as a fitting parameter, while Δ is chosen during the experiment and known precisely. We will also fix the lifetime $\Gamma = 0.15$ eV [78, 246, 247] for all the samples investigated. This approximation is justified, it is the Auger processes – whose cross-section is basically independent from the particular material – that mostly determine the intrinsic lifetime of the intermediate state.

A more recent theoretical work calculated the phonon RIXS response in the limit of a single carrier in a delocalized band [231], and found that the local models for the RIXS cross-section produce stronger phonon peaks with respect to a fully itinerant model. Moreover, the discrepancy between the two types of models increases with a lower value of the localizing core-hole potential. This result suggests that fitting the experimental RIXS spectra with a localized model might *underestimate* the strength of the EPC parameter. Additionally, in the single carrier limit, the momentum structure of the electronic band can also induce a spurious momentum dependence in the intensity of the phonon excitations, unrelated to the real momentum dependence of $M(\mathbf{k}, \mathbf{q})$.

With these caveats in mind, we still proceed by fitting the experimental data with the localized model, with the aim of extracting general trends of the EPC. We stress that despite its limitations, no other alternatives are available at the moment. Other frameworks either neglect the electron mobility [78, 230], do not include multiple phonon modes [247], or cannot account for finite concentration of carriers [231]. At present, it is not known whether these approximation are more or less extreme than the local one in the case of cuprate materials. Nevertheless, in all of these approaches a positive correlation still exists between phonon intensity in the RIXS spectra and the EPC (with possible additional intensity modulations due to electron mobility or orbital character). This fundamental relation survives because phonons are excited by the perturbation in the charge cloud following the photoexcitation of core electrons in the RIXS process. The magnitude of this interaction is, by definition, the electron-phonon coupling.
We, therefore, have to keep in mind that the values of the extracted EPC parameters should not be immediately equated to $M(\mathbf{q})$ in microscopic Hamiltonian.

7.3. Experimental results

7.3.1. RIXS spectra at O K-edge

X-ray absorption spectra (XAS) of the Bi2212 crystals and NBCO films are shown in Fig. 7.2(a) and Fig. 7.2(b), respectively. It is straightforward to identify the Zhang-Rice singlet (ZRS) pre-edge in the O K-spectra of Bi2212. This feature arises from the hybridization between in-plane O $2p_\sigma$ and Cu $3d_{x^2-y^2}$ orbitals [77]. The energy and spectral weight of the ZRS peak changes with doping as expected: in particular, the energy softens and the intensity increases with increasing doping. On the other hand, in NBCO we observe two different features that evolve with doping: a main peak at 528.2 eV, and another one at a slightly smaller energy (~ 527.6 eV). The first is linked to doped holes in the CuO_2 planes, while the second is related to the one-dimensional CuO chains, which in NBCO act as the main charge reservoir [77]. The UD38 sample has very short chains in both in-plane directions because of the tetragonal structure of the substrate, while the OP92 sample has longer chains, but again along both a and b directions. The comparison between less and more doped samples also nicely shows the decrease in the intensity of the upper Hubbard band (UHB) peak, located around 529.5 eV.

To extract the value of the electron-phonon coupling we have measured RIXS spectra at several incident x-ray energies, spanning the range across the different resonances of the XAS. Figs. 7.2(c) and 7.2(d) report an overview of these RIXS spectra for optimally-doped Bi2212 OP91 and NBCO OP92, respectively. The incident x-ray energy of each spectrum is indicated by the tick marks in the XAS curves, which have the same color in panels (a) and (b) for the two compounds. As highlighted by the labels in Fig. 7.2(e), the RIXS spectra are composed of four main features: the elastic peak at zero-energy loss, the phonons plus their overtones below 200 meV, the broad charge continuum which peaks around 800 meV, and higher-energy excitations present above 1.5 eV over dd and charge-transfer (CT) excitations. Additionally, we also identify some non-zero spectral weight at 500 meV, possibly due to bimagnon excitations [248] or even, according to some recent proposals, to an excitonic features. To highlight the phonon excitations in the spectra and to compare the measured intensities in different samples at the main resonant energy, we subtracted the elastic peak and subsequently normalized the spectra to the dd+CT continuum as summarized in Fig. 7.2(f). This procedure is necessary since the RIXS measurements on Bi2212 and NBCO samples have been performed at different beamlines, so that the absolute intensities cannot be compared. Evidently, the phonon excitations have an overall larger spectral weight in NBCO. Also, phonons in Bi2212 OD82 (p_c = 0.19) are clearly stronger than those observed in the optimally-doped OP91 and

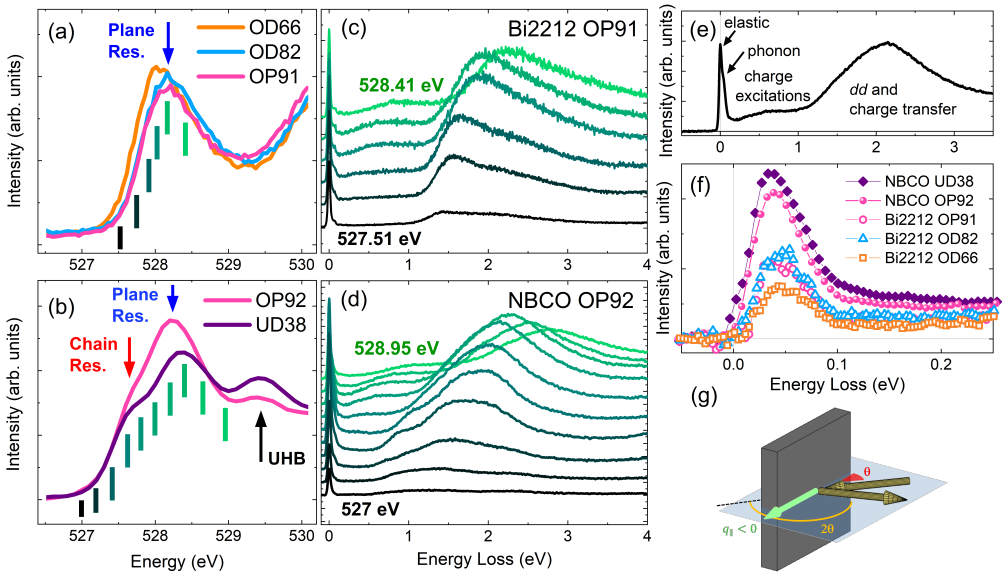

Figure 7.2: Overview of XAS and RIXS measurements at the O K-edge on Bi2212 and NBCO. (a, b) XAS of samples with different doping values, for Bi2212 and NBCO, respectively. The legends report the T_c of the samples, as described in the main text. Zhang-Rice, Upper Hubbard Band and chain resonances are highlighted with blue, black and red arrows, respectively. (c, d) RIXS spectra in optimally-doped Bi2212 and NBCO. The excitation energies for the different spectra are reported with ticks in the XAS in panels (a)-(b), with the same color code for the two samples. (e) Example of a typical RIXS spectrum at Oxygen K-edge (NBCO OP92 at 528.2 eV). Labels describe the different features. (f) Zoom of the low-energy excitations for all NBCO and Bi2212 samples measured at H = −0.15 r.l.u. at the ZR resonance energy. Elastic peak was subtracted for clarity. All the spectra were normalized to the integral of the spectral weight between 1 and 7 eV, which corresponds to the CT continuum. (g) Sketch of the experimental geometry use for RIXS measurements. The incoming and outgoing x-rays are drawn with yellow arrows. The incident (θ) and scattering (2θ) angles are highlighted in red and yellow colors. The parallel component of the transferred momentum $\mathbf{q}$ is reported in light green.

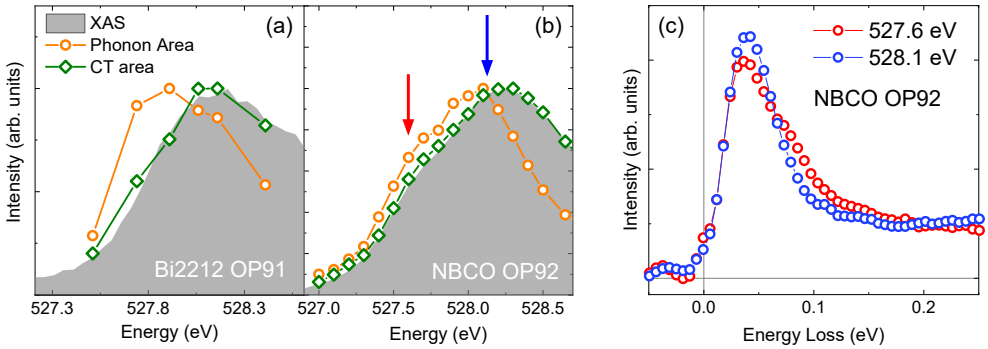

Figure 7.3: Main XAS and phonon resonances in optimally-doped Bi2212 and NBCO. (a, b) XAS spectra (grey shaded area), integrated intensity of phonons (orange circles) and total weight of CT excitations (green diamonds) for Bi2212 OP91 and NBCO OP92, respectively. The red and blue arrows indicate the energy of the chain and plane resonances in NBCO OP92. (c) RIXS spectra collected in optimally-doped NBCO at the chain (red) and plane (blue) resonances, after subtraction of the elastic peaks.

in the heavily-overdoped OD66 samples.

We have then extracted the integrated spectral weight of the phonon signal. This allowed us to determine the resonance energy of phonons, i.e. the energy at which the total phonon intensity reaches its maximum value. To do this, we have removed the elastic peak and the charge excitations from the measured spectra, and then we have integrated the remaining signal in the infrared region ($0 - 0.3$ eV). As a reference, we have also extracted the total weight of the CT continuum. This was done integrating the RIXS scans in a 3 eV-wide window whose center was placed at the maximum value of the CT continuum: this was necessary since the CT signal shows a fluorescent behaviour and "moves" when plotted against the energy-loss. The integrated intensity of phonons and CT excitations are reported in Figs. 7.3(a) and 7.3(b) for optimally-doped Bi2212 and for NBCO, respectively. All the curves have been normalized to their maximum value, and are plotted over the associated XAS profile. The shape of the RIXS spectra (after subtraction of the elastic peak) on the NBCO OP92 sample for two representative energies are reported in Fig. 7.3(c). The one-dimensional bond-stretching mode of the CuO chains has a stronger EPC than its 2D counterpart; this is evident from the ratio between the intensity of the first overtone and the fundamental phonon peak, which is higher at the chain resonance.

The intensity of CT continuum follows closely the shape of the XAS spectrum, confirming its independence from the lifetime of the RIXS intermediate state. On the other hand, the phonon spectral weight has a large shift of $200 - 250$ meV relatively to the resonance of the XAS, in both families of samples. The presence and large value of this energy shift are extremely

puzzling. A small discrepancy, of the order of the characteristic phonon energy ($\approx 50-100$ meV) between the maximum of the XAS and of the phonon intensity has been witnessed before in RIXS measurements [226, 249], and can be explained in the framework of the localized Lang-Firsov model by a strong EPC and a long lifetime of the core-hole. The values observed here is instead very large and would require an unrealistic EPC. As suggested in Ref. [250], a possible interpretation is a change of the curvature of the (phonon) potential energy surface between the initial and intermediate electronic states of the RIXS process.

7.3.2. Detuning measurements

Our first attempt at the extraction of the EPC of buckling and breathing modes was realized using the detuning method, presented in Sec. 7.2.3 and described in detail in Ref. [78]. This method was successfully applied at the Cu L_3 edge [78, 232]. This approach is based on the local Lang-Firsov model described in Sec. 7.2.3. It consists in measuring RIXS spectra at several incident x-ray energies, at and below the main resonance in the XAS. The extraction of the EPC is then performed by globally fitting the RIXS spectra, consisting of the main phonon peaks and their overtones using Eq. (7.6). In order to reduce the number of free parameters, we have fitted all of the detuned spectra of a given sample at the same time, employing a single scale factor and fixed the inverse half lifetime $\Gamma = 0.15$ eV [246, 247], for reasons described in Sec. 7.2.3. This way, the only remaining free parameters are the EPCs M_λ of the bond-buckling and bond-stretching branches and their energies Ω_λ. We have also subtracted the elastic peaks considering just the inelastic features. This is because the elastic peaks carries additional contributions from other types of scattering (e.g. surface roughness, structural disorder in the bulk..), and therefore cannot be properly modelled.

As mentioned in the previous section, the maximum of the phonon intensity is consistently shifted from the resonance of the XAS by ~ 200 meV. This is not captured by the model and represent a serious difficulty. The Lang-Firsov model can account for displacements between the two values of the order of ω_λ in the strong coupling limit, clearly not enough to. Therefore, we have decided to artificially set the zero of the detuning value at the phonon resonance. Since we had already given up on the attempt of extracting the *real* absolute values of the EPC, this approximation will not invalidate more our results.

We have tested the validity of the detuning method using two different datasets: the CuO chain resonance of NBCO OP92, and the plane resonance of Bi2212 OP91. In NBCO, the chain resonance was chosen for two reasons. First, it selects the one-dimensional system, as opposed to the

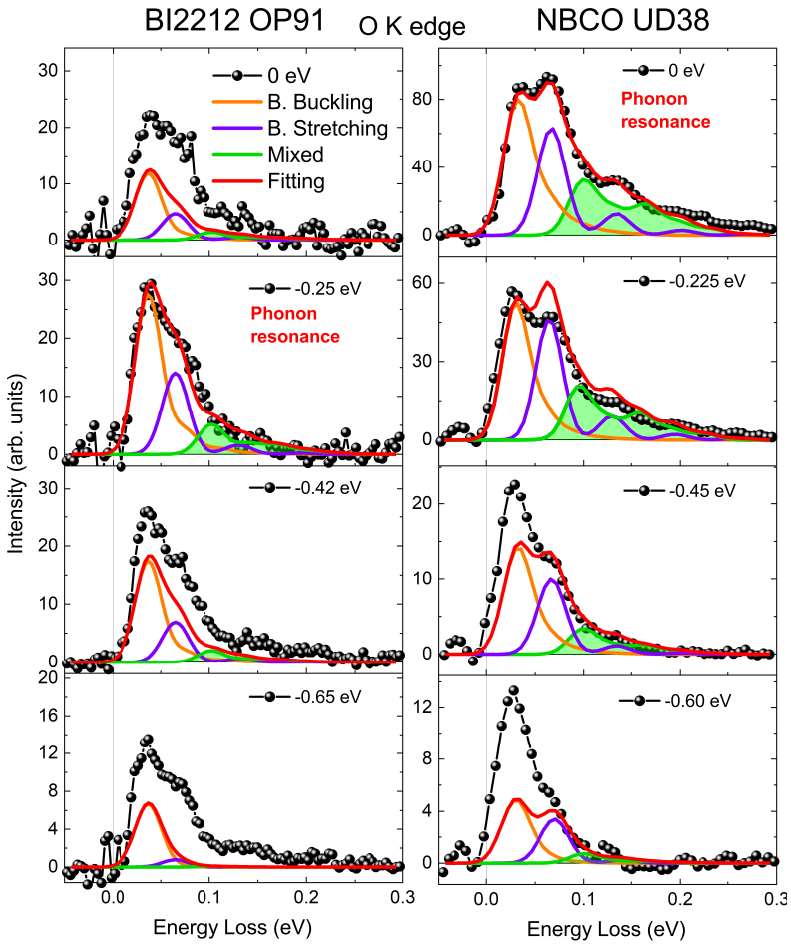

Figure 7.4: Detuning RIXS measurements on optimally-doped Bi2212 (left panels) and underdoped NBCO (right panels). Incident energies were chosen below the plane resonance for Bi2212 and below the chain one for NBCO AF, for the reasons explained in the main text. The chosen momentum transfer was $(-0.25, 0)$ r.l.u. for NBCO and $(-0.15, 0)$ r.l.u. for Bi2212. Fitted curves are reported with solid lines, and are decomposed into the different phonon branches. The were obtained through the global fitting procedure discussed in the text. The model evidently fails at large detuning energies.

two-dimesional planes of Bi2212. This allows us to verify whether there are differences related to the different dimensionality. Secondly, the chain resonance (~ 527.6 eV) is found at lower energies than that of the CuO_2 planes (528.2 eV). This means that the energies select to acquire detuned RIXS spectra will not polluted by additional contributions from the resonance of the CuO_2 planes, while the detuning energies of the two-dimensional planes are obscured by intensity from the chains.

The spectra, along with the fittings, are shown in Fig. 7.4. The solid orange (purple) lines are the bond-buckling (bond-stretching) phonons and their higher harmonics. The green shaded area represents the mixed multi-phonon peaks, which in the model are assumed excited coherently. It is evident from the spectra that the detuning approach is not capable to reproduce the measured intensities for high detuning values. In particular, the intensity id underestimated by more than ~ 50%. The agreement is instead quite good close to the XAS resonance in both NBCO and Bi2212.

The failure of this approach at the Oxygen K edge does not come completely unexpected. This is due to the different nature of the RIXS intermediate state at the Cu L_3- and the O K-edges. At the Cu L_3-edge, the excited electron is strongly bound to the core hole, while this does not hold at the O K-edge. Here, the photoexcited electron is more free to move around the lattice during its characteristic lifetime. In Ref. [231] the authors recently developed a new model, valid for an intermediate state consisting of a single itinerant electron interacting with the core-hole and the phonon branches, in an empty band. Interestingly, the detuning curves (i.e. the intensity of phonons modes versus the detuning energy) are quantitatively different from the one calculated with the localized model. In particular, they display a weaker dependence on the EPC when the core-hole potentials are weak. Still, in the experimental spectra we observe a small discrepancy between the detuning curves of the buckling and breathing branches, as evident from Fig. 7.4. This observation suggests that the real situation of the oxygen bands close to the Fermi energy in copper oxides is intermediate between the localized and fully itinerant electrons. Despite the failure of the localized model to reproduce the RIXS spectra at high detuning energies, it is still useful to report the values of the EPC extracted from this type of fitting procedure. For optimally-doped Bi2212 OP92, we get $M_1 = 120 \pm 15$ meV a ($M_2 = 95 \pm 15$ meV) for the buckling (breathing) phonon branch. Interestingly, these values are actually close to what has been extracted from RIXS spectra at the Copper L_3 edge [78, 232].

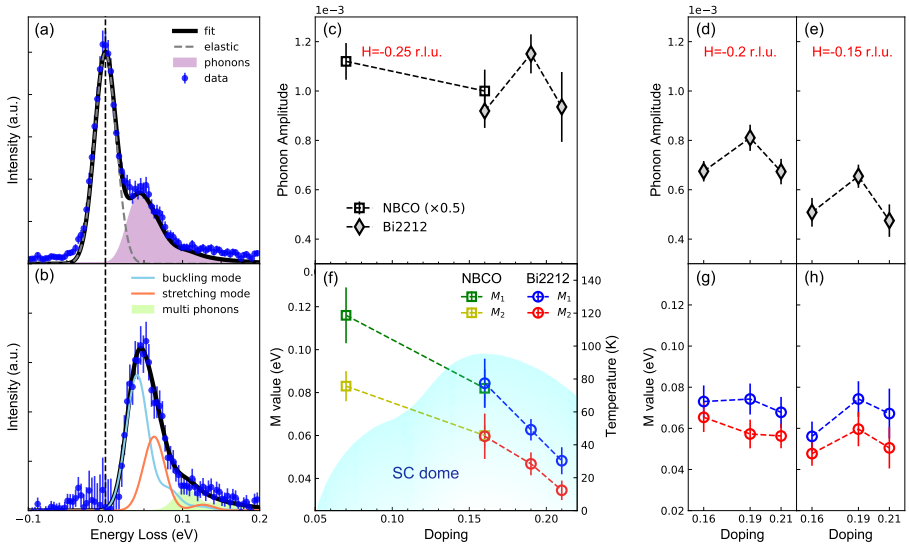

Figure 7.5: (a) Fits of RIXS spectrum after subtraction of the particle-hole excitations for Bi2212 OD82, acquired at $H = -0.2$ r.l.u. . Elastic peak was fitted with a Gaussian profile, with the width corresponding to the measured energy resolution. Phonon excitations are fitted with the Lang-Firsov model considering two branches, i.e. the bond-buckling mode (~ 40 meV) and bond-stretching mode (~ 70 meV). (b) Some spectrum after subtraction of the elastic peak, with the phonon components highlighted. (c-e) Doping dependence of phonon intensity for Bi2212, showing a maximum at $p_c = 0.19$. Phonon amplitude of NBCO is reported in (c) and divided by a factor of 2 for clarity. (f-h) Doping dependence of the EPC strengths M for both Bi2212 and NBCO. The superconducting phase diagram [251] (shaded area) is also shown in (f).

7.3.3. Effect of doping on EPC

The determination of the EPC evolution with doping is a crucial step to understand its role in d-wave pairing in copper oxides. To this aim, we fit just the RIXS spectrum measured at the phonon resonance using Eq. (7.6), after subtracting the features related to other excitations (elastic, particle-hole and CT excitations), as shown in Fig. 7.5. The width of the elastic peak has been determined by measuring non-resonant RIXS spectra on carbon tapes, which is a rather standard and reliable procedure [65, 78, 223, 232]. As discussed above, the use of Eq. (7.6) probably underestimates the overall magnitude of the EPC. This is particularly true at the O K-edge, where the electron mobility in the RIXS intermediate state is stronger than at the Cu L-edge [231]. Nevertheless, we proceed with Eq. (7.6) in a comparative analysis with the aim to identify *trends* in the experimental data, both as

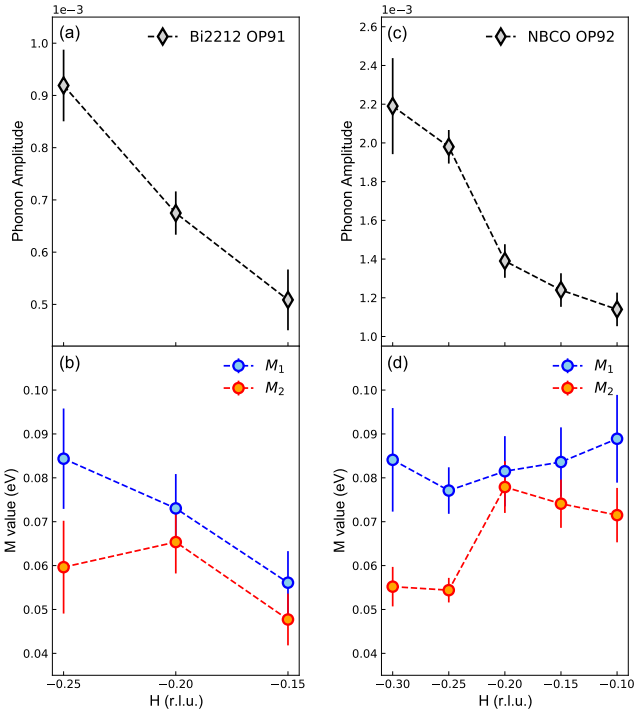

Figure 7.6: Momentum dependence of all the fitting parameters of the Lang-Firsov model in Bi2212 OP91 (a,b) and NBCO OP92 (c,d). Phonon amplitudes increase at large momentum $\mathbf{q}$, while the EPC strength M do not show a clear dependence on momentum. The extracted M values of the two samples are similar.

a function of cuprate famili (Bi2212 vs. NBCO) and doping. It is safe to assume that the degree of itinerancy in these two systems is similar for comparable doping levels. Thus, applying the local model for EPC extraction should yield the same systematic error when applied to both families of samples. We reiterate that the absolute magnitudes of EPC strengths extracted with this analysis cannot be directly mapped onto the $M_\lambda(\mathbf{q})$ parameters entering the microscopic Hamiltonian.

To fit the data, we consider a coherent excitation of just two phonon branches – the bond-buckling branch ($\omega_1 \simeq 40$ meV) and the bond-stretching branch ($\omega_2 \simeq 70$ meV) – and we treat the electron-phonon coupling strengths M_λ as fitting parameters, like in the detuning analysis. We also introduce a global amplitude prefactor C_{scale}, to match the calculated intensity to the measured ones. Using this approach, we are able to obtain a consistent fit of the RIXS spectra as a function of doping. Figs. 7.5(c-e) report the doping evolution of the C_{scale} amplitude factor in Bi2212 for different momentum transfers.

The corresponding extracted M_λ couplings are plotted in Figs. 7.5(f-h). For comparison, in Figs. 7.5(c) and (f) we have also overlaid the same two parameters extracted from NBCO spectra at $H = -0.25$ r.l.u. Remarkably, the values of the extracted scales and couplings in the two samples are very similar at optimal doping.

At $H = -0.25$ r.l.u., we find, in both families of samples and at all dopings p, the EPC of the bond-buckling mode is stronger than the EPC of the bond-breathing mode. This observation is consistent with previous RIXS measurements performed at the Cu L_3 edge on NBCO UD38 sample for small/intermediate momentum transfers [78], and ARPES experiments [46, 207, 209, 211]. As the hole concentration increases, we find a monotonic decrease of the extracted M values for both modes. This behavior can be interpreted as a result of the stronger electronic screening as the system becomes more metallic [46]. The situation instead changes for smaller momentum transfer. For $H = -0.20$ r.l.u., the extracted EPC parameters are only weakly dependent on p, while at $H = -0.15$ r.l.u. the doping dependence becomes non-monotonic: in particular, the EPC of both branches becomes stronger at the critical doping $p_c = 0.19$. Interestingly, we observe that the phonon amplitude of Bi2212 exhibits a clear maximum at the same doping $p_c = 0.19$, at all three momenta. At the same doping, a recent ARPES study has revealed a rapid change of the bosonic coupling strength, possibly correlated with the increase in the superconducting gap [47]. It is still unclear, and surely worthy of future investigation, whether the two phenomena are correlated, and what are the underlying reasons of this phenomenology.

The measured doping dependence, summarized in the previous paragraph, is for both samples consistent with a poor electron screening scenario, discussed in Ref. [46]. The bad conductivity along the c-axis direction (perpendicular to the copper-oxygen planes) gives rise to a non-uniform screening of the EPC, which becomes well-screened at large $\mathbf{q}$ values but is instead poorly screened at smaller momenta. The relative reduction of large $\mathbf{q}$ coupling increases the electron-phonon coupling for the d-wave channel. This suggests that the contribution of the high-energy optical phonon modes to Cooper pairing increases increases with doping, and might become strongest at optimal doping.

7.3.4. Influence of CDW on EPC

The two families of cuprates investigated in this work present a CDW ordering with $q_{\mathrm{CDW}} \simeq 0.29$ r.l.u. (see [62, 185] for NBCO and Bi2212 [252–254]), even though the charge-order signals is weaker with respect to UD samples [62]. Previous RIXS studies performed both at the Cu L_3-edge and the O K-edge on doped materials reported an enhancement of phonon intensity

near the charge-ordering wavevector, which was ascribed to the presence of dispersive CDW excitations that cross the energies of phonons and interfere with them [65, 223]. Therefore, we have searched for possible enhancements of the electron-phonon coupling of buckling and breathing branches correlated with the presence of CDW.

Using again the localized Lang-Firsov model [Eq. (7.7)], we have extracted the evolution of the EPC parameters and of the overall honon intensity (parametrized through the scaling prefactor C_{scale}) along the antinodal $(H, 0)$ direction. Figure 7.6 shows the momentum dependence of the two parameters C_{scale}) and M_λ in optimally-doped NBCO and Bi2212. Evidently, the phonon amplitude increases monotonically when approaching the Charge-ordering wavevector q_{CDW}. On the other hand, the EPC does not show a clear trend, and M_1 is larger than M_2 at all measured momentum values. These results clearly reveal that no enhancement of the EPC corresponds to the measured increase in phonon intensity in the vicinity of q_{CDW}. This conclusion is also confirmed by the fact that no enhancement of the intensity of phonon overtones is visible in the spectra, and therefore robably independent from the paritcular model used for the extraction of the EPC. A possible explanation is the overlapping contribution of CDW *fluctuations*, which have a finite energy [255]. Therefore, our results show that one should be careful in blindly interpreting the bare (single-)phonon intensity as the EPC strength in the proximity of Charge-order instabilities. The explanation of this discrepancy is surely a topic worthy of for further investigation.

7.4. Conclusions

In this Chapter, we have presented a O K-edge RIXS analysis of the EPC in two families of bilayered cuprates. In particular, we have measured the phonon dynamics as a function of doping, incident energy, and momentum, in compounds ranging from the strongly under-doped regime to the heavily overdoped one. Our first experimental result is that the localized Lang-Firsov model, though successful at the Cu L-edge, does not properly model the phonon intensity at large detuning values. We assign the reason behind this failure to the large itinerancy of the photoexcited electrons and the phonon cloud, which is not captured by the model [231]. Therefore, the detuning approach cannot be applied at the O K-edge, at least within the current models.

Our second result is the determination of the doping and momentum dependence of electron-phonon coupling, which we extracted from measurement at resonance. We have revealed a systematic decrease of EPC strength with doping increasing from strongly UD to OD samples. This holds, however, only at high momentum transfer, while the EPC is less affected by screening

closer to the Γ, in agreement with previous calculations [46].
Finally, we also found anomalies in the total phonon intensity in the proximity to the charge-ordering wavevector. However, the momentum dependence of the EPC is clearly different from what has been measured at the Cu L-edge [78], which implies that the RIXS cross section might contain additional form factors. Overall, our results show that studies of phonons in the presence of itinerant electrons must be made with precautions, at least in the framework of the current models. It is therefore necessary to develop new approaches to obtain a quantitative reliability of RIXS results.

Conclusions

In this thesis we have presented a comprehensive study of the fascinating classes of infinite-layer Copper and Nickel oxides.

Our investigation of infinite-layer copper oxides has focused on the magnetic and the orbital excitations. The first part of this thesis was focused on a systematic study of the magnetic spectrum of $CaCuO_2$. While this material had been investigated before, we have shed new light on the nature of the anomalous behaviour displayed in the proximity of the antinodal X point $(1/2, 0)$. This was possible thanks to an unprecedented quality of the RIXS measurements, but also thanks to an innovative combination of measurements. This was done by exploiting the recent technical advancements of the ID32 beamline and the ERIXS spectrometer, Through RIXS measurements with unprecedented energy resolution, with polarization-sensitivity, and with detuning energy, we provide evidence in favour of the partial fractionalization of magnons into spinon pairs close to the X point.

Then, we have studied the orbital spectrum of this material. For the first time, we observe a dispersion of the energy of *dd* excitations, of the order of 50 meV. This behaviour is the fingerprint of a collective behaviour of the orbital excitations, i.e. *orbitons*. While observed before in one-dimensional cuprate chains, it was so far unreported for higher-dimensional materials. Similar results are found in Nd_2CuO_4, and we correlate the similar behaviour to the absence of apical oxygens. We demonstrate that the standard Kugel-Khomskii model, used to describe the motion of orbitons in strongly-correlated materials, is not able to reproduce our experimental observations. Therefore, we present an extension of the model which includes the coupling between next-nearest neighbouring Cu atoms. Using a superexchange model and Exact Diagonalization calculations, we demonstrate that the model can give rise to a free-orbiton dispersion, in very good agreement with the measured one, despite the presence of the antiferromagnetic background. Additionally, we explain the origin of this longer-range coupling thanks to a microscopic charge-transfer (Emery) model. Its sizeable value can be traced back to the large covalency of the system, which explains why the orbiton

dispersion is not observed in La_2CuO_4 and the other cuprates.

Our thesis also present a thorough investigation of the very new class of superconducting infinite-layer nickelates, which have been synthetized only very recently. At the time in which the measurements presented here were taken, very few was known about their electronic and magnetic structure. We have acquired XAS and RIXS measurements at the Nickel L-edge, Oxygen K-edge and Neodymium M-edge. Thanks to this broad set of data, we have been able to provide insights into the electronic structure of this material. In particular, we have demonstrated that these materials have a mixed Mott-Hubbard and Charge-Transfer character, owing to a value of the Charge-Transfer energy two-times larger than in the cuprates. Thanks to RIXS measurements with polarization resolution, we provide the first unambiguous demonstration of the presence of magnetic excitations in undoped and doped materials. Moreover, we show that their doping dependence is starkly different than the one of cuprates. We suggest that this behaviour can be explained by a smaller value of t/U in a single-band Hubbard model. At the same time, we provide the first observation of a charge-ordered phase in films without the STO-capping layer, with peculiar characteristics.

Finally, we present a comprehensive study of the electron-phonon coupling in two families of superconducting cuprates. Using RIXS at the Oxygen K-edge, we demonstrate a reduction of the electron-phonon interaction with increasing doping. This suppression is not uniform in reciprocal space, in agreement with a poor electron screening scenario. Additionally, we show that the current models describing the excitation of phonons in the RIXS process are inadequate at the O K-edge. We ascribe this failure to the large itinerancy of the $2p$ electrons.

In conclusion, this thesis present fundamental results in the field of strongly-correlated materials. At the same time, our results demonstrate the extreme versatility of the RIXS technique, and its new standards in terms of polarization-resolved measurements and energy resolution.

Appendix A

Charge-Transfer model for orbiton superexchange

A.1. Charge transfer model in the 'standard' basis and its parameters for CCO

A charge transfer model with two d orbitals ($d_{x^2-y^2}$ and d_{xy}) and two p orbitals (p_x and p_y) per each copper and oxygen atom serves as the foundation for the computation. Thus, there are a total of six orbitals in the CuO_2 unit cell. There are eight factors in the model. Six parameters of the charge transfer model are specified in the usual way (in the hole language): I the Cu-O hopping ($t_{pd\sigma}$), ($t_{pd\pi}$), (t_{pp}) (nearest neighbor between different oxygen orbitals), (t_{pp}) (charge transfer energy for all oxygen orbitals), and (t_{pp}). Delta, (v) the Hund's exchange J_H, and (vi) the copper Coulomb repulsion U. Additionally, we add two crystal field energies: (i) the energy difference between the π and the σ bonding oxygen orbitals $\varepsilon_{\pi\sigma}$ (which comes from the *higher* energies for holes in the σ bonding, i.e. 'pointing-towards copper', oxygen orbitals), (ii) the crystal field energy of the xy orbital ε_{xy}. Note that we skip the Coulomb repulsion U_p on oxygen, since below we consider bonding or antibonding combinations of oxygen orbitals and the effective repulsion between oxygen holes is strongly reduced (due to the charge delocalisation). Altogether this leads to the following charge transfer Hamiltonian in the hole notation:

$$\mathcal{H} = \mathcal{H}_{\text{kin}} + \mathcal{H}_{\text{coul}}, \tag{A.1}$$

where

$$\begin{aligned}\mathcal{H}_{\text{kin}} = \sum_{i,s\in\{\uparrow\downarrow\}} \Big\{ & \varepsilon_{xy} n_{i,xy,s} + \Delta(n_{i+L,p_x,s} + n_{i+R,p_x,s} + n_{i+B,p_y,s} + n_{i+T,p_y,s}) \\ & + (\Delta + \varepsilon_{\pi\sigma})(n_{i+L,p_y,s} + n_{i+R,p_y,s} + n_{i+B,p_x,s} + n_{i+T,p_x,s}) \\ & + t_{pd\sigma}[c^\dagger_{i,x^2-y^2,s}(c_{i+L,p_x,s} - c_{i+R,p_x,s} - c_{i+B,p_y,s} + c_{i+T,p_y,s}) + \text{h.c.}] \\ & + t_{pd\pi}[c^\dagger_{i,xy,s}(-c_{i+L,p_y,s} + c_{i+R,p_y,s} - c_{i+B,p_x,s} + c_{i+T,p_x,s}) + \text{h.c.}] \\ & + t_{pp}(c^\dagger_{i+B,p_y,s} c_{i+L,p_x,s} - c^\dagger_{i+L,p_x,s} c_{i+T,p_y,s} + c^\dagger_{i+T,p_y,s} c_{i+R,p_x,s} - c^\dagger_{i+R,p_x,s} c_{i+B,p_y,s} + \text{h.c.}) \\ & + t_{pp}(c^\dagger_{i+B,p_x,s} c_{i+L,p_y,s} - c^\dagger_{i+L,p_y,s} c_{i+T,p_x,s} + c^\dagger_{i+T,p_x,s} c_{i+R,p_y,s} - c^\dagger_{i+R,p_y,s} c_{i+B,p_x,s} + \text{h.c.}) \Big\},\end{aligned}$$

and

$$\mathcal{H}_{\text{coul}} = \sum_{i,s\in\{\uparrow\downarrow\}} \left[(U - 3J_H) n_{i,xy,s} n_{i,x^2-y^2,s} + (U - 2J_H) n_{i,xy,s} n_{i,x^2-y^2,\bar{s}} \right]. \quad \text{(A.2)}$$

Here $c^\dagger_{i,f,s}$ ($c_{i,f,s}$) are creation (annihilationn) operators at site i, orbital f and with spin s ($n_{i,f,s}$ are the corresponding number operators). The sum runs over the Cu sites, while the indices $i+L, i+R, i+B, i+T$ describe the nearest-neighbor oxygen sites situated to the left, right, bottom and top of the copper site i.

The used CT parameters for $CaCuO_2$, which yield the observed value of the orbiton bandwidth (see the main text), and also reproduce the on-site xy orbital energies within 20% error (see below) can be found in Tab. A.1. While in general the estimates of the charge transfer parameters given in Tab. A.1 are rather standard, a few of them require a more detailed discussion:

First, the CT energy Δ is quite low for $CaCuO_2$. This can be justified by the absence of apical oxygens: the Δ energy significantly decreases with the distance to apical oxygens, cf. Fig. 2 or Table 1 in the appendix of [9]; we note that the used value is also consistent with optical absorption measurements [11, 12].

Second, the O-O hoppings t_{pp} are a bit larger than sometimes assumed. The considered here estimate follows, for instance, from [9] or the XPS on quasi 1D cuprates (see first column of Table I of [157]). Moreover, a recent review [7] critically advocates that t_{pp} is probably of the order 1 eV for the σ bonding oxygens (cf. [256]). However, this value is a bit larger than e.g. the one estimated by DFT for CCO [156].

Finally, the estimates of the relative on-site energies of the π-bonding oxygen orbitals and of the xy copper orbital are taken from Ref. [156]. These are *pure* crystal field (CF) parameters, and are not affected by interactions (or even covalency effects), so that DFT should yield the correct approach here. Note

$t_{pd\sigma}$	$t_{pd\pi}$	t_{pp}	Δ	$\varepsilon_{\pi\sigma}$	ε_{xy}	U	J_H
1.3	0.7	0.7	1.6	−1.6	1.0	8.0	1.0

Table A.1: Parameters of the charge transfer model (A.1) that are considered to be realistic for CCO (in eV; see text for more details).

that the CF energy of the xy orbital is *not* (and should not be) equal to the xy orbital excitation energy measured by RIXS. The latter, indeed includes the covalency effects and can, in fact, be reproduced by our calculations presented below.

A.2. Charge transfer model in the bonding - antibonding basis

Following [154] we express the CT model in the bonding-antibonding basis:

First, we restrict to the two copper orbitals

1. $|x^2 - y^2\rangle$ at zero energy,
2. $|xy\rangle$ orbital with CF energy ε_{xy},

and build the bonding and antibonding combinations of four oxygen π and four oxygen σ orbitals on a single CuO_4 plaquette. To this aim, we change basis from the p_x and p_y oxygen orbitals to the bonding and antibonding ones. (the non-bonding orbitals do not contribute to the exchange processes considered below and will not be considered). Note that the bonding and antibonding terminology have to be understood in terms of electron language):

1. the σ bonding oxygen orbital $|B\sigma\rangle = \frac{1}{2}(|B\rangle - |R\rangle - |T\rangle + |R\rangle)$ with energy $\varepsilon_{B\sigma} = \Delta + 2t_{pp}$ (this orbital corresponds to $-|\beta\rangle$ in [154]),
2. the σ antibonding oxygen orbital $|A\sigma\rangle = \frac{1}{2}(-|B\rangle - |R\rangle + |T\rangle + |L\rangle)$ with energy $\varepsilon_{A\sigma} = \Delta - 2t_{pp}$ (this orbital corresponds to $-|\alpha\rangle$ in [154]),
3. the π bonding oxygen orbital $|B\pi\rangle = \frac{1}{2}(|B\rangle - |R\rangle - |T\rangle + |L\rangle)$ with energy $\varepsilon_{B\pi} = \Delta + 2t_{pp} + \varepsilon_{\pi\sigma}$,
4. the π antibonding oxygen orbitals $|A\pi\rangle = \frac{1}{2}(-|B\rangle - |R\rangle + |T\rangle + |L\rangle)$ with energy $\varepsilon_{A\pi} = \Delta - 2t_{pp} + \varepsilon_{\pi\sigma}$.

We skip the t_{pp} hopping which mixes the $|B\sigma\rangle$ and $|A\pi\rangle$ orbitals. The first reason is that including the hybridisation between these states hugely complicates the calculations and is also neglected in [154]. The second is that such a hopping does not produce a coherent orbiton propagation, since it is linked to *double* orbiton creation and annihilation.

Second, due to the overlaps between the nearest neighbor CuO_4 plaquettes, we introduce the so-called orthogonalisation factors in the definition of the bonding and antibonding oxygen orbitals. We proceed as in [154]: *inter alia* we use the following values for the relevant orthogonalisation factors (same notation as in [154])

$$\mu(0) = 0.958,\ \nu(0) = 0.727, \quad \mu(1) = -0.14,\ \nu(1) = -0.273, \tag{A.3}$$

$$\mu(\sqrt{2}) = -0.02,\ \nu(\sqrt{2}) = 0.122. \tag{A.4}$$

Introducing these factors changes in the energies of the bonding and antibonding states (cf. [154]). In particular, we obtain for the relevant (see below) σ antibonding and π bonding states

$$\varepsilon_{A\sigma} = \Delta - 2\nu(0)t_{pp}, \quad \varepsilon_{B\pi} = \Delta + 2\nu(0)t_{pp} + \varepsilon_{\pi\sigma}. \tag{A.5}$$

Third, we include hybridisation between all four oxygen and two copper orbitals. Then, it turns out that only the $|A\sigma\rangle$ and $|B\pi\rangle$ orbitals hybridise with copper $x^2 - y^2$ and xy orbitals (respectively). We obtain that the relevant charge transfer model in such a bonding-antibonding basis reads:

$$\mathcal{H} \simeq \mathcal{H}^{(0)}_{\text{kin}} + \mathcal{H}^{(1)}_{\text{kin}} + \mathcal{H}^{(\sqrt{2})}_{\text{kin}} + \mathcal{H}_{\text{coul}}, \tag{A.6}$$

with

$$\begin{aligned}
\mathcal{H}^{(0)}_{\text{kin}} = \sum_{i,s\in\{\uparrow\downarrow\}} \Big[& \varepsilon_{xy} n_{i,xy,s} + \varepsilon_{A\sigma} n_{i,A\sigma,s} + \varepsilon_{B\pi} n_{i,B\pi,s} \\
& + T^{(0)}_{pd\sigma} \left(c^\dagger_{i,x^2-y^2,s} c_{i,A\sigma,s} + \text{h.c.} \right) + T^{(0)}_{pd\pi} \left(c^\dagger_{i,xy,s} c_{i,B\pi,s} + \text{h.c.} \right) \Big], \\
\mathcal{H}^{(1)}_{\text{kin}} = \sum_{\langle i,j\rangle,s\in\{\uparrow\downarrow\}} \Big[& T^{(1)}_{pd\sigma} \left(c^\dagger_{i,x^2-y^2,s} c_{j,A\sigma,s} + \text{h.c.} \right) + T^{(1)}_{pd\pi} \left(c^\dagger_{i,xy,s} c_{j,B\pi,s} + \text{h.c.} \right) \\
& + T^{(1)}_{A\sigma} \left(c^\dagger_{i,A\sigma,s} c_{j,A\sigma,s} + \text{h.c.} \right) + T^{(1)}_{B\pi} \left(c^\dagger_{i,B\pi,s} c_{j,B\pi,s} + \text{h.c.} \right) \Big], \\
\mathcal{H}^{(\sqrt{2})}_{\text{kin}} = \sum_{\langle\langle i,j\rangle\rangle,s\in\{\uparrow\downarrow\}} \Big[& T^{(\sqrt{2})}_{A\sigma} \left(c^\dagger_{i,A\sigma,s} c_{j,A\sigma,s} + \text{h.c.} \right) + T^{(\sqrt{2})}_{B\pi} \left(c^\dagger_{i,B\pi,s} c_{j,B\pi,s} + \text{h.c.} \right) \Big],
\end{aligned}$$

where $\mathcal{H}_{\text{coul}}$ is the same as in the previous section and the relevant hopping elements are (after including the orthogonalisation factors):

$$\begin{aligned}
& T^{(0)}_{pd\sigma} = 2\mu(0)t_{pd\sigma}, \quad T^{(0)}_{pd\pi} = -2\mu(0)t_{pd\pi}, \\
& T^{(1)}_{pd\sigma} = 2\mu(1)t_{pd\sigma}, \quad T^{(1)}_{pd\pi} = -2\mu(1)t_{pd\pi}, \quad T^{(1)}_{A\sigma} = -2\nu(1)t_{pp}, \quad T^{(1)}_{B\pi} = 2\nu(1)t_{pp}, \\
& T^{(\sqrt{2})}_{A\sigma} = -2\nu(\sqrt{2})t_{pp}, \quad T^{(\sqrt{2})}_{B\pi} = 2\nu(\sqrt{2})t_{pp}.
\end{aligned}$$

Note that $\mathcal{H}^{(0)}_{\text{kin}}$ depicts hybridisation between states within the same (or-

thogonalised) plaquette, $\mathcal{H}_{\text{kin}}^{(1)}$ stands for the hybridisation between states on the nearest neigbor (NN) plaquettes, $\mathcal{H}_{\text{kin}}^{(\sqrt{2})}$ stands for the nonnegligible hopping between the next-nearest neighbor (NNN) plaquettes (note that for the NNN the hopping between copper and oxygen orbitals can be neglected due to very small $\mu(\sqrt{2})$ [154]). As in the previous section $c_{i,f,s}$ ($c_{i,f,s}^{\dagger}$) are annihilation (creation) operators at site i, orbital f and with spin s ($n_{i,f,s}$ are the corresponding number operators).

A.3. Basis states of the cell perturbation theory

We construct the *single-particle* cell perturbation theory basis by diagonalising the single cell Hamiltonian $\mathcal{H}_{\text{kin}}^{(0)}$. We obtain four single-particle eigenstates on the single CuO_4 plaquette:

1. $|\psi_-\rangle = \cos\psi|x^2-y^2\rangle + \sin\psi|A\sigma\rangle$ with energy $E_{\psi_-} = \frac{1}{2}\Big[\varepsilon_{A\sigma} - \sqrt{\varepsilon_{A\sigma}^2 + 4(T_{pd\sigma}^{(0)})^2}\Big]$ —this is the CCO ground on the single plaquette,
2. $|\psi_+\rangle = -\sin\psi|x^2-y^2\rangle + \cos\psi|A\sigma\rangle$ with energy $E_{\psi_+} = \frac{1}{2}\Big[\varepsilon_{A\sigma} + \sqrt{\varepsilon_{A\sigma}^2 + 4(T_{pd\sigma}^{(0)})^2}\Big]$ —this is the charge transfer–like excitation on the single plaquette,
3. $|\phi_-\rangle = \cos\phi|xy\rangle + \sin\phi|B\pi\rangle$ with energy $E_{\phi_-} = \frac{1}{2}\Big[\varepsilon_{xy} + \varepsilon_{B\pi} - \sqrt{(\varepsilon_{B\pi}-\varepsilon_{xy})^2 + 4(T_{pd\pi}^{(0)})^2}\Big]$ —this is the xy orbital excitation on the single plaquette (its energy is the one that is observed by RIXS),
4. $|\phi_+\rangle = -\sin\phi|xy\rangle + \cos\phi|B\pi\rangle$ with energy $E_{\phi_+} = \frac{1}{2}\Big[\varepsilon_{xy}+\varepsilon_{B\pi} + \sqrt{(\varepsilon_{B\pi}-\varepsilon_{xy})^2 + 4(T_{pd\pi}^{(0)})^2}\Big]$ —this is the charge transfer–like excitation of the xy character on the single plaquette.

The angles ϕ and ψ can be calculated from the following formulae:

$$\tan(2\psi) = -\frac{2T_{pd\sigma}^{(0)}}{\varepsilon_{A\sigma}}, \quad \tan(2\phi) = -\frac{2T_{pd\phi}^{(0)}}{\varepsilon_{B\pi}-\varepsilon_{xy}}. \tag{A.7}$$

We assume that the *two-particle* cell perturbation theory basis consists of just one state [the other states are not of relevant for the considered (in the next section) exchange of the xy orbital excitation, i.e. $|\phi_-\rangle$]:

$$|\text{INT}\rangle \equiv |\phi_-\rangle|\psi_-\rangle, \tag{A.8}$$

since all other states will have a much higher excitation energy. We can estimate its energy by including contributions from $\mathcal{H}_{\text{kin}}^{(0)}$ and $\mathcal{H}_{\text{coul}}$:

$$E_{\text{INT}} = E_{\psi_-} + E_{\phi_-} + U_{\text{eff}} \approx E_{\psi_-} + E_{\phi_-} + \cos^2\psi\cos^2\phi(U_{\text{eff}}), \tag{A.9}$$

where the last (approximate) equation follows from the fact that U_{eff} is only paid by electrons charge located in the copper orbitals ($\cos^2\psi\cos^2\phi$) and that we define the Hubbard repulsion U_{eff} to be:

$$U_{\text{eff}} = U - 3J_H \tag{A.10}$$

for the NNN orbital exchange (the NNN spins are parallel in the AFM ordered state) and

$$U_{\text{eff}} = U - 2J_H \tag{A.11}$$

for the NN orbital exchange (since the NN spins are antiparallel in the AFM ordered state).

A.4. Next-nearest neighbor orbital superexchange in the cell perturbation theory

Having obtained the proper cell perturbation theory basis, we can now derive the next-nearest neighbor (NNN) orbital superexchange. We use 2$^{\text{nd}}$ order perturbation theory and assume that the initial state is

$$|\text{I}\rangle = |\phi_{-,I}\rangle|\psi_{-,II}\rangle, \tag{A.12}$$

the intermediate is

$$|\text{INT}\rangle = |\text{VAC}_I\rangle|\phi_{-,II}\rangle|\psi_{-,II}\rangle, \tag{A.13}$$

and the final state is

$$|\text{F}\rangle = |\psi_{-,I}\rangle|\phi_{-,II}\rangle, \tag{A.14}$$

where the indices I and II denote the two distinct NNN sites. We obtain:

$$\begin{aligned}
J_{\text{NNN}}^{\text{orb}} &= -4\frac{\langle\text{F}|\mathcal{H}_{\text{kin}}^{(\sqrt{2})}|\text{INT}\rangle\langle\text{INT}|\mathcal{H}_{\text{kin}}^{(\sqrt{2})}|\text{I}\rangle}{E_{\text{INT}} - E_{\text{I}}} = \\
&- 4\frac{\langle\phi_{-,\text{II}}|\langle\psi_{-,\text{I}}|\mathcal{H}_{\text{kin}}^{(\sqrt{2})}|\text{INT}\rangle\langle\text{INT}|\mathcal{H}_{\text{kin}}^{(\sqrt{2})}|\phi_{-,I}\rangle|\psi_{-,II}\rangle}{\cos^2\psi\cos^2\phi(U-3J_H)} = \\
&= 4\frac{\langle\psi_{-,\text{I}}|\mathcal{H}_{\text{kin}}^{(\sqrt{2})}|\psi_{-,II}\rangle\langle\phi_{-,\text{II}}|\mathcal{H}_{\text{kin}}^{(\sqrt{2})}|\phi_{-,I}\rangle}{\cos^2\psi\cos^2\phi(U-3J_H)} = 4\frac{\sin^2\psi T_{A\sigma}^{(\sqrt{2})}\sin^2\phi T_{B\pi}^{(\sqrt{2})}}{\cos^2\psi\cos^2\phi(U-3J_H)} \\
&= -\frac{16\nu(\sqrt{2})^2 t_{pp}^2\sin^2\psi\sin^2\phi}{\cos^2\psi\cos^2\phi(U-3J_H)}.
\end{aligned}$$

This orbiton exchange 'around the corner' is allowed by the finite t_{pp}, which leads to the formation of the bonding (B) and antibonding (A) states of the π and σ orbitals and then their hybridisation on the NNN plaquettes. Besides, the factor four in the formula arises since: (i) there is another superexchange process with the doubly occupied site I in the intermediate state ($|\mathrm{INT}\rangle = |\phi_{-,I}\rangle|\psi_{-,I}\rangle|\mathrm{VAC}_{II}\rangle$) which accounts for a factor of two and (ii) the superexchange constant is implicitly multiplying the orbital pseudospin raising and lowering with a prefactor of 1/2 (hence another factor of two).

The NNN orbital superexchange turns out to be always negative. Moreover, for the realistic parameters of the CT model for $CaCuO_2$ given in Table A.1, we get

$$J^{\mathrm{orb}}_{\mathrm{NNN}} \approx -0.015 \text{ eV}. \tag{A.15}$$

Note that from the above expression for the NNN orbital exchange we can easily extract the NNN hoppings of the ground state $|\psi_-\rangle$

$$t'_a = -2\nu(\sqrt{2})\sin(\psi)^2 t_{pp} \approx -0.072 \text{ eV}, \tag{A.16}$$

and excited orbital $|\phi_-\rangle$

$$t'_b = 2\nu(\sqrt{2})\sin(\phi)^2 t_{pp} \approx 0.078 \text{ eV}. \tag{A.17}$$

Note that in the simplified approach presented in the main text of the paper the t'_a and t'_b hoppings are depicted in the cartoon Fig. 3.

A.5. Nearest neighbor orbital superexchange in the cell perturbation theory

A similar (though a bit more lengthy) derivation as in the previous section above gives also the nearest-neighbour (NN) orbiton superexchange:

$$J^{\mathrm{orb}}_{\mathrm{NN}} = -4\frac{\langle \mathrm{F}|\mathcal{H}^{(1)}_{\mathrm{kin}}|\mathrm{INT}\rangle\langle \mathrm{INT}|\mathcal{H}^{(1)}_{\mathrm{kin}}|\mathrm{I}\rangle}{E_{\mathrm{INT}} - E_{\mathrm{I}}} =$$
$$= \frac{16[-\nu(1)\sin^2\psi\ t_{pp} + \mu(1)\sin\psi\ t_{pd\sigma}][\nu(1)\sin^2\phi\ t_{pp} - \mu(1)\sin 2\phi\ t_{pd\pi}]}{\cos^2\psi\cos^2\phi(U - 2J_H)}.$$

Interestingly, this exchange is *negative* for realistic parameters of the charge transfer model of CCO in Table A.1—in this case we obtain

$$J^{\mathrm{orb}}_{\mathrm{NN}} \approx 0.022 \text{ eV}. \tag{A.18}$$

The fact that it is positive is important, since this means that the small, but effectively free orbiton motion originating from the NN orbital exchange *and* finite Hund's exchange, can lead to the dispersion relation along the 'downwards' direction (i.e. opposite as the fully free NNN orbiton exchange).

Note that (just as in the previous section) from the above expression for the NN orbital exchange we can easily extract the NN hoppings of the ground state $|\psi_-\rangle$

$$t_a = 2[-\nu(1)\sin(\psi)^2\ t_{pp} + 2\mu(1)\sin\psi\cos\psi\ t_{pd\sigma}] \approx 0.52\ \text{eV}, \tag{A.19}$$

and excited orbital $|\phi_-\rangle$

$$t_b = 2[\nu(1)\sin(\phi)^2\ t_{pp} - 2\mu(1)\sin\phi\cos\phi\ t_{pd\pi}] \approx 0.020\ \text{eV}. \tag{A.20}$$

Acknowledgments

During my PhD, I had the opportunity to know and collaborate with a lot of amazing people.

First, I will express my gratitude to Prof. Ghiringhelli, Giacomo. During my student years, I developed my passion for condensed matter physics attending his lectures. During my PhD, in the last four years, he has been my main source of inspiration. He has been a mentor, and a friend. Carrying out the PhD in his group has been an amazing opportunity for me: I studied fascinating physics, met amazing people, and saw wonderful places. Difficult to ask for more.

I want then to thank Prof. Lucio Braicovich, Lucio. For his stubbornness, creativity, intuition, and for the huge amount of experience that he shared with me and with all of us. His profound and unconditioned love for physics and experimental research has been and will continue to be a constant driving force for me. Whenever something does not work at the beamline at 2 am in the night, he will be there to sort things out.

Thanks to Prof. Moretti, Marco. He is one of the most competent and smart persons I have ever met. But Marco has been, at the same time, a very dear friend. I will never forget all the little breaks from work we enjoyed, when I would just bump into his office to talk about anything. But mostly phy(si)cs, of course.

Thanks to Dr. Arpaia, Riccardo, with whom I spent my first beamtime. Thanks for all the night shifts together (watching cooking videos of Giorgione), for all the discussions about physics, and for transmitting me the value of hard work.

Thanks Prof. Puppin, Ezio. During my years as a Master student and my first year as a Ph.D. I had the opportunity to attend his beautiful lectures, and I enjoyed all of them. After a few lunches together, I was able to realize that there was more: he is one of the most funny, witty and good hearted persons I have ever met. Thank you for all the laughs we shared, and for always lighting the fourth flour of the Department.

I want to thank Dr. Nicholas Brookes, Nick, for hosting me and mentoring me during the wonderful year I spent at the ID32 beamline of the ESRF.

Thanks also to all the other staff of the beamline: Kurt, Flora, and Thomas, for always making me feel welcome. I will remember my year in Grenoble forever.

Thanks to Paolo, with whom I have shared the office and the difficulties of the PhD life. It has been a pleasure to correct the madness written by M.M. and to keep an eye on F.T. and his goddamn cellphone.
Thanks to Piero, who I met just 1.5 year ago but has already become one of my dearest friends. You are truly a wonderful person. Thanks to Giacomo (M.), for all the beamtimes and the discussions on physics, for the beers and the laughs, but also for introducing me to that infernal abyss that is *La Zanzara*. MOLTO grave.
Thanks to Serena and all the merende at the coffee machines. Thanks to Cioccoriso© for all the wonderful moments together. Thanks to all the other present and past member of the group, Matteo, Francesco, Marcello, for sharing a part of their adventure in this group with me.

Thanks to Roberto, Davide and Filippo, for brightening even the dark months of Covid at ID32.

Thanks Prof. Marco Salluzzo, Daniele, and Guillaume for all the *topotattìc* together.

Thanks to Armando, Michelangelo, Julia, Octave, Antonella, Elif for the amazing weeks in Les Houches.

I would then like to thank all the people with whom I had the pleasure to collaborate during my PhD project: Tom Devereaux and Krzysztof Wohlfeld (also for the nice beer in front of the Pacific Ocean), Daniele Di Castro, Enrico Schierle, Wei-Sheng Lee, Daniel Jost, Floriana Lombardi, Jonathan Pelliciari.

Thanks to Gabriele, Alessandro, Andrea (x3), Ettore, Luca, the friends of a life.

Thanks to my parents, Luana and Gianni. You have always supported me, and you have shaped the person I am today.

And finally, thanks to you, Charlotte.
No page would be long enough to harbour all the things I want to write you, and you deserve. But at the same time, no words are really needed between us. And probably they never were.
This thesis is dedicated to you.

Bibliography

[1] J. G. Bednorz and K. A. Mueller, "Possible high-t_c superconductivity in the ba$_2$la$_2$cu$_3$o system," Zeitschrift fuer Physik B Condensed Matter **64**, 189–193 (1986).

[2] P. Dai, B. Chakoumakos, G. Sun, K. Wong, Y. Xin, and D. Lu, "Synthesis and neutron powder diffraction study of the superconductor $HgBa_2Ca_2Cu_3O_{8+\delta}$ by Tl substitution," Physica C: Superconductivity **243**, 201–206 (1995).

[3] A. Fujimori and F. Minami, "Valence-band photoemission and optical absorption in nickel compounds," Phys. Rev. B **30**, 957–971 (1984).

[4] G. A. Sawatzky and J. W. Allen, "Magnitude and origin of the band gap in nio," Phys. Rev. Lett. **53**, 2339–2342 (1984).

[5] P. W. Anderson, "New approach to the theory of superexchange interactions," Phys. Rev. **115**, 2–13 (1959).

[6] M. M. Sala, V. Bisogni, C. Aruta, G. Balestrino, H. Berger, N. Brookes, G. De Luca, D. Di Castro, M. Grioni, M. Guarise, *et al.*, "Energy and symmetry of dd excitations in undoped layered cuprates measured by Cu L3 resonant inelastic x-ray scattering," New Journal of Physics **13**, 043026 (2011).

[7] N. Barišić and D. K. Sunko, "High-T_c Cuprates: a Story of Two Electronic Subsystems," Journal of Superconductivity and Novel Magnetism , 1–19 (2022).

[8] B. Keimer, S. A. Kivelson, M. R. Norman, S. Uchida, and J. Zaanen, "From quantum matter to high-temperature superconductivity in copper oxides," Nature **518**, 179–186 (2015).

[9] C. Weber, C. Yee, K. Haule, and G. Kotliar, "Scaling of the transition temperature of hole-doped cuprate superconductors with the charge-transfer energy," Europhysics Letters **100**, 37001 (2012).

[10] A. Damascelli, Z. Hussain, and Z.-X. Shen, "Angle-resolved photoe-

mission studies of the cuprate superconductors," Rev. Mod. Phys. **75**, 473–541 (2003).

[11] M. Yoshida, S. Tajima, N. Koshizuka, S. Tanaka, S. Uchida, and T. Itoh, "Two-magnon and two-phonon excitations in some parent insulating compounds of the high-t_c cuprates," Phys. Rev. B **46**, 6505–6510 (1992).

[12] D. Kan, A. Yamanaka, T. Terashima, and M. Takano, "Preparation and optical properties of single-crystalline cacuo2 thin films with infinite layer structure," Physica C: Superconductivity **412-414**, 298–302 (2004), proceedings of the 16th International Symposium on Superconductivity (ISS 2003). Advances in Superconductivity XVI. Part I.

[13] P. W. Anderson, "The resonating valence bond state in La_2CuO_4 and superconductivity," Science **235**, 1196–1198 (1987).

[14] D. J. Scalapino, "A common thread: The pairing interaction for unconventional superconductors," Rev. Mod. Phys. **84**, 1383–1417 (2012).

[15] J. R. Schrieffer and J. S. Brooks, *Handbook of high-temperature superconductivity: theory and experiment* (Springer, 2007).

[16] Y. S. Lee, R. J. Birgeneau, M. A. Kastner, Y. Endoh, S. Wakimoto, K. Yamada, R. W. Erwin, S.-H. Lee, and G. Shirane, "Neutron-scattering study of spin-density wave order in the superconducting state of excess-oxygen-doped La_2CuO_{4+y}," Phys. Rev. B **60**, 3643–3654 (1999).

[17] R. Coldea, S. M. Hayden, G. Aeppli, T. G. Perring, C. D. Frost, T. E. Mason, S.-W. Cheong, and Z. Fisk, "Spin waves and electronic interactions in La_2CuO_4," Phys. Rev. Lett. **86**, 5377–5380 (2001).

[18] N. S. Headings, S. M. Hayden, R. Coldea, and T. G. Perring, "Anomalous high-energy spin excitations in the high-T_c superconductor-parent antiferromagnet La_2CuO_4," Phys. Rev. Lett. **105**, 247001 (2010).

[19] B. Keimer, N. Belk, R. J. Birgeneau, A. Cassanho, C. Y. Chen, M. Greven, M. A. Kastner, A. Aharony, Y. Endoh, R. W. Erwin, and G. Shirane, "Magnetic excitations in pure, lightly doped, and weakly metallic la_2cuo_4," Phys. Rev. B **46**, 14034–14053 (1992).

[20] P. Bourges, Y. Sidis, H. F. Fong, L. P. Regnault, J. Bossy, A. Ivanov, and B. Keimer, "The Spin Excitation Spectrum in Superconducting $YBa_2Cu_3O_{6.85}$," Science **288**, 1234–1237 (2000), https://www.science.org/doi/pdf/10.1126/science.288.5469.1234 .

[21] L. Braicovich, L. Ament, V. Bisogni, F. Forte, C. Aruta, G. Balestrino, N. Brookes, G. De Luca, P. Medaglia, F. M. Granozio, *et al.*, "Disper-

sion of magnetic excitations in the cuprate La_2CuO_4 and $CaCuO_2$ compounds measured using resonant x-ray scattering," Phys. Rev. Lett. **102**, 167401 (2009).

[22] M. Minola, G. Dellea, H. Gretarsson, Y. Y. Peng, Y. Lu, J. Porras, T. Loew, F. Yakhou, N. B. Brookes, Y. B. Huang, J. Pelliciari, T. Schmitt, G. Ghiringhelli, B. Keimer, L. Braicovich, and M. Le Tacon, "Collective nature of spin excitations in superconducting cuprates probed by resonant inelastic x-ray scattering," Phys. Rev. Lett. **114**, 217003 (2015).

[23] Y. Peng, G. Dellea, M. Minola, M. Conni, A. Amorese, D. Di Castro, G. De Luca, K. Kummer, M. Salluzzo, X. Sun, *et al.*, "Influence of apical oxygen on the extent of in-plane exchange interaction in cuprate superconductors," Nat. Phys. **13**, 1201–1206 (2017).

[24] Y. Y. Peng, E. W. Huang, R. Fumagalli, M. Minola, Y. Wang, X. Sun, Y. Ding, K. Kummer, X. J. Zhou, N. B. Brookes, B. Moritz, L. Braicovich, T. P. Devereaux, and G. Ghiringhelli, "Dispersion, damping, and intensity of spin excitations in the monolayer $(Bi,Pb)_2(Sr,La)_2CuO_{6+\delta}$ cuprate superconductor family," Phys. Rev. B **98**, 144507 (2018).

[25] D. I. Khomskii, *Transition Metal Compounds* (Cambridge University Press, 2014).

[26] J.-Y. P. Delannoy, M. J. P. Gingras, P. C. W. Holdsworth, and A.-M. S. Tremblay, "Low-energy theory of the t- t′ t"- U Hubbard model at half-filling: Interaction strengths in cuprate superconductors and an effective spin-only description of La_2CuO_4," Phys. Rev. B **79**, 235130 (2009).

[27] A. W. Sandvik, "Computational studies of quantum spin systems," in *AIP Conference Proceedings*, Vol. 1297 (American Institute of Physics, 2010) pp. 135–338.

[28] K. Wohlfeld, M. Daghofer, S. Nishimoto, G. Khaliullin, and J. van den Brink, "Intrinsic coupling of orbital excitations to spin fluctuations in mott insulators," Phys. Rev. Lett. **107**, 147201 (2011).

[29] J. B. Goodenough, *Magnetism and the chemical bond*, Vol. 1 (Interscience publishers, 1963).

[30] J. van den Brink, P. Horsch, F. Mack, and A. M. Oleś, "Orbital dynamics in ferromagnetic transition-metal oxides," Phys. Rev. B **59**, 6795–6805 (1999).

[31] D. I. Khomskii and S. V. Streltsov, "Orbital effects in

solids: Basics, recent progress, and opportunities," Chemical Reviews **121**, 2992–3030 (2021), pMID: 33314912, https://doi.org/10.1021/acs.chemrev.0c00579 .

[32] J. Nasu and S. Ishihara, "Vibronic excitation dynamics in orbitally degenerate correlated electron system," Phys. Rev. B **88**, 205110 (2013).

[33] J. Li, L. Xu, M. Garcia-Fernandez, A. Nag, H. C. Robarts, A. C. Walters, X. Liu, J. Zhou, K. Wohlfeld, J. van den Brink, H. Ding, and K.-J. Zhou, "Unraveling the orbital physics in a canonical orbital system kcuf$_3$," Phys. Rev. Lett. **126**, 106401 (2021).

[34] K. Wohlfeld, M. Daghofer, G. Khaliullin, and J. van den Brink, "Dispersion of orbital excitations in 2d quantum antiferromagnets," Journal of Physics: Conference Series **391**, 012168 (2012).

[35] J. Schlappa, K. Wohlfeld, K. Zhou, M. Mourigal, M. Haverkort, V. Strocov, L. Hozoi, C. Monney, S. Nishimoto, S. Singh, *et al.*, "Spin–orbital separation in the quasi-one-dimensional Mott insulator Sr_2CuO_3," Nature **485**, 82–85 (2012).

[36] V. Bisogni, K. Wohlfeld, S. Nishimoto, C. Monney, J. Trinckauf, K. Zhou, R. Kraus, K. Koepernik, C. Sekar, V. Strocov, B. Büchner, T. Schmitt, J. van den Brink, and J. Geck, "Orbital Control of Effective Dimensionality: From Spin-Orbital Fractionalization to Confinement in the Anisotropic Ladder System $CaCu_2O_3$," Phys. Rev. Lett. **114**, 096402 (2015).

[37] R. Fumagalli, J. Heverhagen, D. Betto, R. Arpaia, M. Rossi, D. Di Castro, N. B. Brookes, M. Moretti Sala, M. Daghofer, L. Braicovich, K. Wohlfeld, and G. Ghiringhelli, "Mobile orbitons in Ca_2CuO_3: Crucial role of Hund's exchange," Phys. Rev. B **101**, 205117 (2020).

[38] G. Merzoni, "Temperature dependence of charge excitations in rixs spectra of superconducting cuprates," (2021).

[39] F. C. Zhang and T. M. Rice, "Effective hamiltonian for the superconducting Cu oxides," Phys. Rev. B **37**, 3759–3761 (1988).

[40] N. B. Brookes, G. Ghiringhelli, O. Tjernberg, L. H. Tjeng, T. Mizokawa, T. W. Li, and A. A. Menovsky, "Detection of zhang-rice singlets using spin-polarized photoemission," Phys. Rev. Lett. **87**, 237003 (2001).

[41] H. Bruus and K. Flensberg, *Many-body quantum theory in condensed matter physics: an introduction* (OUP Oxford, 2004).

[42] C. G. Olson, R. Liu, A.-B. Yang, D. W. Lynch, A. J. Arko, R. S. List, B. W. Veal, Y. C. Chang, P. Z. Jiang, and A. P. Paulikas,

"Superconducting Gap in Bi-Sr-Ca-Cu-O by High-Resolution Angle-Resolved Photoelectron Spectroscopy," Science **245**, 731–733 (1989), https://www.science.org/doi/pdf/10.1126/science.245.4919.731 .

[43] Z.-X. Shen, D. S. Dessau, B. O. Wells, D. M. King, W. E. Spicer, A. J. Arko, D. Marshall, L. W. Lombardo, A. Kapitulnik, P. Dickinson, S. Doniach, J. DiCarlo, T. Loeser, and C. H. Park, "Anomalously large gap anisotropy in the a-b plane of $Bi_2Sr_2CaCu_2O_{8+\delta}$," Phys. Rev. Lett. **70**, 1553–1556 (1993).

[44] L. Wang, G. He, Z. Yang, M. Garcia-Fernandez, A. Nag, K. Zhou, M. Minola, M. L. Tacon, B. Keimer, Y. Peng, and Y. Li, "Paramagnons and high-temperature superconductivity in a model family of cuprates," Nature Communications **13**, 3163 (2022).

[45] H.-C. Jiang and T. P. Devereaux, "Superconductivity in the doped Hubbard model and its interplay with next-nearest hopping t'," Science **365**, 1424–1428 (2019), https://www.science.org/doi/pdf/10.1126/science.aal5304 .

[46] S. Johnston, F. Vernay, B. Moritz, Z.-X. Shen, N. Nagaosa, J. Zaanen, and T. P. Devereaux, "Systematic study of electron-phonon coupling to oxygen modes across the cuprates," Phys. Rev. B **82**, 064513 (2010).

[47] Y. He, M. Hashimoto, D. Song, S.-D. Chen, J. He, I. M. Vishik, B. Moritz, D.-H. Lee, N. Nagaosa, J. Zaanen, T. P. Devereaux, Y. Yoshida, H. Eisaki, D. H. Lu, and Z.-X. Shen, "Rapid change of superconductivity and electron-phonon coupling through critical doping in Bi-2212," Science **362**, 62–65 (2018).

[48] W.-S. Lee, I. Vishik, K. Tanaka, D. Lu, T. Sasagawa, N. Nagaosa, T. Devereaux, Z. Hussain, and Z.-X. Shen, "Abrupt onset of a second energy gap at the superconducting transition of underdoped bi2212," Nature **450**, 81–84 (2007).

[49] N. Doiron-Leyraud, C. Proust, D. LeBoeuf, J. Levallois, J.-B. Bonnemaison, R. Liang, D. A. Bonn, W. N. Hardy, and L. Taillefer, "Quantum oscillations and the fermi surface in an underdoped high-tc superconductor," Nature **447**, 565–568 (2007).

[50] S.-D. Chen, M. Hashimoto, Y. He, D. Song, K.-J. Xu, J.-F. He, T. P. Devereaux, H. Eisaki, D.-H. Lu, J. Zaanen, and Z.-X. Shen, "Incoherent strange metal sharply bounded by a critical doping in Bi2212," Science **366**, 1099–1102 (2019), https://www.science.org/doi/pdf/10.1126/science.aaw8850 .

[51] H. Alloul, T. Ohno, and P. Mendels, "^{89}Y nmr evidence for a fermi-liquid behavior in $yba_2cu_3o_{6+x}$," Phys. Rev. Lett. **63**, 1700–1703 (1989).

[52] N. Barišić, M. K. Chan, Y. Li, G. Yu, X. Zhao, M. Dressel, A. Smontara, and M. Greven, "Universal sheet resistance and revised phase diagram of the cuprate high-temperature superconductors," Proceedings of the National Academy of Sciences **110**, 12235–12240 (2013), https://www.pnas.org/doi/pdf/10.1073/pnas.1301989110 .

[53] S. Badoux, W. Tabis, F. Laliberté, G. Grissonnanche, B. Vignolle, D. Vignolles, J. Béard, D. Bonn, W. Hardy, R. Liang, *et al.*, "Change of carrier density at the pseudogap critical point of a cuprate superconductor," Nature **531**, 210–214 (2016).

[54] R. Arpaia, L. Martinelli, M. M. Sala, S. Caprara, A. Nag, N. B. Brookes, P. Camisa, Q. Li, Q. Gao, X. Zhou, *et al.*, "Signature of quantum criticality in cuprates by charge density fluctuations," arXiv preprint arXiv:2208.13918 (2022).

[55] M. Culo, C. Duffy, J. Ayres, M. Berben, Y.-T. Hsu, R. D. H. Hinlopen, B. Bernath, and N. E. Hussey, "Possible superconductivity from incoherent carriers in overdoped cuprates," SciPost Phys. **11**, 012 (2021).

[56] E. Wahlberg, R. Arpaia, G. Seibold, M. Rossi, R. Fumagalli, E. Trabaldo, N. B. Brookes, L. Braicovich, S. Caprara, U. Gran, *et al.*, "Restored strange metal phase through suppression of charge density waves in underdoped $yba_2cu_3o_{7-\delta}$," Science **373**, 1506–1510 (2021).

[57] P. W. Phillips, N. E. Hussey, and P. Abbamonte, "Stranger than metals," Science **377**, eabh4273 (2022), https://www.science.org/doi/pdf/10.1126/science.abh4273 .

[58] J. Zaanen, "Why the temperature is high," Nature **430**, 512–513 (2004).

[59] J. Zaanen, "Lectures on quantum supreme matter," arXiv preprint arXiv:2110.00961 (2021).

[60] J. E. Hoffman, E. W. Hudson, K. M. Lang, V. Madhavan, H. Eisaki, S. Uchida, and J. C. Davis, "A Four Unit Cell Periodic Pattern of Quasi-Particle States Surrounding Vortex Cores in $Bi_2Sr_2CaCu_2O_{8+\delta}$," Science **295**, 466–469 (2002), https://www.science.org/doi/pdf/10.1126/science.1066974 .

[61] J. M. Tranquada, G. Shirane, B. Keimer, S. Shamoto, and M. Sato, "Neutron scattering study of magnetic excitations in $YBa_2Cu_3O_{6+x}$," Phys. Rev. B **40**, 4503–4516 (1989).

[62] S. Blanco-Canosa, A. Frano, E. Schierle, J. Porras, T. Loew, M. Minola, M. Bluschke, E. Weschke, B. Keimer, and M. Le Tacon, "Res-

onant x-ray scattering study of charge-density wave correlations in $YBa_2Cu_3O_{6+x}$," Phys. Rev. B **90**, 054513 (2014).

[63] R. Comin and A. Damascelli, "Resonant x-ray scattering studies of charge order in cuprates," Annual Review of Condensed Matter Physics **7**, 369–405 (2016), https://doi.org/10.1146/annurev-conmatphys-031115-011401 .

[64] M. Le Tacon, G. Ghiringhelli, J. Chaloupka, M. M. Sala, V. Hinkov, M. W. Haverkort, M. Minola, M. Bakr, K. J. Zhou, S. Blanco-Canosa, C. Monney, Y. T. Song, G. L. Sun, C. T. Lin, G. M. De Luca, M. Salluzzo, G. Khaliullin, T. Schmitt, L. Braicovich, and B. Keimer, "Intense paramagnon excitations in a large family of high-temperature superconductors," Nature Physics **7**, 725–730 (2011).

[65] t. . M. Jiemin Li and Abhishek Nag and Jonathan Pelliciari and Hannah Robarts and Andrew Walters and Mirian Garcia-Fernandez and Hiroshi Eisaki and Dongjoon Song and Hong Ding and Steven Johnston and Riccardo Comin and Ke-Jin Zhou , Proceedings of the National Academy of Sciences **117**, 16219–16225 (2020), https://www.pnas.org/doi/pdf/10.1073/pnas.2001755117 .

[66] R. Comin, A. Frano, M. M. Yee, Y. Yoshida, H. Eisaki, E. Schierle, E. Weschke, R. Sutarto, F. He, A. Soumyanarayanan, Y. He, M. L. Tacon, I. S. Elfimov, J. E. Hoffman, G. A. Sawatzky, B. Keimer, and A. Damascelli, "Charge Order Driven by Fermi-Arc Instability in $Bi_2Sr_{2-x}La_xCuO_{6+\delta}$," Science **343**, 390–392 (2014), https://www.science.org/doi/pdf/10.1126/science.1242996 .

[67] V. Marino, F. Becca, and L. F. Tocchio, "Stripes in the extended $t-t'$ Hubbard model: A Variational Monte Carlo analysis," SciPost Phys. **12**, 180 (2022).

[68] M. Daghofer, K. Wohlfeld, A. M. Oleś, E. Arrigoni, and P. Horsch, "Absence of hole confinement in transition-metal oxides with orbital degeneracy," Phys. Rev. Lett. **100**, 066403 (2008).

[69] C. J. Jia, E. A. Nowadnick, K. Wohlfeld, Y. F. Kung, C.-C. Chen, S. Johnston, T. Tohyama, B. Moritz, and T. P. Devereaux, "Persistent spin excitations in doped antiferromagnets revealed by resonant inelastic light scattering," Nature Communications **5**, 3314 (2014).

[70] J. Pelliciari, S. Karakuzu, Q. Song, R. Arpaia, A. Nag, M. Rossi, J. Li, T. Yu, X. Chen, R. Peng, M. García-Fernández, A. C. Walters, Q. Wang, J. Zhao, G. Ghiringhelli, D. Feng, T. A. Maier, K.-J. Zhou, S. Johnston, and R. Comin, "Evolution of spin excitations from bulk to monolayer fese," Nature Communications **12**, 3122 (2021).

[71] L. J. P. Ament, M. van Veenendaal, T. P. Devereaux, J. P. Hill, and J. van den Brink, "Resonant inelastic x-ray scattering studies of elementary excitations," Rev. Mod. Phys. **83**, 705–767 (2011).

[72] M. O. Krause and J. Oliver, "Natural widths of atomic k and l levels, k α x-ray lines and several kll auger lines," Journal of Physical and Chemical Reference Data **8**, 329–338 (1979).

[73] A. Revelli, M. M. Sala, G. Monaco, P. Becker, L. Bohatý, M. Hermanns, T. C. Koethe, T. Fröhlich, P. Warzanowski, T. Lorenz, S. V. Streltsov, P. H. M. van Loosdrecht, D. I. Khomskii, J. van den Brink, and M. Grüninger, "Resonant inelastic x-ray incarnation of young's double-slit experiment," Science Advances **5**, eaav4020 (2019), https://www.science.org/doi/pdf/10.1126/sciadv.aav4020 .

[74] M. Hepting, L. Chaix, E. W. Huang, R. Fumagalli, Y. Y. Peng, B. Moritz, K. Kummer, N. B. Brookes, W. C. Lee, M. Hashimoto, T. Sarkar, J.-F. He, C. R. Rotundu, Y. S. Lee, R. L. Greene, L. Braicovich, G. Ghiringhelli, Z. X. Shen, T. P. Devereaux, and W. S. Lee, "Three-dimensional collective charge excitations in electron-doped copper oxide superconductors," Nature **563**, 374–378 (2018).

[75] A. Geondzhian and K. Gilmore, "Generalization of the franck-condon model for phonon excitations by resonant inelastic x-ray scattering," Phys. Rev. B **101**, 214307 (2020).

[76] J. G. Vale, C. D. Dashwood, E. Paris, L. S. I. Veiga, M. Garcia-Fernandez, A. Nag, A. Walters, K.-J. Zhou, I.-M. Pietsch, A. Jesche, P. Gegenwart, R. Coldea, T. Schmitt, and D. F. McMorrow, "High-resolution resonant inelastic x-ray scattering study of the electron-phonon coupling in honeycomb $\alpha-Li_2IrO_3$," Phys. Rev. B **100**, 224303 (2019).

[77] D. G. Hawthorn, K. M. Shen, J. Geck, D. C. Peets, H. Wadati, J. Okamoto, S.-W. Huang, D. J. Huang, H.-J. Lin, J. D. Denlinger, R. Liang, D. A. Bonn, W. N. Hardy, and G. A. Sawatzky, "Resonant elastic soft x-ray scattering in oxygen-ordered $YBa_2Cu_3O_{6+\delta}$," Phys. Rev. B **84**, 075125 (2011).

[78] L. Braicovich, M. Rossi, R. Fumagalli, Y. Peng, Y. Wang, R. Arpaia, D. Betto, G. M. De Luca, D. Di Castro, K. Kummer, M. Moretti Sala, M. Pagetti, G. Balestrino, N. B. Brookes, M. Salluzzo, S. Johnston, J. van den Brink, and G. Ghiringhelli, "Determining the electron-phonon coupling in superconducting cuprates by resonant inelastic x-ray scattering: Methods and results on $Nd_{1+x}Ba_{2-x}Cu_3O_{7-\delta}$," Phys. Rev. Res. **2**, 023231 (2020).

[79] P. F. Williams, D. L. Rousseau, and S. H. Dworetsky, "Resonance fluorescence and resonance raman scattering: Lifetimes in molecular iodine," Phys. Rev. Lett. **32**, 196–199 (1974).

[80] J. Kim, D. Casa, M. H. Upton, T. Gog, Y.-J. Kim, J. F. Mitchell, M. van Veenendaal, M. Daghofer, J. van den Brink, G. Khaliullin, and B. J. Kim, "Magnetic Excitation Spectra of Sr_2IrO_4 Probed by Resonant Inelastic X-Ray Scattering: Establishing Links to Cuprate Superconductors," Phys. Rev. Lett. **108**, 177003 (2012).

[81] J. Kim, M. Daghofer, A. H. Said, T. Gog, J. van den Brink, G. Khaliullin, and B. J. Kim, "Excitonic quasiparticles in a spin–orbit Mott insulator," Nature Communications **5**, 4453 (2014).

[82] A. Geondzhian, A. Sambri, G. M. De Luca, R. Di Capua, E. Di Gennaro, D. Betto, M. Rossi, Y. Y. Peng, R. Fumagalli, N. B. Brookes, L. Braicovich, K. Gilmore, G. Ghiringhelli, and M. Salluzzo, "Large polarons as key quasiparticles in $srtio_3$ and $srtio_3$-based heterostructures," Phys. Rev. Lett. **125**, 126401 (2020).

[83] G. Ghiringhelli, A. Piazzalunga, C. Dallera, G. Trezzi, L. Braicovich, T. Schmitt, V. N. Strocov, R. Betemps, L. Patthey, X. Wang, and M. Grioni, "Saxes, a high resolution spectrometer for resonant x-ray emission in the 400–1600ev energy range," Review of Scientific Instruments **77**, 113108 (2006).

[84] M. van Veenendaal, "Polarization dependence of l- and m-edge resonant inelastic x-ray scattering in transition-metal compounds," Phys. Rev. Lett. **96**, 117404 (2006).

[85] M. W. Haverkort, "Theory of resonant inelastic x-ray scattering by collective magnetic excitations," Phys. Rev. Lett. **105**, 167404 (2010).

[86] D. Vaknin, S. K. Sinha, D. E. Moncton, D. C. Johnston, J. M. Newsam, C. R. Safinya, and H. E. King, "Antiferromagnetism in la_2cuo_{4-y}," Phys. Rev. Lett. **58**, 2802–2805 (1987).

[87] D. Vaknin, E. Caignol, P. K. Davies, J. E. Fischer, D. C. Johnston, and D. P. Goshorn, "Antiferromagnetism in $(Ca_{0.85}Sr_{0.15})CuO_2$, the parent of the cuprate family of superconducting compounds," Phys. Rev. B **39**, 9122–9125 (1989).

[88] S. Skanthakumar, H. Zhang, T. Clinton, W.-H. Li, J. Lynn, Z. Fisk, and S.-W. Cheong, "Magnetic phase transitions and structural distortion in nd2cuo4," Physica C: Superconductivity **160**, 124–128 (1989).

[89] H. Elnaggar, A. Nag, M. W. Haverkort, K.-j. Zhou, and F. de Groot,

"Novel magnetic excitations beyond the single- and double-magnons," arXiv:2208.03198 [cond-mat] (2022).

[90] N. B. Brookes, F. Yakhou-Harris, K. Kummer, A. Fondacaro, J. C. Cezar, D. Betto, E. Velez-Fort, A. Amorese, G. Ghiringhelli, L. Braicovich, R. Barrett, G. Berruyer, F. Cianciosi, L. Eybert, P. Marion, P. van der Linden, and L. Zhang, "The beamline ID32 at the ESRF for soft X-ray high energy resolution resonant inelastic X-ray scattering and polarisation dependent X-ray absorption spectroscopy," Nucl. Instrum. Methods A **903**, 175–192 (2018).

[91] C. Chen and F. Sette, "Performance of the dragon soft x-ray beamline," Review of Scientific Instruments **60**, 1616–1621 (1989).

[92] A. Amorese, C. Langini, G. Dellea, K. Kummer, N. Brookes, L. Braicovich, and G. Ghiringhelli, "Enhanced spatial resolution of commercial soft x-ray ccd detectors by single-photon centroid reconstruction," Nuclear Instruments and Methods in Physics Research Section A: Accelerators, Spectrometers, Detectors and Associated Equipment **935**, 222–226 (2019).

[93] N. B. Christensen, H. M. Rønnow, D. F. McMorrow, A. Harrison, T. Perring, M. Enderle, R. Coldea, L. Regnault, and G. Aeppli, "Quantum dynamics and entanglement of spins on a square lattice," Proc. Natl. Acad. Sci. U.S.A **104**, 15264–15269 (2007).

[94] Y. Endoh, K. Yamada, R. J. Birgeneau, D. R. Gabbe, H. P. Jenssen, M. A. Kastner, C. J. Peters, P. J. Picone, T. R. Thurston, J. M. Tranquada, G. Shirane, Y. Hidaka, M. Oda, Y. Enomoto, M. Suzuki, and T. Murakami, "Static and dynamic spin correlations in pure and doped La_2CuO_4," Phys. Rev. B **37**, 7443–7453 (1988).

[95] G. Aeppli, S. M. Hayden, H. A. Mook, Z. Fisk, S.-W. Cheong, D. Rytz, J. P. Remeika, G. P. Espinosa, and A. S. Cooper, "Magnetic dynamics of La_2CuO_4 and $La_{2-x}Ba_xCuO_4$," Phys. Rev. Lett. **62**, 2052–2055 (1989).

[96] S. Chakravarty, B. I. Halperin, and D. R. Nelson, "Two-dimensional quantum Heisenberg antiferromagnet at low temperatures," Phys. Rev. B **39**, 2344–2371 (1989).

[97] K. Majumdar, D. Furton, and G. S. Uhrig, "Effects of ring exchange interaction on the Néel phase of two-dimensional, spatially anisotropic, frustrated Heisenberg quantum antiferromagnet," Phys. Rev. B **85**, 144420 (2012).

[98] B. Dalla Piazza, M. Mourigal, N. B. Christensen, G. Nilsen, P. Tregenna-Piggott, T. Perring, M. Enderle, D. F. McMorrow,

D. Ivanov, and H. M. Rønnow, "Fractional excitations in the square-lattice quantum antiferromagnet," Nat. Phys. **11**, 62–68 (2015).

[99] H. Gretarsson, N. H. Sung, J. Porras, J. Bertinshaw, C. Dietl, J. A. N. Bruin, A. F. Bangura, Y. K. Kim, R. Dinnebier, J. Kim, A. Al-Zein, M. Moretti Sala, M. Krisch, M. Le Tacon, B. Keimer, and B. J. Kim, "Persistent paramagnons deep in the metallic phase of $Sr_{2-x}La_xIrO_4$," Phys. Rev. Lett. **117**, 107001 (2016).

[100] J.-i. Igarashi and T. Nagao, "Magnetic excitations in L-edge resonant inelastic x-ray scattering from cuprate compounds," Phys. Rev. B **85**, 064421 (2012).

[101] A. W. Sandvik and R. R. P. Singh, "High-energy magnon dispersion and multimagnon continuum in the two-dimensional heisenberg antiferromagnet," Phys. Rev. Lett. **86**, 528–531 (2001).

[102] J. Lorenzana, J. Eroles, and S. Sorella, "Does the Heisenberg model describe the multimagnon spin dynamics in antiferromagnetic CuO layers?" Phys. Rev. Lett. **83**, 5122–5125 (1999).

[103] M. Powalski, K. P. Schmidt, and G. S. Uhrig, "Mutually attracting spin waves in the square-lattice quantum antiferromagnet," SciPost Phys. **4**, 001 (2018).

[104] D. Betto, R. Fumagalli, L. Martinelli, M. Rossi, R. Piombo, K. Yoshimi, D. Di Castro, E. Di Gennaro, A. Sambri, D. Bonn, G. A. Sawatzky, L. Braicovich, N. B. Brookes, J. Lorenzana, and G. Ghiringhelli, "Multiple-magnon excitations shape the spin spectrum of cuprate parent compounds," Phys. Rev. B **103**, L140409 (2021), publisher: American Physical Society.

[105] C.-M. Ho, V. N. Muthukumar, M. Ogata, and P. W. Anderson, "Nature of spin excitations in two-dimensional Mott insulators: Undoped cuprates and other materials," Phys. Rev. Lett. **86**, 1626–1629 (2001).

[106] A. W. Sandvik, "Evidence for deconfined quantum criticality in a two-dimensional Heisenberg model with four-spin interactions," Phys. Rev. Lett. **98**, 227202 (2007).

[107] Y. Tang and A. W. Sandvik, "Confinement and deconfinement of spinons in two dimensions," Phys. Rev. Lett. **110**, 217213 (2013).

[108] H. Shao, Y. Q. Qin, S. Capponi, S. Chesi, Z. Y. Meng, and A. W. Sandvik, "Nearly deconfined spinon excitations in the square-lattice spin-1/2 Heisenberg antiferromagnet," Phys. Rev. X **7**, 041072 (2017).

[109] J. M. P. Carmelo, M. A. N. Araújo, S. R. White, and M. J. Sampaio,

"Hubbard-model description of the high-energy spin-weight distribution in La_2CuO_4," Phys. Rev. B **86**, 064520 (2012).

[110] A. Ino, C. Kim, T. Mizokawa, Z.-X. Shen, A. Fujimori, M. Takaba, K. Tamasaku, H. Eisaki, and S. Uchida, "Fermi surface and band dispersion in $La_{2-x}Sr_xCuO_4$," J. Phys. Soc. Jpn. **68**, 1496–1499 (1999).

[111] T. Yoshida, X. J. Zhou, K. Tanaka, W. L. Yang, Z. Hussain, Z.-X. Shen, A. Fujimori, S. Sahrakorpi, M. Lindroos, R. S. Markiewicz, A. Bansil, S. Komiya, Y. Ando, H. Eisaki, T. Kakeshita, and S. Uchida, "Systematic doping evolution of the underlying Fermi surface of $La_{2-x}Sr_xCuO_4$," Phys. Rev. B **74**, 224510 (2006).

[112] N. M. R. Peres and M. A. N. Araújo, "Spin-wave dispersion in la_2CuO_4," Phys. Rev. B **65**, 132404 (2002).

[113] H. Schulz, T. Ziman, and D. Poilblanc, "Magnetic order and disorder in the frustrated quantum Heisenberg antiferromagnet in two dimensions," J. Phys., I **6**, 675–703 (1996).

[114] L. Isaev, G. Ortiz, and J. Dukelsky, "Hierarchical mean-field approach to the J_1-J_2 heisenberg model on a square lattice," Phys. Rev. B **79**, 024409 (2009).

[115] L. Capriotti, F. Becca, A. Parola, and S. Sorella, "Resonating valence bond wave functions for strongly frustrated spin systems," Phys. Rev. Lett. **87**, 097201 (2001).

[116] F. Ferrari and F. Becca, "Spectral signatures of fractionalization in the frustrated heisenberg model on the square lattice," Phys. Rev. B **98**, 100405(R) (2018).

[117] J. Takahashi and A. W. Sandvik, "Valence-bond solids, vestigial order, and emergent SO (5) symmetry in a two-dimensional quantum magnet," Phys. Rev. Res. **2**, 033459 (2020).

[118] V. J. Emery and S. Kivelson, "Frustrated electronic phase separation and high-temperature superconductors," Physica C **209**, 597–621 (1993).

[119] H. Zhang, Y. Wang, H. Zhang, V. Dravid, L. Marks, P. Han, D. Payne, P. Radaelli, and J. Jorgensen, "Identity of planar defects in the 'infinite-layer' copper oxide superconductor," Nature **370**, 352–354 (1994).

[120] D. Di Castro, C. Cantoni, F. Ridolfi, C. Aruta, A. Tebano, N. Yang, and G. Balestrino, "High-T_c Superconductivity at the Interface between the $CaCuO_2$ and $SrTiO_3$ Insulating Oxides," Phys. Rev. Lett. **115**, 147001 (2015).

[121] D. D. Castro, C. Aruta, A. Tebano, D. Innocenti, M. Minola, M. M. Sala, W. Prellier, O. Lebedev, and G. Balestrino, "T_c up to 50 K in superlattices of insulating oxides," Superconductor Science and Technology **27**, 044016 (2014).

[122] D. Di Castro, M. Salvato, A. Tebano, D. Innocenti, C. Aruta, W. Prellier, O. I. Lebedev, I. Ottaviani, N. B. Brookes, M. Minola, M. Moretti Sala, C. Mazzoli, P. G. Medaglia, G. Ghiringhelli, L. Braicovich, M. Cirillo, and G. Balestrino, "Occurrence of a high-temperature superconducting phase in $(CaCuO_2)_n/(SrTiO_3)_m$ superlattices," Phys. Rev. B **86**, 134524 (2012).

[123] L. Braicovich, M. Minola, G. Dellea, M. Le Tacon, M. Moretti Sala, C. Morawe, J.-C. Peffen, R. Supruangnet, F. Yakhou, G. Ghiringhelli, *et al.*, "The simultaneous measurement of energy and linear polarization of the scattered radiation in resonant inelastic soft x-ray scattering," Rev. Sci. Instrum. **85**, 115104 (2014).

[124] R. Fumagalli, L. Braicovich, M. Minola, Y. Y. Peng, K. Kummer, D. Betto, M. Rossi, E. Lefrançois, C. Morawe, M. Salluzzo, H. Suzuki, F. Yakhou, M. Le Tacon, B. Keimer, N. B. Brookes, M. M. Sala, and G. Ghiringhelli, "Polarization-resolved Cu l3-edge resonant inelastic x-ray scattering of orbital and spin excitations in $NdBa_2Cu_3O_{7-\delta}$," Phys. Rev. B **99**, 134517 (2019).

[125] M. Rossi, R. Arpaia, R. Fumagalli, M. Moretti Sala, D. Betto, K. Kummer, G. M. De Luca, J. van den Brink, M. Salluzzo, N. B. Brookes, L. Braicovich, and G. Ghiringhelli, "Experimental determination of momentum-resolved electron-phonon coupling," Phys. Rev. Lett. **123**, 027001 (2019).

[126] O. K. Andersen, S. Y. Savrasov, O. Jepsen, and A. I. Liechtenstein, "Out-of-plane instability and electron-phonon contribution to s- and d-wave pairing in high-temperature superconductors; LDA linear-response calculation for doped $CaCuO_2$ and a generic tight-binding model," J. Low. Temp. Phys. **105**, 285–304 (1996).

[127] K. W. Plumb, A. T. Savici, G. E. Granroth, F. C. Chou, and Y.-J. Kim, "High-energy continuum of magnetic excitations in the two-dimensional quantum antiferromagnet $Sr_2CuO_2Cl_2$," Phys. Rev. B **89**, 180410(R) (2014).

[128] M. Le Tacon, G. Ghiringhelli, J. Chaloupka, M. M. Sala, V. Hinkov, M. Haverkort, M. Minola, M. Bakr, K. Zhou, S. Blanco-Canosa, *et al.*, "Intense paramagnon excitations in a large family of high-temperature superconductors," Nat. Phys. **7**, 725–730 (2011).

[129] V. Bisogni, S. Kourtis, C. Monney, K. Zhou, R. Kraus, C. Sekar, V. Strocov, B. Büchner, J. van den Brink, L. Braicovich, T. Schmitt, M. Daghofer, and J. Geck, "Femtosecond dynamics of momentum-dependent magnetic excitations from resonant inelastic x-ray scattering in $cacu_2o_3$," Phys. Rev. Lett. **112**, 147401 (2014).

[130] F. D. M. Haldane, ""Fractional statistics" in arbitrary dimensions: A generalization of the Pauli principle," Phys. Rev. Lett. **67**, 937–940 (1991).

[131] L. Braicovich, J. van den Brink, V. Bisogni, M. M. Sala, L. J. P. Ament, N. B. Brookes, G. M. De Luca, M. Salluzzo, T. Schmitt, V. N. Strocov, and G. Ghiringhelli, "Magnetic excitations and phase separation in the underdoped $la_{2-x}Sr_xCuO_4$ superconductor measured by resonant inelastic x-ray scattering," Phys. Rev. Lett. **104**, 077002 (2010).

[132] C. Jia, K. Wohlfeld, Y. Wang, B. Moritz, and T. P. Devereaux, "Using rixs to uncover elementary charge and spin excitations," Phys. Rev. X **6**, 021020 (2016).

[133] U. Kumar, A. Nag, J. Li, H. Robarts, A. Walters, M. García-Fernández, R. Saint-Martin, A. Revcolevschi, J. Schlappa, T. Schmitt, *et al.*, "Unraveling higher-order corrections in the spin dynamics of RIXS spectra," arXiv:2110.03186 (2021).

[134] N. M. R. Peres and M. A. N. Araújo, "Spin waves in La_2CuO_4: band structure and correlation effects," Phys. Status Solidi (b) **236**, 523–526 (2003).

[135] C. B. Larsen, A. T. Rømer, S. Janas, F. Treue, B. Mønsted, N. E. Shaik, H. M. Rønnow, and K. Lefmann, "Exact diagonalization study of the Hubbard-parametrized four-spin ring exchange model on a square lattice," Phys. Rev. B **99**, 054432 (2019).

[136] S. Toth and B. Lake, "Linear spin wave theory for single-q incommensurate magnetic structures," J. Phys. Condens. Matter **27**, 166002 (2015).

[137] S. M. Hayden, G. Aeppli, T. G. Perring, H. A. Mook, and F. Doğan, "High-frequency spin waves in $YBa_2Cu_3O_{6.15}$," Phys. Rev. B **54**, R6905–R6908 (1996).

[138] A. Auerbach, *Interacting Electrons and Quantum Magnetism* (Springer-Verlag, 1994).

[139] L. Venema, B. Verberck, I. Georgescu, G. Prando, E. Couderc, S. Milana, M. Maragkou, L. Persechini, G. Pacchioni, and L. Fleet, "The quasiparticle zoo," Nature Physics **12**, 1085–1089 (2016).

[140] B. J. Powell, "Emergent particles and gauge fields in quantum matter," Contemporary Physics **61**, 96–131 (2020), https://doi.org/10.1080/00107514.2020.1832350 .

[141] K. Ishii, M. Fujita, T. Sasaki, M. Minola, G. Dellea, C. Mazzoli, K. Kummer, G. Ghiringhelli, L. Braicovich, T. Tohyama, K. Tsutsumi, K. Sato, R. Kajimoto, K. Ikeuchi, K. Yamada, M. Yoshida, M. Kurooka, and J. Mizuki, "High-energy spin and charge excitations in electron-doped copper oxide superconductors," Nature Communications **5**, 3714 (2014).

[142] W. S. Lee, J. J. Lee, E. A. Nowadnick, S. Gerber, W. Tabis, S. W. Huang, V. N. Strocov, E. M. Motoyama, G. Yu, B. Moritz, H. Y. Huang, R. P. Wang, Y. B. Huang, W. B. Wu, C. T. Chen, D. J. Huang, M. Greven, T. Schmitt, Z. X. Shen, and T. P. Devereaux, "Asymmetry of collective excitations in electron- and hole-doped cuprate superconductors," Nature Physics **10**, 883–889 (2014).

[143] M. P. M. Dean, G. Dellea, R. S. Springell, F. Yakhou-Harris, K. Kummer, N. B. Brookes, X. Liu, Y.-J. Sun, J. Strle, T. Schmitt, L. Braicovich, G. Ghiringhelli, I. Božović, and J. P. Hill, "Persistence of magnetic excitations in $La_{2-x}Sr_xCuO_4$ from the undoped insulator to the heavily overdoped non-superconducting metal," Nature Materials **12**, 1019–1023 (2013).

[144] K. I. Kugel and D. Khomskiĭ, "The jahn-teller effect and magnetism: transition metal compounds," Soviet Physics Uspekhi **25**, 231 (1982).

[145] Y. Tokura and N. Nagaosa, "Orbital physics in transition-metal oxides," Science **288**, 462–468 (2000).

[146] J. Heverhagen and M. Daghofer, "Spinon-orbiton repulsion and attraction mediated by hund's rule," Phys. Rev. B **98**, 085120 (2018).

[147] Y. Tanaka, A. Baron, Y.-J. Kim, K. Thomas, J. Hill, Z. Honda, F. Iga, S. Tsutsui, D. Ishikawa, and C. Nelson, "Search for orbitons in $LaMnO_3$, $YTiO_3$ and $KCuF_3$ using high-resolution inelastic x-ray scattering," New Journal of Physics **6**, 161 (2004).

[148] M. Grüninger, R. Rückamp, M. Windt, P. Reutler, C. Zobel, T. Lorenz, A. Freimuth, and A. Revcolevschi, "Experimental quest for orbital waves," Nature **418**, 39–40 (2002).

[149] C. Ulrich, L. J. P. Ament, G. Ghiringhelli, L. Braicovich, M. Moretti Sala, N. Pezzotta, T. Schmitt, G. Khaliullin, J. van den Brink, H. Roth, T. Lorenz, and B. Keimer, "Momentum dependence of orbital excitations in mott-insulating titanates," Phys. Rev. Lett. **103**, 107205 (2009).

[150] I. Bozovic, G. Logvenov, I. Belca, B. Narimbetov, and I. Sveklo, "Epitaxial strain and superconductivity in $la_{2-x}sr_xcuo_4$ thin films," Phys. Rev. Lett. **89**, 107001 (2002).

[151] K.-J. Zhou, A. Walters, M. Garcia-Fernandez, T. Rice, M. Hand, A. Nag, J. Li, S. Agrestini, P. Garland, H. Wang, S. Alcock, I. Nistea, B. Nutter, N. Rubies, G. Knap, M. Gaughran, F. Yuan, P. Chang, J. Emmins, and G. Howell, "I21: An advanced high-resolution resonant inelastic X-ray scattering beamline at Diamond Light Source," Journal of Synchrotron Radiation **29**, 563–580 (2022).

[152] K. Wohlfeld, S. Nishimoto, M. W. Haverkort, and J. van den Brink, "Microscopic origin of spin-orbital separation in sr_2cuo_3," Phys. Rev. B **88**, 195138 (2013).

[153] G. Martinez and P. Horsch, "Spin polarons in the t-j model," Phys. Rev. B **44**, 317–331 (1991).

[154] J. H. Jefferson, H. Eskes, and L. F. Feiner, "Derivation of a single-band model for cuo_2 planes by a cell-perturbation method," Phys. Rev. B **45**, 7959–7972 (1992).

[155] J. C. Slater and G. F. Koster, "Simplified lcao method for the periodic potential problem," Phys. Rev. **94**, 1498–1524 (1954).

[156] A. S. Botana and M. R. Norman, "Similarities and differences between $lanio_2$ and $cacuo_2$ and implications for superconductivity," Phys. Rev. X **10**, 011024 (2020).

[157] R. Neudert, S.-L. Drechsler, J. Málek, H. Rosner, M. Kielwein, Z. Hu, M. Knupfer, M. S. Golden, J. Fink, N. Nücker, M. Merz, S. Schuppler, N. Motoyama, H. Eisaki, S. Uchida, M. Domke, and G. Kaindl, "Four-band extended hubbard hamiltonian for the one-dimensional cuprate sr_2cuo_3 : distribution of oxygen holes and its relation to strong intersite coulomb interaction," Phys. Rev. B **62**, 10752–10765 (2000).

[158] K. Okada and A. Kotani, "Intersite coulomb interactions in quasi-one-dimensional copper oxides," Journal of the Physical Society of Japan **66**, 341–344 (1997).

[159] L. Martinelli, D. Betto, K. Kummer, R. Arpaia, L. Braicovich, D. Di Castro, N. B. Brookes, M. Moretti Sala, and G. Ghiringhelli, "Fractional spin excitations in the infinite-layer cuprate $cacuo_2$," Phys. Rev. X **12**, 021041 (2022).

[160] D. Li, K. Lee, B. Y. Wang, M. Osada, S. Crossley, H. R. Lee, Y. Cui, Y. Hikita, and H. Y. Hwang, "Superconductivity in an infinite-layer nickelate," Nature **572**, 624–627 (2019).

[161] N. Bachar, K. Koteras, J. Gawraczynski, W. Trzciński, J. Paszula, R. Piombo, P. Barone, Z. Mazej, G. Ghiringhelli, A. Nag, K.-J. Zhou, J. Lorenzana, D. van der Marel, and W. Grochala, "Charge-transfer and *dd* excitations in agf_2," Phys. Rev. Res. **4**, 023108 (2022).

[162] J. Gawraczyński, D. Kurzydłowski, R. A. Ewings, S. Bandaru, W. Gadomski, Z. Mazej, G. Ruani, I. Bergenti, T. Jaroń, A. Ozarowski, S. Hill, P. J. Leszczyński, K. Tokár, M. Derzsi, P. Barone, K. Wohlfeld, J. Lorenzana, and W. Grochala, "Silver route to cuprate analogs," Proceedings of the National Academy of Sciences **116**, 1495–1500 (2019), https://www.pnas.org/doi/pdf/10.1073/pnas.1812857116 .

[163] V. I. Anisimov, D. Bukhvalov, and T. M. Rice, "Electronic structure of possible nickelate analogs to the cuprates," Phys. Rev. B **59**, 7901–7906 (1999).

[164] J. Chaloupka and G. Khaliullin, "Orbital order and possible superconductivity in $LaNiO_3/LaMO_3$ superlattices," Phys. Rev. Lett. **100**, 016404 (2008).

[165] J. Chakhalian, J. M. Rondinelli, J. Liu, B. A. Gray, M. Kareev, E. J. Moon, N. Prasai, J. L. Cohn, M. Varela, I. C. Tung, M. J. Bedzyk, S. G. Altendorf, F. Strigari, B. Dabrowski, L. H. Tjeng, P. J. Ryan, and J. W. Freeland, "Asymmetric orbital-lattice interactions in ultrathin correlated oxide films," Phys. Rev. Lett. **107**, 1–4 (2011).

[166] A. S. Disa, D. P. Kumah, A. Malashevich, H. Chen, D. A. Arena, E. D. Specht, S. Ismail-Beigi, F. J. Walker, and C. H. Ahn, "Orbital engineering in symmetry-breaking polar heterostructures," Phys. Rev. Lett. **114**, 026801 (2015).

[167] E. Benckiser, M. W. Haverkort, S. Brück, E. Goering, S. MacKe, A. Frañ, X. Yang, O. K. Andersen, G. Cristiani, H. U. Habermeier, A. V. Boris, I. Zegkinoglou, P. Wochner, H. J. Kim, V. Hinkov, and B. Keimer, "Orbital reflectometry of oxide heterostructures," Nat. Mater. **10**, 189–193 (2011).

[168] Y. Cao, X. Liu, M. Kareev, D. Choudhury, S. Middey, D. Meyers, J.-W. Kim, P. J. Ryan, J. W. Freeland, and J. Chakhalian, "Engineered Mott ground state in a $LaTiO_{3+\delta}/LaNiO_3$ heterostructure," Nat. Commun. **7**, 10418 (2016).

[169] M. Osada, B. Y. Wang, B. H. Goodge, S. P. Harvey, K. Lee, D. Li, L. F. Kourkoutis, and H. Y. Hwang, "Nickelate Superconductivity without Rare-Earth Magnetism: $(La,Sr)NiO_2$," Adv. Mater. **33**, 2104083 (2021).

[170] M. Hepting, D. Li, C. J. Jia, H. Lu, E. Paris, Y. Tseng, X. Feng, M. Osada, E. Been, Y. Hikita, Y.-D. Chuang, Z. Hussain, K. J. Zhou, A. Nag, M. Garcia-Fernandez, M. Rossi, H. Y. Huang, D. J. Huang, Z. X. Shen, T. Schmitt, H. Y. Hwang, B. Moritz, J. Zaanen, T. P. Devereaux, and W. S. Lee, "Electronic structure of the parent compound of superconducting infinite-layer nickelates," Nat. Mater. **19**, 381–385 (2020).

[171] M. Rossi, H. Lu, A. Nag, D. Li, M. Osada, K. Lee, B. Y. Wang, S. Agrestini, M. Garcia-Fernandez, Y. D. Chuang, Z. X. Shen, H. Y. Hwang, B. Moritz, K.-J. Zhou, T. P. Devereaux, and W. S. Lee, "Orbital and Spin Character of Doped Carriers in Infinite-Layer Nickelates," Phys. Rev. B **104**, L220505 (2021).

[172] B. H. Goodge, D. Li, K. Lee, M. Osada, B. Y. Wang, G. A. Sawatzky, H. Y. Hwang, and L. F. Kourkoutis, "Doping evolution of the Mott-Hubbard landscape in infinite-layer nickelates," Proc. Natl. Acad. Sci. **118**, 2007683118 (2021).

[173] A. S. Botana and M. R. Norman, "Similarities and Differences between $LaNiO_2$ and $CaCuO_2$ and Implications for Superconductivity," Phys. Rev. X **10**, 11024 (2020).

[174] H. Zhang, L. Jin, S. Wang, B. Xi, X. Shi, F. Ye, and J.-W. Mei, "Effective Hamiltonian for nickelate oxides $Nd_{1-x}Sr_xNiO_2$," Phys. Rev. Res. **2**, 13214 (2020).

[175] J. Karp, A. S. Botana, M. R. Norman, H. Park, M. Zingl, and A. Millis, "Many-Body Electronic Structure of $NdNiO_2$ and $CaCuO_2$," Phys. Rev. X **10**, 21061 (2020).

[176] M. Jiang, M. Berciu, and G. A. Sawatzky, "Critical Nature of the Ni Spin State in Doped $NdNiO_2$," Phys. Rev. Lett. **124**, 207004 (2020).

[177] Y. Shen, J. Sears, G. Fabbris, J. Li, J. Pelliciari, I. Jarrige, X. He, I. Božović, M. Mitrano, J. Zhang, J. F. Mitchell, A. S. Botana, V. Bisogni, M. R. Norman, S. Johnston, and M. P. M. Dean, "Role of oxygen states in the low valence nickelate $la_4ni_3o_8$," Phys. Rev. X **12**, 011055 (2022).

[178] E. Pellegrin, N. Nücker, J. Fink, S. L. Molodtsov, A. Gutiérrez, E. Navas, O. Strebel, Z. Hu, M. Domke, G. Kaindl, S. Uchida, Y. Nakamura, J. Markl, M. Klauda, G. Saemann-Ischenko, A. Krol, J. L. Peng, Z. Y. Li, and R. L. Greene, "Orbital character of states at the Fermi level in $La_{2-x}Sr_xCuO_4$ and $R_{2-x}Ce_xCuO_4$," Phys. Rev. B **47**, 3354–3367 (1993).

[179] N. B. Brookes, G. Ghiringhelli, O. Tjernberg, L. H. Tjeng, T. Mi-

zokawa, T. W. Li, and A. A. Menovsky, "Detection of Zhang-Rice Singlets Using Spin-Polarized Photoemission," Phys. Rev. Lett. **87**, 237003 (2001).

[180] E. Been, W.-S. Lee, H. Y. Hwang, Y. Cui, J. Zaanen, T. Devereaux, B. Moritz, and C. Jia, "Electronic Structure Trends Across the Rare-Earth Series in Superconducting Infinite-Layer Nickelates," Phys. Rev. X **11**, 011050 (2021).

[181] H. Lu, M. Rossi, A. Nag, M. Osada, D. F. Li, K. Lee, B. Y. Wang, M. Garcia-Fernandez, S. Agrestini, Z. X. Shen, E. M. Been, B. Moritz, T. P. Devereaux, J. Zaanen, H. Y. Hwang, K.-J. Zhou, and W. S. Lee, "Magnetic excitations in infinite-layer nickelates," Science **373**, 213–216 (2021).

[182] S. Zeng, C. S. Tang, X. Yin, C. Li, M. Li, Z. Huang, J. Hu, W. Liu, G. J. Omar, H. Jani, Z. S. Lim, K. Han, D. Wan, P. Yang, S. J. Pennycook, A. T. S. Wee, and A. Ariando, "Phase Diagram and Superconducting Dome of Infinite-Layer $Nd_{1-x}Sr_xNiO_2$ Thin Films," Phys. Rev. Lett. **125**, 147003 (2020).

[183] C. Castellani, C. Di Castro, and M. Grilli, "Singular quasiparticle scattering in the proximity of charge instabilities," Phys. Rev. Lett. **75**, 4650 (1995).

[184] C. Castellani, C. Di Castro, and M. Grilli, "Non-fermi-liquid behavior and d-wave superconductivity near the charge-density-wave quantum critical point," Z. Phys. B **103**, 137–144 (1996).

[185] G. Ghiringhelli, M. Le Tacon, M. Minola, S. Blanco-Canosa, C. Mazzoli, N. B. Brookes, G. M. De Luca, A. Frano, D. G. Hawthorn, F. He, T. Loew, M. M. Sala, D. C. Peets, M. Salluzzo, E. Schierle, R. Sutarto, G. A. Sawatzky, E. Weschke, B. Keimer, and L. Braicovich, "Long-Range Incommensurate Charge Fluctuations in $(Y,Nd)Ba_2Cu_3O_{6+x}$," Science **337**, 821–825 (2012).

[186] A. Achkar, R. Sutarto, X. Mao, F. He, A. Frano, S. Blanco-Canosa, M. Le Tacon, G. Ghiringhelli, L. Braicovich, M. Minola, *et al.*, "Distinct charge orders in the planes and chains of ortho-iii-ordered yba 2 cu 3 o 6+ δ superconductors identified by resonant elastic x-ray scattering," Phys. Rev. Lett. **109**, 167001 (2012).

[187] R. Comin and A. Damascelli, "Resonant X-Ray Scattering Studies of Charge Order in Cuprates," Annu. Rev. Condens. Matter Phys. **7**, 369–405 (2016).

[188] R. Arpaia, S. Caprara, R. Fumagalli, G. De Vecchi, Y. Y. Peng, E. Andersson, D. Betto, G. M. De Luca, N. B. Brookes, F. Lombardi, M. Sal-

luzzo, L. Braicovich, C. Di Castro, M. Grilli, and G. Ghiringhelli, "Dynamical charge density fluctuations pervading the phase diagram of a Cu-based high-Tc superconductor," Science **365**, 906–910 (2019).

[189] G. Seibold, R. Arpaia, Y. Y. Peng, R. Fumagalli, L. Braicovich, C. Di Castro, M. Grilli, G. C. Ghiringhelli, and S. Caprara, "Strange metal behaviour from charge density fluctuations in cuprates," Commun. Phys. **4**, 7 (2021).

[190] R. Arpaia and G. Ghiringhelli, "Charge Order at High Temperature in Cuprate Superconductors," J. Phys. Soc. Japan **90**, 111005 (2021).

[191] G. Krieger, L. Martinelli, S. Zeng, L. E. Chow, K. Kummer, R. Arpaia, M. Moretti Sala, N. B. Brookes, A. Ariando, N. Viart, M. Salluzzo, G. Ghiringhelli, and D. Preziosi, "Charge and spin order dichotomy in ndnio$_2$ driven by the capping layer," Phys. Rev. Lett. **129**, 027002 (2022).

[192] G. Krieger, A. Raji, L. Schlur, G. Versini, C. Bouillet, M. Lenertz, J. Robert, A. Gloter, N. Viart, and D. Preziosi, "Synthesis of infinite-layer nickelates and influence of the capping-layer on magnetotransport," Journal of Physics D: Applied Physics **56**, 024003 (2022).

[193] S. W. Zeng, C. J. Li, L. E. Chow, Y. Cao, Z. T. Zhang, C. S. Tang, X. M. Yin, Z. S. Lim, J. X. Hu, P. Yang, and A. Ariando, "Superconductivity in infinite-layer lanthanide nickelates," arXiv (2021), arXiv:2105.13492 .

[194] "Berkeley x-ray attenuation length calculator," `https://henke.lbl.gov/optical_constants/atten2.html`.

[195] J. Karp, A. S. Botana, M. R. Norman, H. Park, M. Zingl, and A. Millis, "Many-Body Electronic Structure of $NdNiO_2$ and $CaCuO_2$," Phys. Rev. X **10**, 021061 (2020).

[196] J. Zaanen, G. A. Sawatzky, and J. W. Allen, "Band gaps and electronic structure of transition-metal compounds," Phys. Rev. Lett. **55**, 418–421 (1985).

[197] R. A. House, G. J. Rees, M. A. Pérez-Osorio, J.-J. Marie, E. Boivin, A. W. Robertson, A. Nag, M. Garcia-Fernandez, K.-J. Zhou, and P. G. Bruce, "First-cycle voltage hysteresis in li-rich 3d cathodes associated with molecular o2 trapped in the bulk," Nature Energy **5**, 777–785 (2020).

[198] Y. Peng, L. Martinelli, Q. Li, M. Rossi, M. Mitrano, R. Arpaia, M. M. Sala, Q. Gao, X. Guo, G. M. De Luca, A. Walters, A. Nag, A. Barbour, G. Gu, J. Pelliciari, N. B. Brookes, P. Abbamonte, M. Salluzzo,

X. Zhou, K.-J. Zhou, V. Bisogni, L. Braicovich, S. Johnston, and G. Ghiringhelli, "Doping dependence of the electron-phonon coupling in two families of bilayer superconducting cuprates," Phys. Rev. B **105**, 115105 (2022).

[199] Q. Gao, S. Fan, Q. Wang, J. Li, X. Ren, I. Biało, A. Drewanowski, P. Rothenbühler, J. Choi, Y. Wang, *et al.*, "Magnetic Excitations in Strained Infinite-layer Nickelate $PrNiO_2$," arXiv preprint arXiv:2208.05614 (2022).

[200] Y. Y. Peng, R. Fumagalli, Y. Ding, M. Minola, S. Caprara, D. Betto, M. Bluschke, G. M. De Luca, K. Kummer, E. Lefrançois, M. Salluzzo, H. Suzuki, M. Le Tacon, X. J. Zhou, N. B. Brookes, B. Keimer, L. Braicovich, M. Grilli, and G. Ghiringhelli, "Re-entrant charge order in overdoped $(Bi,Pb)_{2.12}Sr_{1.88}CuO_{6+\delta}$ outside the pseudogap regime," Nat. Mater. **17**, 697–702 (2018).

[201] M. Fidrysiak and J. Spałek, "Unified theory of spin and charge excitations in high-T_c cuprate superconductors: A quantitative comparison with experiment and interpretation," Phys. Rev. B **104**, L020510 (2021).

[202] J. Zhang, Y.-S. Chen, D. Phelan, H. Zheng, M. R. Norman, and J. F. Mitchell, "Stacked charge stripes in the quasi-2D trilayer nickelate $La_4Ni_3O_8$," Proc. Natl. Acad. Sci. **113**, 8945–8950 (2016).

[203] J. Zhang, D. M. Pajerowski, A. S. Botana, H. Zheng, L. Harriger, J. Rodriguez-Rivera, J. P. C. Ruff, N. J. Schreiber, B. Wang, Y.-S. Chen, W. C. Chen, M. R. Norman, S. Rosenkranz, J. F. Mitchell, and D. Phelan, "Spin Stripe Order in a Square Planar Trilayer Nickelate," Phys. Rev. Lett. **122**, 247201 (2019).

[204] J. Bardeen, L. N. Cooper, and J. R. Schrieffer, "Theory of superconductivity," Phys. Rev. **108**, 1175–1204 (1957).

[205] W. L. McMillan and J. M. Rowell, "Lead phonon spectrum calculated from superconducting density of states," Phys. Rev. Lett. **14**, 108–112 (1965).

[206] A. Lanzara, P. V. Bogdanov, X. J. Zhou, S. A. Kellar, D. L. Feng, E. D. Lu, T. Yoshida, H. Eisaki, A. Fujimori, K. Kishio, J.-I. Shimoyama, T. Noda, S. Uchida, Z. Hussain, and Z.-X. Shen, "Evidence for ubiquitous strong electron-phonon coupling in high-temperature superconductors," Nature **412**, 510 (2001).

[207] T. Cuk, F. Baumberger, D. H. Lu, N. Ingle, X. J. Zhou, H. Eisaki, N. Kaneko, Z. Hussain, T. P. Devereaux, N. Nagaosa, and Z.-X.

Shen, "Coupling of the B_{1g} phonon to the antinodal electronic states of $Bi_2Sr_2Ca_{0.92}Y_{0.08}Cu_2O_{8+\delta}$," Phys. Rev. Lett. **93**, 117003 (2004).

[208] T. P. Devereaux, T. Cuk, Z.-X. Shen, and N. Nagaosa, "Anisotropic electron-phonon interaction in the cuprates," Phys. Rev. Lett. **93**, 117004 (2004).

[209] T. Cuk, D. H. Lu, X. J. Zhou, Z.-X. Shen, T. P. Devereaux, and N. Nagaosa, "A review of electron-phonon coupling seen in the high-T_c superconductors by angle-resolved photoemission studies (ARPES)," Phys. Status Solidi B **242**, 11–29 (2005).

[210] J. Graf, M. d'Astuto, C. Jozwiak, D. R. Garcia, N. L. Saini, M. Krisch, K. Ikeuchi, A. Q. R. Baron, H. Eisaki, and A. Lanzara, "Bond Stretching Phonon Softening and Kinks in the Angle-Resolved Photoemission Spectra of Optimally Doped $Bi_2Sr_{1.6}La_{0.4}Cu_2O_{6+\delta}$ Superconductors," Phys. Rev. Lett. **100**, 227002 (2008).

[211] S. Johnston, I. M. Vishik, W. S. Lee, F. Schmitt, S. Uchida, K. Fujita, S. Ishida, N. Nagaosa, Z. X. Shen, and T. P. Devereaux, "Evidence for the Importance of Extended Coulomb Interactions and Forward Scattering in Cuprate Superconductors," Phys. Rev. Lett. **108**, 166404 (2012).

[212] J. Lee, K. Fujita, K. McElroy, J. A. Slezak, M. Wang, Y. Aiura, H. Bando, M. Ishikado, T. Masui, J. X. Zhu, A. V. Balatsky, H. Eisaki, S. Uchida, and J. C. Davis, "Interplay of electron–lattice interactions and superconductivity in $Bi_2Sr_2CaCu_2O_{8+\delta}$," Nature **442**, 546–550 (2006).

[213] G. Zhao, "Fine structure in the tunneling spectra of electron-doped cuprates: No coupling to the magnetic resonance mode," Phys. Rev. Lett. **103**, 236403 (2009).

[214] G. Zhao, "Strong coupling to multiple phonon modes in high-temperature superconductors," Phys. Rev. B **75**, 214507 (2007).

[215] N. Bulut and D. J. Scalapino, "$d_{x^2-y^2}$ symmetry and the pairing mechanism," Phys. Rev. B **54**, 14971–14973 (1996).

[216] T. A. Maier, D. Poilblanc, and D. J. Scalapino, "Dynamics of the pairing interaction in the hubbard and t–J models of high-temperature superconductors," Phys. Rev. Lett. **100**, 237001 (2008).

[217] C. C. Tsuei and J. R. Kirtley, "Pairing symmetry in cuprate superconductors," Rev. Mod. Phys. **72**, 969–1016 (2000).

[218] E. Fradkin, S. A. Kivelson, and J. M. Tranquada, "Colloquium: The-

ory of intertwined orders in high temperature superconductors," Rev. Mod. Phys. **87**, 457–482 (2015).

[219] D. F. Agterberg, J. S. Davis, S. D. Edkins, E. Fradkin, D. J. Van Harlingen, S. A. Kivelson, P. A. Lee, L. Radzihovsky, J. M. Tranquada, and Y. Wang, "The physics of pair-density waves: Cuprate superconductors and beyond," Annu. Rev. Condens. Matter Phys. **11**, 231–270 (2020).

[220] R. Arpaia, E. Andersson, E. Trabaldo, T. Bauch, and F. Lombardi, "Probing the phase diagram of cuprates with $YBa_2Cu_3O_{7-\delta}$ thin films and nanowires," Phys. Rev. Materials **2**, 024804 (2018).

[221] R. Arpaia and G. Ghiringhelli, "Charge order at high temperature in cuprate superconductors," Journal of the Physical Society of Japan **90**, 111005 (2021).

[222] X. Zhu, Y. Cao, J. Zhang, E. W. Plummer, and J. Guo, "Classification of charge density waves based on their nature," Proceedings of the National Academy of Sciences **112**, 2367–2371 (2015).

[223] L. Chaix, G. Ghiringhelli, Y. Y. Peng, M. Hashimoto, B. Moritz, K. Kummer, N. B. Brookes, Y. He, S. Chen, S. Ishida, Y. Yoshida, H. Eisaki, M. Salluzzo, L. Braicovich, Z.-X. Shen, T. P. Devereaux, and W.-S. Lee, "Dispersive charge density wave excitations in $Bi_2Sr_2CaCu_2O_{8+\delta}$," Nat. Phys. **13**, 952 (2017).

[224] H. Miao, D. Ishikawa, R. Heid, M. Le Tacon, G. Fabbris, D. Meyers, G. D. Gu, A. Q. R. Baron, and M. P. M. Dean, "Incommensurate Phonon Anomaly and the Nature of Charge Density Waves in Cuprates," Phys. Rev. X **8**, 011008 (2018).

[225] J. Q. Lin, H. Miao, D. G. Mazzone, G. D. Gu, A. Nag, A. C. Walters, M. García-Fernández, A. Barbour, J. Pelliciari, I. Jarrige, M. Oda, K. Kurosawa, N. Momono, K.-J. Zhou, V. Bisogni, X. Liu, and M. P. M. Dean, "Strongly Correlated Charge Density Wave in $La_{2-x}Sr_xCuO_4$ Evidenced by Doping-Dependent Phonon Anomaly," Phys. Rev. Lett. **124**, 207005 (2020).

[226] Y. Y. Peng, A. A. Husain, M. Mitrano, S. X.-L. Sun, T. A. Johnson, A. V. Zakrzewski, G. J. MacDougall, A. Barbour, I. Jarrige, V. Bisogni, and P. Abbamonte, "Enhanced electron-phonon coupling for charge-density-wave formation in $La_{1.8-x}Eu_{0.2}Sr_xCuO_{4+\delta}$," Phys. Rev. Lett. **125**, 097002 (2020).

[227] T. Timusk and B. Statt, "The pseudogap in high-temperature superconductors: an experimental survey," Reports on Progress in Physics **62**, 61 (1999).

[228] E. E. M. Chia, D. Springer, S. K. Nair, X. Zou, S. A. Cheong, C. Panagopoulos, T. Tamegai, H. Eisaki, S. Ishida, S. ichi Uchida, A. J. Taylor, and J.-X. Zhu, "Doping dependence of the electron–phonon and electron–spin fluctuation interactions in the high-T_c superconductor $Bi_2Sr_2CaCu_2O_{8+\delta}$," New Journal of Physics **15**, 103027 (2013).

[229] L. J. P. Ament, M. van Veenendaal, and J. van den Brink, "Determining the electron-phonon coupling strength from Resonant Inelastic X-ray Scattering at transition metal L-edges," EPL **95**, 27008 (2011).

[230] T. P. Devereaux, A. M. Shvaika, K. Wu, K. Wohlfeld, C. J. Jia, Y. Wang, B. Moritz, L. Chaix, W.-S. Lee, Z.-X. Shen, G. Ghiringhelli, and L. Braicovich, "Directly Characterizing the Relative Strength and Momentum Dependence of Electron-Phonon Coupling Using Resonant Inelastic X-Ray Scattering," Phys. Rev. X **6**, 041019 (2016).

[231] K. Bieniasz, S. Johnston, and M. Berciu, "Beyond the single-site approximation modeling of electron-phonon coupling effects on resonant inelastic X-ray scattering spectra," SciPost Phys. **11**, 62 (2021).

[232] M. Rossi, R. Arpaia, R. Fumagalli, M. Moretti Sala, D. Betto, K. Kummer, G. M. De Luca, J. van den Brink, M. Salluzzo, N. B. Brookes, L. Braicovich, and G. Ghiringhelli, "Experimental Determination of Momentum-Resolved Electron-Phonon Coupling," Phys. Rev. Lett. **123**, 027001 (2019).

[233] C. T. Chen, F. Sette, Y. Ma, M. S. Hybertsen, E. B. Stechel, W. M. C. Foulkes, M. Schulter, S.-W. Cheong, A. S. Cooper, L. W. Rupp, B. Batlogg, Y. L. Soo, Z. H. Ming, A. Krol, and Y. H. Kao, "Electronic states in $La_{2-x}Sr_xCuO_{4+\delta}$ probed by soft-x-ray absorption," Phys. Rev. Lett. **66**, 104–107 (1991).

[234] N. B. Brookes, F. Yakhou-Harris, K. Kummer, A. Fondacaro, J. Cezar, D. Betto, E. Velez-Fort, A. Amorese, G. Ghiringhelli, L. Braicovich, R. Barrett, G. Berruyer, F. Cianciosi, L. Eybert, P. Marion, P. van der Linden, and L. Zhang, "The beamline ID32 at the ESRF for soft X-ray high energy resolution resonant inelastic X-ray scattering and polarisation dependent X-ray absorption spectroscopy," Nucl. Instr. Meth. Phys. Res. A **903**, 175 – 192 (2018).

[235] I. G. Lang and Y. A. Firsov, Sov. Phys. JETP **16**, 1301 (1962).

[236] A. Geondzhian and K. Gilmore, "Generalization of the franck-condon model for phonon excitations by resonant inelastic x-ray scattering," Phys. Rev. B **101**, 214307 (2020).

[237] A. Geondzhian, A. Sambri, G. M. De Luca, R. Di Capua, E. Di Gennaro, D. Betto, M. Rossi, Y. Y. Peng, R. Fumagalli, N. B. Brookes,

L. Braicovich, K. Gilmore, G. Ghiringhelli, and M. Salluzzo, "Large Polarons as Key Quasiparticles in $SrTiO_3$ and $SrTiO_3$-Based Heterostructures," Phys. Rev. Lett. **125**, 126401 (2020).

[238] M. Salluzzo, G. De Luca, R. Di Capua, A. Gambardella, Z. Ristic, and R. Vaglio, "Electric field effect and superconducting–insulating transition in '123' cuprate superconductors," Superconductor Science and Technology **22**, 034010 (2009).

[239] G. De Luca, G. Ausanio, M. Salluzzo, and R. Vaglio, "Growth mode selection and transport properties in $Nd_1Ba_2Cu_3O_7$ superconducting films deposited by high oxygen pressure diode sputtering," Superconductor Science and Technology **18**, 791 (2005).

[240] M. Salluzzo, G. M. de Luca, D. Marrè, M. Putti, M. Tropeano, U. Scotti di Uccio, and R. Vaglio, "Thickness effect on the structure and superconductivity of $Nd_{1.2}Ba_{1.8}Cu_3O_z$ epitaxial films," Phys. Rev. B **72**, 134521 (2005).

[241] B. Liang and C. T. Lin, "On the growth of underdoped $Bi_2Sr_2CaCu_2O_{8+\delta}$ single crystals by TSFZ method," J. Cryst. Growth **237**, 756 (2002).

[242] J. S. Wen, Z. J. Xu, G. Y. Xu, M. Hücker, J. M. Tranquada, and G. D. Gu, "Large Bi-2212 single crystal growth by the floating-zone technique," J. Cryst. Growth **310**, 1401 (2008).

[243] Y.-X. Zhang, L. Zhao, G.-D. Gu, and X.-J. Zhou, "A Reproducible Approach of Preparing High-Quality Overdoped $Bi_2Sr_2CaCu_2O_{8+\delta}$ Single Crystals by Oxygen Annealing and Quenching Method," Chinese Physics Letters **33**, 067403 (2016).

[244] K.-J. Zhou, A. Walters, M. Garcia-Fernandez, T. Rice, M. Hand, A. Nag, J. Li, S. Agrestini, P. Garland, H. Wang, S. Alcock, I. Nistea, B. Nutter, N. Rubies, G. Knap, M. Gaughran, F. Yuan, P. Chang, J. Emmins, and G. Howell, "I21: an advanced high-resolution resonant inelastic X-ray scattering beamline at Diamond Light Source," Journal of Synchrotron Radiation **29** (2022), 10.1107/S1600577522000601.

[245] I. Jarrige, V. Bisogni, Y. Zhu, W. Leonhardt, and J. Dvorak, "Paving the way to ultra-high-resolution resonant inelastic x-ray scattering with the six beamline at NSLS-II," Synchrotron Radiation News **31**, 7–13 (2018).

[246] W. S. Lee, S. Johnston, B. Moritz, J. Lee, M. Yi, K. J. Zhou, T. Schmitt, L. Patthey, V. Strocov, K. Kudo, Y. Koike, J. van den Brink, T. P. Devereaux, and Z. X. Shen, "Role of Lattice Cou-

pling in Establishing Electronic and Magnetic Properties in Quasi-One-Dimensional Cuprates," Phys. Rev. Lett. **110**, 265502 (2013).

[247] S. Johnston, C. Monney, V. Bisogni, K.-J. Zhou, R. Kraus, G. Behr, V. N. Strocov, J. Málek, S.-L. Drechsler, J. Geck, T. Schmitt, and J. van den Brink, "Electron-lattice interactions strongly renormalize the charge-transfer energy in the spin-chain cuprate Li_2CuO_2," Nat. Commun. **7**, 10563 (2016).

[248] V. Bisogni, L. Simonelli, L. J. P. Ament, F. Forte, M. Moretti Sala, M. Minola, S. Huotari, J. van den Brink, G. Ghiringhelli, N. B. Brookes, and L. Braicovich, "Bimagnon studies in cuprates with resonant inelastic x-ray scattering at the O K edge. I. Assessment on La_2CuO_4 and comparison with the excitation at Cu L_3 and Cu K edges," Phys. Rev. B **85**, 214527 (2012).

[249] X. Feng, S. Sallis, Y.-C. Shao, R. Qiao, Y.-S. Liu, L. C. Kao, A. S. Tremsin, Z. Hussain, W. Yang, J. Guo, and Y.-D. Chuang, "Disparate exciton-phonon couplings for zone-center and boundary phonons in solid-state graphite," Phys. Rev. Lett. **125**, 116401 (2020).

[250] A. Geondzhian and K. Gilmore, "Demonstration of resonant inelastic x-ray scattering as a probe of exciton-phonon coupling," Phys. Rev. B **98**, 214305 (2018).

[251] L. Taillefer, "Scattering and Pairing in Cuprate Superconductors," Annual Review of Condensed Matter Physics **1**, 51–70 (2010).

[252] M. Hashimoto, G. Ghiringhelli, W.-S. Lee, G. Dellea, A. Amorese, C. Mazzoli, K. Kummer, N. B. Brookes, B. Moritz, Y. Yoshida, H. Eisaki, Z. Hussain, T. P. Devereaux, Z.-X. Shen, and L. Braicovich, "Direct observation of bulk charge modulations in optimally doped $Bi_{1.5}Pb_{0.6}Sr_{1.54}CaCu_2O_{8+\delta}$," Phys. Rev. B **89**, 220511 (2014).

[253] E. H. da Silva Neto, P. Aynajian, A. Frano, R. Comin, E. Schierle, E. Weschke, A. Gyenis, J. Wen, J. Schneeloch, Z. Xu, S. Ono, G. Gu, M. Le Tacon, and A. Yazdani, "Ubiquitous interplay between charge ordering and high-temperature superconductivity in cuprates," Science **343**, 393–396 (2014).

[254] W. S. Lee, K.-J. Zhou, M. Hepting, J. Li, A. Nag, A. C. Walters, M. Garcia-Fernandez, H. C. Robarts, M. Hashimoto, H. Lu, B. Nosarzewski, D. Song, H. Eisaki, Z. X. Shen, B. Moritz, J. Zaanen, and T. P. Devereaux, "Spectroscopic fingerprint of charge order melting driven by quantum fluctuations in a cuprate," Nature Physics **17**, 53–57 (2021).

[255] R. Arpaia, S. Caprara, R. Fumagalli, G. De Vecchi, Y. Y. Peng, E. An-

dersson, D. Betto, G. M. De Luca, N. B. Brookes, F. Lombardi, M. Salluzzo, L. Braicovich, C. Di Castro, M. Grilli, and G. Ghiringhelli, "Dynamical charge density fluctuations pervading the phase diagram of a Cu-based high-Tc superconductor," Science **365**, 906 (2019).

[256] E. Pavarini, I. Dasgupta, T. Saha-Dasgupta, O. Jepsen, and O. K. Andersen, "Band-structure trend in hole-doped cuprates and correlation with $t_{c\max}$," Phys. Rev. Lett. **87**, 047003 (2001).

List of publications

[1] L. Martinelli, D. Betto, K. Kummer, R. Arpaia, L. Braicovich, D. Di Castro, N. B. Brookes, M. Moretti Sala, and G. Ghiringhelli, "Fractional Spin Excitations in the Infinite-Layer Cuprate $CaCuO_2$", Phys. Rev. X **12**, 021041 (2022).

[2] G. Krieger, L. Martinelli, S. Zeng, L. E. Chow, K. Kummer, R. Arpaia, M. Moretti Sala, N. B. Brookes, A. Ariando, N. Viart, M. Salluzzo, G. Ghiringhelli, and D. Preziosi, "Charge and spin order dichotomy in $NdNiO_2$ driven by the capping layer", Phys. Rev. Lett. **129**, 027002 (2022).

[3] Y. Peng, L. Martinelli, Q. Li, M. Rossi, M. Mitrano, R. Arpaia, M. M. Sala, Q. Gao, X. Guo, G. M. De Luca, A. Walters, A. Nag, A. Barbour, G. Gu, J. Pelliciari, N. B. Brookes, P. Abbamonte, M. Salluzzo, X. Zhou, K.-J. Zhou, V. Bisogni, L. Braicovich, S. Johnston, and G. Ghiringhelli, "Doping dependence of the electron-phonon coupling in two families of bilayer superconducting cuprates", Phys. Rev. B **105**, 115105 (2022).

[4] D. Betto, R. Fumagalli, L. Martinelli, M. Rossi, R. Piombo, K. Yoshimi, D. Di Castro, E. Di Gennaro, A. Sambri, D. Bonn, G. A. Sawatzky, L. Braicovich, N. B. Brookes, J. Lorenzana, and G. Ghiringhelli, "Multiple-magnon excitations shape the spin spectrum of cuprate parent compounds", Phys. Rev. B **103**, L140409 (2021).

[5] R. Arpaia, L. Martinelli, M. M. Sala, S. Caprara, A. Nag, N. B. Brookes, P. Camisa, Q. Li, Q. Gao, X. Zhou, M. Garcia-Fernandez, K.-J. Zhou, E. Schierle, T. Bauch, Y. Y. Peng, C. D. Castro, M. Grilli, F. Lombardi, L. Braicovich, and G. Ghiringhelli, "Signature of quantum criticality in cuprates by charge density fluctuations", arXiv.org (2022). Under review.